COLLEGE DOCTORAL BRETAGNE
SCIENCES DE LA MATIERE DES MOLECULES ET MATERIAUX

Université de Rennes

THÈSE DE DOCTORAT DE

L'UNIVERSITÉ DE RENNES

ÉCOLE DOCTORALE N° 638
Sciences de la Matière, des Molécules et Matériaux
Spécialité : *Sciences des Matériaux*

Par
Valentin CHERRUAULT

Étude acoustique, magnétique, et structurale de matériaux corrélés via l'optique ultrarapide

De la diffusion Brillouin et du couplage spin-réseau à la transition supraconductrice et à l'optique non linéaire

Thèse présentée et soutenue à Rennes, le 18 décembre 2025
Unité de recherche : Institut de Physique de Rennes, UMR 6251

Rapporteur·trice·s avant soutenance :

Vitali GOUSSEV	Professeur, Le Mans Université
Mathieu DUCOUSSO	Professeur / chercheur, ENSAM Paris / Safran

Composition du Jury :

Présidente :	Laura THEVENARD	Directrice de recherche CNRS, Institut des Nanosciences de Paris
Examinateur·trice·s :	Vitali GOUSSEV	Professeur, Le Mans Université
	Mathieu DUCOUSSO	Professeur / chercheur, ENSAM Paris / Safran
	Laura THEVENARD	Directrice de recherche CNRS, Institut des Nanosciences de Paris
	Benoit CORRAZE	Maitre de conférences, Institut des Matériaux Jean Rouxel de Nantes
Dir. de thèse :	Thomas PEZERIL	Directeur de recherche CNRS, Institut de physique de Rennes
Co-dir. de thèse :	Ievgeniia CHABAN	Chargée de recherche CNRS, Ecole Polythechique

COLLEGE SCIENCES DE LA MATIERE
DOCTORAL DES MOLECULES
BRETAGNE ET MATERIAUX

Université de Rennes

DOCTORAL THESIS OF THE

UNIVERSITY OF RENNES

DOCTORAL SCHOOL N°638
Sciences of Matter, Molecules, and Materials
Specialization : Material Sciences

By

Valentin CHERRUAULT

Ultrafast Optical Studies of Acoustic, Magnetic, and Structural Phase Dynamics in Correlated Materials

From Brillouin Scattering and Spin-Lattice Coupling to Superconductivity and Nonlinear Optics

Thesis presented and defended in Rennes on December 18th, 2025
Research Unit : Rennes Institute of Physics, UMR 6251

Reviewers :

Vitali GOUSSEV	Professor, Le Mans University
Mathieu DUCOUSSO	Professor / researcher, ENSAM Paris / Safran

Jury :

President :	Laura THEVENARD	CNRS Research Director / Nanosciences Institute of Paris
Members :	Vitali GOUSSEV	Professor, Le Mans University
	Mathieu DUCOUSSO	Professor / researcher, ENSAM Paris / Safran
	Laura THEVENARD	CNRS Research Director / Nanosciences Institute of Paris
	Benoit CORRAZE	Associate Professor, Jean Rouxel Institute of Materials, Nantes
Supervisor :	Thomas PEZERIL	CNRS Research Director, Rennes Institute of Physics
Co-Supervisor :	Ievgeniia CHABAN	CNRS Research Scientist, École Polytechnique, Paris

Acknowledgments

I would like to express my deepest gratitude to my supervisors, Thomas Pezeril and Ievgeniia Chaban, for offering me the opportunity to undertake this work and for their continuous guidance and support, which were essential to its completion. I am also thankful for the numerous opportunities they provided to attend conferences and thematic schools throughout my PhD journey, as well as for the wide variety of topics explored. I am particularly grateful to both of them for the time they dedicated to my thesis project and for always striking the perfect balance between too much and too little supervision.

I sincerely thank the members of my individual follow-up committee, Maciej Lorenc and Etienne Janod, for their careful attention to the progress of this thesis and their constructive feedback.

I am deeply appreciative of my colleagues and collaborators at the Institute of Physics of Rennes, particularly those from the Materials and Glass Department, with whom I had the pleasure of working. Their assistance and stimulating discussions made this journey both productive and enjoyable. I am especially grateful to Nathalie Mabic and Nathalie Gicquiaux for their support with administrative matters, and to Julien Chollet and Mickael Le Fur for designing and fabricating custom mechanical parts for our experiments with remarkable responsiveness. I also thank Nicolas Godin, Elzbieta Trzop, and Marina Servol from the Materials and Light Department for their assistance, particularly during the initial installation of our experiments in a new laboratory.

I would also like to thank Julien Morin, Ronan Lefort, and Thierry Guizouarn for sharing their expertise in microscopy, ellipsometry, and helium cryogenics. Without their contributions, several key results of this work would not have been possible.

I am indebted to the GigaSpin ANR project collaborators from the Bordeaux Optics Institute—Eric Cormier, Giorgio Santarelli, and Paolo Paris—for the enriching discussions and the opportunity to work in their laboratory. I also thank the other collaborators of the project, particularly Jamal Ben Youssef, who fabricated the samples used in the linear TDBS investigations.

I wish to thank the team from the Institut Jean Lamour, who designed and fabricated the magnetic epitaxial superlattices—especially Thomas Hauet and Corentin Pfaff. Without their unique epitaxial growth process and expertise, it would not have been possible to reveal spin-lattice coupling on the picosecond timescale.

I am grateful to the members of the Rennes Institute of Chemical Sciences—Frédéric Paul, Franck Camerel, and Olivier Mongin—for the opportunity to study their organoruthenium two-photon absorber. It was a real pleasure to extend our TDBS studies to organic matter and to characterize promising materials for medical applications.

During my PhD, I also had the opportunity to investigate superconducting materials, and I wish to thank Javier Briatico and Abdelmadjid Anane for their valuable advice and for providing the YBCO samples.

I would also like to thank the interns—Tom Monnier, Théo Huguenin, and Maxence Paly—who worked with me, for their dedication and involvement in the various research topics.

I gratefully acknowledge the financial support of the ANR, without which this research would not have been possible.

My sincere thanks also go to the reviewers of this thesis, Vitaly Goussev and Mathieu Ducousso, for their time and constructive comments.

Finally, I am grateful to the other members of the jury, Laura Thevenard and Benoît Corraze, for their participation and interest in this work.

Contents

Acknowledgments **1**

General introduction **5**

I Ultrafast photoacoustics in transparent materials: from linear transparency to multiphoton absorption regimes **7**

1 Context **7**

2 Theory: Time-domain Brillouin scattering **8**
2.1 Ultrashort laser pulse heating . . . 8
2.2 Thermoelastic excitation of acoustic waves . . . 13
2.3 Photoelastic detection of longitudinal acoustic waves . . . 16

3 Investigations in the linear transparency regime **21**
3.1 Experimental setup . . . 21
3.1.1 Acousto-optic modulator . . . 22
3.1.2 Delay stage . . . 23
3.1.3 BBO . . . 23
3.1.4 Glan-Taylor polarizer . . . 24
3.1.5 PBS and QWP . . . 24
3.1.6 Balanced photodetection . . . 25
3.1.7 Synchronous detection . . . 25
3.2 Results . . . 26
3.3 Outlook: TDBS investigations in the linear transparency regime . . . 37

4 Multiphoton generation of longitudinal acoustic waves **38**
4.1 Experimental setup . . . 39
4.2 Two-photon activation of thermal response in complex organometallic . . . 39
4.3 Two-photon absorption for direct LAWs generation in SrTiO3 . . . 47
4.4 Multi-photon absorption for direct LAWs generation in LiNbO3 and LaAlO3 . . . 49
4.5 Summary of multiphoton LAWs generation . . . 53

5 Conclusion **53**

II Ultrafast opto-acousto-magnetism in correlated materials **55**

1 Context **55**

2 Theory: Magnetism, magneto-optics, magneto-acoustics **55**
2.1 Origin of magnetism and magnetic phases . . . 56
2.2 Magneto-optic effects . . . 59
2.2.1 Magneto-optic Faraday effect . . . 59
2.2.2 Magneto-optic Kerr effect . . . 61
2.3 Ultrafast laser demagnetization . . . 65

2.4 Magnetoacoustics . . . 69
2.4.1 Magnetostriction and the Villari effect . . . 69
2.4.2 Piezomagnetism . . . 70
2.5 Magnetic precession . . . 70
2.6 Interfacial anisotropy . . . 72

3 Spin-lattice interactions at picosecond timescale 73
3.1 Magneto-optical experimental setup . . . 74
3.2 Static investigations . . . 75
3.3 Dynamical investigations . . . 77
3.4 Outlook: Spin-lattice interactions at picosecond timescale . . . 86

4 Giant surface acoustic waves for the manipulation of magnetization 86
4.1 Theory of giant surface acoustic wave generation and propagation . . . 86
4.2 Nanosecond time-domain MOKE setup for probing SAW effects in ferromagnetic thin films . . . 89
4.3 Nanosecond time-domain MOKE probing of SAW effects in ferromagnetic cobalt thin film . . . 93
4.4 Summary: Giant surface acoustic waves for the manipulation of magnetization . . . 94

5 Ultrafast optical probing of the superconducting transition 94
5.1 Theoretical considerations about YBCO, superconductivity, and the Meissner effect . 95
5.2 Time-resolved optical probing of the YBCO superconducting transition: experimental setup . . . 97
5.3 Time-resolved optical probing of the YBCO superconducting transition: TDBS results 98
5.4 Time-resolved optical probing of the YBCO superconducting transition: MOKE results 101
5.5 Outlook: Optical probing and future directions for superconductivity in cuprates . . . 104

6 Conclusion 105

General conclusion 107

Résumé en français 109

References 115

Appendix 130

A: Second harmonic generation in crystals 130
A.1 Theory: Second harmonic generation . . . 130
A.2 Investigations of mono-atomic layer material structures through SHG: Experiments . . 131

B: Custom femtosecond laser 138

C: Mira 900/RegA laser 140

D: Numerical simulations using Python **142**
D.3 Numerical simulation of the two-temperature model 142
D.4 Numerical simulation of the strain profile in Thomsen's formalism 144
D.5 Numerical simulation of the photoelastic detection of longitudinal acoustic waves . . . 145
D.6 Numerical simulation of the three-temperature model 149
D.7 Numerical simulation of the Landau-Lifshitz-Gilbert equation 151
D.8 Numerical simulation of giant SAW generation from optical ring pump 152

General introduction

The aim of this thesis is to contribute to the development of an all-optical tool for analyzing the acoustic and magnetic properties of materials, as well as their ultrafast dynamical responses at the picosecond timescale. This work was carried out within the framework of an ANR project in which two PhD theses were initiated in parallel. The present document corresponds to one of these two theses. Its objectives, in view of the completion of the project, were to implement picosecond-resolved all-optical pump-probe experiments for two main purposes. The first was the optical generation and detection of longitudinal acoustic waves (LAWs) in transparent materials in order to determine their Brillouin frequencies and the attenuation of the acoustic waves, with the ultimate goal of identifying candidate materials for resonant excitation of longitudinal modes. This resonant excitation constitutes the central focus of the Paolo Paris thesis, the second doctoral work of the project, for which he and his team developed a GHz-tunable repetition rate laser. The second objective of the present work was to study magnetic precession and to identify materials potentially suitable for resonant optical excitation.

The first chapter dictated to picosecond acoustics begins by the characterization of the elastic properties of transparent materials, and more specifically their Brillouin frequencies. For this purpose, a femtosecond-laser-based pump–probe experimental setup was implemented, and its working principle is detailed. The theoretical description of the photothermal generation of acoustic waves and their photoelastic probing are also presented in this first chapter. Using the experimental setup, about a dozen transparent substrates were characterized, and the results were compared with values reported in the literature. Once the linear-regime investigations results were established, we extended the experimental study to complex organometallics specifically designed for two-photon absorption in the near-infrared. Such materials are actively investigated owing to their promising performance as contrast agents and their ability to target specific cells. Of particular interest is their potential application in cancer treatment, where thermal activation of selected organometallics, combined with their capacity to release singlet oxygen, can destroy malignant cells without collateral damage. In this context, the thermal response of the investigated material was quantified via the longitudinal acoustic waves induced by its ultrafast relaxation dynamics involving intersystem electronic transitions. The use of nonlinear activation in the near-infrared is particularly attractive, since this spectral region lies within the transparency window of human skin. The time domain Brillouin scattering (TDBS) setup was then further used to investigate transparent solids in order to investigate nonlinear acoustic generation via two-photon absorption. This work extended the linear-regime study of transparent materials, where a metallic transducer was required. In the nonlinear regime, we examined one material with an optical gap below the two-photon excitation energy, as well as two materials with larger gaps: one centrosymmetric and one non-centrosymmetric.

A second chapter is dedicated to ultrafast opto-acousto-magnetism. This chapter extends the scope of ultrafast all-optical studies to spin-lattice coupling in epitaxial ferromagnetic heterostructures, surface acoustic waves (SAWs) in ferromagnetic thin films, and optical probing of superconducting transition. Following a theoretical introduction of magnetic phases, ultrafast optical demagnetization, magnetoelastics, magnetic precession, and interfacial anisotropy, the spin-lattice coupling determination of the ferromagnetic multilayer is experimentally investigated. The investigated samples are designed to exhibit an out-of-plane magnetization and to allow optical generation of acoustic waves while delaying their arrival in the ferromagnetic stack from the laser demagnetization. Then we present the measurement of the influence of giant surface acoustic waves on the magnetization state of a cobalt ferromagnetic thin film. The giant surface acoustic waves are optically generated from a ring-shaped pump and probed with optical interferometry. The magnetic state of the ferromagnetic

film is probed from magnetic precession induced by an optical femtosecond pump. Finally, the second chapter of this work concludes with a study on the feasibility of detecting a superconducting transition optically. The long-term goal is to investigate, at the picosecond timescale, the effect of strong lattice deformations on the critical temperature of superconductors. Both optical and mechanical influences on the critical temperature of cuprates are subjects of strong current interest. However, before addressing this question, it was necessary to establish whether our pump–probe setup could detect the superconducting transition. To this end, temperature-dependent TDBS measurements were carried out on a YBCO/STO:Nb sample, in which YBCO acted as the transducer and STO:Nb as the substrate for detecting acoustic waves originating from YBCO. In parallel, time- and temperature-resolved magneto-optical Kerr measurements were performed on cobalt discs in order to test the detection of the superconducting transition through the Meissner effect. In this configuration, a YBCO layer was placed between the cobalt dots and an external magnet. If magnetic flux is expelled by the Meissner effect, the magnetization of cobalt reorients into the plane, and thus, a polar magneto-optic Kerr effect (MOKE) geometry cannot detect magnetic precession.

In addition to these two chapters, a short appendix presents the investigation of crystallographic structures using second harmonic generation. Particular attention is given to atomic monolayer dichalcogenides, as well as to the study of twisted bilayers. We also provide in the appendix Python-based numerical implementations of the phenomena introduced in the theoretical sections.

Part I

Ultrafast photoacoustics in transparent materials: from linear transparency to multiphoton absorption regimes

1 Context

Brillouin scattering of light is a common method used to study the elastic characteristics of materials. This phenomenon, predicted by Léon Brillouin in 1922, involves the scattering of light and X-rays by acoustic waves [1], and has been extensively utilized in the examination of condensed matter. The review [2], released a century after Brillouin's theory was first published, details significant advancements achieved through this theory. This historical overview showcases a wide range of applications, from optical propagation in free space to optical waveguides and even microscale uses like optical resonators. In parallel with the development of Brillouin spectroscopy—initially performed using a Fabry–Pérot spectrometer and, more recently, with the virtually imaged phased array (VIPA) spectrometer, which has enabled the emergence of Brillouin microscopy [3] for in-depth investigations of both organic and inorganic materials—the advent of ultrafast lasers has opened a new window for studying Brillouin scattering in the time domain. In this regime, the Brillouin signal is encoded in the time domain, giving rise to time-domain Brillouin scattering (TDBS), characterized by coherent control over both the excitation and detection of acoustic waves. Unlike conventional Brillouin spectroscopy, which relies on thermally induced or quantum fluctuations to generate the acoustic wavepackets that scatter light, TDBS employs an all-optical pump–probe approach that enables fully coherent generation and detection of these wavepackets. The first measurements of TDBS have been performed in solid materials since, at least, the 1980s [4–7].

In this manuscript, we focus on a specific regime of TDBS, which enables the study of longitudinal acoustic wave excitation and propagation at frequencies reaching several tens of gigahertz. To achieve the necessary temporal resolutions, typically below one picosecond, the all-optical pump-probe method stands out as the technique of choice and arguably the only one currently capable of delivering such fine temporal resolution. Such resolution requires the use of ultrashort optical excitation, made possible by femtosecond laser sources. The pump pulse, absorbed by a semi-transparent or opaque material that serves as an optical transducer, generates a transient acoustic wave, while the probe pulse is used to optically detect the acoustic wave that travels in the surrounding media. The propagation of the acoustic wave is recorded thanks to a precisely controlled optical delay between the pump and probe pulses. The first objective of this chapter is to establish the Brillouin frequencies of a wide range of transparent substrates in order to identify potential candidates for resonant pumping investigations. In this chapter, we begin by introducing the basic principles and theoretical framework underlying picosecond photoacoustics. We will explain how a femtosecond optical pulse can generate an acoustic wave in a material and how this wave can be optically probed. Once the theory is introduced, we will present the experimental results obtained on various substrate materials, as well as the experimental setup used to acquire these results. We then extend our study to the nonlinear optical generation of acoustic waves via multiphoton absorption. In this section, we demonstrate how this method enables the investigation of a complex organic material with potential applications in biomedical imaging and photothermal therapy. Nonlinear generation will also be explored in crystalline solids.

2 Theory: Time-domain Brillouin scattering

The detection of ultrafast phenomena in the picosecond timescale cannot be achieved using conventional electronic methods due to their inherent limitations in temporal resolution. This is why we have chosen an entirely optical approach, based on TDBS. In practice, an acoustic phonon corresponds to a local mechanical deformation that propagates through the material. This propagating deformation manifests itself as a transient overpressure, which induces a local variation of the optical properties of the material that enables the optical detection of the acoustic wave.

Before delving into the mechanisms of optical detection, it is essential to understand how the acoustic wave is generated. In our case, the excitation is driven by absorption of femtosecond laser pulse energy, which induces an ultrafast thermoelastic expansion that generates the acoustic wave.

2.1 Ultrashort laser pulse heating

The optical generation of LAWs in transparent materials generally requires the use of an absorbing film. A simple and commonly employed method consists of depositing a thin metallic film on one side of the material under investigation. This metallic film, referred to as the transducer, is responsible for absorbing the energy of the femtosecond laser pulse. The ultrafast thermal expansion of the transducer then induces a mechanical stress at the interface with the studied material, called substrate. Considering the typical dimensions of the laser spot as compared to the optical penetration depth of the laser, we will consider in the following a 1D planar situation with a single spatial depth coordinate z.

We begin here by describing the thermal expansion mechanism of a metallic film induced by the absorption of a femtosecond optical pulse. Upon such ultrashort excitation, it is primarily the free electrons in the metal that respond first. Their temperature rises sharply within a timescale on the order of a femtosecond. This electronic energy is then progressively transferred to the atomic lattice via electron-phonon coupling. This heat transfer from the electrons to the lattice drives the thermoelastic expansion of the metal. To maximize the efficiency of this transfer, one must take into account the electron-phonon coupling strength, specific to each metal, in order to select a transducer material best suited for our studies.

To model the distinct heating dynamics of the electrons and the lattice following femtosecond excitation, the two-temperature model (TTM) appears to be perfectly adapted [8–12]. This model introduces two separate temperatures: the electron temperature T_e and the lattice temperature T_l, which evolve according to a system of coupled thermal equations that describe the energy exchange between these two subsystems. In order to establish the appropriate system of equations for our case, it is necessary to first recall the general law of heat conduction, which forms the foundation for describing these thermal transfer processes. The canonical expression of this is:

$$C\frac{\partial T}{\partial t} = -\nabla \mathbf{Q} + S, \tag{1}$$

where C_V is the volumetric specific heat, $\mathbf{Q}$ is the heat flux vector, and S is the source term from the excitation. In our case S comes from the energy absorbed from the optical femtosecond pump pulse. Equation (1) is expressed separately for electronic and lattice temperatures, and linked to each other by introducing an electron/phonon coupling factor G.

$$C_e\frac{\partial T_e}{\partial t} = -\nabla \mathbf{Q_e} - G(T_e - T_l) + S \tag{2}$$

$$C_l\frac{\partial T_l}{\partial t} = \nabla \mathbf{Q_l} + G(T_e - T_l) \tag{3}$$

Note the absence of a source term in the lattice heat conduction, Equation (3). This is due to the ultrafast nature of femtosecond optical excitation that is faster than the response time of the lattice but slower than the electronic response time. The electron-phonon coupling factor is given by:

$$G = \frac{9}{16} \cdot \frac{n_e \, k_B^2 \, T_D^2 \, \nu_F}{\Lambda(T_l) \, T_l \, E_F}, \tag{4}$$

where T_D is the Debye temperature, ν_F is the Fermi velocity, $\Lambda(T_l)$ is the electron mean free path at the lattice temperature, and E_F is the Fermi energy. This expression is derived within a quantum-mechanical framework assuming a Debye phonon spectrum and explicitly accounts for size effects through a size-limited electron mean free path, which are relevant for optical heating of nanometric metallic films [13–15]. Now, we detail the volumetric specific heats C_e and C_l that are different depending on whether it is for the free electron cloud or for the whole lattice.

$$C_l = \rho \cdot C_p \tag{5}$$

$$C_e = \frac{\pi^2 \, n_e \, k_B^2}{2E_F} T_e \tag{6}$$

In Equation (5), ρ is the volumetric mass and C_p the heat capacity of the material that partially absorbs the laser pulse. Here, the lattice volumetric specific heat is supposed to be temperature independent. It is an acceptable assumption in our investigation range of temperature. In Equation (6), n_e is the free electron density, k_B is the Boltzmann constant, and E_F is the Fermi energy. Equation (6) is based on the Sommerfeld model, and here the electron volumetric specific heat is temperature-dependent. The C_e dependence on T_e is justified by the strong temperature rise of the free electron cloud after absorption of the femtosecond optical pulse. The analytical expressions of the heat flux in Equations (2) and (3) are distinct whether it is for the electronic cloud or for the atomic lattice. We use the semi-relativistic Cattaneo-Vernotte model for $\mathbf{Q_e}$, and for the lattice, $\mathbf{Q_l}$ is given by Fourier's heat conduction law, as follows:

$$\tau_e \frac{\partial \mathbf{Q_e}}{\partial t} + \mathbf{Q_e} = -k_e \nabla T_e, \tag{7}$$

$$\mathbf{Q_l} = -k_l \nabla T_l. \tag{8}$$

In Equation (7), τ_e is the electron relaxation time and k_e is the thermal conductivity of the free electron cloud. Respectively, in Equation (8), k_l is the thermal conductivity of the atomic lattice. In order to determine the electron relaxation time, a key parameter in the TTM and a critical factor in selecting metallic transducers for picosecond acoustics, we exploit its relationship with the metal resistivity ϱ, given by the following expression:

$$\varrho = \frac{m^*}{n_e \, q^2 \, \tau_e}, \tag{9}$$

where m^* denotes the effective mass of the electron, n_e is the free electron density, and q is the elementary charge of the electron. The effective mass ratio m^*/m_e is extracted from literature [16–27]. The values reported in Table [1] should be interpreted with caution, as they vary depending on both the source and the method of determination. Typically, effective masses are determined using either the de Haas-Van Alphen effect or density functional theory (DFT). Furthermore, the effective mass is highly anisotropic, strongly depending on the crystallographic axis and the specific energy band of the Fermi surface under consideration. For these reasons, discrepancies between sources are expected. Despite these uncertainties, the estimation of the electronic relaxation time remains

reasonably reliable. For the other parameters in Equation (9), it is more simple. The resistivity ϱ is taken from C. Kittel [28], and the free electron density n_e is calculated from:

$$n_e = Z \cdot \frac{N_A \cdot \rho}{M}, \tag{10}$$

where Z corresponds to the number of conduction electrons per atom at room temperature, N_A is the Avogadro number, ρ is the density, and M is the molar mass. We obtain Z from the electronic configuration of the element. This is why it is important to note that, in Table [1], the configurations listed for Cr, Cu, Ag, Au, and Gd do not follow the standard Klechkowski rule for subshell filling. Instead, they reflect experimentally observed configurations that are stabilized by half-completed subshells. For Cr, Cu, Ag, and Au, this involves a half-completed d subshell, while for Gd, the stabilization arises from a half-completion of the 4f subshell. Based on the values in Table [1] and

Metal	Electronic structure	m^*/m_e	n_e (10^{28} m^{-3})	ϱ_{295K} (n$\Omega \cdot$ m)	τ_e (fs)
Mg	[Ne] $3s^2$	1.0	8.6	43.0	9.11
Al	[Ne] $3s^2\,3p^1$	1.2	18.1	27.4	8.59
V (100)	[Ar] $3d^3\,4s^2$	1.8	14.4	199	2.23
V (111)		1.8	14.4	199	2.23
V (110)		2.2	14.4	199	2.72
Cr	[Ar] $3d^5\,4s^1$	1.2	8.33	129	3.97
Fe	[Ar] $3d^6\,4s^2$	8.0	17.0	98	17.1
Co	[Ar] $3d^7\,4s^2$	1.3	18.2	58	4.37
Ni	[Ar] $3d^8\,4s^2$	1.1	18.3	70	3.05
Cu	[Ar] $3d^{10}\,4s^1$	1.3	8.49	17.0	32.0
Ga	[Ar] $3d^{10}\,4s^2\,4p^1$	0.62	1.53	148.5	0.98
Ag	[Kr] $4d^{10}\,5s^1$	0.85	5.90	16.1	31.8
Gd	[Xe] $4f^7\,5d^1\,6s^2$	1.2	9.06	1300	0.36
Au	[Xe] $4f^{14}\,5d^{10}\,6s^1$	1.1	5.90	22.0	30.1

Table 1: Electronic configuration, effective mass ratio, free electron density, resistivity at 295 K, and electron relaxation time for various materials.

considering that our femtosecond laser delivers pulses lasting over one hundred femtoseconds, it is, in some cases, possible to neglect the τ_e-dependent term in Equation (7) and instead use the simpler Fourier law of heat conduction. However, we choose not to do this simplification a priori in our model. One simplification that is done in our two-temperature model stems from the fact that we are only investigating heat transport along the z-axis. This allows us to project the full model onto this single axis. The resulting 1D form of the model is given as follows:

$$C_e(T_e)\frac{\partial T_e}{\partial t} = k_e\frac{\partial^2 T_e}{\partial z^2} + \tau_e\frac{\partial}{\partial z}\left[\frac{\partial Q_e}{\partial t}\right] - G(T_e - T_l) + S, \tag{11}$$

$$C_l\frac{\partial T_l}{\partial t} = k_l\frac{\partial^2 T_l}{\partial z^2} + G(T_e - T_l). \tag{12}$$

Note that in Equation (12), Q_l is neglected since the lattice heat conduction is two orders of magnitude lower than for the free electron gas. The last parameter that we need to express is the source term S. In the TTM, the laser heating source term is commonly given by:

$$S(z,t) = \sqrt{\frac{4ln(2)}{\pi}} \cdot \frac{(1-R)\Phi}{\xi\, t_p} \cdot exp\left\{-\frac{z}{\xi} - 4ln(2)\left(\frac{(t-2t_p)}{t_p}\right)^2\right\}, \tag{13}$$

where R is the optical reflectivity, Φ is the laser fluency, t_p is the pulse duration, and ξ is the optical penetration depth [29, 30]. The optical penetration depth is given by the Beer-Lambert law,

$$\xi = \frac{1}{\alpha_{abs}}. \tag{14}$$

The absorption coefficient α_{abs} can be calculated using the following expression:

$$\alpha_{abs} = \frac{4\pi}{\lambda} \operatorname{Im}(\bar{n}(\lambda)), \tag{15}$$

where $\bar{n} = n + i\kappa$ is the complex refractive index, and κ denotes the extinction coefficient. In practice, however, it is often unnecessary to compute α_{abs} explicitly, as it is commonly available in optical property databases. In the established TTM framework, Equations (11) and (12) describe the coupled evolution of the electron and lattice temperatures. However, numerical simulations of these equations typically converge toward a final state where $T_e \simeq T_l$ at a temperature higher than the initial one. This behavior is expected, as no thermal dissipation mechanisms are included. To render the model more realistic, a thermal relaxation channel is introduced in the lattice temperature equation to account for heat transfer from the metallic layer to its surrounding environment. This energy dissipation process follows Newton's law of cooling, and the associated heat loss term is expressed as:

$$Q_{\text{loss}} = h\,(T_l - T_\infty), \tag{16}$$

where h is the thermal exchange coefficient, and T_∞ is the asymptotic equilibrium temperature reached at long times after excitation (typically the ambient temperature). Including this dissipation term, the coupled equations of the TTM become:

$$C_e(T_e)\,\frac{\partial T_e}{\partial t} = k_e\,\frac{\partial^2 T_e}{\partial z^2} + \tau_e\,\frac{\partial}{\partial z}\left[\frac{\partial Q_e}{\partial t}\right] - G\,(T_e - T_l) + S(z,t), \tag{17}$$

$$C_l\,\frac{\partial T_l}{\partial t} = k_l\,\frac{\partial^2 T_l}{\partial z^2} + G\,(T_e - T_l) - h\,(T_l - T_\infty). \tag{18}$$

For a thin metallic film strongly coupled to a substrate, the interfacial heat exchange coefficient h can reach values on the order of 10^5 to 10^7 W·m^{-2}·K^{-1} [31–33]. Conversely, for weakly conducting interfaces such as those involving air or trapped gases, h typically lies between 10 and 10^3 W·m^{-2}·K^{-1}. Equation (18) thus enables the modeling of post-excitation thermal relaxation, characterized by a slow exponential decay of the lattice temperature. In practice, the value of h is often unknown and is typically adjusted to reproduce experimentally observed thermal decay dynamics. With this refined model and known values of the electron relaxation time for a wide range of materials, we can now perform numerical simulations to estimate the evolution of electron and lattice temperatures following a femtosecond laser pulse. The Python script used for the simulations is provided in Appendix D.1. The parameters n_e and τ_e are taken from the established Table [1]. Material densities are sourced from [28], while optical parameters (reflectivity and penetration depth) are extracted from refractiveindex.info for a wavelength of 776 nm. Other material properties are obtained from the NIST Chemistry WebBook, MathWeb, and the CRC Handbook of Chemistry and Physics 97th edition [34]. The numerical results presented below are obtained using a laser fluence $\Phi = 10$ J/m^{-2}, a pulse duration $\tau_p = 100$ fs, and an arbitrarily chosen dissipation coefficient $h = 10^7$ W·m^{-2}·K^{-1}. The results for chromium, the most commonly used transducer in our experiments, are shown in Figure 1(a). Simulations for cobalt, nickel, and gold are presented in Figures 1(b), 1(c), and 1(d), respectively. For chromium, cobalt, and nickel, the early-time (before 0.2 ps) responses of both the electron and lattice systems exhibit similar dynamics, differing primarily in the amplitude of the electron temperature. The absence of an observable lattice temperature response in this initial regime stems from the ultrafast

(femtosecond-scale) nature of the laser excitation—this is precisely the motivation behind introducing the TTM formalism. The amplitude of the ultrafast electron response varies between materials, largely due to differences in optical reflectivity and free electron density. After the initial 0.2 ps, the lattice temperature begins to rise as the electron temperature reaches its peak. Subsequently, the electron energy is rapidly transferred to the lattice, with the lattice temperature reaching a maximum at the point where thermal equilibrium between electrons and lattice is achieved. For chromium, cobalt, and nickel, this thermal equilibration and lattice temperature peak occur within approximately 0.45 ps of the laser pulse. The system then gradually returns to thermal equilibrium with the environment over a timescale of several nanoseconds. The specific case of gold is depicted in Figure 1(d). While the same general excitation pattern is observed for the electrons, the transfer of heat from the electron cloud to the lattice is significantly slower compared to the other studied metals. In gold, the lattice temperature peaks approximately 6 ps after laser excitation, and due to the slow heat transfer, the lattice temperature elevation is insufficient to produce a thermal expansion large enough to generate detectable acoustic waves. This sluggish thermal response is consistent with the weak electron-phonon coupling and long electron relaxation time determined for gold. Consequently, gold is not suitable as a transducer in picosecond acoustics applications, and in future studies it can be safely ignored as a source of acoustic wave generation.

Now that a theoretical framework for modeling ultrafast laser-induced heating in metals has been established and a Python script provided for performing numerical simulations, we can proceed to analyze how the resulting lattice heating in the metallic transducer leads to the generation of acoustic waves in the underlying substrate.

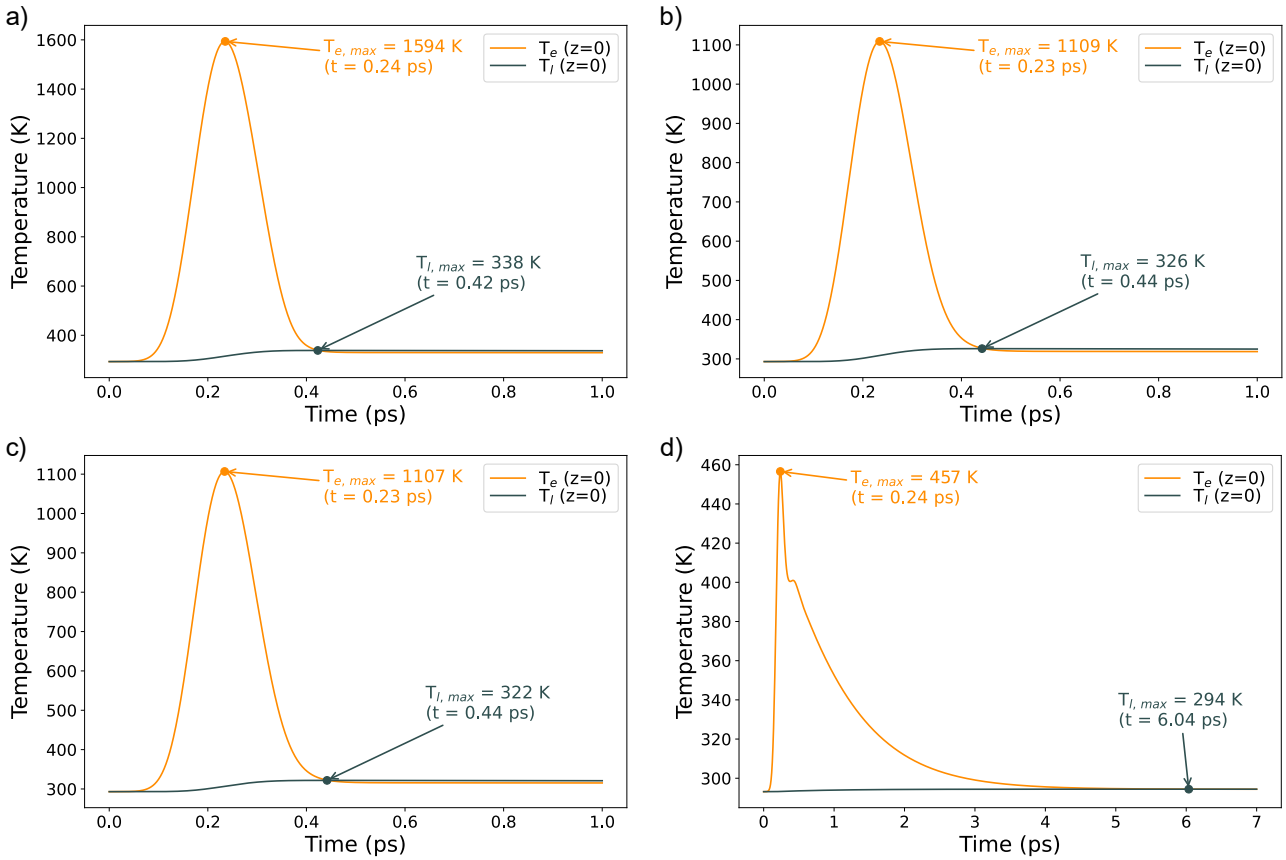

Figure 1: Numerical simulations using the established TTM model for various metals. a) Chromium. b) Cobalt. c) Nickel. d) Gold.

2.2 Thermoelastic excitation of acoustic waves

We now turn to the description of the thermal expansion induced by the ultrashort laser pulse. This expansion is modeled using the principles of thermoelasticity, limited to the linear deformation regime. This assumption is justified by the fact that, in our experiments, the temperature rise of the atomic lattice remains relatively small, leading to only weak mechanical strain. It is important to clarify that linear does not imply isotropy. Rather, it means that the thermodynamic state potential per unit volume Ψ is expressed as a quadratic form of the components of the strain tensor ε. This quadratic dependence leads directly to the linear stress-strain relationship used in elasticity theory. In this context, the mechanical response of the material is governed by:

$$\Psi = \frac{1}{2}\varepsilon_{ij}\, E_{ijkl}\, \varepsilon_{kl}, \tag{19}$$

where E is the elastic stiffness tensor, often referred to as the Hooke tensor. We will use the notation E for the stiffness of the transducer and C for the stiffness in the substrate to avoid confusion. The prefactor $1/2$ in Equation (19) compensates for the double-counting of symmetric strain components in the summation and ensures that the elastic is not overestimated. In elasticity theory, the stress tensor σ is described as the variation of the thermodynamic state potential induced by strain. It is obtained by differentiating the potential with respect to the strain tensor. The resulting relation,

$$\sigma_{ij} = \frac{\partial \Psi}{\partial \varepsilon_{ij}} = E_{ijkl}\, \varepsilon_{kl} \tag{20}$$

is the general form of Hooke's law, linking stress and strain in the linear regime. The $1/2$ coefficient disappears upon differentiation due to the quadratic nature of the thermodynamic state potential. Given the assumption of small lattice deformations and moderate heating, the specific heat at constant volume C_V can be considered to be constant. In this context, it is related to the thermodynamic potential by:

$$C_V = -T_0 \frac{\partial^2 \Psi}{\partial T^2}. \tag{21}$$

Under these assumptions, the thermodynamic potential $\Psi(\varepsilon, T)$ can be expanded via a Taylor series around $\varepsilon \to 0$ and $T \to T_0$, where T_0 is the room temperature. This follows the formalism presented in [35].

$$\Psi(\varepsilon, T) \simeq \Psi_0 - \Delta T \cdot S_0 - \Delta T \cdot E_{ijkl}\, \alpha_{kl}\, \varepsilon_{ij} + \frac{1}{2}\varepsilon_{ij}\, E_{ijkl}\, \varepsilon_{kl} - \frac{(\Delta T)^2}{2} \cdot \frac{C_V}{T_0} \tag{22}$$

In Equation (22), $\Psi_0 = \Psi(0, T_0)$ is the reference thermodynamic potential, $S_0 = -\partial\Psi/\partial T|_0$ is the entropy per volume unit at equilibrium, and α_{kl} is the thermal expansion tensor. The term $\Delta T \cdot E_{ijkl}\, \alpha_{kl}\, \varepsilon_{ij}$ captures the thermoelastic coupling. Differentiating Equation (22) with respect to ε_{ij}, leads to the linear thermoelastic stress-strain relation,

$$\sigma_{ij} = \frac{\partial \Psi(\varepsilon, T)}{\partial \varepsilon_{ij}} = E_{ijkl}\, \varepsilon_{kl} - E_{ijkl}\, \alpha_{kl}\, \Delta T. \tag{23}$$

In Equation (23), the first term corresponds to the elastic response, while the second term represents the thermal stress induced by a temperature change.

We now focus on the thermal expansion. Because we probe deformation along the z-axis only, we consider isotropic expansion. In metals, where elastic properties are often nearly isotropic, this assumption is particularly appropriate. If anisotropic effects are significant, they would manifest themselves in both optical absorption and strain along non-equivalent crystallographic directions. For isotropic materials, the Hooke tensor takes the following standard form:

$$E_{ijkl} = \lambda\, \delta_{ij}\, \delta_{kl} + \mu(\delta_{ik}\, \delta_{jl} + \delta_{il}\, \delta_{jk}), \tag{24}$$

where λ and μ are the Lamé coefficients, and δ_{ij} is the Kronecker delta. Substituting Equation (24) into the linear thermoelastic law, Equation (23), gives the stress tensor for the isotropic case:

$$\sigma_{ij} = \lambda\,\varepsilon_{kk}\,\delta_{ij} + 2\mu\,\varepsilon_{ij} - (3\lambda + 2\mu)\alpha\,\Delta T\,\delta_{ij}, \tag{25}$$

where α is the scalar thermal expansion coefficient. In the absence of external stress, the strain is purely thermal and becomes:

$$\varepsilon_{ij}^{th} = \alpha\,\Delta T\,\delta_{ij}. \tag{26}$$

We consider thermal expansion along the z-axis only. The total length change of the transducer in the z-direction is given by:

$$\frac{\Delta L}{L_0} = \alpha\,\Delta T. \tag{27}$$

This expansion induces a mechanical stress on the substrate, which will propagate as a strain wave. The propagation of elastic waves is governed by the laws of elasticity [36, 37]. The displacement vector $\mathbf{u}$ is related to the stress by:

$$\rho\frac{\partial^2 u_i}{\partial t^2} = \frac{\partial \sigma_{ij}}{\partial x_j}, \tag{28}$$

where the position vector is $\mathbf{x} = (x_1, x_2, x_3) = (x, y, z)$, and ρ is the mass density. Using the expression of the stress given in Equation (25) and knowing that $C_{ijkl}\varepsilon_{kl} = \lambda\,\varepsilon_{kk}\,\delta_{ij} + 2\mu\,\varepsilon_{ij}$ and $C_{ijkl}\,\varepsilon_{kl}^{th} = (3\lambda + 2\mu)\alpha\Delta T\delta_{ij}$, we have:

$$\rho\frac{\partial^2 u_i}{\partial t^2} = C_{ijkl}\left[\frac{\partial \varepsilon_{kl}}{\partial x_j} - \frac{\partial \varepsilon_{kl}^{th}}{\partial x_j}\right], \tag{29}$$

where C_{ijkl} is the stiffness tensor for the substrate. In our case, the ultrashort laser pulse generates a single-cycle acoustic pulse that propagates into the substrate. The resulting strain profile typically exhibits a bipolar shape, characterized by a compressive front followed by a tensile tail (or vice versa), depending on the boundary conditions and the sign of the thermal expansion coefficient. This behavior is well described by the analytical model introduced by Thomsen *et al.* (1986) [38]:

$$\varepsilon(z,t) = \frac{\alpha(1-R)\Phi}{\rho C\xi}F(z - v_s t), \tag{30}$$

where $\dfrac{\alpha(1-R)\Phi}{\rho C\xi}$ defines the amplitude of the source resulting from laser absorption. All parameters are defined as in the previous section: α is the thermal expansion coefficient, R is the reflectivity, Φ is the incident laser fluence, ρ the mass density, ξ the optical penetration depth, and C is the specific heat per unit volume. The function $F(z - v_s t)$ describes the spatiotemporal evolution of the strain and takes different analytical forms depending on whether $z > v_s t$ or $z < v_s t$, where v_s is the sound velocity in the substrate.

This model assumes that the laser directly excites the medium in which the acoustic wave propagates. However, in our experimental configuration, the femtosecond laser pulse is absorbed by a thin metallic transducer deposited on the substrate. The substrate itself is therefore not optically excited and does not undergo any local thermoelastic expansion. The ultrafast thermoelastic expansion of the metallic film generates a transient normal stress at the film/substrate interface, which launches a longitudinal acoustic pulse into the substrate. To account for this transducer-based generation, Equation (30) is reformulated as:

$$\varepsilon(z,t) = \varepsilon_0\,H(t)\,F(z - v_s t)\,e^{-\gamma z}, \tag{31}$$

where $\varepsilon_0 = \dfrac{1+\nu_f}{1-\nu_f}\,\varepsilon^{th}\,t_{ac}\,\dfrac{v_f}{v_s}$, with ν_f the Poisson's ratio of the metallic film, t_{ac} the acoustic transmission coefficient from the film to the substrate, and v_f and v_s the sound velocities in the film and

substrate, respectively. The acoustic reflection and transmission at the film/substrate interface are defined by:

$$r_{\mathrm{ac}} = \frac{Z_s - Z_f}{Z_s + Z_f}, \qquad t_{\mathrm{ac}} = \frac{2Z_s}{Z_s + Z_f}, \tag{32}$$

where $Z = \rho v$ is the acoustic impedance, ρ is the density, and v is the longitudinal sound velocity of the considered medium as described by Lin *et al.* [39]. Finally, in Equation (31), $H(t)$ is the Heaviside function ensuring causality, $F(z - v_s t)$ encodes the strain profile, and $e^{-\gamma z}$ describes the acoustic damping in the substrate.

As shown by our TTM simulations, the maximum lattice temperature is reached within approximately 0.4 ps, which is short compared to the acoustic transit time across the absorption depth. Therefore, the thermoelastic source can be considered instantaneous, and $\varepsilon^{th} = \alpha\,\Delta T_{\max}$ is used in the source term ε_0, which defines the amplitude of the acoustic pulse injected at the film/substrate interface at $t = 0^+$.

$$\varepsilon(z,t) = \varepsilon_0\, H(t)\, e^{-\gamma z} \begin{cases} -\dfrac{1}{2} e^{-(z - v_s t)/\xi} & \text{if } z > v_s t, \\ +\dfrac{1}{2} e^{(z - v_s t)/\xi} & \text{if } z < v_s t. \end{cases} \tag{33}$$

Finally, to determine the associated displacement field $u(z,t)$, we integrate the strain over depth:

$$u(z,t) = -\int_z^{\infty} \epsilon(z',t)\, dz', \tag{34}$$

assuming the boundary condition $\lim_{z\to\infty} u(z,t) = 0$. The analytical result of this integration is:

$$u(z,t) = \frac{\varepsilon_0\, \xi}{2}\, H(t)\, e^{-\gamma z} \begin{cases} e^{-(z - v_s t)/\xi}, & \text{if } z > v_s t, \\ 2 - e^{(z - v_s t)/\xi}, & \text{if } z < v_s t. \end{cases} \tag{35}$$

This analytical approach provides a physically consistent and computationally efficient means to model the generation and propagation of thermoelastic pulses in a pump-probe experiment. It is fully compatible with the results of the TTM and follows the theoretical description of bipolar acoustic pulse proposed by Thomsen.

Having described how thermal expansion in the metallic transducer gives rise to strain waves in the substrate, and having established both the strain profile and its propagation, we now turn to the photoelastic detection of these acoustic waves.

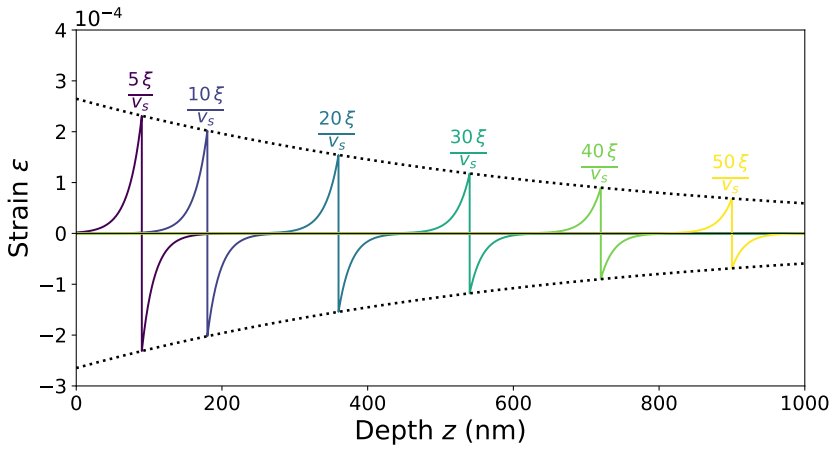

Figure 2: Spatial profile of the strain pulse at various times after the optical pump pulse.

2.3 Photoelastic detection of longitudinal acoustic waves

The optical detection of photothermally induced strain waves is based on the scattering of electromagnetic waves, as originally predicted by L. Brillouin [1]. The fundamental principle relies on the modulation of the refractive index by strain fields via the photoelastic effect. In the specific case of picosecond acoustic interferometry, the reflectivity of a time-delayed optical probe pulse is modulated by the propagating strain pulse generated by the femtosecond laser pump, as previously described. The photothermal generation of transient stress as well as its bipolar profile have been introduced before. In addition, the acoustic transmission at the film-substrate interface, governed by the acoustic impedance mismatch, as described by Lin *et al.* [39] as been introduced in Equation (32), as well as the strain propagation and attenuation in the substrate (Equation 33).

We now continue the formalism introduced by Lin *et al.* [39], while keeping the adapted bipolar strain geometry. To establish the relationship between the strain field and the refractive index modulation, we recall that it is governed by the photoelastic effect, which can be expressed through the inverse square of the refractive index, $B = 1/n^2$ [38, 40–43]:

$$\Delta B_{ij} = \Delta\left(\frac{1}{n^2}\right)_{ij} = p_{ijkl} \cdot \varepsilon_{kl}. \tag{36}$$

where p_{ijkl} is the photoelastic tensor and ε_{kl} is the strain tensor. Applying a first-order Taylor expansion for $n \to n + \Delta n$, we find:

$$\Delta\left(\frac{1}{n^2}\right) \simeq -\frac{2\Delta n}{n^3}, \tag{37}$$

$$\Delta n \simeq -\frac{n^3}{2}\Delta\left(\frac{1}{n^2}\right). \tag{38}$$

This yields, in the limit of small strain and under the assumption of uniaxial propagation along z:

$$\Delta n(z,t) = -\frac{n^3}{2}\, p_{33}\, \varepsilon(z,t), \tag{39}$$

where n is the unperturbed refractive index and p_{33} is the longitudinal photoelastic coefficient of the substrate. The detection configuration is illustrated in Figure 3, where three reflected probe beams are identified. Beam A corresponds to partial reflection at the film-substrate interface, beam B is partially reflected by the front of the strain wave (before reaching the film), and beam C is reflected by the rear of the strain pulse and also passes through the film-substrate interface. This configuration, introduced by Lin *et al.* [39], matches our experimental geometry, where the reflectivity variation results from coherent interference between these contributions. Assuming normal incidence and weak strain, the reflection coefficients r_B and r_C due to the strain pulse, and the background reflection coefficient r_A, which accounts for the total optical response of the unperturbed film–substrate system and any non-acoustic modulation, are expressed as:

$$r_A = r_{sf} + \delta r_{sf}, \tag{40}$$

$$r_B(t) = ik_0 \int_0^\infty \Delta n(z,t)\, e^{-2ikz}\, dz, \tag{41}$$

$$r_C(t) = i\, r_{sf}^2\, k_0 \int_0^\infty \Delta n(z,t)\, e^{+2ikz}\, dz. \tag{42}$$

Here, $k_0 = 2\pi/\lambda$ is the vacuum wavevector, and $k = n_s\, k_0$ is the wavevector in the substrate.

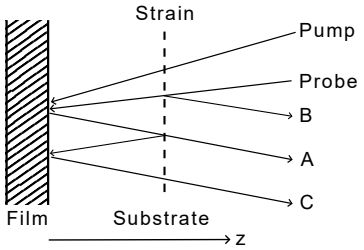

Figure 3: Photoacoustic detection with a three-beam reflection model. Illustration adapted from [39].

The effective reflection coefficient r_{sf} of the film-substrate stack is derived from Fresnel coefficients:

$$r_{sf} = r_1 + \frac{t_1\,\tau_1\,r_2\,e^{2ik_f d}}{1 + r_1 r_2 e^{2ik_f d}}, \tag{43}$$

$$r_1 = \frac{n_s - n_f - i\kappa_f}{n_s + n_f + i\kappa_f}, \tag{44}$$

$$r_2 = \frac{n_f - 1 + i\kappa_f}{n_f + 1 + i\kappa_f}, \tag{45}$$

$$t_1 = \frac{2n_s}{n_s + n_f + i\kappa_f}, \tag{46}$$

$$\tau_1 = \frac{2n_f + 2i\kappa_f}{n_s + n_f + i\kappa_f}, \tag{47}$$

where r_1 and r_2 are the complex reflection coefficients at the film-substrate and film-air interfaces, respectively. Similarly, t_1 defines the optical transmission from the substrate to the film, and τ_1 denotes the transmission from the film to the substrate. The total reflectivity variation is then given by:

$$\Delta R = |r_A + r_B + r_C|^2 - |r_{sf}|^2\,. \tag{48}$$

Assuming that the strain-induced perturbation of the refractive index is weak ($|\Delta n| \ll n$), the expression for ΔR can be linearized:

$$\begin{aligned}\Delta R(t) &\simeq |r_{sf}|^2 + 2\,\mathrm{Re}\big[r_{sf}^*(\delta r_{sf} + r_B + r_C)\big] - |r_{sf}|^2 \\ &= 2\,\mathrm{Re}\big[r_{sf}^*(\delta r_{sf} + r_B + r_C)\big]\,.\end{aligned} \tag{49}$$

Neglecting the slowly varying thermal background term δr_{sf} for the moment leads to:

$$\Delta R(t) \approx 2\,\mathrm{Re}\big[r_{sf}^*(r_B + r_C)\big]\,. \tag{50}$$

Computing the $r_B + r_C$ sum yields:

$$r_B + r_C = k_0\,(1 - r_{sf}^2)\int_0^\infty \Delta n(z,t)\sin(2kz)\,dz + i\,k_0\,(1 + r_{sf}^2)\int_0^\infty \Delta n(z,t)\cos(2kz)\,dz. \tag{51}$$

Injecting Equation (51) in Equation (50), and knowing that $r_{sf} = |r_{sf}|\,e^{i\phi}$ and $|r_{sf}|^2 = R$, we have:

$$\Delta R(t) = 2k_0\sqrt{R}\,(1 - R)\left[\cos(\phi)\int_0^\infty \Delta n(z,t)\sin(2kz)\,dz + \sin(\phi)\int_0^\infty \Delta n(z,t)\cos(2kz)\,dz\right], \tag{52}$$

which simplifies into:

$$\Delta R(t) = 2k_0\sqrt{R}\,(1 - R)\int_0^\infty \Delta n(z,t)\sin(2kz + \phi)\,dz. \tag{53}$$

In the presence of multiple optical reflections within the metallic transducer (Fabry-Pérot effect), the reflection coefficient $r_{sf} = |r_{sf}|\, e^{i\phi}$ introduces an additional phase shift into the detection process. The phase accumulated in the substrate is further modified by the finite acoustic thickness $d' = d\, v_s/v_f$ and by partial reflections of the acoustic wave at the film-substrate interface. According to the model developed by Lin *et al.* [39], the total phase shift is given by:

$$\psi = \pi + 2kd' - \phi - \tan^{-1}\left[\frac{r_{ac}\sin(4kd')}{1 + r_{ac}\cos(4kd')}\right], \tag{54}$$

where the phase term ψ accounts for the optical interference between the strain-scattered field and the field reflected from the film–substrate interface, and implicitly includes the effect of multiple acoustic reflections within the transducer through its thickness dependence. In this formulation, the contributions of successive acoustic echoes are coherently summed and encoded in the phase and amplitude prefactors, rather than treated as a discrete sequence of time-delayed pulses. Under these conditions, the reflectivity change becomes:

$$\Delta R(t) = 2k_0 \frac{\sqrt{R}\,(1-R)}{|1 + r_{ac}e^{4ikd'}|}(1 - \cos(2kd')) \int_0^\infty \Delta n(z,t)\cos(2kz - \psi)\, dz. \tag{55}$$

Furthermore, to model the finite temporal coherence of the optical probe pulse of duration τ_p, we introduce a Gaussian temporal coherence function:

$$G(t) = \exp\left[-\frac{4\,\ln 2}{\tau_p^2}\left(\frac{n_s\, v_s}{c}t\right)^2\right], \tag{56}$$

leading to:

$$\Delta R(t) = -k_0\, n_s^3\, p_{33}\, \frac{\sqrt{R}\,(1-R)}{|1 + r_{ac}e^{4ikd'}|}(1 - \cos(2kd'))\, G(t) \int_0^\infty \varepsilon(z,t)\cos(2kz - \psi)\, dz, \tag{57}$$

where $\Delta n(z,t)$ has been replaced by its expression depending on the strain given in Equation (39).

Additional systematic effects are known to impact the accuracy of time-domain Brillouin measurements. The present model assumes one-dimensional acoustic propagation and perfect spatial overlap between the pump and probe beams, which remains valid as long as the acoustic propagation length is below the diffraction limit defined by the Fresnel condition: $z \ll a^2/\lambda_a$, where a is the beam waist and λ_a is the acoustic wavelength. In addition, long-term thermal effects may slowly modulate the baseline reflectivity through the term δr_{sf}, thereby adding a background signal to the acoustic response. Following the analysis of Lin *et al.* [39], the total transient reflectivity variation $\Delta R_{total}(t)$ can be decomposed into three distinct contributions:

$$\Delta R_{total}(t) = \Delta R_{elec}(t) + \Delta R_{th}(t) + \Delta R(t), \tag{58}$$

where $\Delta R_{elec}(t)$ represents the ultrafast electronic response, and $\Delta R_{th}(t)$ the slowly varying thermal background. The electronic peak $\Delta R_{elec}(t)$ arises from the sub-picosecond modification of the dielectric function of the metallic transducer following the photoexcitation of hot carriers. It is modeled here as a symmetric Gaussian centered at t = 0:

$$\Delta R_{elec}(t) = A_{elec} \cdot \exp\left(-\frac{t^2}{2\sigma_{elec}^2}\right), \tag{59}$$

where A_{elec} is the amplitude of the electronic response, and σ_{elec} is its temporal standard deviation. The thermal background $\Delta R_{th}(t)$ is initiated after a characteristic thermal response delay t_{th}:

$$\Delta R_{th}(t) = 0 \quad \text{if } t < t_{th}\,; \quad A_{th} \cdot \exp\left(-\frac{t}{\tau_{th}}\right) \quad \text{if } t \geq t_{th}. \tag{60}$$

where A_{th} is the amplitude, and τ_{th} is the thermal relaxation time.

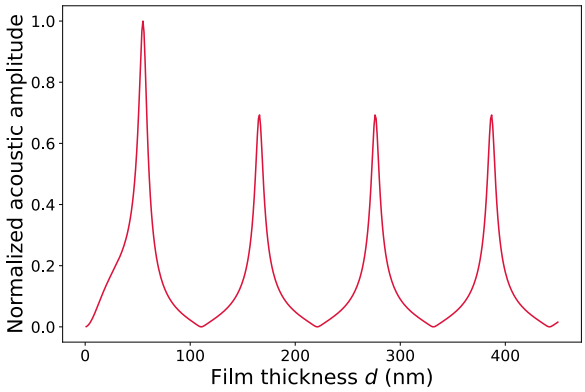

Figure 4: Dependence of the acoustic amplitude on the gold film thickness, probed at 587 nm. The acoustic amplitude is defined as the FFT amplitude of the time derivative of the transient reflectivity between 20 and 500 ps at the Brillouin frequency (29.3 GHz for LAWs in SiO_2 probed at 587 nm).

With the total reflectivity $\Delta R_{total}(t)$ theoretically described, we model it using the Python script provided in Appendix D.3. Figure 4 shows the Fabry-Pérot resonances of the optical probing sensitivity as a function of the thickness of a gold film deposited on a glass substrate. These simulations were performed using a 587 nm probe wavelength to allow direct comparison with the results obtained by Lin *et al.* [39]. In our case, the acoustic oscillations amplitude is extracted from the magnitude of the Fourier transform of the time derivative of the reflectivity signal, computed between 20 ps and 500 ps. The use of the derivative suppresses the thermal background, while excluding the first 20 ps effectively removes the electronic peak. Representative examples of simulated $\Delta R(t)$ signals for gold films on fused silica probed at 587 nm are shown in Figure 5. The strain pulse exhibits a spatial periodicity of $2d'$ within the substrate, and the condition for enhanced detection (constructive interference of r_B and r_C) occurs when $2d' \simeq \lambda/3$ (empirically determined). This corresponds to a film thickness of $d \simeq$ 54 nm, in good agreement with the numerical results. Figure 5(a) presents the simulated transient reflectivity signal at the detection enhancement peak ($d = 55.3$ nm), as automatically determined by the numerical analysis. In contrast, Figure 5(b) shows the signal for $d = 70$ nm, where the detection is not optimized by the film thickness. In both cases, the electronic peak and thermal background are modeled identically; the only parameter varied is the film thickness d.

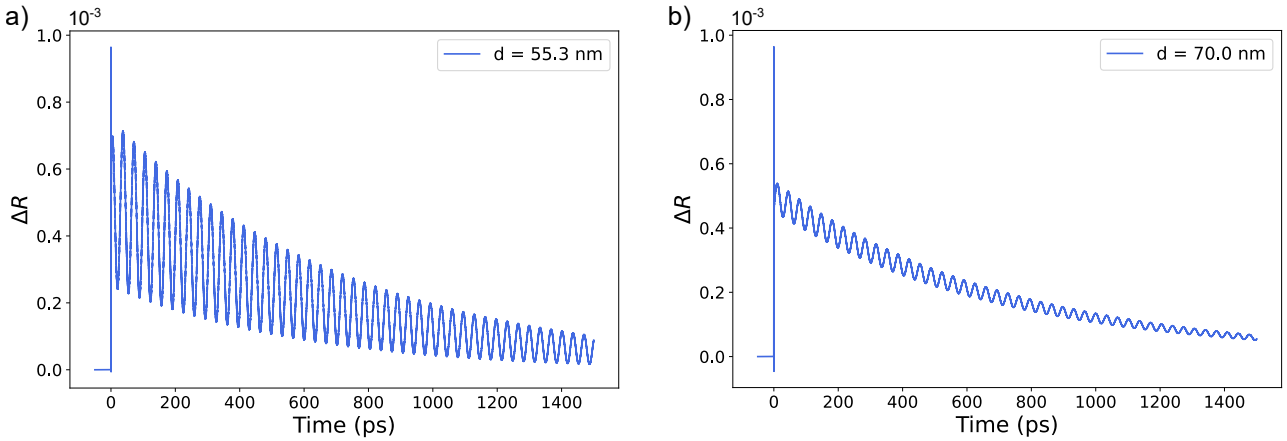

Figure 5: Numerical simulations of transient reflectivity changes in SiO_2 induced by LAWs generated in a gold film, probed at 587 nm. a) Reflectivity signal at the detection enhancement condition ($d = 55.3$ nm). b) Reflectivity signal for a non-enhanced configuration ($d = 70$ nm).

Thanks to the reliability of our simulations, we performed numerical calculations for a configuration closer to our experimental conditions. In practice, gold is not used as a transducer in our experiments because, as predicted by the TTM simulations and confirmed experimentally, it is not an efficient transducer. The previous simulations of transient reflectivity change were performed using gold solely to validate the reliability of the model by comparing it to the results of Lin *et al.* [39]. In our experiments on transparent substrates, a chromium film is used as the transducer. Furthermore, the pump and probe wavelengths differ, whereas the previous simulations with gold assumed the same 587 nm wavelength for both.

Figure 6 presents the simulation results for a chromium transducer deposited on a fused silica substrate, under optimal detection conditions. The simulations explore combinations of 400/800 nm pump and probe wavelengths. Figure 6(a) and 6(b) both use a 400 nm probe wavelength, with 400 nm and 800 nm pump wavelengths, respectively. Figure 6c and 6(d) both use an 800 nm probe, with pump wavelengths of 400 nm and 800 nm, respectively. All simulations assume identical ultrafast electronic heating and thermal background contributions. They also assume the same amplitude of thermal expansion in the chromium film, leading to an identical initial ε_0 strain amplitude. Acoustic attenuation in the substrate is also kept constant across simulations. These fixed conditions allow us to isolate and highlight the crucial role of the optical penetration depth ξ of the pump in determining the strain amplitude. The stronger amplitude observed with an 800 nm pump compared to a 400 nm pump originates from the higher penetration depth of the 800 nm light in chromium ($\xi_{800} \simeq 18$ nm

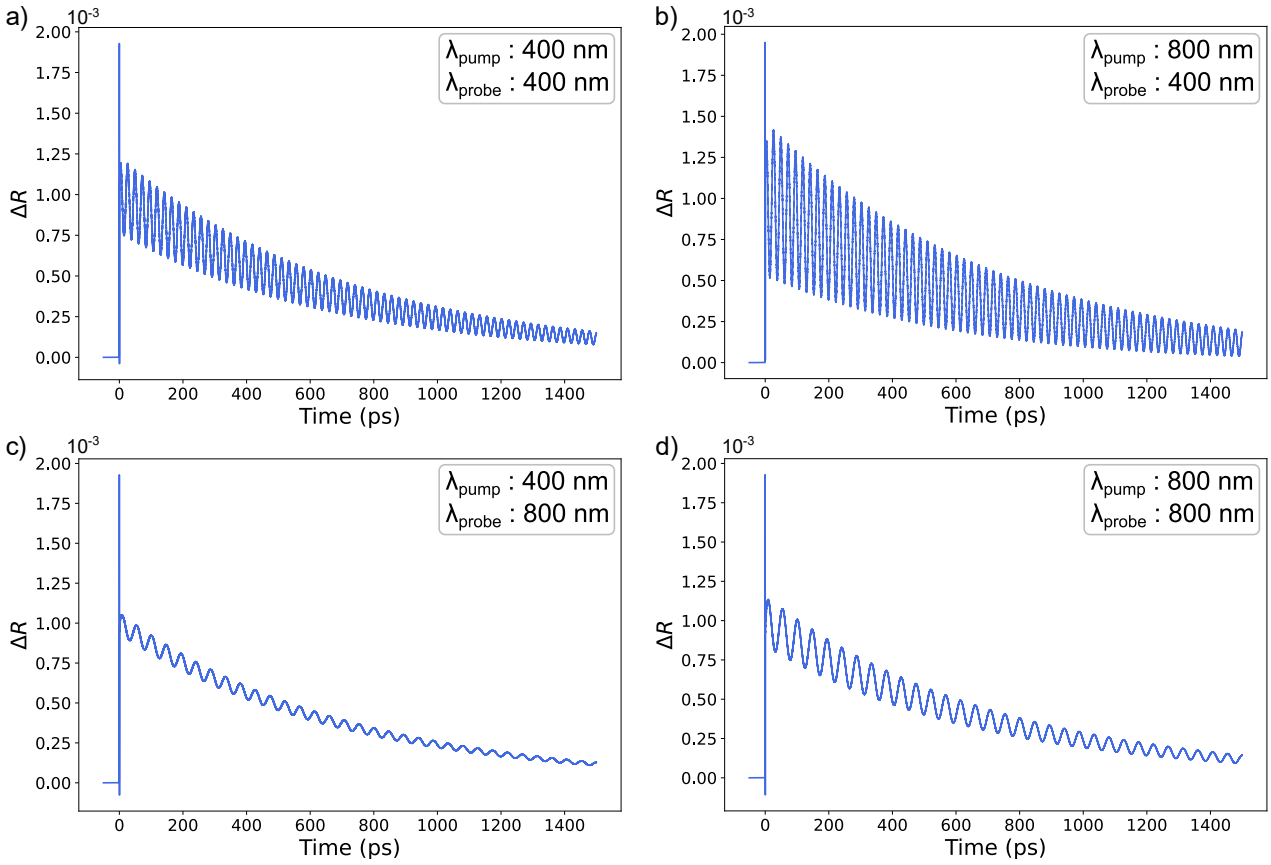

Figure 6: Simulations of transient reflectivity change induced by a strain pulse in SiO_2, generated from a chromium film. The four sub-figures present different combinations of 400/800 nm pump and probe wavelengths. a) 400 nm probe, 400 nm pump. b) 400 nm probe, 800 nm pump. c) 800 nm probe, 400 nm pump. d) 800 nm probe, 800 nm pump.

and $\xi_{400} \simeq 11$ nm), which enhances the generated strain ε. We also observe that the two top panels (a and b) exhibit higher oscillation frequencies than the bottom panels (c and d). This dependence on the probe wavelength is expected, since the detection relies on optical interferometry. The oscillation frequency corresponds to the Brillouin frequency, which naturally emerges from the optical interference term $\cos(2k\,z - \psi) = \cos(2k\,v_s\,t)$ in the temporal reflectivity $\Delta R(t)$:

$$f_B = \frac{2k\,v_s}{2\pi} = \frac{2\,n_s\,v_s}{\lambda}, \tag{61}$$

where v_s is the sound velocity in the substrate, n_s is its refractive index, and λ the probe wavelength. Applying Equation (61) to the two probe wavelengths, using the optical parameters of fused silica, yields $f_B(\lambda = 400\text{ nm}) \simeq 43.37$ GHz and $f_B(\lambda = 800\text{ nm}) \simeq 21.44$ GHz. These two frequencies are also clearly identified in the simulations through Fourier analysis, confirming the expected dependence on the probe wavelength.

3 Investigations in the linear transparency regime

An adapted theoretical description of the optical generation and detection of LAWs has been presented in the previous section. We now turn to the practical implementation of these phenomena, with the objective of extracting quantitative information from a wide range of materials. This section is devoted to the detailed presentation of the experimental setup used to perform TDBS measurements. Particular attention is first given to the optical configuration and its specific features. After providing a complete description of the optical setup, we will proceed to the presentation and analysis of the experimental results obtained using this method.

3.1 Experimental setup

The complete optical setup, as well as the purpose of each part of this assembly, is presented in this subsection. The scheme of the optical setup is given in Figure 7.

The first element of the optical setup is the femtosecond laser source. The base of this laser source is a Coherent Mira 900, which emits pulses with a duration of 130 fs at a repetition rate of 76 MHz. The laser wavelength is tunable between 750 nm and 900 nm; for our experiments, we set the wavelength at 776 nm, with a spectral bandwidth of 10 nm FWHM (full width at half maximum). Some measurements with this 76 MHz laser source have provided results with a high thermal background that compromises the quality of results. To overcome limitations due to cumulative laser heating, we have built a custom cavity dumper (see Appendix B). It basically consists of a pulse picker inserted into the Mira 900 cavity. The acousto-optic pulse picker is driven electronically and controls the repetition rate of the pulses extracted from the cavity. The advantage of this system is that it enables lowering the repetition rate, typically in the range of 250 kHz, and, thanks to the high ejection efficiency of the pulse picker, increases the energy output from roughly 10 nJ to 40 nJ. Furthermore, the system achieves an excellent signal-to-noise ratio owing to the intrinsically low shot noise characteristic of Ti:Sapphire femtosecond oscillators. Nevertheless, the available pulse energy remains relatively low compared to amplified laser systems. To reach pulse energies in the microjoule range, sufficient for many high-energy experiments performed through microscope objectives, while retaining the benefits of intermediate repetition rates in the hundreds of kilohertz range, we implemented a Rega 900 regenerative amplifier (see Appendix C). This system, generously donated by Prof. Keith Nelson (Massachusetts Institute of Technology), delivers 250 fs pulses at a tunable repetition rate in the range from single shot up to 4.7 MHz (typically it was set to operate at 250 kHz), with pulse energies up to 4 μJ, at a wavelength kept at 776 nm.

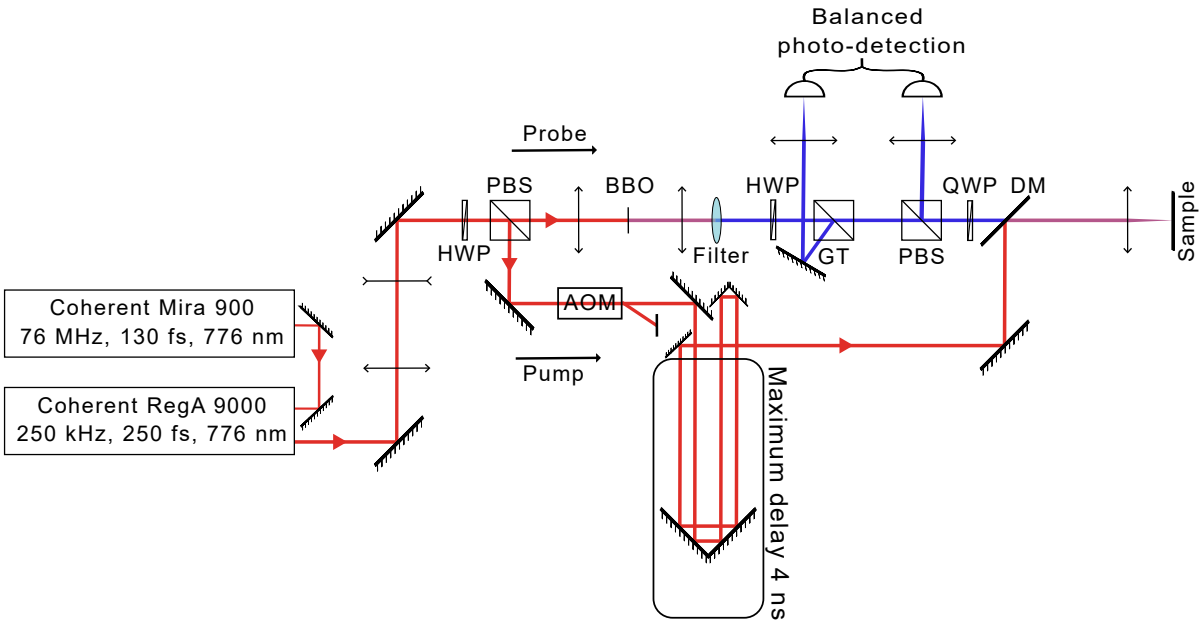

Figure 7: Experimental femtosecond pump-probe setup for TDBS measurements. HWP: Half Wave Plate. PBS: Polarizing Beam Splitter. BBO: barium β-borate. GT: Glan-Taylor. QWP: Quarter Wave Plate. AOM: Acousto-Optic Modulator.

The first node in the optical setup is a polarized beam splitter (PBS), which separates the incoming laser beam into two parts: the pump and the probe. After spatial collimation of the laser output beam and control of its direction of propagation, the beam enters into the PBS. The probe beam corresponds to the P-polarized component and is transmitted through the PBS, while the S-polarized component is reflected at 90° and is used as the pump beam. We begin by detailing the optical components along the pump path. The first element is an acousto-optic modulator (AOM), used to modulate the transmitted pump beam.

3.1.1 Acousto-optic modulator

The AOM is used to modulate the pump beam in order to generate a reference signal for synchronous detection. Specifically, the AOM imposes a square-wave modulation that deflects a selected number of laser pulses from the zero-order beam into the first-order diffracted beam. For sample excitation, we keep the zero-order and block the first-order. Depending on the type of measurement being performed, we adapt the modulation pattern applied to the pump. Two main modulation schemes are commonly used. The first consists of transmitting only a single pulse per modulation cycle. This effectively creates a virtual femtosecond laser source with a repetition rate equal to the AOM modulation frequency. It is particularly necessary while we use two optical pumps of different nature, while one cannot emit at 250 kHz. The second scheme is a 50/50 modulation pattern, in which an equal number of pulses are transmitted and deflected during each cycle. In this case, the system behaves like a virtual source emitting bursts themselves repeated at the AOM modulation frequency. This modulation is the one used to obtain the results in the actual section because this modulation enhances the signal-to-noise ratio. A brief overview of the working principle of an AOM, illustrated in Figure 8, is presented here. As shown in this figure, a piezoelectric transducer generates a stationary acoustic wave inside a transparent crystal. By modulating the electrical drive applied to the piezoelectric transducer, this acoustic wave can be dynamically controlled, thereby enabling the creation of various modulation

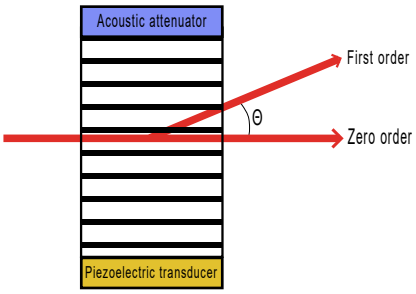

Figure 8: Principle of acousto-optic deflection of light.

patterns. As previously described in the theoretical section, the acoustic wave induces a periodic variation in the refractive index of the crystal, effectively forming a diffraction grating. This grating deflects the incident electromagnetic wave with a deflection angle Θ, given by Equation (62), where m is the diffraction order, λ the optical wavelength, and Λ the acoustic wavelength.

$$\sin(\Theta) = \frac{m\lambda}{2\Lambda} \tag{62}$$

3.1.2 Delay stage

After the AOM, the transmitted zero-order beam constitutes the optically modulated pump. The next stage along its path to the sample is the optical delay line. This delay line consists of a motorized translation stage with two mirrors arranged to retroreflect the incoming beam without introducing any spatial drift to the reflected beam. By translating the platform along its 30 cm range, the optical path length is varied. Since the beam undergoes a double pass through the delay line, the maximum accessible temporal delay is close to 4 ns. The optical setup should be made such that, for a given position of the delay line, the pump and probe optical paths are identical. Ideally, this temporal overlap should occur near the maximum pump path length to allow the longest accessible time window for measurement. In practice, during data acquisition, the delay stage moves continuously and sends periodic triggers to the synchronous detection system. These triggers are used to record the measured signal at the corresponding time delay.

Now that the main components of the optical pump path have been introduced, the next step consists of describing the elements of the probe path.

3.1.3 BBO

Beta barium borate (BBO, β-BaB_2O_4) is a nonlinear optical crystal commonly used for frequency doubling of coherent light in the wavelength range from 410 nm to 2 µm. In our case, the BBO crystal is used to convert the 776 nm incident beam into a 388 nm beam via second harmonic generation (SHG). This approach offers a straightforward way to generate a second probing wavelength. Using both wavelengths, 388 nm and 776 nm, enables dual-wavelength probing of the sample, which allows two Brillouin frequency extractions. From these two Brillouin frequencies, two calculations of LAW velocity can be done, reducing the uncertainty on its value. In addition, using two different wavelengths allows adaptation to various material optical properties. Using degenerate wavelengths for the pump and the probe also simplifies optical filtering, minimizing pump leakage into the detection photodiodes and thereby reducing background noise in the detected signal. In the optical setup shown in Figure 7, the BBO crystal is placed in the probe path. However, if probing at 776 nm is desired, the BBO can be moved from the probe path to the pump path.

The working principle of a second harmonic generation based on sum-frequency mixing in nonlinear crystals is fully addressed in Appendix A, which presents an investigation of crystallographic structures via SHG.

3.1.4 Glan-Taylor polarizer

The next element in the probe path is a Glan-Taylor (GT) polarizer, coupled with an HWP, used to split the incoming probe beam into two parts: a reference beam and an effective probe beam (see Figure 9). The reference beam does not interact with the sample and thus remains unaffected by any photoacoustic or photoinduced phenomena occurring within the sample. During photodetection, a balanced detection scheme is used. This detection scheme is based on the subtraction of the reference beam from the effective probe beam to enhance the signal-to-noise ratio and isolate the modulated component originating from the sample. The GT polarizer was chosen for this function due to its precise polarization separation and its compact beam-splitting geometry. The high extinction ratio of the GT prism enables precise balancing between the reference and signal probe beams, while the beam-splitting geometry contributes to space optimization within the optical setup.

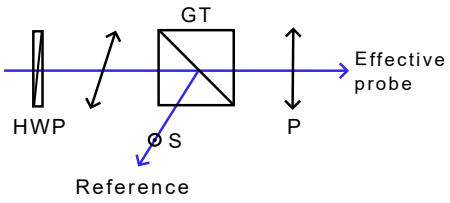

Figure 9: Polarization splitting geometry of a Glan-Taylor prism.

3.1.5 PBS and QWP

After passing through the GT polarizer, the probe beam is fully transmitted by a PBS and subsequently passes through a quarter-wave plate (QWP). This serial association of the PBS and QWP enables efficient collection and polarization-based isolation of the probe beam reflected by the sample. The principle of this polarization-based isolator is that the incident probe beam is linearly polarized (P-polarized), which allows it to be fully transmitted by the PBS. Upon traversing the QWP, this linear polarization is converted into a right-handed circular polarization. After reflecting from the sample, the polarization state of the probe beam becomes left-handed circular. When this reflected beam passes back through the same QWP, its polarization is converted into a linearly S-polarized beam. This S-polarized beam is then reflected by the PBS. The working principle of this polarization-based isolator is illustrated in Figure 10. The isolation of both the probe beam and the reference beam has now been explained. The next step in the description of the optical setup concerns the implementation of balanced photodetection.

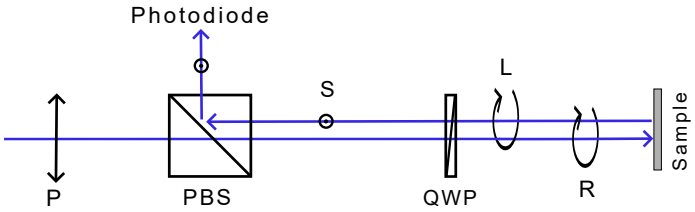

Figure 10: Principle of the isolation of the probe beam from the sample.

3.1.6 Balanced photodetection

The balanced photodetection scheme is illustrated in Figure 11. As briefly mentioned earlier, the principle relies on subtracting a reference beam from the probe beam that carries the information on the laser-excited sample. This technique enhances the signal-to-noise ratio by canceling out common noise and laser intensity fluctuations. To achieve this, it is necessary to start by balancing the optical intensities incident on both photodiodes under equilibrium condition, that is, when no pump pulse is applied and the sample remains unperturbed. At equilibrium, the voltage generated by the reference photodiode must match the voltage from the probe photodiode, resulting in a net differential signal of zero. This initial setting is achieved by adjusting the angle of the HWP placed before the GT polarizer to tune the beams intensities. When the pump is turned on, and the optical path of the pump is shorter than that of the probe, a reflectivity change occurs in the sample due to the propagation of LAW. This transient reflectivity variation induces a voltage change, δV, on the signal photodiode. It is the time-resolved voltage modulation that forms the basis of the acquired TDBS signal ($\Delta R/R \propto \delta V/V$).

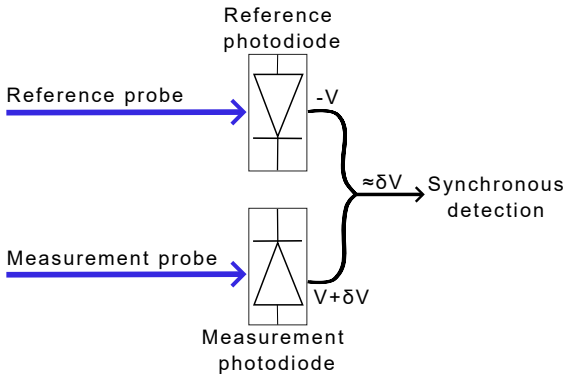

Figure 11: Principle of balanced photodetection

3.1.7 Synchronous detection

The extraction of weak signals is achieved through synchronous detection using a lock-in amplifier. This technique enables the isolation of a periodic signal with a known reference frequency, even when it is buried in noise several orders of magnitude higher. The fundamental principle relies on modulating the excitation, in our case the optical femtosecond pump, at a well-defined reference frequency. As described earlier, this modulation is performed using an AOM. The AOM periodically turns the pump beam on and off, thereby alternating the sample between excited and equilibrium states. During the equilibrium phase, the probe beam detects only the background signal, including contributions from ambient noise and electronic offsets. During the excitation phase, the probe captures both the background and the modulated response induced by LAW. A significant portion of the static background is already removed by the balanced photodetection, and the remaining noise is further removed by the lock-in amplifier. The lock-in amplifier achieves this by demodulating the probe signal at the AOM modulation frequency. This phase-sensitive detection isolates only the signal components that are synchronous with the pump modulation. A mathematical description of the demodulation consists of multiplying the input signal by a reference sine wave at the AOM modulation frequency and low-pass filtering the results. The synchronous detection is performed using a Stanford Research Systems SR830 lock-in amplifier. Figure 12 presents a simplified illustration of the operating principle of the SR830, adapted from the user manual.

With the experimental setup now fully characterized, we proceed to the analysis and interpretation of experimental results.

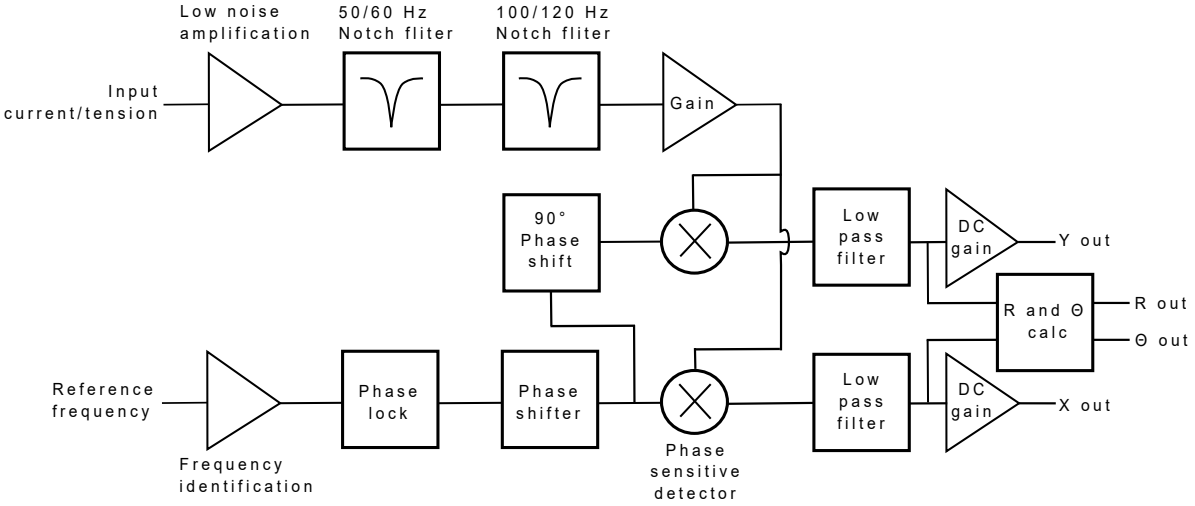

Figure 12: Simplified operating principle of the SR830 lock-in amplifier, adapted from the user manual.

3.2 Results

Having well-characterized Brillouin frequencies is particularly valuable for the synchronous excitation or detection of specific longitudinal acoustic (LA) modes, either to enhance the overall acoustic amplitude or to optimize the optical detection process. For instance, by alternating different substrates for Brillouin detection, it has been possible to explore a frequency range, as broad as possible, from 15 GHz to 60 GHz, to study the viscoelastic properties of ultrathin liquids [44]. Using the so-called "Death-Star" pulse shaper [44], specific Brillouin frequencies were selectively enhanced by exciting the sample with a train of laser pulses synchronized to the Brillouin frequency. This approach enabled the isolation and amplification of weak signals arising from shear acoustic waves transmitted through the studied liquids. To extend these measurements and exploit the full potential of coherent excitation and detection using sequential pulse trains, within the framework of the ANR-funded project associated with this PhD thesis, we have carried out a series of TDBS experiments on a range of unconventional substrates, with the goal of establishing a full dataset of Brillouin frequencies for future studies.

TDBS measurements were performed on a large variety of substrates using two different probe wavelengths: 388 nm and 776 nm. Each investigated substrate was coated with a thin chromium layer on one side, serving as the transducer, as previously described in the theoretical section. The Brillouin frequency for each wavelength was extracted from the fast Fourier transform (FFT) of the time derivative of the reflectivity signal. Taking the signal derivative allows us to eliminate the baseline offset present in the raw signal, thereby enhancing the FFT resolution and improving the accuracy of the Brillouin frequency determination.

The first investigated material was fused silica (SiO_2), which is widely considered as an ideal reference material due to its well-known properties. It is isotropic, amorphous, and exhibits low acoustic attenuation. For these reasons, fused silica was chosen as the initial test substrate to optimize the experimental setup, validate the acquisition procedure, and benchmark the accuracy of our measurements.

The analysis begins by computing the numerical time derivative of the reflectivity signals in order to suppress the baseline offset and enhance the oscillatory component. The derivatives are plotted in Figure 13(b) over a 1 ns window. FFTs of the derivatives are then computed, and the resulting spectra are presented in Figure 13(c). Two clear frequency peaks are identified. These peaks correspond to the Brillouin frequencies of 21.7 GHz and 43.9 GHz for the 776 nm probe and the 388 nm probe,

respectively. The extraction of the LAW velocity in fused silica can be done straightforwardly. We apply Equation (61) assuming normal incidence ($\cos\Theta = 1$). We also recall the SiO_2 refractive indices, $n_{388}(SiO_2) = 1.4715$ and $n_{776}(SiO_2) = 1.4537$.

Figure 13(a) presents the TDBS-measured reflectivity change (in percent) over a 1.5 ns time window, using probe wavelengths of 388 nm and 776 nm. Both signals exhibit a sharp peak at time zero, corresponding to the electronic response induced by femtosecond pulse absorption. This is commonly referred to as the "electronic peak". Following this initial peak, we observe a slow relaxation, characterized by a decaying thermal baseline. This feature reflects the rapid transfer of energy from the free electron cloud to the atomic lattice via electron-phonon coupling. During this relaxation phase, we observe damped oscillations, which result from the interferometric detection of LAW propagation and attenuation in the fused silica substrate. For clarity and ease of visualization, only 1.5 ns of the total acquisition window (3.5 ns) is shown in Figure 13(a). However, the determination of the Brillouin frequency is performed over the full time range, from 0 to 3500 ps.

We consider the LAW velocity in fused silica to be the average of the two velocities extracted from the Brillouin frequencies measured at the two probe wavelengths. This averaging yields of $v_l(SiO_2) = 5790\ \mathrm{m \cdot s^{-1}}$. Whenever this averaging procedure is applicable in future investigations, it will be systematically used.

Throughout the manuscript, we denote the sound velocity as v_s. Sometimes, we used the v_l notation for the sound velocity of the longitudinal acoustic mode in order to make the distinction with v_t for the transverse mode. From this experimentally determined value of LAW velocity, it is possible to deduce the elastic stiffness coefficient C_{11} using the well-known relation $v_l = \sqrt{C_{11}/\rho}$. Assuming a

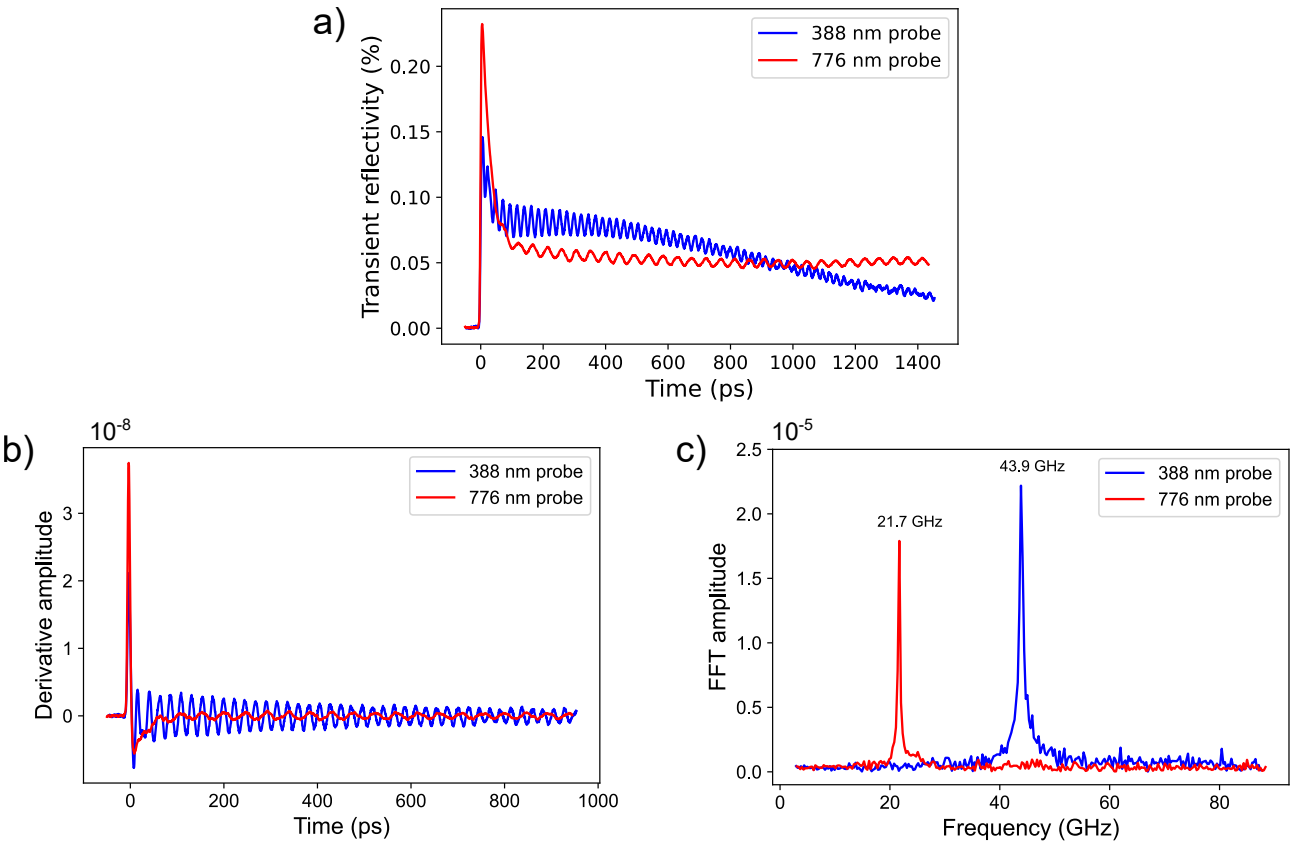

Figure 13: TDBS measurements on fused silica (SiO_2) at 388 nm and 776 nm probe wavelengths. a) Measured transient reflectivity change from pump probe experiments, b) Derivatives of the raw signals, c) FFTs of the signals derivatives.

mass density of $\rho = 2200\ \mathrm{kg \cdot m^{-3}}$, we obtain an estimated value of $C_{11} \simeq 73.75$ GPa. For comparison, literature reports $v_l = 5953\ \mathrm{m \cdot s^{-1}}$ for fused silica [45], which corresponds to a deviation of ∼2.8 % from our experimental result. This good agreement validates both the measurement protocol and the data analysis procedure. The measured frequencies and corresponding sound velocities for the investigated substrates, as well as the theoretical calculation of LAW velocities, are reported in Table [2].

$$v_l(338\ \mathrm{nm}) = \frac{\lambda \cdot \nu_B}{2n \cdot \cos(\Theta)} = \frac{388 \cdot 10^{-9} \times 43.9 \cdot 10^{9}}{2 \times 1.4715} \simeq 5788\ \mathrm{m \cdot s^{-1}}$$

$$v_l(776\ \mathrm{nm}) = \frac{776 \cdot 10^{-9} \times 21.7 \cdot 10^{9}}{2 \times 1.4537} \simeq 5792\ \mathrm{m \cdot s^{-1}}$$

Now that the advantage of using the time derivative to extract the Brillouin frequency has been demonstrated, we will no longer systematically display the derivative plots, as they do not provide additional insight in the subsequent cases.

Following these initial results on fused silica, the study was extended to two single-crystal magnesium oxide samples, each probed along a different crystallographic orientation. The first corresponds to MgO (001), and the second to MgO (111). TDBS measurements on MgO (001), Figure 14(a), and on MgO (111), Figure 15(a), reveal Brillouin oscillations of lower amplitude compared to those observed in fused silica. This reduced signal amplitude is further confirmed by the Fourier spectra shown in Figures 14(b) and 15(b), where the Brillouin peaks remain clearly identifiable despite the overall weaker intensity. For MgO (001), the extracted Brillouin frequencies are 80.3 GHz for the 388 nm probe and 39.6 GHz for the 776 nm probe. In the case of MgO (111), the corresponding Brillouin frequencies are 90.0 GHz and 44.1 GHz, respectively. These results confirm that the Brillouin frequency, and thus the acoustic wave velocity, depends on the crystallographic direction along which the measurement is performed, due to elastic anisotropy. The refractive index of MgO is isotropic, as expected from its cubic crystal symmetry, and thus we take $n_{388}(\mathrm{MgO}) = 1.7652$ and $n_{776} = 1.7284$ for the calculation of LAW velocity in both MgO (001) and MgO (111). The calculation of LAW velocities follows the same procedure as described previously for fused silica.

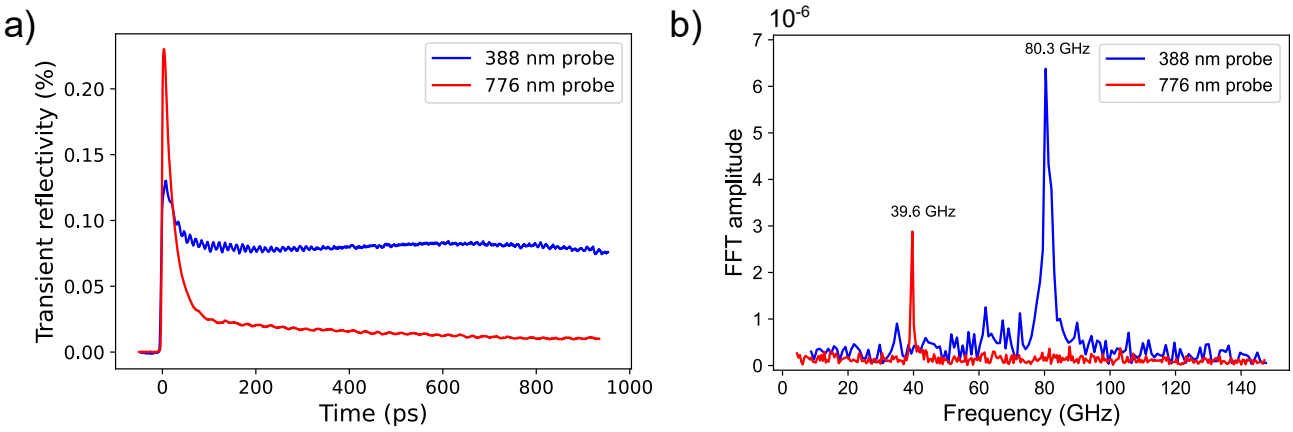

Figure 14: TDBS measurements on MgO (001) at 388 nm and 776 nm probe wavelengths. a) Measured transient reflectivity change from pump probe experiments, b) FFTs of the signals derivatives.

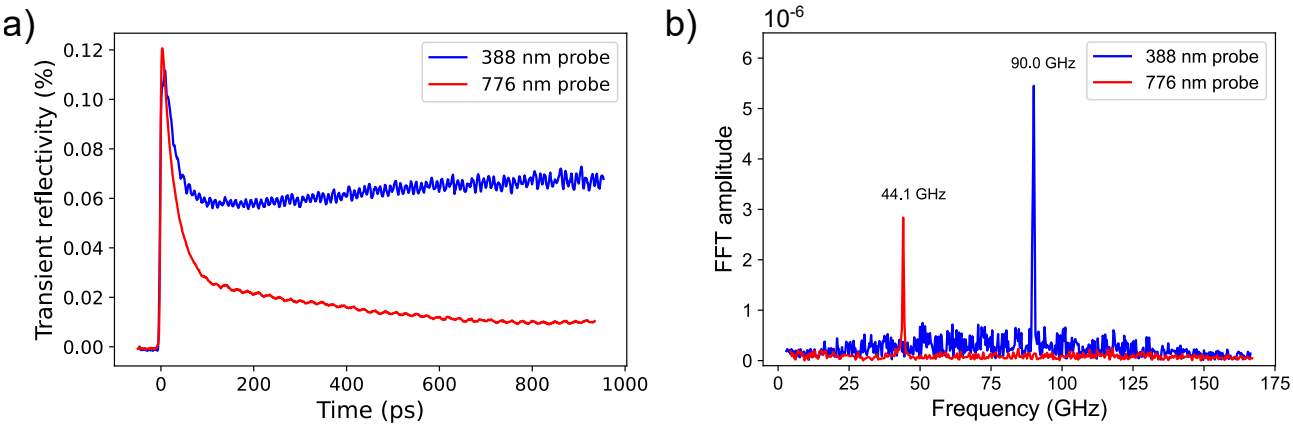

Figure 15: TDBS measurements on MgO (111) at 388 nm and 776 nm probe wavelengths. a) Measured transient reflectivity change from pump probe experiments, b) FFTs of the signals derivatives.

$$v_{l,388}(\mathrm{MgO(001)}) \simeq 8792 \text{ m} \cdot \text{s}^{-1}$$

$$v_{l,776}(\mathrm{MgO(001)}) \simeq 8890 \text{ m} \cdot \text{s}^{-1}$$

$$v_{l,388}(\mathrm{MgO(111)}) \simeq 9891 \text{ m} \cdot \text{s}^{-1}$$

$$v_{l,776}(\mathrm{MgO(111)}) \simeq 9900 \text{ m} \cdot \text{s}^{-1}$$

Taking the average of the two values obtained at each wavelength yields $v_l(\mathrm{MgO\ (001)}) \simeq 8841 \text{ m} \cdot \text{s}^{-1}$ and $v_l(\mathrm{MgO\ (111)}) \simeq 9896 \text{ m} \cdot \text{s}^{-1}$.

These results clearly demonstrate the elastic anisotropy of magnesium oxide. The significant difference in velocity between the (001) and (111) crystallographic directions reflects the anisotropic nature of the elastic stiffness tensor and confirms that TDBS can be used as a sensitive probe of directional elastic anisotropy. Based on our measurements, we calculate the stiffness coefficient C_{11} using the Christoffel relation:

$$det(\Gamma_{ik} - \rho v_s^2 Id) = 0, \tag{63}$$

where Γ_{ik} is the Christoffel tensor defined by:

$$\Gamma_{ik} = \sum_{j,l=1}^{3} C_{ijkl}\mathbf{n_j}\mathbf{n_l}. \tag{64}$$

In cubic structures, like MgO, the elastic stiffness has the following form:

$$C = \begin{bmatrix} C_{11} & C_{12} & C_{12} & 0 & 0 & 0 \\ C_{12} & C_{11} & C_{12} & 0 & 0 & 0 \\ C_{12} & C_{12} & C_{11} & 0 & 0 & 0 \\ 0 & 0 & 0 & C_{44} & 0 & 0 \\ 0 & 0 & 0 & 0 & C_{44} & 0 \\ 0 & 0 & 0 & 0 & 0 & C_{44} \end{bmatrix}$$

In the (001) direction, with $\mathbf{n}$ = (0,0,1), the Christoffel tensor is diagonal and yields $\rho v_s^2 = C_{11}$. Using the measured value $v_l^{(001)} = 8841 \text{ m} \cdot \text{s}^{-1}$ and $\rho = 3580 \text{ kg} \cdot \text{m}^{-3}$, we obtain $C_{11} \simeq 280$ GPa. For comparison, the literature reports $C_{11} = 291$ GPa [46], which corresponds to a discrepancy of ∼4 %. The reverse calculation using the literature value gives $v_l^{(001)} \simeq 9016 \text{ m} \cdot \text{s}^{-1}$.

In the (111) direction, $\mathbf{n} = \frac{1}{\sqrt{3}}(1,1,1)$, the LAW velocity is given by:

$$\rho v_l^2 = \frac{C_{11} + 2C_{12} + 4C_{44}}{3}. \tag{65}$$

Since our experimental setup only provides access to C_{11}, a determination of $v_l^{(111)}$ from experiment is not possible. However, using literature values $C_{11} = 291$ GPa, $C_{12} = 91$ GPa, and $C_{44} = 139$ GPa, the theoretical LAW velocity along the (111) direction can be calculated: $v_l^{(111)} \simeq 9788\ \mathrm{m \cdot s^{-1}}$.

The experimentally observed elastic anisotropy, with a higher LAW velocity along (111) compared to (001), is confirmed by theoretical analysis based on the Christoffel equation.

We have also carried out TDBS investigations on single crystals of strontium titanate (STO, $SrTiO_3$) perovskite, a widely used substrate material for thin-film deposition and a standard choice in our experiments involving high-strain loading. This substrate is particularly advantageous due to its high stiffness and ability to withstand significant pressure without fracturing. Moreover, in the case of Nb-doped STO, it can efficiently generate large-amplitude surface acoustic waves [47], making it an ideal substrate for our purposes. The two extracted Brillouin frequencies from TDBS are 105.6 GHz and 46.2 GHz at the probe wavelengths of 388 nm and 776 nm, respectively (see Figure 16). Given the refractive indices $n_{388}(\mathrm{STO}) = 2.7037$ and $n_{776}(\mathrm{STO}) = 2.3468$, the final LAW velocity, after averaging, is $v_l(\mathrm{STO}) \simeq 7608\ \mathrm{m \cdot s^{-1}}$.

In this experiment, the crystallographic direction of the acoustic propagation is not known a priori. In order to determine the investigated direction, we assume a cubic structure for STO, and we take the stiffness tensor components from literature [48], $C_{11} = 313$ GPa, $C_{12} = 98$ GPa, and $C_{44} = 109$ GPa. Due to the cubic symmetry, the LAW velocity is the same along (100), (010), and (001), and similarly along the diagonals (110), (101), and (011). The formulas for the calculation of the LAW velocity along (100) and (111) are identical to those used for MgO. The LAW velocity along (110) is given by:

$$v_l^{(110)} = \sqrt{\frac{C_{11} + C_{12} + 2C_{44}}{2\rho}}, \tag{66}$$

where the taken value for the volumetric mass of STO is $\rho = 5090\ \mathrm{kg \cdot m^{-3}}$. After computation, we obtain $v_l^{(100)} \simeq 7842\ \mathrm{m \cdot s^{-1}}$, $v_l^{(110)} \simeq 7861\ \mathrm{m \cdot s^{-1}}$ and $v_l^{(111)} \simeq 7867\ \mathrm{m \cdot s^{-1}}$. The small variations between these velocities confirm the weak elastic anisotropy of STO in its cubic phase. Given the experimental uncertainty (∼3 %), it is not possible to unambiguously assign the measured velocity to a specific

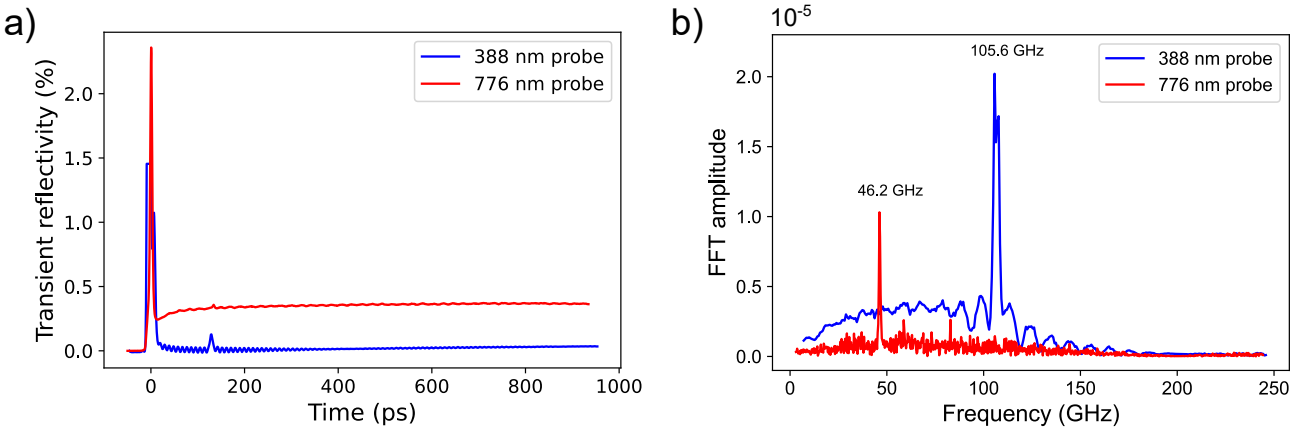

Figure 16: TDBS measurements on STO at 388 nm and 776 nm probe wavelengths. a) Measured transient reflectivity change from pump probe experiments, b) FFTs of the signals derivatives.

crystallographic direction. Nevertheless, the measured velocity is obviously too high to correspond to a transverse wave in any direction, confirming that our experimental setup is only sensitive to LAW.

Subsequently to the investigations of STO, two additional perovskite crystals were studied: $SmScO_3$ (110) and $GdScO_3$ (110), which are both as well rather common substrates for thin-film deposition. The experimental results are presented in Figure 17 and 18, respectively. We first focus on $SmScO_3$ (110). In this case, the extracted Brillouin frequency is 35.1 GHz using the 776 nm probe. However, no Brillouin oscillations were visible with the 388 nm probe, and no frequency could be extracted at this wavelength.

One major limitation encountered in the analysis of $SmScO_3$ is the lack of available data for its optical refractive index. In the absence of such information, direct calculation of the LAW velocity from the Brillouin frequency is not possible. However, this limitation is an opportunity to approach the problem in reverse by calculating the refractive index from the theoretical calculation of LAW velocity along the (110) direction. $SmScO_3$ (110) has an orthorhombic structure, for which the elastic stiffness tensor takes the following form:

$$C = \begin{bmatrix} C_{11} & C_{12} & C_{13} & 0 & 0 & 0 \\ C_{12} & C_{22} & C_{23} & 0 & 0 & 0 \\ C_{13} & C_{23} & C_{33} & 0 & 0 & 0 \\ 0 & 0 & 0 & C_{44} & 0 & 0 \\ 0 & 0 & 0 & 0 & C_{55} & 0 \\ 0 & 0 & 0 & 0 & 0 & C_{66} \end{bmatrix}$$

For acoustic propagation along the (110) direction, the propagation unit vector is $\mathbf{n} = \frac{1}{\sqrt{2}}(1,1,0)$. The Christoffel tensor, defined by Equation (64), takes the following form:

$$\Gamma = \begin{bmatrix} \Gamma_{11} & \Gamma_{12} & 0 \\ \Gamma_{12} & \Gamma_{22} & 0 \\ 0 & 0 & \Gamma_{33} \end{bmatrix}$$

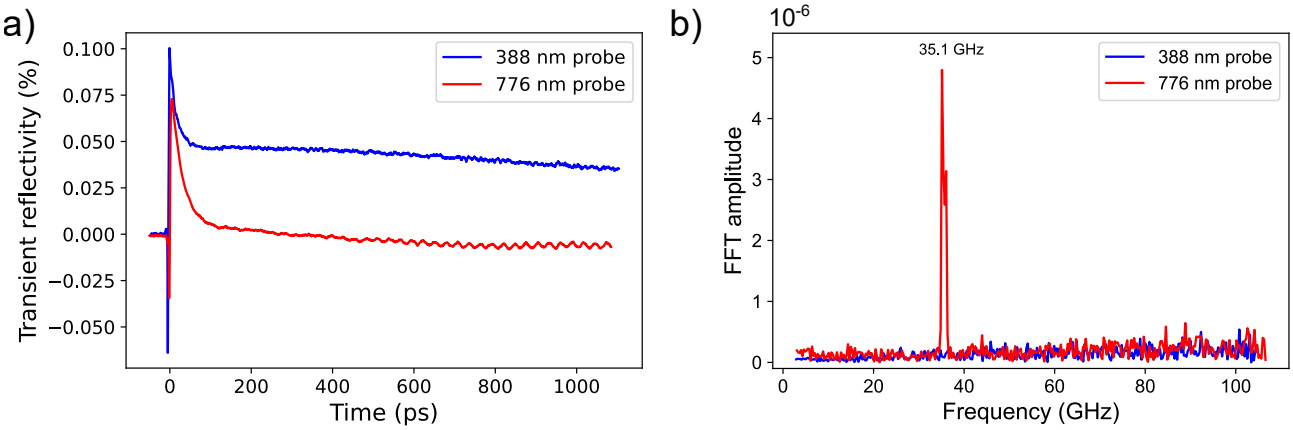

Figure 17: TDBS measurements on $SmScO_3$ (110) perovskite at 388 nm and 776 nm probe wavelengths. a) Measured transient reflectivity change from pump probe experiments, b) FFTs of the signals derivatives.

The computation of the Γ_{ik} values is done using the C_{ik} values from [49].

$$\Gamma_{11} = (C_{11} + C_{66})/2 = 184.2 \text{ GPa} \tag{67}$$

$$\Gamma_{22} = (C_{22} + C_{66})/2 = 191.6 \text{ GPa} \tag{68}$$

$$\Gamma_{33} = (C_{55} + C_{44})/2 = 91.2 \text{ GPa} \tag{69}$$

$$\Gamma_{12} = (C_{12} + C_{66})/2 = 108.5 \text{ GPa} \tag{70}$$

Formal calculation of Equation (63) leads to:

$$(\Gamma_{11} - \rho v_s^2)(\Gamma_{22} - \rho v_s^2)(\Gamma_{33} - \rho v_s^2) - \Gamma_{12}^2(\Gamma_{33} - \rho v_s^2) = 0 \tag{71}$$

Assuming that $\Gamma_{33} - \rho v_s^2 \neq 0$ allows simplification of Equation (71). This assumption removes the shear modes from the problem.

$$(\Gamma_{11} - \rho v_s^2)(\Gamma_{22} - \rho v_s^2) - \Gamma_{12}^2 = 0 \tag{72}$$

Equation (72) could be solved as a second-order polynomial equation by introducing the variable substitution $X = \rho v_s^2$. Two solutions of this equation will be extracted. The biggest corresponds to the longitudinal mode and the smallest to the transverse mode.

$$v_l^2 = \frac{\Gamma_{11} + \Gamma_{22} + \sqrt{(\Gamma_{11} - \Gamma_{22})^2 + 4\Gamma_{12}^2}}{2\rho} \tag{73}$$

$$v_t^2 = \frac{\Gamma_{11} + \Gamma_{22} - \sqrt{(\Gamma_{11} - \Gamma_{22})^2 + 4\Gamma_{12}^2}}{2\rho} \tag{74}$$

Note that, if the component $\Gamma_{33} - \rho v_s^2$ is not simplified from Equation (71), a third evident root of the equation is $v_s^2 = \Gamma_{33}/\rho$. This solution gives the velocity of the shear horizontal mode (SH mode).

Considering the computed values for Γ_{ik} and $\rho = 6325 \text{ kg} \cdot \text{m}^{-3}$, we determine that $v_l \simeq 6846 \text{ m} \cdot \text{s}^{-1}$. From this estimation of the sound velocity and with the measured value of the Brillouin frequency, we estimate the refractive index of $SmScO_3$ at 776 nm using Equation (61),

$$n_{776}(SmScO_3(110)) = \frac{35.1 \cdot 10^9 \times 776 \cdot 10^{-9}}{2 \times 6846} \simeq 1.99\,.$$

This result should be taken with care because it is subject to uncertainties in the elastic constant measurements and in the Brillouin frequency determination by TDBS measurements.

The third perovskite oxide investigated is $GdScO_3$. The experimental results are presented in Figure 18. The measured Brillouin frequencies are 73.0 GHz for the 388 nm probe and 34.5 GHz for the 776 nm probe.

As with $SmScO_3$, we face the limitation that no reliable values for the refractive index at 388 nm or 776 nm are readily available. An approach to address this limitation is to estimate the refractive indices by fitting the partial data reported in [50] with a 4th-order polynomial, given as follows:

$$P(X) = 1.539 \cdot 10^{-12}X^4 - 5.206 \cdot 10^{-9}X^3 + 6.494 \cdot 10^{-6}X^2 - 0.004X + 2.849 \tag{75}$$

Based on this polynomial fit, plotted in Figure 19, we estimate the refractive indices as $n_{388}(GdScO_3\ (110)) \simeq 2.16$ and $n_{776}(GdScO_3\ (110)) \simeq 2.09$.

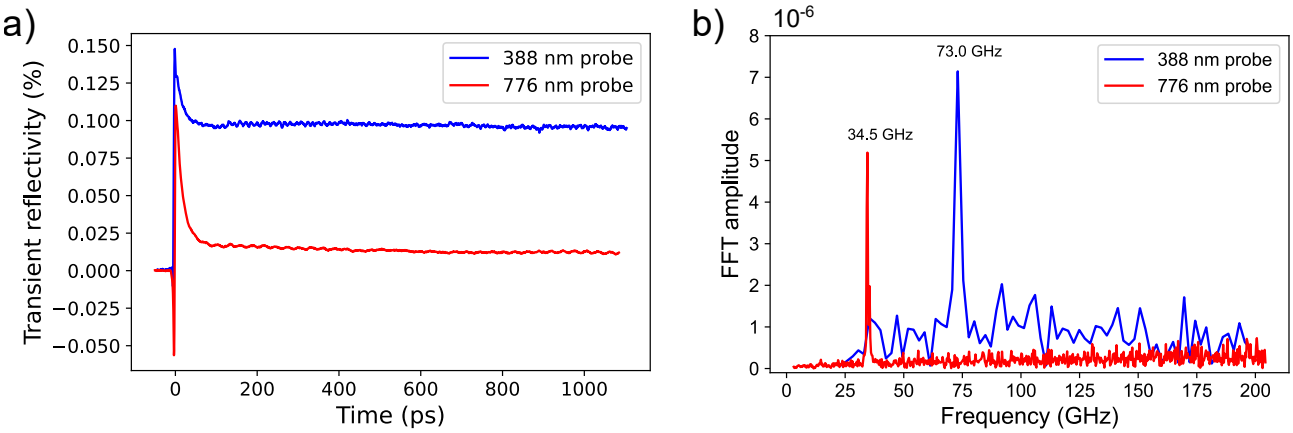

Figure 18: TDBS measurements on $GdScO_3$ (110) perovskite at 388 nm and 776 nm probe wavelengths. a) Measured transient reflectivity change from pump probe experiments, b) FFTs of the signals derivatives.

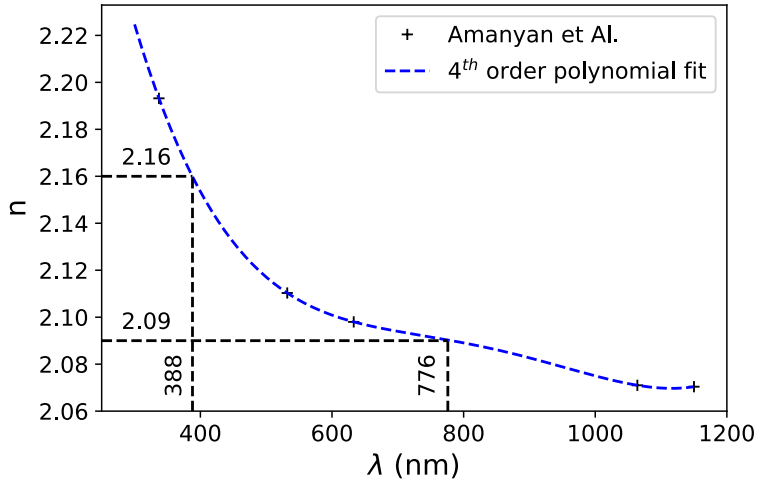

Figure 19: Polynomial fitting of partial data for $GdScO_3$ refractive indices.

Using the estimated values for the refractive indices, we calculate the LAW velocity along the (110) direction,

$$v_{l,388}(GdScO_3) = \frac{73.0 \cdot 10^9 \times 388 \cdot 10^{-9}}{2 \times 2.16} \simeq 6556 \text{ m} \cdot \text{s}^{-1},$$

$$v_{l,776}(GdScO_3) = \frac{34.5 \cdot 10^9 \times 776 \cdot 10^{-9}}{2 \times 2.09} \simeq 6405 \text{ m} \cdot \text{s}^{-1}.$$

Taking the average of these two values, we estimate the LAW velocity in $GdScO_3$ as $v_l(GdScO_3) \simeq 6481 \text{ m} \cdot \text{s}^{-1}$. This can be compared to a theoretical value obtained from the Christoffel equation, as it was done for $SmScO_3$. The elastic stiffness tensor values are taken from [51], and the symmetry of the Christoffel matrix remains identical as for $SmScO_3$ due to the structural and directional similarity. The calculated Christoffel components are $\Gamma_{11} \simeq 189$ GPa, $\Gamma_{22} \simeq 200$ GPa, $\Gamma_{33} \simeq 91$ GPa, and $\Gamma_{12} \simeq 106$ GPa. Solving the Christoffel equation leads to an estimated theoretical velocity for the longitudinal acoustic mode of $v_l(GdScO_3) \simeq 6728 \text{ m} \cdot \text{s}^{-1}$. The difference between the theoretical and experimental velocities is ∼3.8 %, which is within a reasonable range given the uncertainties in refractive index estimation and experimental precision.

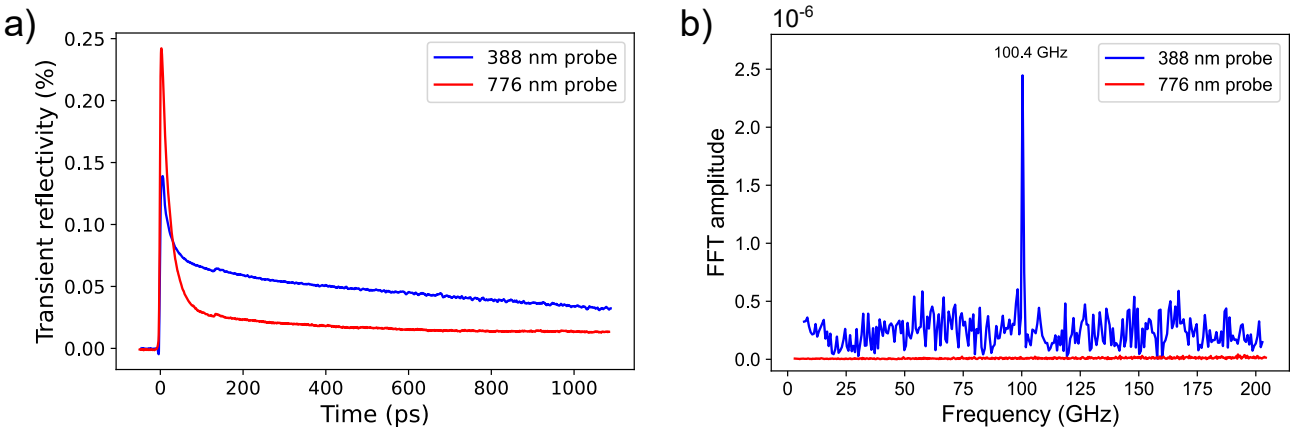

Figure 20: TDBS measurements on sapphire c-cut at 388 nm and 776 nm probe wavelengths. a) Measured transient reflectivity change from pump probe experiments, b) FFTs of the signals derivatives.

After investigating three perovskite crystals, we turn our attention to a single crystal of sapphire (Al_2O_3), oriented along the c-face (the face normal to the (0001) direction). The experimental results are presented in Figure 20. No Brillouin oscillations are visible for the 776 nm probe; thus, no frequency can be extracted from TDBS measurements, despite a significant electronic response to the femtosecond excitation. However, a clear Brillouin oscillation is observed with the 388 nm probe, yielding a measured frequency of 100.4 GHz. Given the refractive index of sapphire at 388 nm, $n_{388}(Al_2O_3) = 1.7887$, we estimate the LAW velocity along the (0001) direction as $v_l(Al_2O_3\ (0001)) \simeq 10889\ \mathrm{m \cdot s^{-1}}$. To compare this experimentally extracted LAW velocity with theory, we apply the Christoffel equation, taking into account the trigonal symmetry of sapphire. For an acoustic wave propagating along the c-axis, $\mathbf{n}$=(0,0,1), the elastic stiffness tensor C_{ij} and the form of the Christoffel matrix Γ are given below,

$$C = \begin{bmatrix} C_{11} & C_{12} & C_{13} & C_{14} & 0 & 0 \\ C_{12} & C_{11} & C_{13} & -C_{14} & 0 & 0 \\ C_{13} & C_{13} & C_{33} & 0 & 0 & 0 \\ C_{14} & -C_{14} & 0 & C_{44} & 0 & 0 \\ 0 & 0 & 0 & 0 & C_{44} & C_{14} \\ 0 & 0 & 0 & 0 & C_{14} & C_{66} \end{bmatrix},$$

$$\Gamma = \begin{bmatrix} C_{44} & 0 & 0 \\ 0 & C_{44} & 0 \\ 0 & 0 & C_{33} \end{bmatrix}.$$

In the trigonal symmetry, it is common to assume $C_{14} \simeq 0$ and to use the identity $C_{66} = (C_{11}\text{-}C_{12})/2$. The relevant elastic stiffness constants, taken from literature, are $C_{33} = 498$ GPa and $C_{44} = 148$ GPa. We also take $\rho = 3970\ \mathrm{kg \cdot m^{-3}}$. Resolution of the Christoffel determinant equation yields:

$$(C_{44} - \rho v_s^2)(C_{44} - \rho v_s^2)(C_{33} - \rho v_s^2) = 0\,. \tag{76}$$

Equation (76) has a double root for $v_s^2 = C_{44}/\rho$, corresponding to two degenerate transverse acoustic waves, and a simple root for $v_s^2 = C_{33}/\rho$, corresponding to the LAW. This gives:

$$v_l = \sqrt{C_{33}/\rho} \simeq 11200\ \mathrm{m \cdot s^{-1}}, \tag{77}$$

$$v_t = \sqrt{C_{44}/\rho} \simeq 6106\ \mathrm{m \cdot s^{-1}}. \tag{78}$$

These theoretical values confirm the experimental results, with a relative deviation of ∼2.9 %. This agreement supports the validity of our TDBS results.

After the investigation of Al_2O_3, TDBS measurements were conducted on YAl_2O_3 (001), which is another exotic substrate. The experimental results are presented in Figure 21. In contrast to the case of c-cut sapphire, Brillouin oscillations are well visible for both probe wavelengths in YAl_2O_3, and two Brillouin frequencies are extracted, even at 388 nm, where the FFT spectrum is notably noisier. The measured Brillouin frequencies are 80.7 GHz for the 388 nm probe and 39.4 GHz for the 776 nm probe.

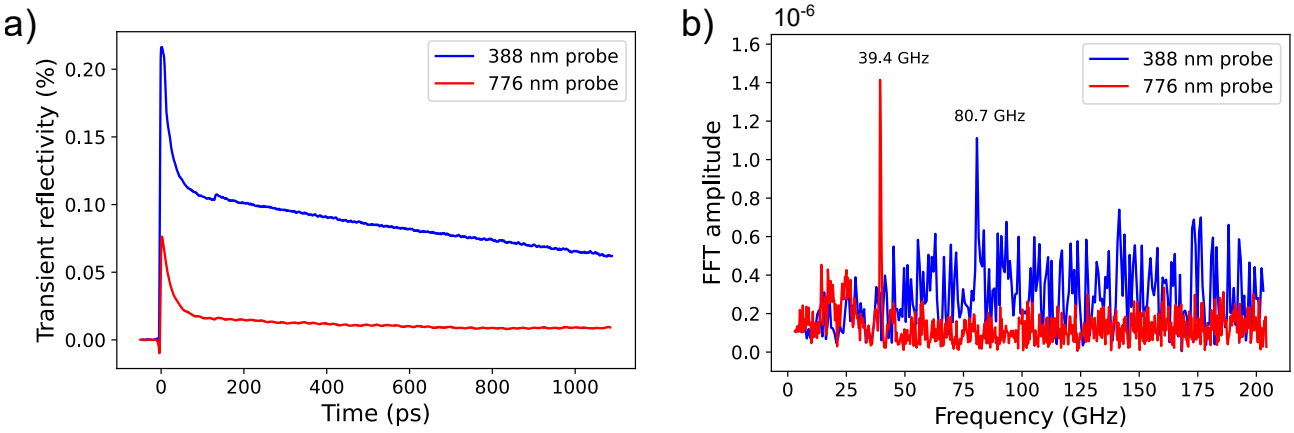

Figure 21: TDBS measurements on YAl_2O_3 at 388 nm and 776 nm probe wavelengths. a) Measured transient reflectivity change from pump probe experiments, b) FFTs of the signals derivatives.

However, as in other less-characterized materials, the main limitation here is the lack of data on refractive index for YAl_2O_3 at the wavelengths of interest. Unlike the previously investigated perovskite oxide, where reliable interpolation or extrapolation of the refractive index is possible, few optical studies exist on YAl_2O_3. It is reasonable to expect the refractive index to be similar to that of structurally related materials such as YAG ($Y_3Al_5O_{12}$) or YAP ($YAlO_3$), but without precise data, any assumption would introduce a large uncertainty to support a reliable determination of the LAW velocity and further, elastic parameters.

A thorough optical characterization of YAl_2O_3, including precise measurements of its refractive index across the visible and near-UV spectrum, would therefore be a valuable next step to support and extend the TDBS findings.

To conclude these TDBS measurements, we investigated gadolinium gallium garnet ($Gd_3Ga_5O_{12}$), referred to as GGG, and its substituted variant (SGGG), which is the only substrate for thin film deposition of yttrium iron garnet (YIG), a very interesting ferrimagnetic material. The results for GGG are presented in Figure 22. As shown, no data is available for the 776 nm probe due to the absence of a detected signal at this wavelength. Nevertheless, a Brillouin frequency of 65.1 GHz was successfully extracted using the 388 nm probe. If we assume the refractive index at 388 nm from literature [52], this yields $n_{388}(\mathrm{GGG}) \simeq 1.96$. Using this refractive index and the measured Brillouin frequency, we estimate the LAW velocity in GGG to be $v_l(\mathrm{GGG}) = 6444\ \mathrm{m \cdot s^{-1}}$.

Now the question is: along which direction is this LAW propagating? To answer this question, we assume that the GGG has a cubic structure, and we take the elastic stiffness coefficient, $C_{11} = 305.2$ GPa, $C_{12} = 125.1$ GPa, and $C_{44} = 81.45$ GPa, from literature [53]. The density is taken from the technical data given by the seller: $\rho = 7080\ \mathrm{kg \cdot m^{-3}}$. The equations for calculation of LAW velocity

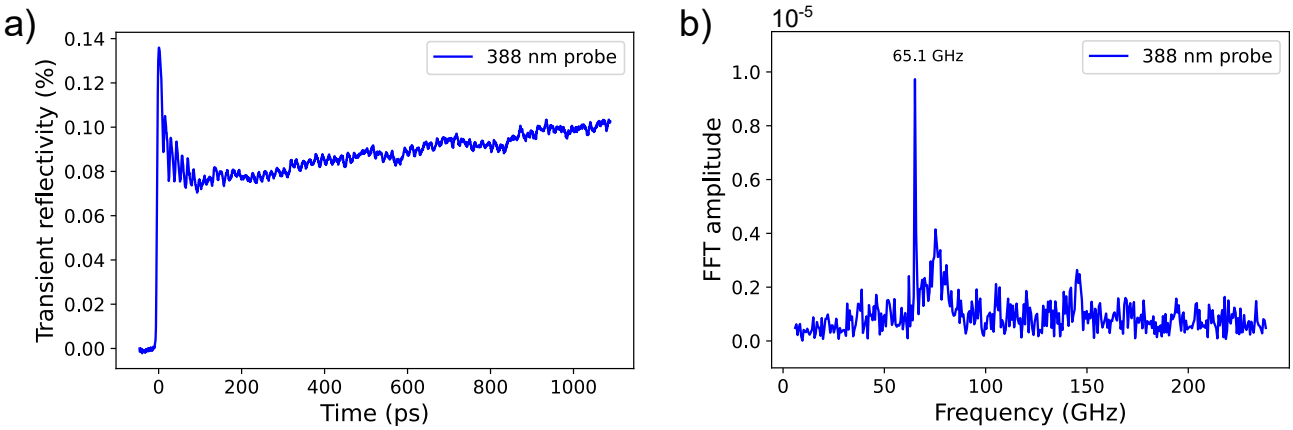

Figure 22: TDBS measurements on GGG at 388 nm probe. a) Measured transient reflectivity change from pump probe experiments, b) FFT of the signal derivative.

along the (100), (110), and (111) directions in a cubic structure are recalled below, while the numerical applications are done for GGG.

$$v_l^{(100)} = \sqrt{C_{11}/\rho} \simeq 6567 \text{ m} \cdot \text{s}^{-1} \tag{79}$$

$$v_l^{(110)} = \sqrt{\frac{C_{11} + C_{12} + 2C_{44}}{2\rho}} \simeq 6472 \text{ m} \cdot \text{s}^{-1} \tag{80}$$

$$v_l^{(111)} = \sqrt{\frac{C_{11} + 2C_{12} + 4C_{44}}{3\rho}} \simeq 6441 \text{ m} \cdot \text{s}^{-1} \tag{81}$$

We identify a less than one percent deviation between our experimentally determined LAW velocity and $v_l^{(111)}$. According to this result, we could confidently conclude that we have investigated GGG along the (111) direction.

Final investigations were carried out on a doped variant of GGG, known as substituted gadolinium gallium garnet ($(Gd_{2.6}Ca_{0.4})(Ga_{4.1}Mg_{0.25}Zr_{0.65})O_{12}$, SGGG). The experimental results are presented in Figure 23. As previously observed for YAl_2O_3, the FFT spectrum is noisy, particularly at 388 nm, but still enables the identification of a Brillouin frequency of 64.4 GHz at this probe wavelength. For the

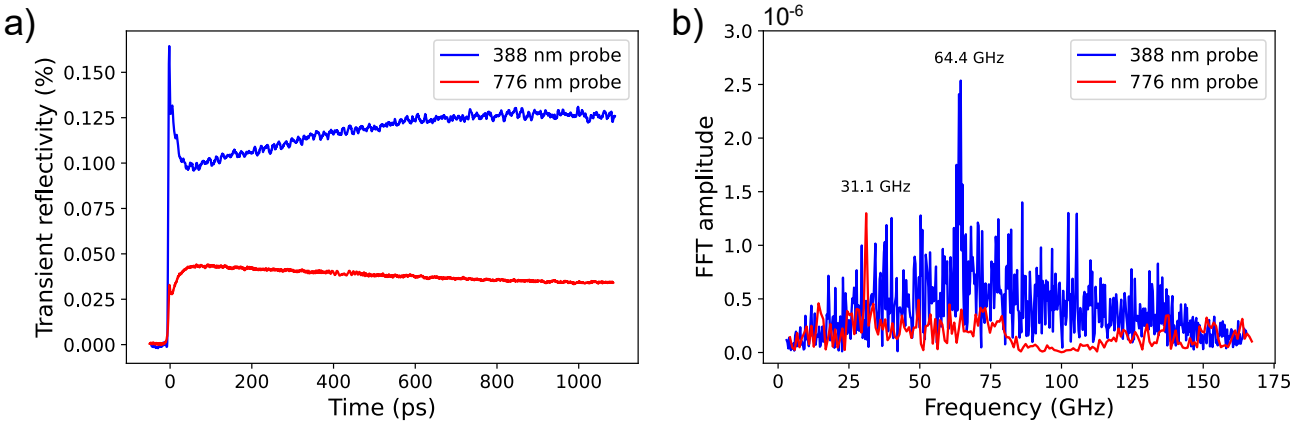

Figure 23: TDBS measurements on SGGG at 388 nm and 776 nm probe wavelengths. a) Measured transient reflectivity change from pump probe experiments, b) FFTs of the signals derivatives.

776 nm probe, the identified Brillouin frequency is 31.1 GHz. The most commonly reported refractive index for SGGG is approximately 1.92 at 1 µm. However, available optical data in the visible range remains scarce. Most investigations on doped gadolinium gallium garnets focus on optical phonon behavior and the epitaxial growth of magneto-optic films, leaving both the elastic and visible-range optical properties of SGGG poorly characterized.

Due to the current limitations in the literature regarding both the elastic constants and wavelength-dependent refractive index of SGGG, it is not possible to quantitatively determine the acoustic velocity or elastic moduli from our TDBS measurements. Nonetheless, based on the consistency of our results across other well-characterized materials, including GGG, we maintain confidence in the accuracy of the Brillouin frequencies extracted from the experimental data.

3.3 Outlook: TDBS investigations in the linear transparency regime

To conclude this section, which presented a series of TDBS investigations on a wide variety of transparent substrates, we summarize the main results in Table [2]. It reports the experimentally measured Brillouin frequencies, the corresponding LAW velocities, and theoretical values calculated from literature data. The small discrepancies confirm both the accuracy of the measurements and the reliability of our setup, even for substrates for which no direct comparison with published values was available. In addition, these results highlight that our setup allows not only the determination of elastic constants but also the identification of crystallographic orientations.

	Brillouin frequency in GHz at λ=		Sound velocity ($m \cdot s^{-1}$)	
Substrate	388 nm	776 nm	Experiments	Literature
SiO_2	43.9	21.7	5790	5953
MgO (001)	80.3	39.6	8841	9016
MgO (111)	90.0	44.1	9896	9788
STO	105.6	46.2	7608	7842
$SmScO_3$ (110)	/	35.1	/	6846
$GdScO_3$ (110)	73.0	34.5	6481	6728
Al_2O_3 c-face	100.4	/	10889	11200
YAl_2O_3 (001)	80.7	39.4	/	/
GGG	65.1	/	6444	6441
SGGG	64.4	31.1	/	/

Table 2: Measured Brillouin frequencies, experimentally extracted LAW velocities, and theoretical calculations of LAW velocities.

As mentioned previously, one of the objectives of TDBS investigations in linear transparent materials is to enable resonant excitation and detection, thereby enhancing acoustic intensity and improving signal-to-noise ratio. Figure 24 presents resonant TDBS experiments on fused silica, performed by Paolo Paris, Giorgio Santarelli, Eric Cormier, and collaborators at the Bordeaux Optics Institute.

Experimentally, the pump source was tuned close to half the Brillouin frequency, $f_B/2 \simeq 16.75$ GHz (for a 515 nm probe), and fine adjustments were performed to reach resonance. Figure 24(a) shows time-domain signals, where five successive steps correspond to the five-pulse burst. The effect of the time interval between pulses within the burst is also clearly seen.

Figure 24(b) displays the normalized acoustic amplitude as a function of the pump repetition rate for 5-, 10-, and 20-pulse bursts. As expected, the acoustic amplitude reaches a maximum when the repetition rate matches the Brillouin frequency. The larger the number of pump pulses in the burst,

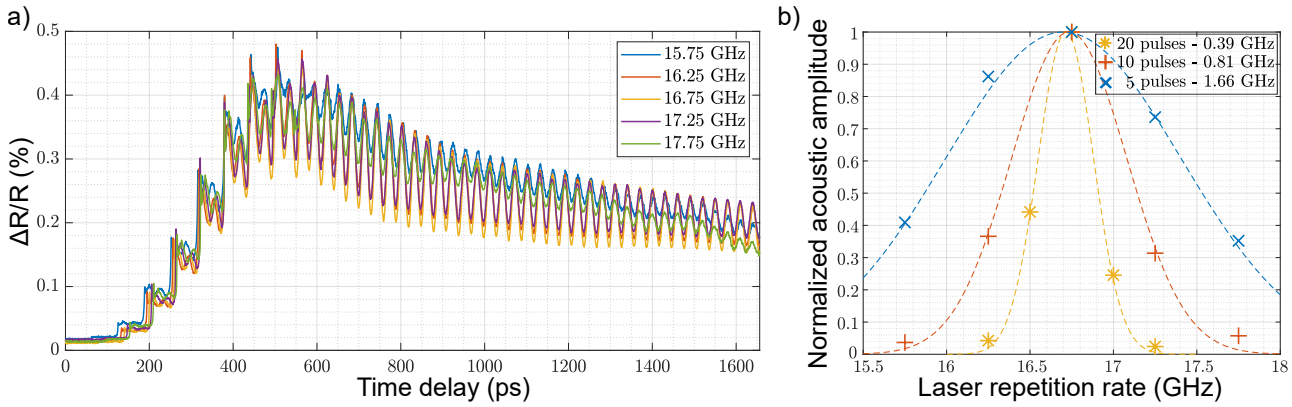

Figure 24: Resonant TDBS performed by Paolo Paris, Giorgio Santarelli, and Eric Cormier on fused silica probed at 515 nm. (a) Five-pulse burst generation of LAWs for different laser repetition rates around half the Brillouin frequency. (b) Sensitivity of acoustic generation to the number of pulses per burst.

the more sensitive the generation becomes to detuning, leading in some cases to a complete suppression of the signal.

Finally, resonant excitation requires a pump repetition rate of the form f_B/n, with n an integer. In contrast, repetition rates of the form $n \cdot f_B$ (with $n > 1$) only cause cumulative heating without enhancing the generation process. The ideal condition would therefore be a repetition rate equal to f_B, although this was not technically achievable during the reported measurements. These resonant TDBS investigations, combined with our linear studies on exotic substrates, now make it possible to extend the work toward stronger LAW-induced perturbations while simultaneously reducing acquisition time and improving the signal-to-noise ratio.

4 Multiphoton generation of longitudinal acoustic waves

In the previous sections, we introduced the principles of optical generation and detection commonly used to investigate acoustic propagation in solids. We also demonstrated the reliability of our setup across a wide variety of transparent substrates. However, a significant limitation remains: all materials studied so far were transparent and therefore required a thin chromium coating to act as a transducer. This thin metallic layer was essential because the relative transparency of the materials prevented from the efficient direct generation of any type of acoustic waves. Moreover, the transparency at the probe wavelength was also necessary to allow the in-depth detection of acoustic waves propagating within the substrate. The limitation arises when metallic coating is either not technically possible or not desirable due to fabrication constraints or material properties. An example of limitation is the organic materials. To address this limitation, several methods of direct acoustic wave generation have been explored in the literature. For instance, LAWs can be generated by direct excitation of the Raman-active modes using a mid-infrared optical pump [54]. However, this technique requires wavelengths that lie out of the operating range of our laser source. Another interesting approach is the excitation of ionic Raman scattering, which also uses an infrared optical excitation, but at wavelengths closer to 800 nm [55]. Although this spectral range is accessible with our laser system, we have chosen to set our pump wavelength at 776 nm to match the specifications and coatings of our optical components.

In this context, we explored the possibility of direct acoustic generation via nonlinear multiphoton absorption. The physical principles governing the subsequent processes, femtosecond laser heating, thermoelastic expansion, acoustic wave propagation, and optical detection, remain the same as in

the case of generation via a metallic transducer. However, the absorption process and the ultrafast relaxation dynamics leading to acoustic generation differ significantly depending on the material and its electronic structure. Therefore, in the following, we focus only on the relevant energy relaxation mechanisms for each investigated material. We first introduce the experimental setup used for direct nonlinear generation of acoustic waves before presenting and analyzing the studied materials.

4.1 Experimental setup

To investigate LAW generation via nonlinear multiphoton absorption, few modifications were made to the original setup (Figure 7), as presented in the updated configuration (Figure 25). The major change is the addition of a spinning mirror placed between the dichroic mirror, which multiplexes the pump and probe beams, and the microscope objective, which focuses them onto the sample. This spinning mirror directs the beams along a circular trajectory, thereby continuously displacing the excitation spot on the sample. This spatial propagation reduces cumulative heating effects and minimizes the risk of optical damage. As a result, the pump fluence can be increased, enhancing the efficiency of multiphoton absorption. A second modification involves the use of a non-polarizing beam splitter (NPBS) instead of a PBS to redirect the probe beam toward the photodiode. This adjustment was made to avoid polarization-dependent transmission variations that may occur due to slight changes in the beam propagation direction coming from the spinning mirror.

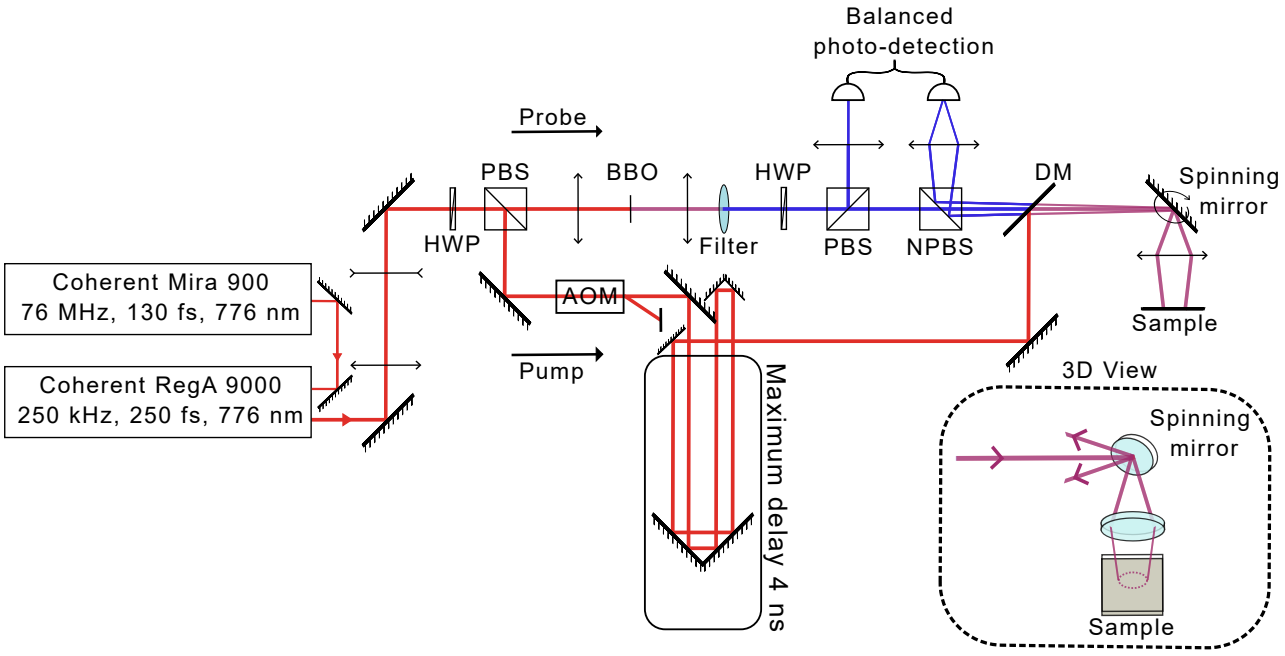

Figure 25: Experimental setup used to investigate multiphoton excitation of longitudinal acoustic waves.

4.2 Two-photon activation of thermal response in complex organometallic

Photoacoustic imaging has recently emerged as a key technique in molecular bioimaging due to its ability to combine high optical contrast with ultrasonic resolution [56–58]. As shown in the previous section, ultrasonics is a powerful method for in-depth investigations and therefore for reconstructing 3D images. Despite significant advances in instrumentation and image processing, photoacoustic microscopy still faces a major challenge: a rapid loss of resolution when imaging deep inside tissue. To address this, researchers have proposed replacing conventional one-photon absorbing (1PA) contrast

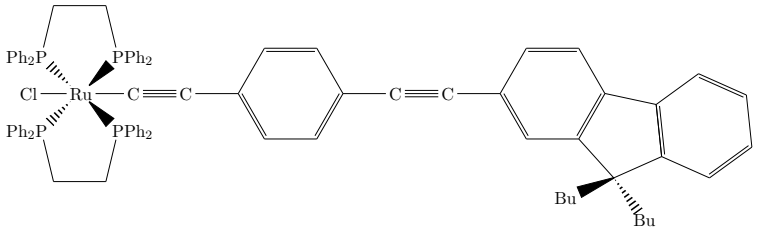

Figure 26: Semi-developed chemical formula of the investigated organoruthenium complex.

agents with two-photon absorbing (2PA) compounds. This approach offers multiple advantages. It allows the use of near-infrared wavelengths, which penetrate deeper into biological tissue, and reduces unwanted photodamage, since 2PA occurs only at the laser focus. Additionally, the nonlinear intensity dependence of 2PA provides enhanced spatial selectivity and contrast. Nevertheless, despite promising studies, the development of practical 2PA-based photoacoustic imaging remains limited. Current techniques are designed for linear optical regimes and are poorly suited to study the highly localized phenomena involved in nonlinear regimes. This underlines the need for experimental methods capable of characterizing nonlinear photothermal and photoacoustic responses in 2PA contrast agents.

In this context, organometallic compounds are particularly attractive candidates due to their strong two-photon absorption, tunable photophysical properties, and chemical stability. In the following, we investigate a representative ruthenium-based organometallic complex specifically engineered for 2PA activation within the near-infrared region I (NIR-I, 700 nm to 1000 nm). This compound was originally developed for biomedical imaging and photothermal therapy. Therefore, quantifying its nonlinear optical activation and thermal response, particularly within the NIR-I region where biological tissues such as skin are relatively transparent, is of critical importance. The molecular structure of the compound is shown in Figure 26. Its two-photon absorption cross section σ_2 has been previously reported as 1075 ± 190 GM in [59], where GM denotes a Goppert-Mayer unit (1 GM = 10^{-50} cm^4·s). To experimentally assess its two-photon-induced thermal activation, we determine its effective nonlinear absorption cross section using TDBS. For this purpose, a thin film of the organoruthenium complex was deposited on a glass substrate via spin coating. In this configuration, the organoruthenium complex acts as a two-photon activable transducer in the NIR-I spectral range. A femtosecond laser pulse at 1.6 eV (780 nm) is used as the optical pump, while the generated LAW, arising from thermoelastic expansion of the organic film, is probed as it propagates through the underlying glass substrate. Using a well-characterized substrate for acoustic detection reduces uncertainties and simplifies the interpretation of the measured nonlinear absorption efficiency.

The electronic excitation/relaxation pathway of the studied organoruthenium complex is schematically illustrated in Figure 27. Upon nonlinear excitation, the process is initiated by 2PA, in which two photons of energy $\hbar\omega_1 = 1.6$ eV are absorbed simultaneously, promoting the system to a higher-lying electronic state. The total excitation energy is $E = 2\hbar\omega_1 = 3.2$ eV, corresponding to a single photon transition at frequency $\omega_2 = 2\omega_1$. This nonlinear optical process promotes electrons from the ground singlet state S_0 to an excited singlet state S_n. Subsequently, ultrafast internal conversion relaxes the system to the first singlet state S_1. From S_1, relaxation can proceed via two competing pathways: radiative decay to the ground state through fluorescence (F) or intersystem crossing (ISC) to the lowest triplet state T_1, a nonradiative transition facilitated by the strong spin-orbit coupling introduced by the ruthenium presence. In the context of our TDBS experiments, this nonradiative ISC pathway, accompanied by phonon emission, constitutes the primary mechanism for the generation of acoustic phonon wave packets. A second possible phonon-emitting transition occurs during the relaxation via ISC from the triplet state T_1 to the singlet ground state S_0, but this transition is typically governed by

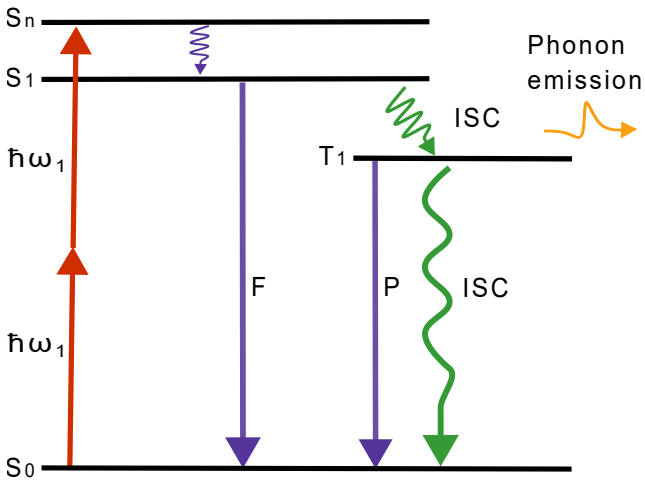

Figure 27: Generation of acoustic phonons from two-photon absorption and intersystem crossing relaxation. S_i: singlet state, T_i: triplet state, F: fluorescence, P: phosphorescence, ISC: intersystem crossing.

longer-living triplet dynamics (on the order of nanoseconds), which lie outside the temporal resolution of our pump-probe experimental setup. As a result, only ultrafast relaxation dynamics contribute to the acoustic signal recorded from our TDBS setup.

To investigate the nonlinear excitation of strain waves via 2PA, we performed a series of TDBS measurements over a wide range of pump fluences. The results are presented in Figure 28. Figure 28(a) shows the TDBS signals recorded at various pump fluences using a 1.6 eV femtosecond laser. The time-domain responses exhibit features comparable to those previously observed in experiments involving metallic transducers. Notably, a sharp, pronounced spike at time zero, corresponding to the ultrafast absorption of the pump photons by the organoruthenium complex electrons, inducing rapid changes in the compound's optical properties and a strong reflectivity change of the probe light. Following this initial spike, a long-lasting background signal extends over hundreds of picoseconds. This baseline reflects the progressive relaxation of excited electrons back to the ground state S_0, as outlined in Figure 27. The sharp onset of this background indicates a fast internal conversion from the excited singlet state S_n to the lower singlet state S_1, whereas the flatter prolonged background decay is attributed to the relaxation from the lower triplet T_1 to the ground state S_0. In the case of the investigated organoruthenium complex, this $T_1 \rightarrow S_0$ transition may kinetically dominate the $S_1 \rightarrow S_0$ transition due to low-energy triplet ligand field states [59]. As in previous analysis, the Brillouin frequency was extracted via FFT of the signal derivative. The 44 GHz frequency peak highlighted in FFTs, Figure 28(b), is unambiguously the Brillouin frequency in fused silica probed at 390 nm. The transparency of fused silica at 1.6 eV and 3.2 eV, and the film transparency at 1.6 eV confirm that the observed Brillouin signals originate from nonlinear optical absorption processes in organoruthenium, which exhibit a nonlinear dependence on the pump fluence. As shown in Figure 28(c), the amplitude of the FFT at fused silica Brillouin frequency increases nonlinearly with increasing optical pump fluence. More specifically, a quadratic dependence on the pump fluence is observed, indicating that the underlying process is of second order. This quadratic behavior becomes clearly distinguishable above a fluence threshold of approximately 0.30 $mJ \cdot cm^{-2}$. Below this threshold, as shown at 240 $mJ \cdot cm^{-2}$ in Figure 28(b), the Brillouin frequency peak is no longer visible.

Control experiments were also conducted on the glass substrate alone with 1.6 eV and 3.2 eV optical sources and confirm the absence of any Brillouin scattering. Furthermore, the consistency of the Brillouin phase across the range of pump fluences, as shown in Figure 28(d), indicates the mate-

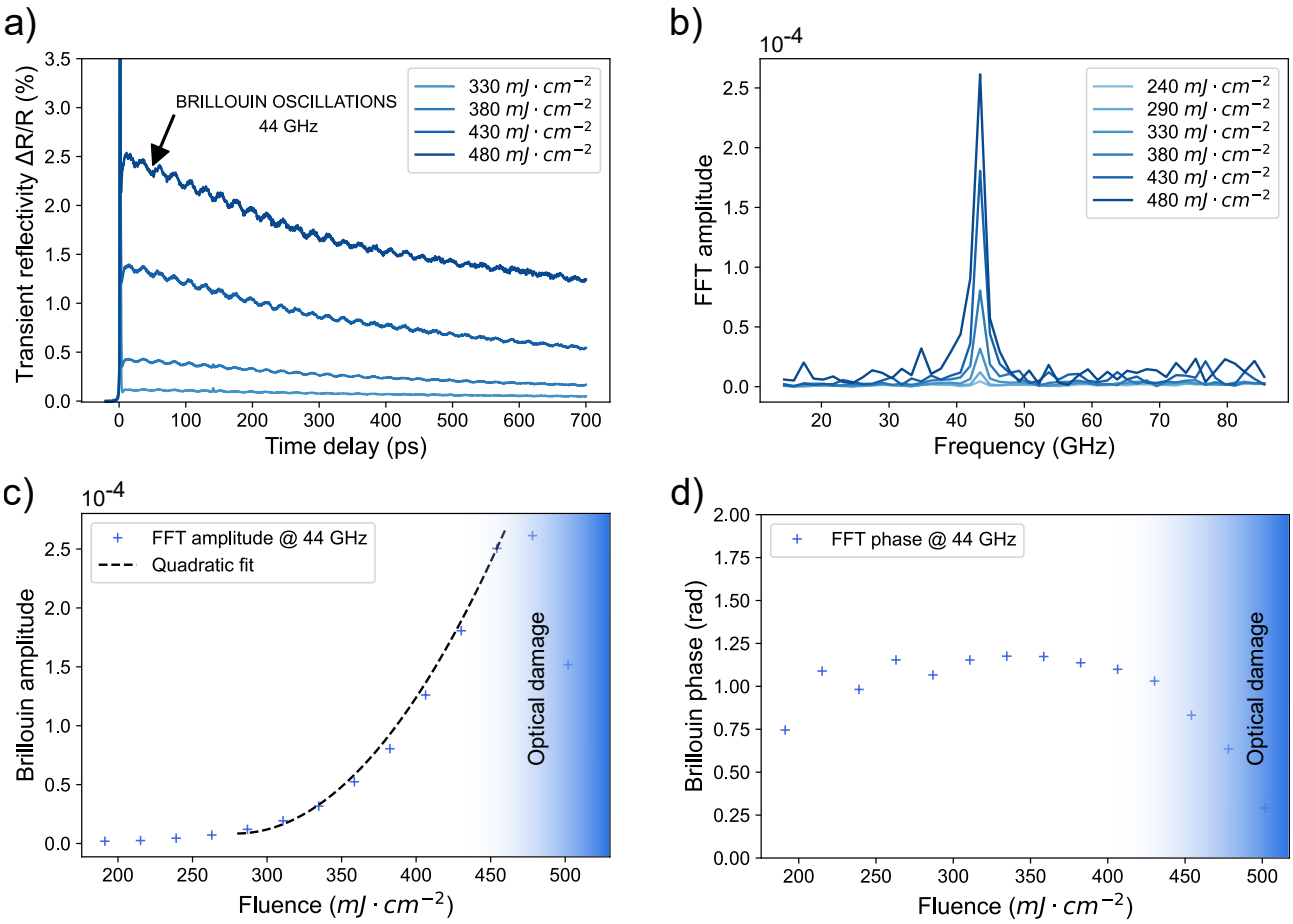

Figure 28: TDBS data at varying pump fluences at a pump wavelength of 780 nm. a) Time-domain transient reflectivity data. b) FFT of the transient reflectivity data after slow background removal. c) FFT amplitude of the Brillouin peak at 44 GHz versus pump fluence. d) FFT phase of the Brillouin peak at 44 GHz versus pump fluence.

rial properties stability [60, 61], until optical damage occurs at higher pump fluences. These results conclusively demonstrate that the investigated organoruthenium compound is effectively photothermally and photoacoustically activated through two-photon absorption in the NIR-I region, validating its potential use as a nonlinear contrast agent in medical imaging or phototherapy applications. As discussed earlier, TDBS is intrinsically sensitive to acoustic phonon wavepackets generated on the picosecond timescale and is not suited to detect phonons with durations longer than a fraction of the Brillouin period. Therefore, the observation of Brillouin oscillations in the substrate implies that the $S_1 \rightarrow T_1$ transition must occur within a few picoseconds. If the transition were slower, no acoustic signal would be observed. This temporal selectivity enables TDBS to isolate fast relaxation processes while filtering slower ones, which can still appear as a slow-varying electronic background in the reflectivity signal, as seen in Figure 28(a). To further investigate the relation between the Brillouin signal and the slow electronic relaxation background, we replotted Figure 28(c) on a logarithmic scale and added the electronic transitions background amplitude. This background was estimated as the average transient reflectivity in the 10 to 100 ps time window to exclude the initial time-zero spike and to average out the Brillouin oscillations, providing a better estimation of the thermal baseline. This replot on a logarithmic scale is given in Figure 29.

Figure 29 reveals that both the Brillouin amplitude and the electronic transitions background exhibit a quadratic dependence on the pump fluence. This shared scaling behavior indicates that both

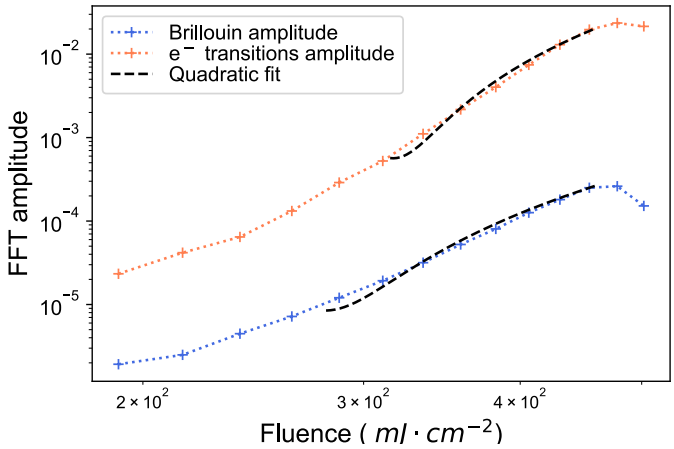

Figure 29: Brillouin and electronic transitions background amplitudes of Figure 28(a), plotted on a logarithmic scale.

phenomena are driven by the same underlying nonlinear optical process, the 2PA. While the Brillouin scattering reflects the fast thermoelastic response, the slower electronic background is attributed to slow electronic transitions.

The strain generation via 2PA is quantitatively described by Equation (82), adapted from [62]. In this expression, η_{33}^{2PA} is the unidirectional longitudinal strain propagating along the sample normal direction, $\mathcal{F}_{2PA}$ is the effective laser fluence for 2PA, ρ is the organoruthenium film density, C_p is the specific heat, γ is the linear thermal expansion coefficient, τ is the laser pulse duration (FWHM), and $\alpha^{(2)}$ is the 2PA coefficient. The effective fluence $\mathcal{F}_{2PA}$ accounts for reflections at the air/film interface and is related to the incident fluence $\mathcal{F}_0$ through $\mathcal{F}_{2PA} = \mathcal{F}_0(1-\mathcal{R})$, where $\mathcal{R}$ denotes the air/film interface optical reflectivity at the pump wavelength.

$$\eta_{33}^{2PA} = \frac{\gamma}{\rho C_p}\sqrt{\frac{ln4}{\pi}}\left(\alpha^{(2)}\frac{\mathcal{F}_{2PA}^2}{\tau}\right) \tag{82}$$

The strain η_{33} is directly proportional to the Brillouin signal amplitude recorded in the glass substrate. Therefore, to go beyond a qualitative analysis and extract the coefficient $\alpha^{(2)}$ quantitatively from Equation (82), several key parameters (density, heat capacity, and thermal expansion) are required. These parameters are difficult to determine accurately for thin films and may necessitate additional independent measurements. However, we demonstrate that this complexity can be bypassed by performing TDBS measurements at two different pump wavelengths, allowing a comparative approach that eliminates the need for separate material characterizations.

Additional experiments were conducted by changing the pump photon energy from 1.6 eV, where 2PA is required to generate LAWs, to 3.2 eV, while maintaining the probe wavelength fixed at 390 nm. The 3.2 eV pump was generated via second harmonic generation in a β-BBO crystal from the 1.6 eV pump (a process already introduced in previous sections). The conversion efficiency of the BBO is in the percent range, resulting in pump fluences at 3.2 eV that were only a small fraction of those used at 1.6 eV. At this higher photon energy, 1PA becomes sufficient to induce excitation, leading to an expected linear photoacoustic response. Although the maximum one-photon pump could not reach the same fluence as the two-photon one, Figure 30(a) clearly shows that Brillouin scattering is detectable under 1PA excitation. In contrast to the 2PA case shown in Figure 28(a), the one-photon recorded signals, Figure 30(a), exhibit no significant long-living electronic or thermal background. The different TDBS acquisitions at various fluences are superimposed. The Brillouin frequency in

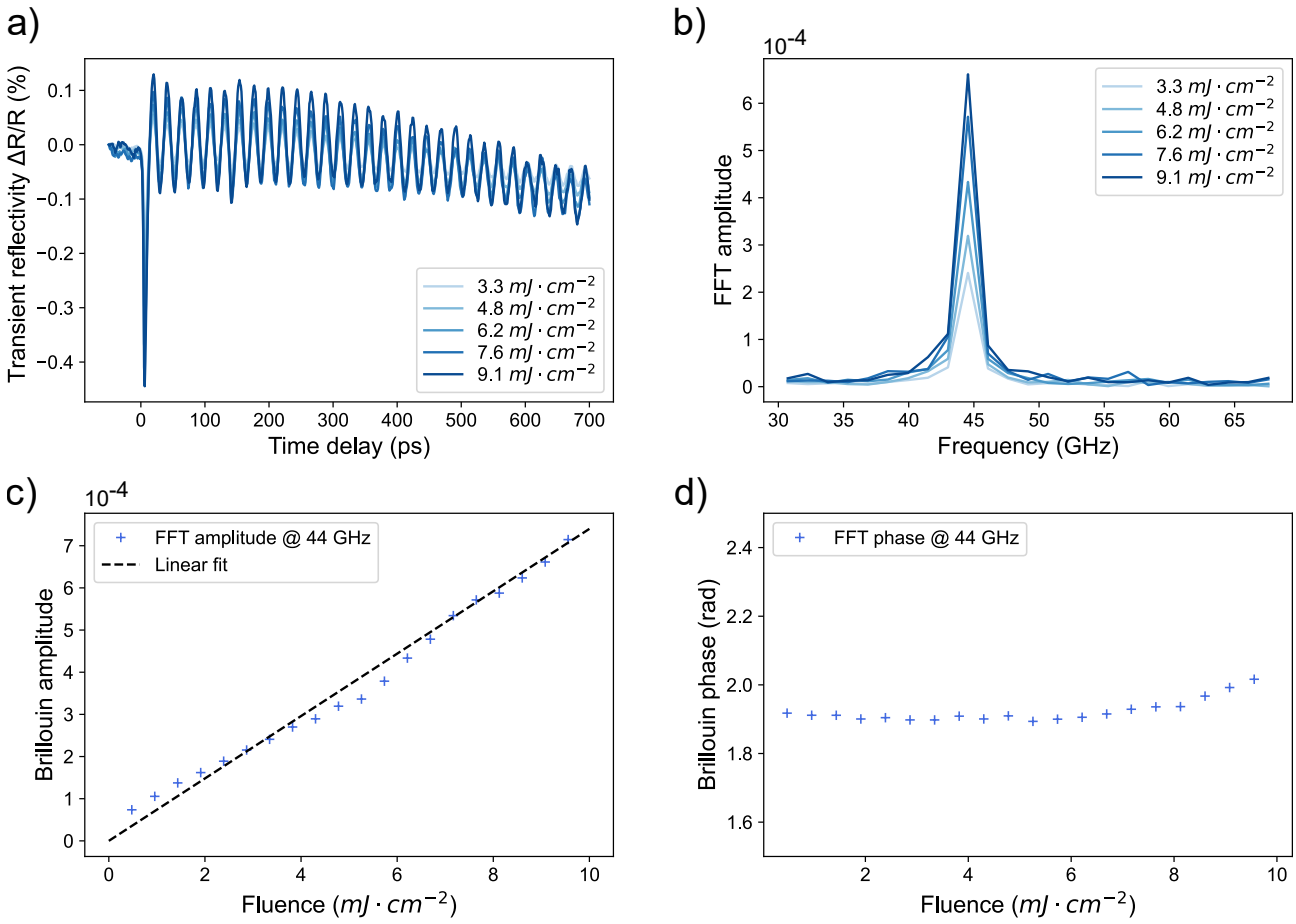

Figure 30: TDBS data at varying pump fluences at a pump wavelength of 390 nm. a) Time-domain transient reflectivity data. b) FFT of the the transient reflectivity data after slow background removal. c) FFT amplitude of the Brillouin peak at 44 GHz versus pump fluence. d) FFT phase of the Brillouin peak at 44 GHz versus pump fluence.

the glass substrate is clearly resolved (see Figure 30(b)). As expected, the Brillouin amplitude scales linearly with the pump fluence, as shown in Figure 30(c), while the Brillouin phase remains constant across fluences, Figure 30(d), confirming the stability of the material response in the 1PA regime. Notably, the Brillouin amplitude from 1PA excitation shown in Figure 30(c) reaches approximately 4×10^{-4} at a fluence of 6 mJ $\cdot$ cm^{-2}, while for 2PA the same amplitude is reached at a fluence as high as 450 mJ $\cdot$ cm^{-2}. This implies that 2PA is roughly 75 times less efficient than 1PA in this context. These results highlight the potential of our TDBS-based technique to be used as a tool for assessing and comparing a wide range of compounds and optimizing those that can exhibit better performance in the 2PA regime. In the 1PA case, the laser-excited strain is theoretically deduced from Equation (83), also extracted from [62]. In this equation, d is the film thickness, $\alpha^{(1)}$ is the 1PA optical absorption coefficient, and $\mathcal{F}_{1PA}$ is the effective fluence of the 1PA pump.

$$\eta_{33}^{1PA} = \frac{\gamma}{\rho\, C_p\, d}\left(1 - e^{-\alpha^{(1)} d}\right)\mathcal{F}_{1PA} \tag{83}$$

Equation (83) corresponds to the averaged strain over the film thickness, in contrast to the 2PA case, Equation (82), which models a more uniform excitation due to spatial confinement of 2PA at laser focus.

Since the probe wavelength is identical for both 1PA and 2PA measurements, the Brillouin amplitudes scale linearly with the respective strain amplitudes. This linear relationship can be expressed

as follows:

$$\begin{aligned} A_B^{1PA} &= K_{1PA} \cdot \eta_{33}^{1PA}, \\ A_B^{2PA} &= K_{2PA} \cdot \eta_{33}^{2PA}. \end{aligned} \tag{84}$$

The proportionality constants K_{1PA} and K_{2PA} encapsulate the influence of material specific parameters, including the photoelastic coefficient of the glass substrate, the refractive index, the acoustic impedance mismatch, and the shape of the strain profile [39]. Assuming that the optical absorption profile is effectively homogeneous in both 1PA and 2PA regimes (a reasonable assumption in thin films), we may simplify the analysis by setting $K_{1PA} = K_{2PA} = K$. While these constants can be computed via finite element simulations as in [63], this simplifying assumption removes the need for such calculations. Based on quadratic and linear fits of the 2PA and 1PA Brillouin amplitudes, Figure 28(c) and Figure 30(c), respectively, we obtained the following equation set:

$$\begin{aligned} A_B^{2PA} &= a\mathcal{F}_{2PA}^2, \\ A_B^{1PA} &= b\mathcal{F}_{1PA}. \end{aligned} \tag{85}$$

The fitted parameters are $a = 7.9 \cdot 10^{-9}$ mJ$^{-2} \cdot$cm^4 and $b = 7.4 \cdot 10^{-5}$ mJ$^{-1} \cdot$cm^2. Equating the Brillouin amplitude, $A_B^{1PA} = A_B^{2PA}$, implies equal strain amplitude, $\eta_{33}^{1PA} = \eta_{33}^{2PA}$, allowing the ratio a/b to be related to the absorption coefficients through:

$$\frac{a}{b} = \sqrt{\frac{\ln 4}{\pi}} \left(\frac{\alpha^{(2)}}{\tau} \right) \frac{d}{(1 - e^{-\alpha^{(1)} d})}, \tag{86}$$

The last two unknown parameters in Equation (86) are the one-photon absorption coefficient $\alpha^{(1)}$ and the film thickness d. To determine $\alpha^{(1)}$, we performed ellipsometry measurements. These measurements were carried out on a second sample consisting of the same organoruthenium compound spin-coated onto a silicon wafer. The use of a silicon substrate eliminates backside reflections that can interfere with the accuracy of ellipsometric data. To fit the experimental data shown in Figure 31(a), we used a two-oscillator dispersion model, defined by Equation (87). In this expression, ε is the dielectric permittivity, ε_∞ is the high-frequency permittivity, f_j is the strength of the jth oscillator, ω_j is its resonance frequency, and γ_j is its damping factor. The ω parameter denotes the optical pulsation. The fitted parameter values are given in Table [3].

$$\varepsilon(\omega) = \varepsilon_\infty + \sum_{j=1}^{2} \frac{f_j \cdot \omega_j^2}{\omega_j^2 - \omega^2 + i\gamma_j \omega} \tag{87}$$

Parameter	ε_∞	f_1	ω_1 (eV)	γ_1 (eV)	f_2	ω_2 (eV)	γ_2 (eV)
Value	0.8868633	0.0213638	2.9450393	0.3978620	0.6964802	5.7832460	1.8927698

Table 3: Fitted parameters of the two-oscillator dispersion model for the investigated organoruthenium thin film on silicon.

As shown in Figure 31(b), the two-oscillator dispersion model provides an excellent fit to the experimental data, confirming the reliability of the extracted optical parameters. The complex refractive index is obtained from the dielectric function via $\bar{n} = n + i\kappa = \sqrt{\epsilon(\omega)}$. For our purposes, the linear absorption coefficient is determined as $\alpha^{(1)} = 4\pi\kappa/\lambda = 3.72 \cdot 10^4$ cm^{-1}.

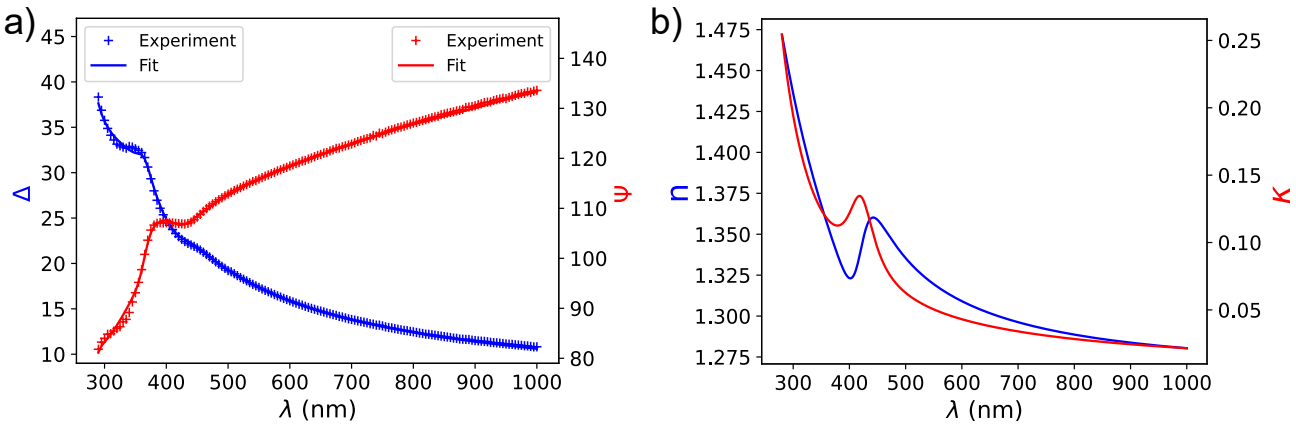

Figure 31: Ellipsometric determination of the complex refractive index of the investigated organoruthenium compound. a) Experimental measurements of the ellipsometric parameters Δ and Ψ with corresponding fits. b) Real and imaginary parts, n and κ, of the refractive index.

The final required parameter is the film thickness d, which was measured using atomic force microscopy (AFM), which was used as well to control the sample smoothness, as shown in Figure 32. The measured thickness is $d = 100 \pm 5$ nm.

Returning to Equation (86), we determine the 2PA coefficient to be $\alpha^{(2)} = 1.7$ cm/GM. The relationship between $\alpha^{(2)}$ 2PA cross section σ_2 is given in Equation (88) [64], where N_0 is the molecular density and E the photon energy. X-ray structural analysis of the organoruthenium complex reported in [59] provides a molecular density of $N_0 = 5.04 \cdot 10^{20}$ cm^{-3}.

$$\alpha^{(2)} = \sigma_2 \cdot \frac{N_0}{E} \tag{88}$$

After calculation, we obtain $\sigma_2 = 81$ GM. Interestingly, this value is approximately thirteen times lower than that obtained using the conventional z-scan technique [59]. While both femtosecond-based methods are subject to experimental uncertainty, the observed discrepancy remains well within an order of magnitude and within acceptable error margins. This divergence highlights the specificity of the TDBS approach, which is uniquely sensitive to thermoelastic responses occurring on the picosecond timescale. As such, the coefficient derived from Brillouin measurements reflects only a portion of

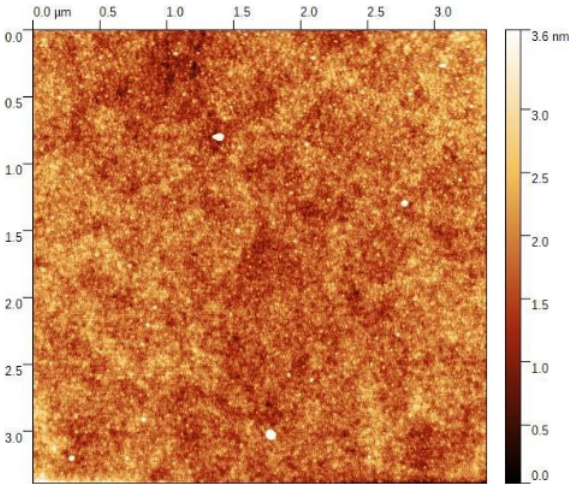

Figure 32: AFM topography of the organoruthenium thin film spin-coated on a glass substrate. The sample roughness is in the range of 5 nm.

the total 2PA coefficient obtained with z-scan. Based on this interpretation, we tentatively propose that only about one-tenth of the absorbed energy that promotes the organoruthenium complex to its S_1 state is converted into heat and acoustic energy on the picosecond timescale accessible by TDBS. This distinction between z-scan and Brillouin methodologies underscores the ability of TDBS to selectively probe the fastest relaxation dynamics involved in photothermal and photoacoustic processes. Extending this method to a wider variety of materials will offer deeper insights into the nonlinear optical behavior of candidate contrast agents, thereby supporting the development of next-generation tools for biomedical imaging.

4.3 Two-photon absorption for direct LAWs generation in $SrTiO_3$

After demonstrating the capability of our setup, with spatially displaced pump and probe beams, to generate LAWs via two-photon absorption in complex organic materials and to detect the resulting acoustic response in a separate substrate, we now aim to explore the simultaneous generation and detection of LAWs within the same material. For this purpose, we selected $SrTiO_3$ (100), owing to its optical bandgap of 3.03 eV at the (100) surface [65], which is slightly lower than the energy of the two photons at 776 nm ($2 \times 1.6 = 3.2$ eV). In addition, the bulk bandgap of STO is 3.27 eV, which exceeds the energy of the two-photon excitation and thus prevents significant absorption and acoustic generation in the bulk. This makes the (100) surface particularly well suited for surface-confined two-photon excitation of LAW. The excitation and relaxation mechanisms are illustrated in Figure 33, adapted from [66], where the generation of coherent acoustic phonons was achieved via single-photon absorption. In our case, however, the energy of a single 1.6 eV photon is not sufficient to overcome the bandgap of STO and thus cannot promote an electron from the valence band (VB) to the conduction band (CB). Consequently, two-photon absorption is required to enable this transition. Once excited into higher energy CB states, the electrons undergo intraband relaxation, cascading down to the bottom of the CB. This rapid relaxation process leads to a localized thermoelastic response, thereby generating a coherent LAW. The final step involves electron-hole recombination, in which excited electrons return from CB to VB, completing the relaxation cycle.

Investigations were carried out using the setup presented in Figure 25, with a 1.6 eV pump (780 nm) and a 3.2 eV probe (390 nm). Measurements were performed for two different pump polarizations, S and P, to evaluate the polarization dependence of the two-photon induced LAW generation in STO. The results are presented in Figure 34.

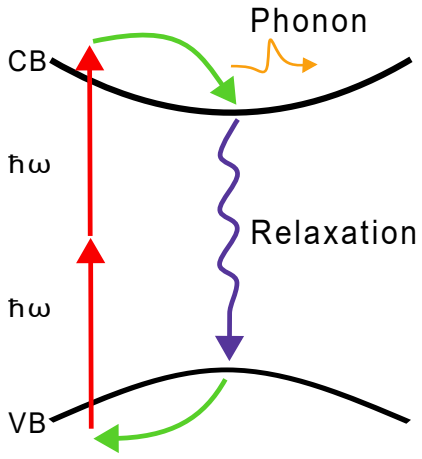

Figure 33: Generation of coherent acoustic phonons from nonlinear two-photon absorption and intraband electronic relaxations. VB: valence band, CB: conduction band.

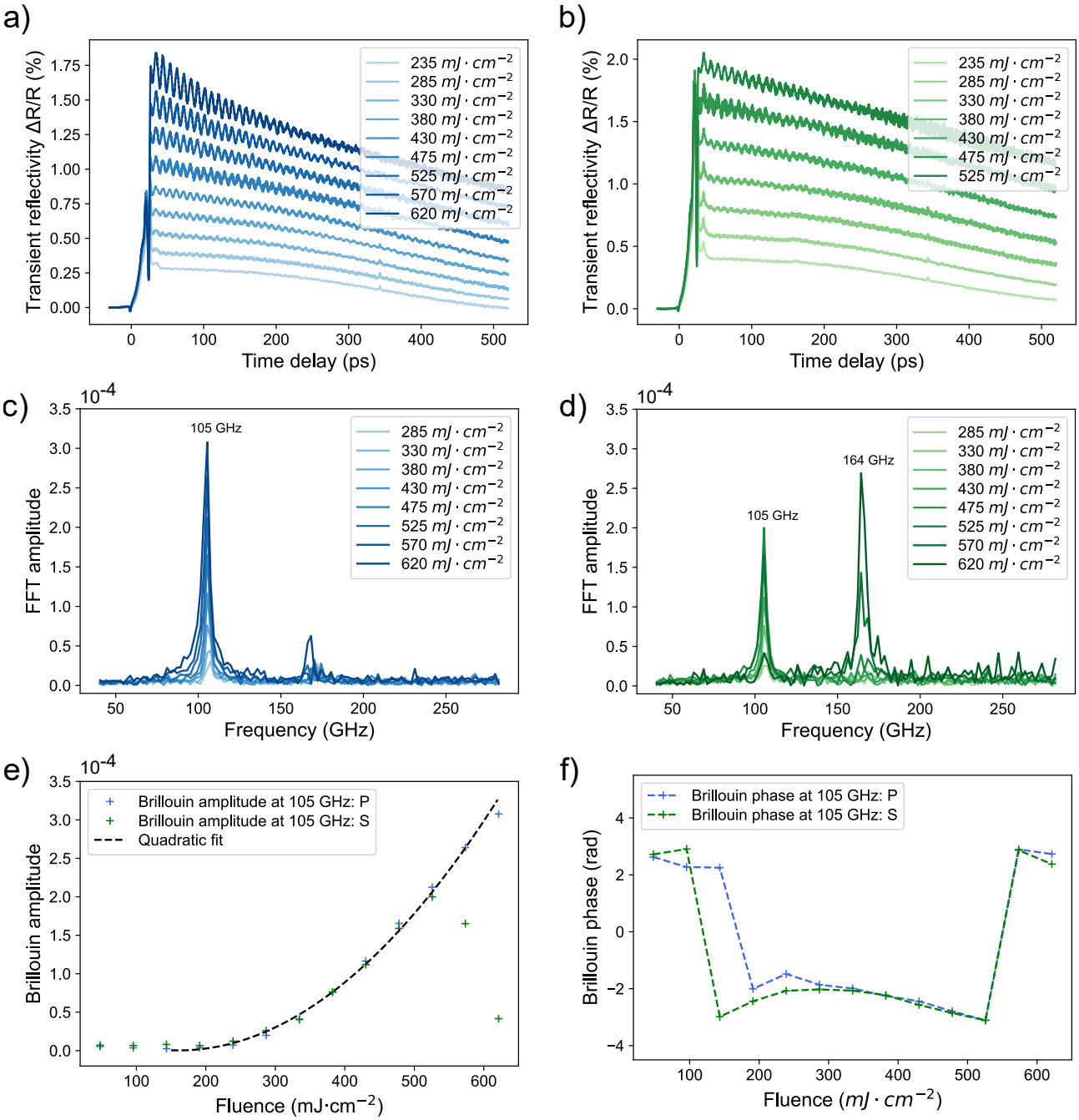

Figure 34: TDBS data at various pump fluences at a pump wavelength of 776 nm for two linear cross polarizations. a) Time-domain transient reflectivity data with P-polarized pump. b) Time-domain transient reflectivity data with S-polarized pump. c) FFT of the transient reflectivity data after slow background removal for P-polarized pump. d) FFT of the transient reflectivity data after slow background removal for S-polarized pump. e) FFT amplitude of the Brillouin peak at 105 GHz versus pump fluence for both P and S polarizations. f) FFT phase of the Brillouin peak at 105 GHz versus pump fluence for both P and S polarizations.

The TDBS signals corresponding to two pump polarizations, recorded at various pump fluences, are shown in Figures 34(a) (P-polarization) and 34(b) (S-polarization). For both data sets, we computed the FFTs of the time derivative of the signals, as done in previous analyses. The resulting FFT spectra are presented in Figures 34(c) and 34(d) for P and S polarizations, respectively. In both

cases, a Brillouin frequency of 105 GHz is unambiguously identified, matching the LAW frequency in STO as previously measured using a chromium transducer. At higher fluences, particularly under S-polarization excitation, an additional frequency component emerges at 164 GHz. This signal appears as the sample begins to exhibit signs of optical damage. Following local degradation of the material, both 105 GHz and 164 GHz peaks disappear. We therefore interpret the emergence of frequency components different from the Brillouin frequency as a precursor or marker of sample damage. From the FFTs, we extracted the Brillouin amplitude as the FFTs amplitudes at 105 GHz and plotted its evolution with the pump fluence for both polarizations in Figure 34(e). The result reveals a clear quadratic dependence of the Brillouin amplitude on pump fluence, consistent with a two-photon absorption process. Both polarizations yield comparable responses up to optical damage. Here, the experimental fit is driven by $A_B(\mathcal{F}) = 1.55 \cdot 10^{-9}\ \mathcal{F}_{2PA}^2$. To determine the two-photon absorption coefficient $\alpha^{(2)}$ of STO, we attempted to apply the same method used for the organoruthenium compound. However, despite several attempts, we were unable to obtain exploitable results using a 3.2 eV pump. Nevertheless, isolating $\alpha^{(2)}$ from Equation (82) leads to:

$$\alpha^{(2)} = \frac{a \cdot \rho\, C_p\, \tau}{K\, \gamma} \sqrt{\frac{\pi}{ln4}} \tag{89}$$

where $a = 6.45 \cdot 10^{-9}$, $\rho = 5.11\ \mathrm{g \cdot cm^{-3}}$, $C_p = 0.46\ \mathrm{J \cdot g^{-1} \cdot K^{-1}}$, $\tau = 250$ fs, $\gamma = 9.4 \cdot 10^{-6}\ \mathrm{K^{-1}}$, and K is an undetermined geometric and detection-related constant.

Finally, Figure 34(f) shows the evolution of the Brillouin phase at 105 GHz as a function of pump fluence for both S and P polarizations. A clear phase inversion is observed at the threshold fluence where the Brillouin signal first appears. This behavior likely indicates a change in the STO, corresponding to the onset of efficient two-photon absorption (STO is no longer transparent) that enables electron excitation from the valence band to the conduction band. A second abrupt phase inversion occurs at higher fluence, coinciding with the emergence of a secondary frequency peak and optical damaging of STO. The relative stability of the Brillouin phase in the two-photon absorption regime confirms the consistency of the LAW generation mechanism within this fluence window. Moreover, the similar trends observed for both pump polarizations further support the weak optical anisotropy of STO, which is consistent with its cubic structure.

4.4 Multi-photon absorption for direct LAWs generation in $LiNbO_3$ and $LaAlO_3$

The direct generation of LAWs from multi-photon absorption has also been investigated in a lithium niobate prism (LNB prism) and in a $LaAlO_3$ (LAO) substrate. We present here the results of these two experiments. However, no definitive conclusion can be drawn regarding these two materials.

The direct optical generation of LAWs was attempted in an LNB prism designed for terahertz generation and lightly doped with magnesium to improve its resilience to optical damage. The experiments were conducted using the spinning-mirror setup. In this case, the 10× microscope objective used to focus on the sample was replaced by a 20× objective, thereby increasing the optical fluence on the sample. The pump energy was 1.62 eV and the probe energy was 3.2 eV. The experimental configuration is presented in Figure 35. The beams propagate in the zy-plane, which corresponds to the basal plane of LNB. Although the spinning configuration induces a small z-component in the incidence, it can be reasonably neglected due to the extremely small top angle of the conical beams propagation.

The acquired signals at various fluences, presented in Figure 36(a), exhibit the typical behavior of TDBS signals: an electronic peak at time zero, oscillations in the relaxation phase, and a thermal baseline. FFTs performed on the signal derivatives are shown in Figure 36(b). A dominant frequency of 81.9 GHz is identified.

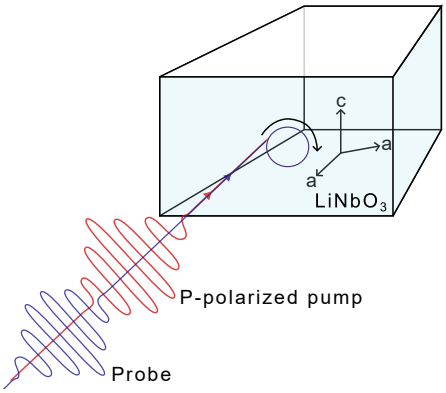

Figure 35: Schematic view of the spinning pump-probe experiment on a $LiNbO_3$ prism.

The refractive indices were calculated from the dispersion formula reported in [67], yielding $n_{388} = 2.4594$ and $n_{776} = 2.2585$. Using Equation (61), we determine a LAW velocity $v_s = 6460\ \mathrm{m \cdot s^{-1}}$. For comparison with literature, we use the compliance tensor and the density ($\rho = 4636\ \mathrm{kg \cdot m^{-3}}$) of LNB reported in [68].

$$C = \begin{bmatrix} C_{11} & C_{12} & C_{13} & C_{14} & 0 & 0 \\ C_{12} & C_{11} & C_{13} & -C_{14} & 0 & 0 \\ C_{13} & C_{13} & C_{33} & 0 & 0 & 0 \\ C_{14} & -C_{14} & 0 & C_{44} & 0 & 0 \\ 0 & 0 & 0 & 0 & C_{44} & C_{14} \\ 0 & 0 & 0 & 0 & C_{14} & C_{66} \end{bmatrix}$$

The rhombohedral structure of LNB is commonly described as a hexagonal setting, from which two longitudinal velocities are extracted: one for the basal plane (a-axis) and one along the polar symmetry axis (c-axis). Only $C_{11} = 199.50$ GPa and $C_{33} = 235.22$ GPa are required to estimate these velocities.

$$v_l^{(a)} = \sqrt{\frac{C_{11}}{\rho}} \simeq 6560\ \mathrm{m \cdot s^{-1}}, \qquad v_l^{(c)} = \sqrt{\frac{C_{33}}{\rho}} \simeq 7123\ \mathrm{m \cdot s^{-1}}$$

The $\sim$1.5% deviation between our measurement and the calculated $v_l^{(a)}$ confirms that we have effectively generated LAWs in LNB. To identify the generation process, the Brillouin amplitude was plotted as a function of pump fluence in Figure 36(c). The data reveal a dependence that can be reasonably fitted by a quadratic function. A decrease in intensity is observed beyond $350\ \mathrm{mJ \cdot cm^{-2}}$, consistent with the FFT results in Figure 36(b). Above this fluence, signals were still acquired, but no dominant frequency could be identified in their Fourier spectra. These high-fluence acquisitions were omitted from the plots for readability. Beyond $350\ \mathrm{mJ \cdot cm^{-2}}$, surface damage of the LNB prism is observed. Changes in the Brillouin phase around $350\ \mathrm{mJ \cdot cm^{-2}}$ further support the onset of sample modification. The quadratic dependence of the Brillouin amplitude on the pump could suggest a two-photon abortion process. However, the optical bandgap of the LNB is around 3.8 eV at room temperature [69], which exceeds the accessible two-photon energy from our laser source. In non-centrosymmetric crystals such as LNB, the quadratic scaling of the signal may also be explained by optical rectification. The second-order susceptibility $\chi^{(2)}$ produces a quasi-static polarization $P^{(2)}(t) \propto \chi^{(2)} E^2(t)$ under intense femtosecond illumination. This rectified polarization induces an effective piezoelectric stress through the coupling tensor e_{ijk}, thereby launching coherent acoustic phonons. For longitudinal acoustic waves, a rectified polarization aligned with the c-axis couples efficiently to longitudinal strain via e_{33}. When the pump is polarized within the basal plane, weaker but non-zero contributions

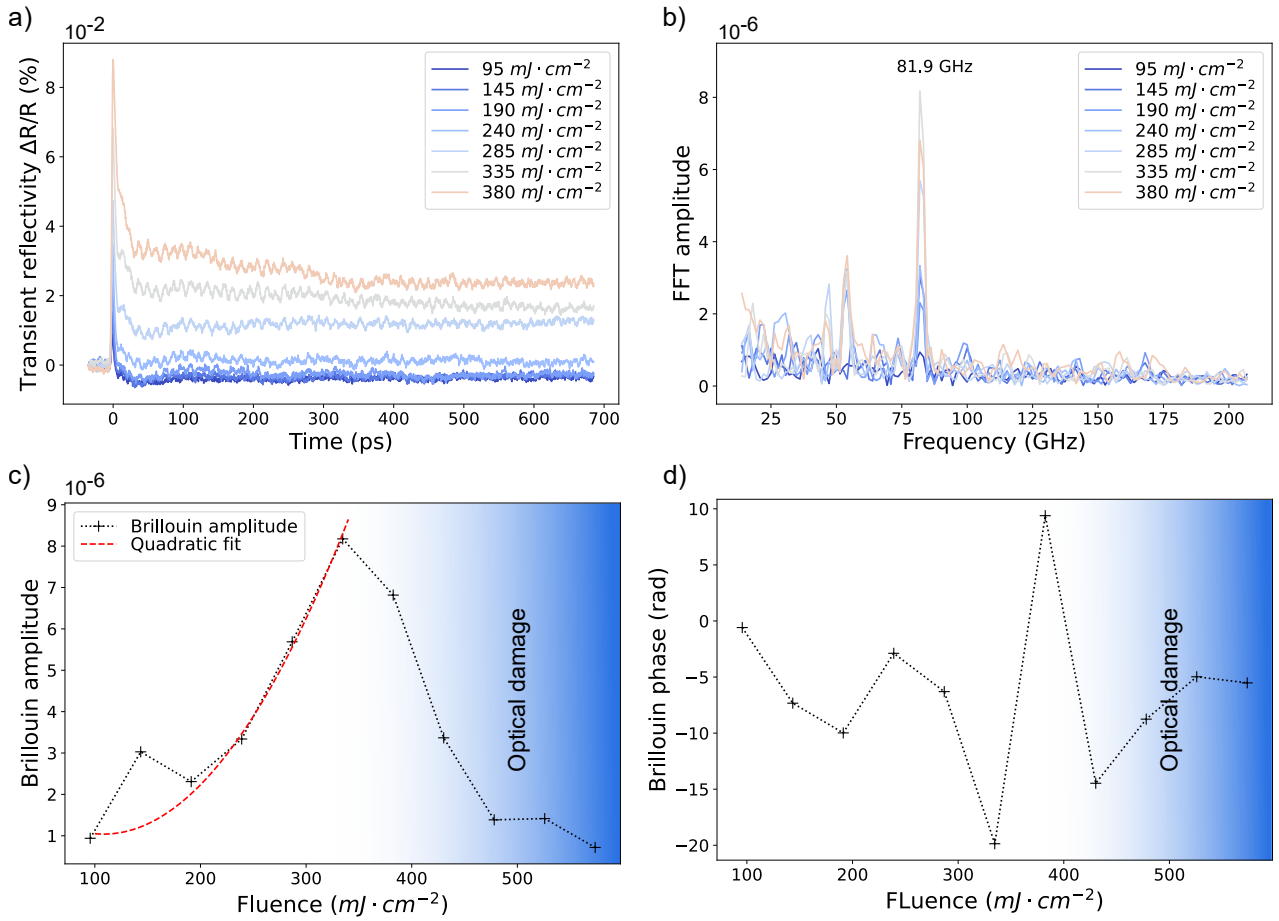

Figure 36: TDBS data at various pump fluences at a pump wavelength of 776 nm. a) Time-domain transient reflectivity data. b) FFTs of the transient reflectivity data after slow background removal. c) FFT amplitude of the Brillouin peak at 81.9 GHz versus pump fluence. d) FFT phase of the Brillouin peak at 81.9 GHz versus pump fluence.

mediated by e_{22} and e_{31} may also generate in-plane LAWs. The experimentally observed quadratic dependence is therefore consistent with an optical rectification process.

The present data do not allow us to unambiguously distinguish between multiphoton absorption and optical rectification. However, if a strong sensitivity of coherent phonon generation to pump polarization, as previously reported in [70], could be confirmed in complementary investigations, this would suggest that the mechanism is not purely thermal, supporting the hypothesis of optical rectification. In our case, multiphoton-induced thermal generation can be excluded at the pump photon energy. In addition, investigations on a z-cut LNB plate (c-axis) did not reveal any signal, which is consistent with LAWs originating from optical rectification. These measurements along the c-axis were carried out on a second sample, since the c-axis face of our prism was unpolished and did not allow such experiments.

A similar experiment to directly generate through multi-photon absorption LAWs was carried out in LAO (100). The experimental conditions were identical to those used for LNB, and three complete pump-fluence cycles (rise and fall) were performed to test the reproducibility of the response. The acquired signals for the first cycle are shown in Figure 37(a). For each fluence, two closely spaced signals are observed, which demonstrates the high resistance of LAO to the maximum pump fluence accessible with our setup. This stability is further confirmed by the reproducibility of the second

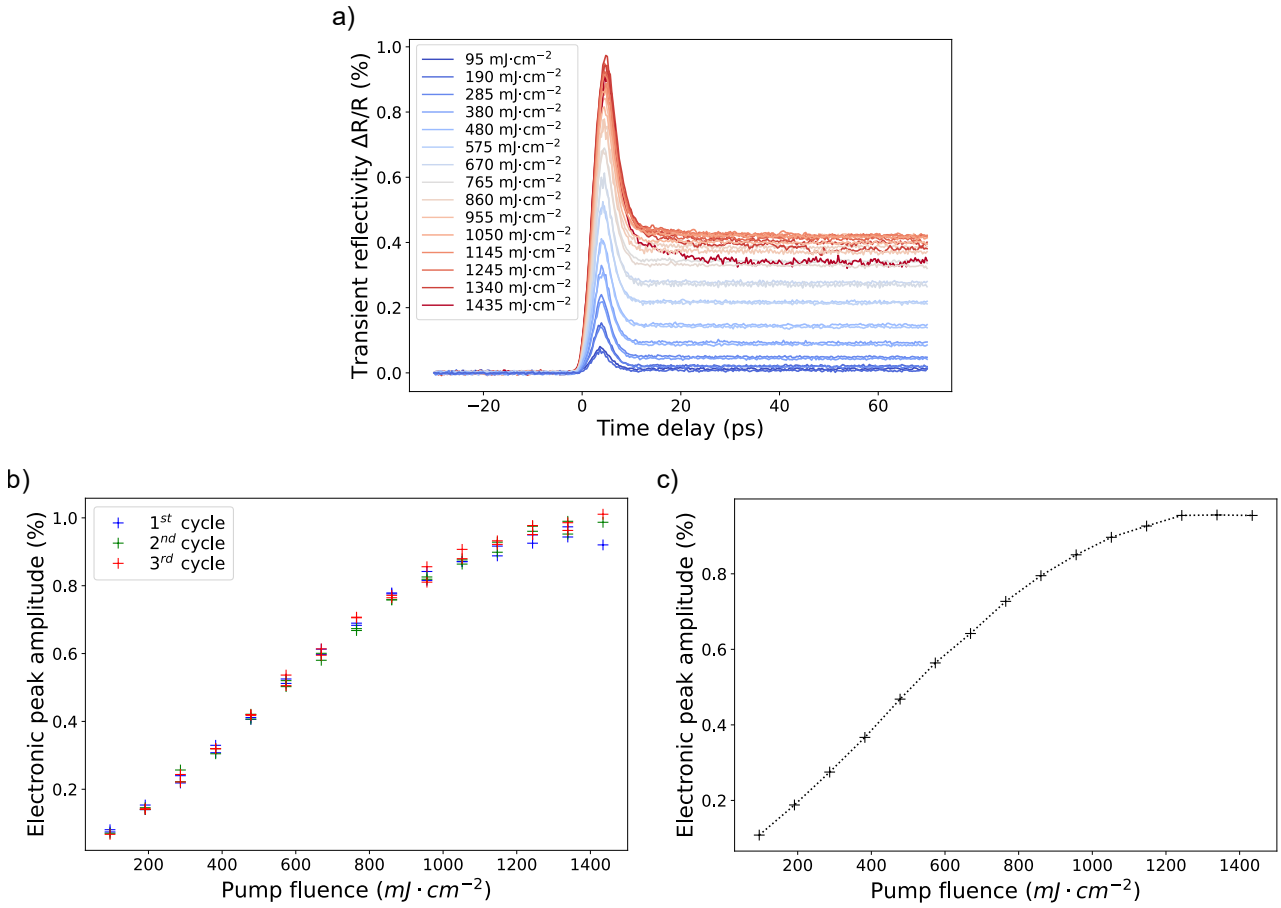

Figure 37: TDBS data at various pump fluences at a pump wavelength of 776 nm. a) Time-domain transient reflectivity data for the first fluence cycle. b) Electronic peak amplitude for the three fluence cycles. c) Mean electronic peak amplitude over the three cycles.

and third cycles. Figure 37(b) shows the amplitude of the electronic peak as a function of pump fluence for the three cycles, while Figure 37(c) presents the mean electronic peak amplitude at each fluence, averaged over six measurements (two signals per fluence across three cycles). In this last plot, a linear increase of the electronic peak with fluence is observed, followed by a saturation plateau at high fluences. Such a response points to a finite density of available states involved in the excitation process. Considering that the optical bandgap of LAO is ∼5.6 eV [71, 72], neither single- nor two-photon interband excitation can occur at the employed pump photon energy (1.62 eV), which explains the absence of Brillouin oscillations in the recorded signals. Nevertheless, the femtosecond pump induces a measurable change in reflectivity. Due to the centrosymmetric nature of LAO, second-order nonlinearities ($\chi^{(2)}$) are forbidden, but third-order contributions ($\chi^{(3)}$) are allowed. In this regime, the reflectivity variation can be attributed to a Kerr-type electronic effect, where $\Delta R \propto \chi^{(3)} I$. The absence of Brillouin oscillations and the observed linear dependence rule out a dominant contribution from three-photon absorption. Instead, the observed behavior is most plausibly explained by the population of intraband defect states. Such defect levels within the gap can act as intermediate states, leading to sub-bandgap absorption and subsequent changes in reflectivity. Their presence can be consistent with oxygen vacancies, substitutional impurities, or dislocations.

These results suggest that our femtosecond pump–probe setup can serve as a sensitive probe of defect-related electronic states in wide-bandgap insulators such as LAO, even in the absence of coherent acoustic generation.

These two sets of investigations in LNB and LAO do not allow us to draw a definitive conclusion regarding the underlying processes. However, further studies could help clarify the role of optical rectification in LAW generation and provide a means to quantify defect-related electronic excitation in wide-bandgap insulators.

4.5 Summary of multiphoton LAWs generation

The primary motivation for exploring generation of LAWs through multiphoton absorption was to investigate materials without necessitating deposition of a metallic transducer, which can be detrimental for some specific samples. In this section, we have demonstrated the capability of our TDBS setup to probe complex organometallic compounds by exploiting their role as two-photon absorbing transducers. This strategy enables a quantitative assessment of the effective nonlinear optical response of complex organic compounds through the acoustic waves they induce—via thermal processes—in a secondary, well-characterized material.

We further extended the two-photon LAW generation studies to crystalline solids such as STO, thereby demonstrating the ability of our setup to both generate and detect LAWs within the same material. This capability paves the way for non-contact, non-destructive elastic characterization of materials that are otherwise difficult to study using standard pump–probe techniques.

A notable limitation of this approach lies in the requirement for relatively high optical fluences, which arises from the inherently low probability of multiphoton absorption. This constraint must be carefully considered when applying the technique, particularly for sensitive materials such as organic compounds.

Finally, although the results obtained in LNB and LAO are not yet conclusive, they nonetheless highlight promising directions for future studies, suggesting the potential of optical rectification in LAW generation and defect-related electronic excitation in wide-bandgap insulators.

5 Conclusion

In this first chapter, we have demonstrated the efficiency of our fully optical TDBS setup and obtained several significant results. Firstly, in the linear transparency regime using metallic transducers, a wide variety of solid-state materials were characterized, and the results compared favorably with literature values. In addition, the determination of a wide dataset of available Brillouin frequencies paves the way for resonant excitation, as mentioned in the general introduction.

From this dataset, and thanks to the experimental experience developed, the collaborators of the supporting ANR project from the Bordeaux Optics Institute managed to achieve resonant TDBS with 5-pulse bursts, and up to 20-pulse bursts, using their homemade laser with a tunable repetition rate.

Beyond the linear regime, we have also demonstrated nonlinear LAW generation through multiphoton absorption by designing an original investigation method reducing cumulative heating using a spinning mirror. This advantageous modification of the experimental setup enabled us to design a method for quantifying the effective two-photon activation and the subsequent thermal release in complex organometallic compounds. With this demonstration complete, this method can now be systematically applied to a range of organometallic complexes in order to identify the most promising candidates for medical applications.

The spinning mirror configuration has also provided interesting results in transparent solid-state materials without metallic transducers. In particular, in STO, which is transparent at the single-photon energy but absorptive at two, we demonstrated two-photon absorption generation of LAWs.

This approach facilitates the use of TDBS, as it enables the direct investigation of materials provided that their optical bandgap lies below the two-photon pump energy.

Finally, the same method used for the organoruthenium complex and STO was applied to two solids with a bandgap exceeding the two-photon pump energy. The first was a $LiNbO_3$ prism, a non-centrosymmetric material widely used for terahertz generation via optical rectification. The study presented here suggests that the detected longitudinal acoustic waves may originate from optical rectification, although a definitive conclusion cannot yet be drawn. The second investigated high-bandgap material was $LaAlO_3$, a centrosymmetric material. In this case, no acoustic waves were detected, but a clear dependence of the electronic excitation on pump power was observed, suggesting the electronic population of defect states.

These time-resolved photoacoustic studies, in addition to demonstrating the reliability of our measurements, reveal the versatility of our experimental setup and open the way to future studies and improvements. Regarding the scientific investigations, extending the study of acoustic generation via optical rectification would be of great interest, as would performing a systematic exploration of other organic materials for potential medical applications. Concerning the experimental setup itself, broadening the accessible wavelength range would enhance the scope of nonlinear investigations. In addition, reducing the acquisition time through delay spectral-encoding [73–76] could prove extremely advantageous.

Part II

Ultrafast opto-acousto-magnetism in correlated materials

1 Context

In the first part of this work, we focused on the optical investigation of elastic properties of materials. To broaden the scope of contactless, ultrafast light-based material characterization, we now turn to the study of the interplay of LAW and electronic or magnetic degrees of freedom in the sample. This extension is motivated by the rich variety of interactions between electrons, phonons, and spins that manifest across a wide range of temporal and spatial scales in correlated materials. These phenomena not only provide fundamental insights into condensed matter physics but also underpin numerous technological applications. One prominent example is magnetic data storage, where the control of magnetization dynamics is crucial for writing and retaining information. In particular, ultrafast optical control of magnetic states for data storage has seen significant advances in recent years [77].

Another motivation for exploring magnetic dynamics is the strong technical compatibility between the time-resolved optical setup used for TDBS and that required for time-resolved magnetic dynamics. In practice, investigating magnetization dynamics optically requires only minor adaptations in the detection part of the TDBS experimental setup. A common feature is the femtosecond nature of the laser source. Our setup is inherently limited to resolving ultrafast phenomena with timescales longer than the duration of the femtosecond pulses of about 200 femtoseconds, thus excluding faster processes such as direct spin exchange or sub-picosecond electronic relaxation.

In the second part of this document, time-resolved MOKE measurements are employed to probe magnetization dynamics induced by femtosecond optical excitation. These dynamics may arise from various electronic and lattice perturbations, including the modulation of Cooper pairs in superconductors, spin excitations, acoustic wave propagation, or transient thermal effects. The systems investigated encompass ferromagnetic thin films and superconductors, as well as more complex epitaxial ferromagnetic heterostructures.

We begin with a theoretical overview of the key concepts and phenomena all related to magnetism, necessary to provide a solid foundation for understanding the optical setup and for interpreting the experimental results.

2 Theory: Magnetism, magneto-optics, magneto-acoustics

As outlined earlier, we start by introducing the theoretical concepts most relevant to our magneto-acousto-optic investigations. We start with the quantum origin of magnetism and review the various magnetic phases that arise from electron spin interactions and exchange mechanisms. Then, we introduce the magneto-optic Faraday and Kerr effects, which enable optical probing of magnetization. Once these phenomena are introduced, we introduce the basics of magneto-acoustic coupling and describe how femtosecond laser pulses interact with magnetic materials, perturbing their magnetic order on ultrafast timescales. The theoretical description of the magnetism origin and the resulting magnetic phases are based on the following sources [78–81].

2.1 Origin of magnetism and magnetic phases

Magnetism in solids is fundamentally a quantum-mechanical phenomenon. It originates from the intrinsic magnetic moments of electrons, associated with their spin and orbital angular momentum, and from their exchange interactions. Contributions from nuclear magnetic moments are typically negligible due to the much larger nuclear mass, and ionic displacement currents are rare in solids. In superconductors, Cooper-pair currents can also contribute to magnetic phenomena, but we postpone the discussion to a dedicated section.

Based on these considerations, the magnetic moment $\boldsymbol{\mu}$ associated with an angular momentum $\mathbf{J}$ is generally given by:

$$\boldsymbol{\mu} = \gamma \mathbf{J}, \tag{90}$$

where γ is the gyromagnetic ratio. For a free electron, the gyromagnetic ratio is

$$\gamma = \frac{-e}{2m_e}, \tag{91}$$

with e the elementary charge and m_e the electron mass. The gyromagnetic ratio allows us to define the Bohr magneton μ_B, which is the fundamental unit of magnetic moment, as:

$$\mu_B = \frac{e\hbar}{2m_e} = \hbar\,|\gamma|. \tag{92}$$

The spin and orbital contributions to the total magnetic moment are then

$$\boldsymbol{\mu}_s = -g_s \mu_B \frac{\mathbf{S}}{\hbar}, \tag{93}$$

$$\boldsymbol{\mu}_L = -\mu_B \frac{\mathbf{L}}{\hbar}, \tag{94}$$

where $g_s \simeq 2.0023$ is the Landé factor for the spin, $\mathbf{S}$ is the total spin angular momentum, and $\mathbf{L}$ is the total orbital angular momentum. The total angular momentum is $\mathbf{J} = \mathbf{L} + \mathbf{S}$. The projection of the magnetic moment along $\mathbf{J}$ can be derived using standard identities

$$\mathbf{J}\cdot\mathbf{L} = \frac{\hbar^2}{2}\big[J(J+1) + L(L+1) - S(S+1)\big], \tag{95}$$

$$\mathbf{J}\cdot\mathbf{S} = \frac{\hbar^2}{2}\big[J(J+1) + S(S+1) - L(L+1)\big]. \tag{96}$$

Under $g_s = 2$, one obtains an effective moment

$$\mu_J = -g_J\,\mu_B\,J, \tag{97}$$

where

$$g_J = 1 + \frac{J(J+1) + S(S+1) - L(L+1)}{2J(J+1)} \tag{98}$$

For an atom with N electrons, the total spin and orbital angular momenta are defined by:

$$\mathbf{S} = \sum_{i=1}^{N} \mathbf{s_i}\,, \tag{99}$$

$$\mathbf{L} = \sum_{i=1}^{N} \mathbf{l_i}\,. \tag{100}$$

On the macroscopic scale, the magnetization M is defined as the magnetic moment per unit volume:

$$M = \frac{1}{V}\sum_i \mu_i \simeq n\langle\mu\rangle, \tag{101}$$

where V is the considered volume, μ_i is the magnetic moment of the ith atom, $\langle\mu\rangle$ is the average magnetic moment per atom, and n is the density of magnetic moments. The equilibrium value of $\langle\mu\rangle$ is determined by the interplay between thermal fluctuations, external magnetic fields, and exchange interactions between neighboring spins. For atoms with an effective magnetic moment μ_J, the thermal average magnetic moment is given by:

$$\langle\mu\rangle = \mu_J \mathcal{B}_J(x), \tag{102}$$

where $\mathcal{B}_J$ is the Brillouin function defined by:

$$\mathcal{B}_J(x) = \frac{2J+1}{2J}\coth\left(\frac{2J+1}{2J}x\right) - \frac{1}{2J}\coth\left(\frac{1}{2J}x\right). \tag{103}$$

The x-argument of the Brillouin function is given by the following expression:

$$x = \frac{g_J \mu_B J B}{k_B T}, \tag{104}$$

where g_J is the Landé factor, μ_B the Bohr magneton, k_B the Boltzmann constant, T the temperature, and B the effective magnetic induction acting on the atomic moments.

Depending on the nature of the magnetic induction B and on the presence or absence of exchange-driven internal fields, different magnetic phases emerge.

- Paramagnetic phase:

  In the paramagnetic phase, there is no spontaneous magnetization ($M = 0$ when $H = 0$), and the magnetic moments align only in the presence of an external magnetic field. In this case, the magnetic induction simplifies to $B = \mu_0 H$. For small external fields, the magnetization can be approximated by:

  $$M \simeq n\,\mu_J \frac{J+1}{3J}\frac{g_J\,\mu_B\,J\,\mu_0\,H}{k_B\,T}. \tag{105}$$

  This expression is obtained by expanding the Brillouin function in the limit $x \to 0$, which corresponds to weak external field conditions. The Taylor expansion of the two hyperbolic cotangent terms leads to the simplified form of the Brillouin function:

  $$\lim_{x\to 0}\mathcal{B}(x) = \frac{J+1}{3J}x. \tag{106}$$

  Equation (105) can be rewritten using the temperature-dependent magnetic susceptibility $\chi(T)$, giving the Curie law for an ideal paramagnet.

  $$M = \chi(T)H \tag{107}$$

  $$\chi(T) = \frac{C}{T} = \frac{n\,\mu_J(J+1)g_J\,\mu_B\,\mu_0}{3k_B\,T} \tag{108}$$

  For stronger external fields, the full Brillouin function must be used to evaluate the magnetization. If the resulting magnetization is opposite to the external field, the material is said to be diamagnetic.

- Ferromagnetic phase:

  In the ferromagnetic phase, there is spontaneous magnetization even in the absence of an external field ($M \neq 0$ when $H = 0$). This arises from exchange interaction (Hund-type coupling) that favors parallel alignment of neighboring magnetic moments. The self-consistent expression for M is given by:

$$M = n\,\mu_J\,\mathcal{B}_J\left(\frac{g_J\,\mu_B\,J\,\mu_0(H+\lambda M)}{k_B\,T}\right). \tag{109}$$

  where $B = \mu_0(H + \lambda M)$, with λ the molecular-field constant accounting for the exchange interaction between neighboring spins. Linearizing this expression in the high-temperature regime ($T > T_C$), one recovers the Curie-Weiss law,

$$M = \chi(T)H \quad \text{with} \quad \chi = \frac{C}{T - T_C}. \tag{110}$$

  Here, C is the Curie constant and T_C is the Curie temperature, which characterizes the strength of internal magnetic interactions.

- Antiferromagnetic phase:

  In antiferromagnetic materials, neighboring magnetic moments couple antiparallel to one another, resulting in a net magnetization $M = 0$ despite the presence of long-range magnetic order. To describe this, two interpenetrating magnetic sublattices, A and B, are defined. Each sublattice behaves similarly to a ferromagnet, but the total magnetization cancels out if the two sublattices are identical.

$$\begin{cases} M_A = n\,\mu_J\,\mathcal{B}_J\left(\dfrac{g_J\,\mu_B\,J(B+\lambda M_B)}{k_B\,T}\right) \\ M_B = n\,\mu_J\,\mathcal{B}_J\left(\dfrac{g_J\,\mu_B\,J(B+\lambda M_A)}{k_B\,T}\right) \end{cases} \tag{111}$$

  We note that above the Néel temperature T_N, antiferromagnets become paramagnetic.

- Ferrimagnetic phase:

  Ferrimagnetism shares the antiparallel characteristic of antiferromagnets, but the magnetic moments of the two sublattices differ in magnitude, leading to a nonzero net magnetization even in a zero external field. In this phase there is spontaneous magnetization.

During the discussion of magnetic phases, two key characteristic temperatures were introduced: the Curie temperature T_C for ferromagnetic materials, above which they lose their spontaneous magnetization and transition into a paramagnetic state, and the Néel temperature T_N for antiferromagnetic materials, beyond which the antiparallel magnetic ordering vanishes and the material also becomes paramagnetic. Representative values of T_C and T_N for a selection of materials are summarized in Table [4]. In addition to these conventional magnetic phases, several exotic magnetic states also exist. These include spin glasses [82, 83], which exhibit disordered and frustrated spin configurations. An example of such spin glass is the gadolinium gallium garnet, studied in the first part of this document, which displays frustrated magnetism that can undergo spin freezing below $\sim$ 125 mK [84]. Other exotic states include skyrmions [85], which are topologically protected spin textures; ferrofluids [86], consisting of suspended magnetic nanoparticles in a carrier liquid; and superparamagnetism [87], a phenomenon where small ferromagnetic particles exhibit paramagnetic-like behavior due to thermal fluctuations. While these exotic magnetic states are of considerable interest in modern condensed matter physics, they lie outside the scope of our experiments. In this work, we focus exclusively on the primary magnetic phases described previously.

Ferromagnet	T_C (K)	Antiferromagnet	T_N (K)
Co	1388	CoO	291
Ni	627	CoF_2	39
Gd	292	NiO	525
Tb	219	$NiCl_2$	50
Dy	88	CuO	230
Fe α	1043	FeO	198
Fe_2O_3	948	Fe_2	78
Fe_3O_4	858	$MgCr_2O_4$	16
Fe_2B	1015	MnO	116
MnBi	630	MnO_2	92
MnB	578	MnS	160
MnSb	587	MnTe	307
MnAs	318	MnF_2	67
CrO_2	386	Cr	308
$Nd_2Fe_{14}B$	593	Cr_2O_3	307
AlNiCo	810	Nd_2O_3	10

Table 4: Curie and Néel temperatures for various materials.

2.2 Magneto-optic effects

Now that we have established how magnetization arises in materials and the various forms it can take, we turn our attention to how the magnetic state can be optically probed. For this purpose, we use the magneto-optic Kerr effect. To clearly introduce the MOKE, we begin by introducing the Faraday effect. Both phenomena rely on the same fundamental principles; however, the Faraday effect occurs in a transmission geometry, which makes it conceptually simpler to describe. The MOKE can therefore be considered as the reflection analogue of the Faraday effect [88, 89].

2.2.1 Magneto-optic Faraday effect

The Faraday effect refers to the rotation of the linear polarization of a light beam as it propagates through a magnetized medium [90, 91]. In other words, a linearly polarized light beam traversing a magnetic material emerges elliptically polarized, but its polarization axis is rotated. This effect is illustrated in Figure 38.

The rotation angle, known as the Faraday rotation Θ_F, depends linearly on the magnetic induction B, the optical path length d through the material, and the Verdet constant ν of the material:

$$\Theta_F = \nu B d. \tag{112}$$

The Verdet constant ν depends both on the wavelength of the light and on the temperature of the magnetic medium. Moreover, the sign of the Verdet constant determines the sense of rotation: $\nu > 0$ corresponds to a left-handed rotation, whereas $\nu < 0$ results in a right-handed rotation [88].

The Faraday effect originates from the difference in propagation velocities between the right- and left-circularly polarized components of the light inside a magnetized medium. This difference arises from magnetic circular birefringence induced by the magnetization. Although the optical frequency is far above typical magnetic resonance frequencies, the magneto-optical response can be strongly enhanced when the magnetization dynamics is resonantly driven, for instance near the ferromagnetic

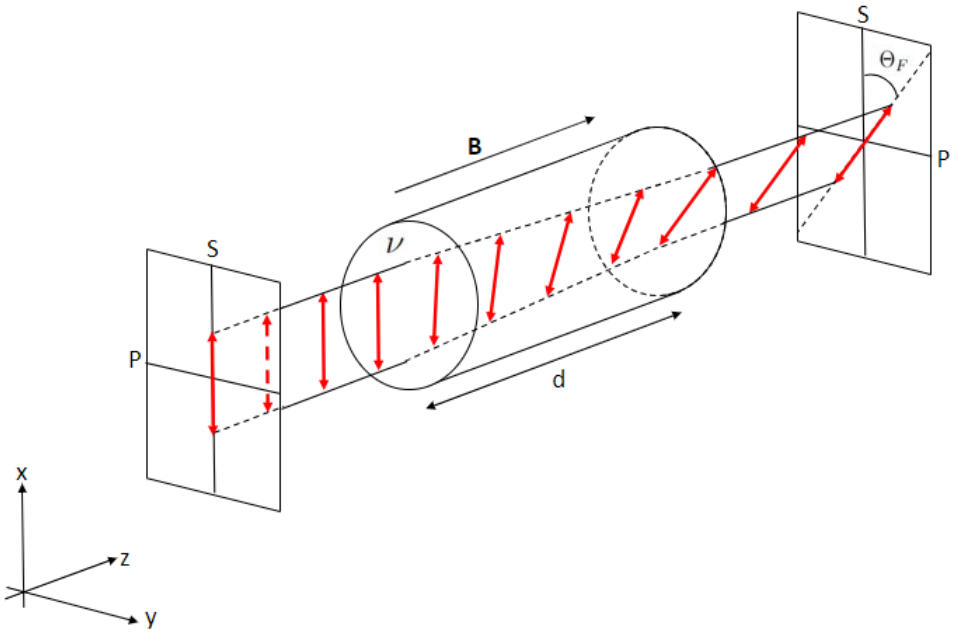

Figure 38: Illustration of polarization rotation due to the Faraday effect in a magnetized medium.

resonance [92]. To mathematically describe this mechanism, the electric field of the propagating wave is expressed as the superposition of two circularly polarized components [93].

$$\mathbf{E} = \frac{1}{2}E_0(\mathbf{e_x} + e^{j\delta}\mathbf{e_y})e^{j(\omega t - kz)} + \text{c.c.} \tag{113}$$

Equation (113) represents an elliptically polarized wave. For circular polarization, the phase delay δ equals $\pm\pi/2$: $\delta = \pi/2$ for right-circular, and $\delta = -\pi/2$ for left-circular polarization.

$$\mathbf{E}_R = \frac{1}{2}E_0(\mathbf{e_x} + j\mathbf{e_y})e^{j(\omega t - kz)} + \text{c.c.} \tag{114}$$

$$\mathbf{E}_L = \frac{1}{2}E_0(\mathbf{e_x} - j\mathbf{e_y})e^{j(\omega t - kz)} + \text{c.c.} \tag{115}$$

We consider a linearly polarized wave propagating along $\mathbf{z}$ with its polarization along $\mathbf{x}$. To describe the Faraday effect, we decompose it into right- and left-circular components, each propagating with its own complex refractive index $\bar{n}_r$ and $\bar{n}_l$:

$$\mathbf{E} = \frac{1}{2}E_0\Big[(\mathbf{e_x} + j\mathbf{e_y})e^{j(\omega t - 2\pi\bar{n}_r z/\lambda)} + (\mathbf{e_x} - j\mathbf{e_y})e^{j(\omega t - 2\pi\bar{n}_l z/\lambda)}\Big]. \tag{116}$$

Refactoring Equation (116) by $\mathbf{e_x}$ and $\mathbf{e_y}$ gives:

$$\mathbf{E} = \frac{1}{2}E_0\Big[(e^{j\phi_r} + e^{j\phi_l})\mathbf{e_x} + j(e^{j\phi_r} - e^{j\phi_l})\mathbf{e_y}\Big], \quad \text{with} \quad \phi_{r,l} = \omega t - 2\pi\bar{n}_{r,l}z/\lambda. \tag{117}$$

Using standard trigonometric identities:

$$e^{j\phi_r} + e^{j\phi_l} = 2e^{j\bar{\phi}}\cos(\Delta\phi),$$

$$j(e^{j\phi_r} - e^{j\phi_l}) = -2e^{j\bar{\phi}}\sin(\Delta\phi),$$

where $\bar{\phi} = \omega t - \dfrac{\pi}{\lambda}(\bar{n}_r + \bar{n}_l)z$ and $\Delta\phi = \dfrac{\pi}{\lambda}(\bar{n}_r - \bar{n}_l)z$. Substituting into Equation (117) yields:

$$\mathbf{E} = E_0 e^{j\bar{\phi}}\big[\cos(\Delta\phi)\mathbf{e_x} - \sin(\Delta\phi)\mathbf{e_y}\big]. \tag{118}$$

The complex average refractive index $\bar{n}$ is defined as:

$$\bar{n} = \frac{\bar{n}_r + \bar{n}_l}{2}. \tag{119}$$

With this definition, the electric field becomes:

$$\mathbf{E} = E_0 e^{j(\omega t - 2\pi \bar{n} z/\lambda)} \left[\cos\left(\frac{\bar{\delta}}{2}\right) \mathbf{e_x} - \sin\left(\frac{\bar{\delta}}{2}\right) \mathbf{e_y} \right], \tag{120}$$

where $\bar{\delta} = \dfrac{2\pi}{\lambda}(\bar{n}_r - \bar{n}_l)z$. The Faraday rotation Θ_F and the ellipticity ε_F (arising from differential absorption) are obtained from the real and imaginary parts of $\bar{\delta}/2$ [92, 94]:

$$\Theta_F(z) = \mathrm{Re}\left(\frac{\bar{\delta}}{2}\right) = \frac{\pi}{\lambda}(n_r - n_l)z, \tag{121}$$

$$\varepsilon(z) = -\tanh\left(\mathrm{Im}\left(\frac{\bar{\delta}}{2}\right)\right) = \tanh\left(\frac{\pi}{\lambda}(\kappa_r - \kappa_l)z\right), \tag{122}$$

where $n_{r,l}$ and $\kappa_{r,l}$ are the real and imaginary parts of $\bar{n}_{r,l}$, respectively. The Faraday rotation accumulates over the propagation distance z within the medium; beyond the magnetic layer ($z > d$), no further rotation occurs. The difference in refractive indices of the two circular modes is proportional to the magnetic induction, $n_r - n_l = \mathrm{cste} \times B$. This proportionality defines the Verdet constant ν:

$$\nu = \frac{\pi}{\lambda} \times \mathrm{cste}. \tag{123}$$

The Faraday effect provides a clear example of how magnetization modifies the polarization state of light. Based on the same underlying mechanism, the following section extends this description to the magneto-optic Kerr effect, the reflective counterpart of the Faraday effect.

2.2.2 Magneto-optic Kerr effect

The MOKE is based on the same physical principles as the Faraday effect. However, whereas the Faraday effect occurs during the transmission of light through a magnetic material, MOKE arises from the reflection of light at the surface of a magnetized material [88, 92, 95]. To describe this effect, we use the same representation of linearly polarized light as for the Faraday effect, given in Equation (118), with some modifications. In particular, Equation (118) assumes normal incidence. To generalize this, we introduce an angle of incidence θ_i, which modifies the wave vector as:

$$\mathbf{k} = k_0(\sin\theta_i\, \boldsymbol{e}_x + \cos\theta_i\, \boldsymbol{e}_z). \tag{124}$$

This expression corresponds to a light propagation in the (xz) plane. Linearly polarized light can then be decomposed into components along the $\mathbf{e}_s$ and $\mathbf{e}_p$ directions, perpendicular and parallel, respectively, to the plane of incidence. We define these two vectors in the Cartesian basis as follows:

$$\boldsymbol{e}_s = \boldsymbol{e}_y, \tag{125}$$

$$\boldsymbol{e}_p = \cos\theta_i \boldsymbol{e}_x - \sin\theta_i \boldsymbol{e}_z. \tag{126}$$

The incident electric field can thus be written as $\mathbf{E}^{(\mathrm{inc})} = E_s \boldsymbol{e}_s + E_p \boldsymbol{e}_p$. Using the definitions $E_s = -E_0 \sin(\Delta\phi)$ and $E_p = E_0 \cos(\Delta\phi) \cdot \boldsymbol{e}_x \cdot \boldsymbol{e}_p$, one can recast Equation (118) into:

$$\mathbf{E}^{(\mathrm{inc})} = E_0 e^{j\bar{\phi}} \big[\cos(\Delta\phi)(\cos\theta_i \boldsymbol{e}_p + \sin\theta_i \boldsymbol{e}_z) - \sin(\Delta\phi)\boldsymbol{e}_s\big]. \tag{127}$$

At the air-magnetic material interface where MOKE occurs, only the tangential components of the electric field are physically relevant, since $\boldsymbol{e}_z$ is normal to the interface. Thus, Equation (127) simplifies to:

$$\mathbf{E}_{int}^{(\mathrm{inc})} = E_0 e^{j\bar{\phi}} \big[\cos(\Delta\phi)\cos\theta_i \boldsymbol{e}_p - \sin(\Delta\phi)\boldsymbol{e}_s\big]. \tag{128}$$

The reflected electric field can then be expressed as:

$$\mathbf{E}^{(\mathrm{ref})} = r_{pp}E_p\boldsymbol{e}_p + r_{sp}E_p\boldsymbol{e}_s + r_{ss}E_s\boldsymbol{e}_s + r_{ps}E_s\boldsymbol{e}_p, \tag{129}$$

where r_{ij} is the reflection coefficient for incident polarization j into reflected polarization i. The cross terms r_{sp} and r_{ps} encode the magneto-optical Kerr rotation and ellipticity induced by the magnetization anisotropy [96, 97]. To determine the reflection coefficients, we introduce the electric permittivity tensor $\boldsymbol{\varepsilon}$, which is given by:

$$\boldsymbol{\varepsilon} = \varepsilon_{iso}\boldsymbol{I} + j\mathcal{Q}(\mathbf{M}\times\boldsymbol{I}) \tag{130}$$

where ε_{iso} is the isotropic permittivity, $\mathbf{M} = (M_x, M_y, M_z)$ is the unit magnetization vector, $\mathcal{Q}$ is the gyrotropic parameter (analogous to the Verdet constant), and $\boldsymbol{I}$ is the Levi-Civita antisymmetric tensor. The $\mathbf{M}\times\boldsymbol{I}$ product is explicitly given by:

$$\mathbf{M}\times\boldsymbol{I} = \begin{bmatrix} 0 & -M_z & M_y \\ M_z & 0 & -M_x \\ -M_y & M_x & 0 \end{bmatrix}.$$

The reflection coefficients, which depend on the incidence angle θ_i, the transmission angle θ_t, the complex refractive index $\bar{n}$ of the magnetic medium, and the magnetization geometry, are given by:

$$r_{pp} = r_{pp}^{(0)} + \delta r_{pp}, \tag{131}$$

$$r_{ss} = r_{ss}^{(0)} + \delta r_{ss}, \tag{132}$$

$$r_{sp} = j\mathcal{Q}\frac{2\bar{n}\cos\theta_i\cos\theta_t}{(\bar{n}\cos\theta_i + \cos\theta_t)^2}\mathcal{F}_{sp}, \tag{133}$$

$$r_{ps} = j\mathcal{Q}\frac{2\bar{n}\cos\theta_i\cos\theta_t}{(\cos\theta_i + \bar{n}\cos\theta_t)^2}\mathcal{F}_{ps}. \tag{134}$$

These expressions assume incidence from air with a refractive index of one. The parameters $r_{pp}^{(0)}$ and $r_{ss}^{(0)}$ are the usual Fresnel coefficients for nonmagnetic reflection [88, 98]:

$$r_{pp}^{(0)} = \frac{\bar{n}\cos\theta_i - \cos\theta_t}{\bar{n}\cos\theta_i + \cos\theta_t}, \tag{135}$$

$$r_{ss}^{(0)} = \frac{\cos\theta_i - \bar{n}\cos\theta_t}{\cos\theta_i + \bar{n}\cos\theta_t}. \tag{136}$$

The gyrotropic corrections δr_{pp}, δr_{ss}, and the cross-coupling coefficients $\mathcal{F}_{sp}$ and $\mathcal{F}_{ps}$ depend on the magnetization geometry. The transmission angle θ_t is given by:

$$\theta_t = \sqrt{1 - \left(\frac{1}{\bar{n}}\sin\theta_i\right)^2}. \tag{137}$$

We distinguish three principal MOKE geometries: polar ($\mathbf{M} \parallel \boldsymbol{e}_z$), longitudinal ($\mathbf{M} \parallel \boldsymbol{e}_x$), and transverse ($\mathbf{M} \parallel \boldsymbol{e}_y$), as illustrated in Figure 39.

MOKE geometry	δr_{pp}	δ_{ss}	$\mathcal{F}_{sp}$	$\mathcal{F}_{ps}$
Polar ($\mathbf{M} \parallel \boldsymbol{e}_z$)	0	0	$+M_z$	$-M_z$
Longitudinal ($\mathbf{M} \parallel \boldsymbol{e}_x$)	0	0	$+M_x \cos\theta_i$	$+M_x \cos\theta_i$
Transverse ($\mathbf{M} \parallel \boldsymbol{e}_y$)	$+j\mathcal{Q}M_y \cdot C_{pp}$	$+j\mathcal{Q}M_y \cdot C_{ss}$	0	0

Table 5: Gyrotropic correction terms and $\mathcal{F}$ coefficients for MOKE in the three principal geometries.

The gyrotropic correction terms and $\mathcal{F}$ coefficients for each geometry are given in Table [5], where geometrical correction factors C_{pp} and C_{ss} are defined by incidence and transmission angles:

$$C_{pp} = \frac{4\bar{n}\cos\theta_i \cos\theta_t}{(\bar{n}\cos\theta_i + \cos\theta_t)^2}, \tag{138}$$

$$C_{ss} = \frac{4\bar{n}\cos\theta_i \cos\theta_t}{(\cos\theta_i + \bar{n}\cos\theta_t)^2}. \tag{139}$$

Once the full reflected field is expressed, its S- and P-polarized components are:

$$E_s^{(ref)} = r_{sp}E_p + r_{ss}E_s, \tag{140}$$

$$E_p^{(ref)} = r_{pp}E_p + r_{ps}E_s. \tag{141}$$

From the ratio of these two components, we define the Kerr rotation Θ_K and the Kerr ellipticity ε_K:

$$\Theta_K = \mathrm{Re}\left(\frac{E_s^{(\mathrm{ref})}}{E_p^{(\mathrm{ref})}}\right), \tag{142}$$

$$\varepsilon_K = \mathrm{Im}\left(\frac{E_s^{(\mathrm{ref})}}{E_p^{(\mathrm{ref})}}\right). \tag{143}$$

The expressions of $E_s^{(\mathrm{ref})}$ and $E_p^{(\mathrm{ref})}$, depending on the magnetization geometry, are summarized in Table [6], where we introduce the cross-polarization term:

$$C_{cross} = \frac{2\bar{n}\cos\theta_i \cos\theta_t}{(\bar{n}\cos\theta_i + \cos\theta_t)^2}. \tag{144}$$

It should be noted that, in the specific case of transverse MOKE, $C_{cross} = 0$, no cross-polarization terms appear. This means that no Kerr rotation occurs in this configuration. Instead, the magneto-optic signal manifests as an intensity contrast rather than a change in polarization direction or ellipticity.

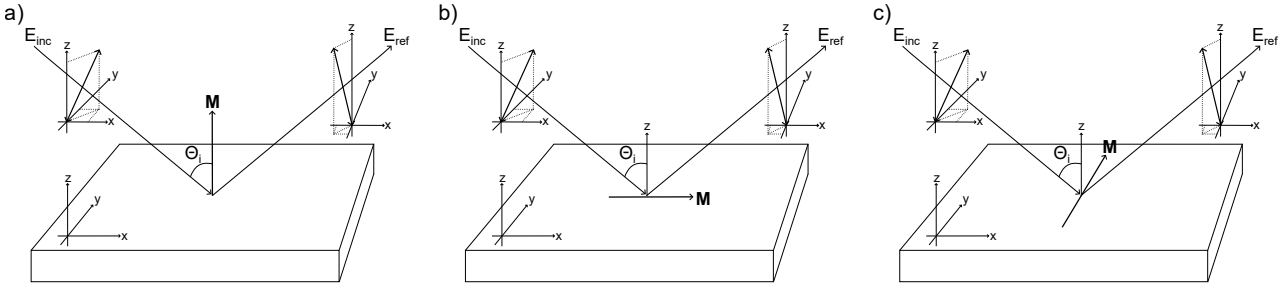

Figure 39: Schemes of the principal MOKE configurations. a) polar ($\mathbf{M} \parallel \boldsymbol{e}_z$), b) longitudinal ($\mathbf{M} \parallel \boldsymbol{e}_x$), and c) transverse ($\mathbf{M} \parallel \boldsymbol{e}_y$).

MOKE geometry	$E_s^{(ref)}$	$E_p^{(ref)}$
Polar	$j\mathcal{Q}\cdot M_z\cdot C_{cross}E_p + r_{ss}^{(0)}E_s$	$r_{pp}^{(0)}E_p - j\mathcal{Q}\cdot M_z\cdot C_{cross}E_s$
Longitudinal	$j\mathcal{Q}\cdot M_x\cos\theta_i\cdot C_{cross}E_p + r_{ss}^{(0)}E_s$	$r_{pp}^{(0)}E_p + j\mathcal{Q}\cdot M_x\cos\theta_i\cdot C_{cross}E_s$
Transverse	$j\mathcal{Q}\cdot M_y C_{ss}E_s + r_{ss}^{(0)}E_s$	$r_{pp}^{(0)}E_p + j\mathcal{Q}\cdot M_y C_{pp}E_p$

Table 6: S- and P-polarized components of the electric field reflected from a magnetic medium, for the three principal magnetization geometries.

In a realistic experimental configuration, the spontaneous magnetization M_s lies within the sample plane (xy), forming an angle α with the x-axis. To enhance the Kerr effect, one applies an out-of-plane magnetic field $\mathbf{H} = H_z\boldsymbol{e}_z$ to induce an out-of-plane component to the magnetization. The initial in-plane magnetization $\mathbf{M}_0$ is:

$$\mathbf{M}_0 = M_s(\cos\alpha\ \boldsymbol{e}_x + \sin\alpha\ \boldsymbol{e}_y) \tag{145}$$

Assuming $|\mathbf{M}| = M_s = \text{cste}$, which is valid as long as the temperature remains well below the Curie temperature, the magnetization under $\mathbf{H}$ becomes:

$$\mathbf{M} = M_s(\cos\alpha\cos\beta\ \boldsymbol{e}_x + \sin\alpha\cos\beta\ \boldsymbol{e}_y + \sin\beta\ \boldsymbol{e}_z). \tag{146}$$

The equilibrium angle β is determined by minimizing the energy $\varepsilon(\beta)$,

$$\varepsilon(\beta) = -\mu_0\,\mathbf{M}\cdot\mathbf{H} + K_u\sin^2\beta, \tag{147}$$

$$\varepsilon(\beta) = -\mu_0\,M_s\,H_z\sin\beta + K_u\sin^2\beta. \tag{148}$$

Setting $d\varepsilon(\beta)/d\beta = 0$ yields:

$$-\mu_0\,M_s\,H_z\cos\beta + 2K_u\sin\beta\cos\beta = 0. \tag{149}$$

Two cases must be considered. In the first case, the applied magnetic field is strong enough to completely pull the magnetization out of the plane ($|\mu_0 M_s H_z| \geq 2K_u$). In this case, the system reaches full saturation in the polar MOKE configuration, with $\beta = \pm\pi/2$ and $\mathbf{M} = \pm M_s\boldsymbol{e}_z$. In the second case, $\beta \neq \pm\pi/2$, and the equilibrium angle is given by:

$$\sin\beta = \frac{\mu_0\,M_s\,H_z}{2K_u}. \tag{150}$$

The general Kerr rotation in practice can be expressed as a linear combination of the magnetization components:

$$\Theta_K = \mathrm{Re}\{a_x M_x + a_y M_y + a_z M_z\}. \tag{151}$$

The Kerr sensitivity coefficients a_x, a_y, and a_z depend on $\mathcal{Q}$, incidence geometry, and correction factors C and have implicitly been introduced in Table [6], it reads,

$$a_x = j\,\mathcal{Q}\,C_{\text{cross}}\cos\theta_i, \tag{152}$$

$$a_y = j\,\mathcal{Q}\,C_{\text{ss}}, \tag{153}$$

$$a_z = j\,\mathcal{Q}\,C_{\text{cross}}. \tag{154}$$

Having established the orientation of the magnetization and its dependence on the external magnetic field, we now describe the practical detection scheme. Experimentally, the reflected probe beam passes

through an HWP and a Wollaston prism. The Wollaston prism acts as a polarization beam splitter that separates the S- and P-polarized components. Each beam is then directed onto a photodiode. These two photodiodes are balanced, and the HWP is adjusted so that, in the absence of Kerr rotation, the beam is linearly polarized at 45°, ensuring that the S and P components have equal intensity, resulting in a zero total voltage. Mathematically, the S- and P-polarization components can be written in the form

$$E_s^{(\mathrm{ref})} = E_0 \cos(45^\circ + \Theta_K), \tag{155}$$

$$E_p^{(\mathrm{ref})} = E_0 \sin(45^\circ + \Theta_K). \tag{156}$$

The Kerr rotation is generally small, which allows trigonometric simplifications and Taylor expansion of Equations (155) and (156). We obtain

$$E_s^{(\mathrm{ref})} \simeq \frac{E_0}{\sqrt{2}}(1 - \Theta_K), \tag{157}$$

$$E_p^{(\mathrm{ref})} \simeq \frac{E_0}{\sqrt{2}}(1 + \Theta_K). \tag{158}$$

Since the photodiode voltage is proportional to the intensity, we introduce the intensities of the S and P components of the probe beam,

$$I_s = |E_s^{(\mathrm{ref})}|^2 \simeq \frac{E_0^2}{2}(1 - 2\Theta_K), \tag{159}$$

$$I_p = |E_p^{(\mathrm{ref})}|^2 \simeq \frac{E_0^2}{2}(1 + 2\Theta_K), \tag{160}$$

and their difference yields a voltage difference $\delta V = V_p - V_s$ proportional to $I_p - I_s$:

$$\delta V \propto I_p - I_s = \frac{E_0^2}{2} \cdot 4\Theta_K. \tag{161}$$

Identifying the equilibrium voltage ($V \propto E_0^2/2$), one obtains:

$$\Theta_K \propto \frac{\delta V}{4V}, \tag{162}$$

where the proportionality factor is determined by the gain of the photodiodes and any electronic amplification used.

In summary, the MOKE has now been described both for realistic experimental conditions and for the three classical geometries. The canonical relation between the Kerr rotation and the measured photodiode voltage has also been established. The next step is to introduce the ultrafast optical excitation that perturbs the magnetic equilibrium, enabling us to probe its dynamics on the picosecond timescale.

2.3 Ultrafast laser demagnetization

By measuring the Kerr rotation angle, we gain optical access to the magnetization state of the investigated sample. In our case, we use time-resolved MOKE to probe ultrafast magnetization dynamics with picosecond temporal resolution. These dynamics are triggered by femtosecond laser pulses, which induce transient changes in the magnetic order through optically driven electronic, thermal, and spin-related processes.

In the first part, a two-temperature model was introduced to describe the ultrafast optical generation of acoustic waves. To account for the influence of a femtosecond optical pulse on the magnetization, a third temperature, the spin temperature, is introduced. This leads to the three-temperature model, as described in references [99–101].

$$C_e(T_e)\frac{dT_e}{dt} = G_{el}(T_l - T_e) + G_{es}(T_s - T_e) + S(t) \tag{163}$$

$$C_s(T_s)\frac{dT_s}{dt} = G_{es}(T_e - T_s) + G_{sl}(T_l - T_s) \tag{164}$$

$$C_l(T_l)\frac{dT_l}{dt} = G_{el}(T_e - T_l) + G_{sl}(T_s - T_l) \tag{165}$$

In this model, C_e, C_l, and C_s denote the specific heat capacities of the electrons, lattice, and spin subsystems, respectively. Similarly, T_e, T_l, and T_s represent their corresponding temperatures. The coefficients G_{el}, G_{es}, and G_{sl} are the energy exchange coupling constants between these subsystems. The term $S(t)$ represents the energy input from the femtosecond laser pulse, as previously defined in Equation (13).

To evaluate the laser-induced changes in magnetization, it is necessary to compute the spin temperature T_s, which can then be used as input for the temperature-dependent Brillouin function derived earlier. However, the coupling constants G_{ij} are not all easily accessible. Among them, the electron-lattice coupling constant G_{el} is the best known and has already been discussed in the theoretical section on photoacoustics. The electron-spin coupling constant G_{es} is governed by spin-relaxation processes within the electron system. Although its determination is challenging, several theoretical models exist, notably the Elliott-Yafet mechanism [102] and the Kamberský torque-correlation model [103]. The spin-lattice coupling constant G_{sl} is the least accessible and is often determined empirically. Nevertheless, it is possible to estimate the characteristic spin-lattice relaxation time using Mössbauer spectroscopy or related techniques [104–106]. The determination of the coupling constants is beyond the scope of the present work. Instead, the values are taken from literature [100, 107–112] and adapted to our experimental conditions.

A homemade Python script has been used to simulate the 3TM (see Appendix D.4). To validate our code, we compare its output for nickel with the same parameters used by Beaurepaire *et al.* [107], namely $G_{el} = 8 \cdot 10^{17}$ W$\cdot$m$^{-3}\cdot$K^{-1}, $G_{es} = 6 \cdot 10^{17}$ W$\cdot$m$^{-3}\cdot$K^{-1}, $G_{sl} = 0.3 \cdot 10^{17}$ W$\cdot$m$^{-3}\cdot$K^{-1}, $\gamma_e = 6 \cdot 10^{3}$ J$\cdot$m$^{-3}\cdot$K^{-2}, $C_l = 2.2 \cdot 10^{6}$ J$\cdot$m$^{-3}\cdot$K^{-1}, $C_s = 7 \cdot 10^{5}$ J$\cdot$m$^{-3}\cdot$K^{-1}, $\phi = 7$ mJ$\cdot$cm^{-2}, and $\tau_p = 60$ fs. For the laser source, we continue using our definition from Equation (13). Figure 40 compares our simulation results with those reported by Beaurepaire *et al.* [107]. Figure 40(a) shows our simulations, which match the predictions of Beaurepaire *et al.* (their FIG. 3), confirming the validity of our model.

Figure 40(c) provides an estimation of ultrafast demagnetization using the phenomenological Bloch relation:

$$M(T_s) = 1 - B\left(\frac{T_s}{T_C}\right)^{3/2}, \tag{166}$$

where B is an empirical adjustment factor. This relation predicts an 82 % ultrafast demagnetization, which is consistent with a maximum spin temperature $T_s^{max} \simeq 576$ K, close to the Curie temperature.

From FIG. 2 of Beaurepaire *et al.*, we observe that such a strong perturbation induces only about a 40 % variation in the MOKE signal. This is expected since MOKE does not solely depends on magnetization but also on the gyrotropic ratio $\mathcal{Q}$, which is strongly affected by out-of-equilibrium electronic states.

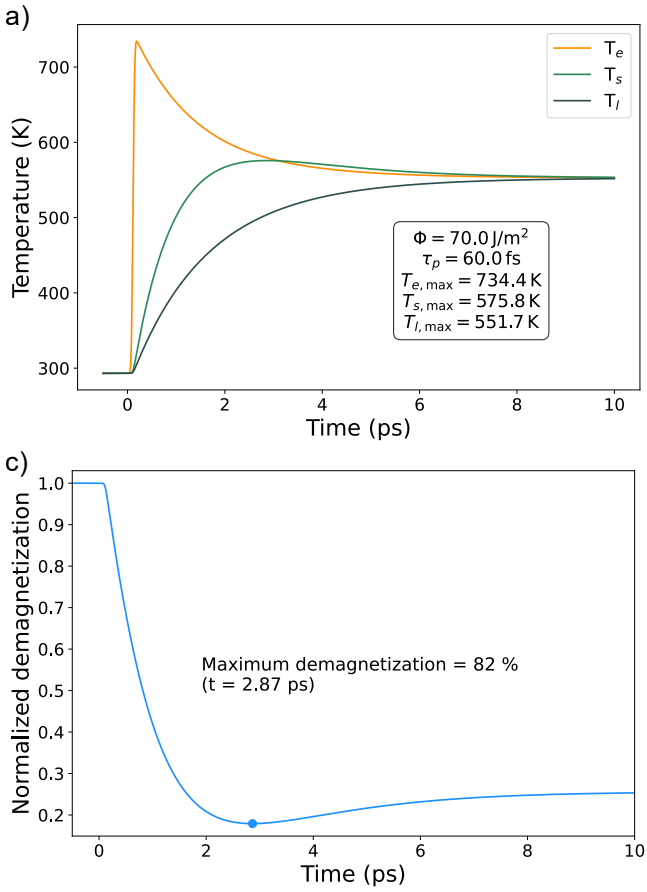

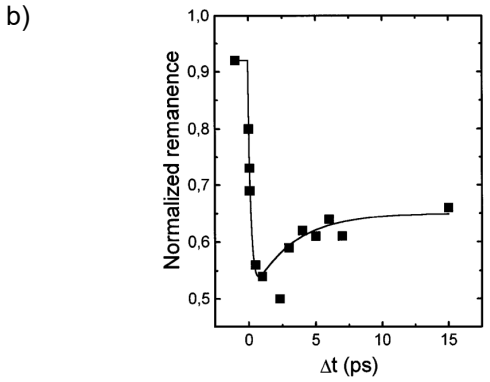

FIG. 2. Transient remanent longitudinal MOKE signal of a Ni(20 nm)/MgF_2(100 nm) film for 7 mJ cm^{-2} pump fluence. The signal is normalized to the signal measured in the absence of pump beam. The line is a guide to the eye.

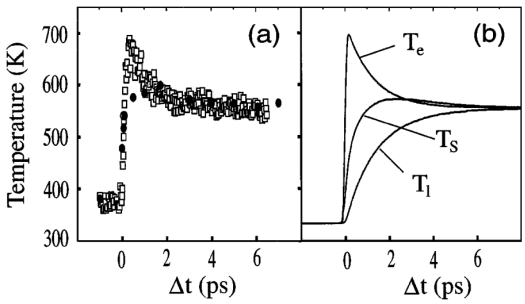

FIG. 3. (a) Experimental spin (T_s) and electron (T_e) temperatures estimated as explained in the text. The experimental conditions are those of Fig. 2. (b) Calculated spin (T_s), electron (T_e), and lattice (T_l) temperatures from Eqs. (1). The relevant parameters are given in the text.

Figure 40: Comparison of our 3TM simulation on nickel with Beaurepaire *et al.* [107] using identical parameters. a) Our 3TM simulation. b) Beaurepaire *et al.* investigations of the influence of a femtosecond pulse on MOKE and fitting of experimental T_e and T_s with 3TM. c) Estimation of ultrafast demagnetization from the phenomenological Bloch relation.

Although the 3TM can predict ultrafast demagnetization, we note that with the parameters used, electronic heating is underestimated, as is the electron-lattice heat transfer. Additionally, the relaxation dynamics appear too slow for picosecond-scale investigations. To match the TTM prediction on the strong ultrafast electronic response, and based on more recent modeling of spin-lattice-electron dynamics [113], we injected the G_{el}, γ_e, C_e, and C_l parameters used in our TTM simulation for nickel into the 3TM. The remaining parameters were then empirically adjusted to preserve the electronic heating predicted by the TTM and the spin-temperature trend reported by Beaurepaire *et al.*. Figure 41 shows the estimated electronic, spin, and lattice heating on nickel from the 3TM using our adjusted parameters: $G_{el} = 9.4 \cdot 10^{17}$ W $\cdot$ m^{-3} $\cdot$ K^{-1}, $G_{es} = 1.31 \cdot 10^{18}$ W $\cdot$ m^{-3} $\cdot$ K^{-1}, $G_{sl} = 0.3 \cdot 10^{17}$ W $\cdot$ m^{-3} $\cdot$ K^{-1}, $\gamma_e = 92$ J $\cdot$ m^{-3} $\cdot$ K^{-2}, $C_l = 3.9 \cdot 10^6$ J $\cdot$ m^{-3} $\cdot$ K^{-1}, $C_s = 2.78 \cdot 10^6$ J $\cdot$ m^{-3} $\cdot$ K^{-1}. The newly adjusted 3TM parameters, shown in Figure 41(b), successfully reproduce the electronic temperature predicted by the TTM (Figure 41(a)), as well as the spin temperature experimentally reported by Beaurepaire *et al.*. In addition, the lattice temperature remains consistent with that predicted by the TTM. Moreover, the response time remains within the sub-picosecond regime, which is consistent with ultrafast dynamics. Keeping the same parameters but changing the laser source from $\phi = 7$ mJ $\cdot$ cm^{-2} and $\tau_p = 60$ fs to $\phi = 1$ mJ $\cdot$ cm^{-2} and $\tau_p = 100$ fs leads to the predictions shown in Figure 41(c) for the TTM and Figure 41(d) for the 3TM. We observe that the 3TM correctly predicts the spin temperature while preserving the TTM trends for electronic and lattice heating, as well as the characteristic timescales.

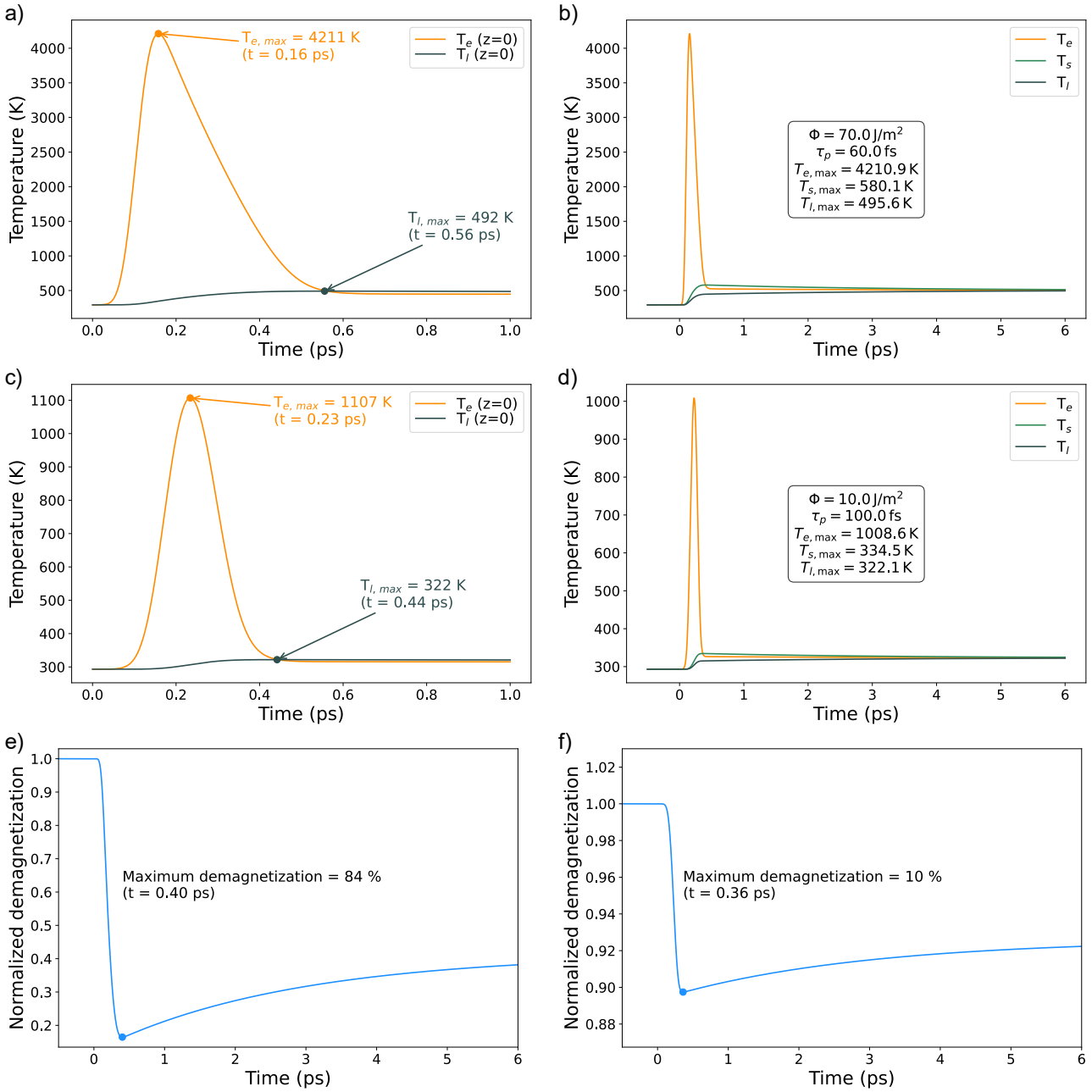

Figure 41: 3TM model with G_{el}, γ_e, C_e, and C_l parameters taken from TTM theory and empirical adjustments of the spin-related constants to reproduce electronic and spin heating. a) TTM simulation on Ni with the Beaurepaire laser source. b) 3TM adjusted from TTM simulations using the Beaurepaire laser source. c) TTM on nickel with a 10 J m^{-2}, 100 fs laser source. d) 3TM with a 10 J m^{-2}, 100 fs laser source. e) Estimated ultrafast demagnetization induced by the Beaurepaire laser source. f) Estimated ultrafast demagnetization induced by a 10 J m^{-2}, 100 fs laser source.

Finally, Figure 41(e) and Figure 41(f) show the estimated ultrafast demagnetization induced by a 7 mJ cm^{-2}, 60 fs laser, and a 1 mJ cm^{-2}, 100 fs laser, respectively. We note that the estimated demagnetization in Figure 41(e) is very similar to that predicted using the original Beaurepaire *et al.* parameters (Figure 40(c)), confirming the validity of our modified parameter set for modeling ultrafast laser-induced demagnetization.

2.4 Magnetoacoustics

We now have introduced the magnetic modification of light polarization and the influence of a femtosecond laser pulse on magnetization. As discussed in the first part of this work, a femtosecond laser pulse can generate acoustic waves, and metals are commonly used as transducers to absorb the optical energy. Since acoustic waves induce lattice distortions, it becomes essential to assess their impact on magnetization. In this context, we introduce two relevant magnetoelastic phenomena: magnetostriction and piezomagnetism [28, 114, 115].

2.4.1 Magnetostriction and the Villari effect

Magnetostriction refers to the transduction of strain as a result of changes in magnetization. Its reciprocal effect, known as the Villari effect, corresponds to a modification of the magnetization under mechanical strain. Unlike piezomagnetism, both magnetostriction and the Villari effect exhibit a quadratic dependence between the strain and the magnetization components [116–118].

$$\varepsilon_{ij} = \lambda_{ijkl}\, M_k\, M_l \tag{167}$$

Equation (167) constitutes the fundamental relation of magnetostriction. It describes how the strain tensor ε_{ij} arises from a change in the magnetization vector M_k, mediated by the fourth-rank magnetostrictive tensor λ_{ijkl}.

Conversely, the Villari effect describes the change in magnetization M_k under applied strain ε_{ij}. Although there is no direct analytical inversion of Equation (167), the fundamental relation governing the Villari effect can be derived from the magnetomechanical free energy given by:

$$F(M, \varepsilon) = F_{mag}(M) + F_{el}(\varepsilon) + F_{mag-el}(M, \varepsilon), \tag{168}$$

where F_{mag} is the magnetic energy, typically modeled using a Curie-Weiss law, F_{el} is the elastic energy derived from Hooke's law, and F_{mag-el} is the magnetoelastic coupling energy that accounts for magnetostriction. Substituting standard expressions for these components into Equation (168) yields the explicit form given by:

$$F(M, \varepsilon) = \frac{1}{2}\chi_{kl}^{-1}\, M_k\, M_l + \frac{1}{2}C_{ijkl}\, \varepsilon_{ij}\, \varepsilon_{kl} - \frac{1}{2}\lambda_{ijkl}\, M_k\, M_l\, \varepsilon_{ij}. \tag{169}$$

The Villari effect is then obtained by minimizing the free energy $F(M, \varepsilon)$ with respect to the magnetization:

$$\frac{\partial F}{\partial M_k} = \frac{\partial F_{mag}}{\partial M_k} - \frac{1}{2}\lambda_{ijkl}\, \varepsilon_{ij}\, M_l = 0. \tag{170}$$

Which leads to the implicit equation:

$$\frac{\partial F_{mag}}{\partial M_k} = \frac{1}{2}\lambda_{ijkl}\, \varepsilon_{ij}\, M_l. \tag{171}$$

Equation (171), obtained from the minimization condition in Equation (170), provides an implicit description of the Villari effect. It illustrates how the equilibrium magnetization M_k depends on the strain ε_{ij}. The explicit relationship $M_k = f(\varepsilon_{ij})$ can be obtained by solving Equation (170) and depends on both the crystallographic symmetry and the magnetic phase of the material.

Importantly, it should be noted that the change in free energy described in Equation (171), induced by a strain, involves the magnetization vector **M**. In other words, the magnetization change depends on the magnetization state itself. In particular, if the magnetization reverses its sign, the strain-induced change in magnetization will also reverse. This behavior is fundamentally different from piezomagnetism.

2.4.2 Piezomagnetism

Magnetostriction is a second-order phenomenon in which a mechanical strain arises with an amplitude proportional to the square of the magnetization or of the applied magnetic field. By contrast, the first-order magnetoelastic coupling, known as piezomagnetism, corresponds to a linear relationship between magnetization and applied stress or strain. This linear effect has been reported only rarely, mostly in antiferromagnetic systems, even though symmetry considerations suggest that it could also occur in single-crystal ferromagnets [119–126]. Furthermore, theoretical studies have predicted that piezomagnetism might emerge at the interfaces of ferromagnetic nanoscale systems, even when the corresponding bulk materials show no such response. To date, however, these interfacial predictions have not been verified experimentally. If a linear magnetoelastic coupling could be effectively harnessed in conventional ferromagnets, it would offer direct control over both the magnitude and the sign of the magnetization, thus extending the possibilities beyond those accessible through quadratic magnetostrictive effects.

The coupling between the magnetization and the mechanical stress σ for a piezomagnetic material is described by the third-rank piezomagnetic tensor q_{kij} [127]. The free energy can then be expressed as:

$$F(M,\varepsilon) = \frac{1}{2}\chi_{kl}^{-1} M_k M_l + \frac{1}{2} C_{ijkl}\,\varepsilon_{ij}\,\varepsilon_{kl} - q_{kij}\,M_k\,\varepsilon_{ij}. \tag{172}$$

Minimization of the free energy with respect to the magnetization yields the linear stress-induced magnetization. In Voigt notation, the stress-induced magnetization change is:

$$\begin{bmatrix}\Delta M_x\\ \Delta M_y\\ \Delta M_z\end{bmatrix} = \begin{bmatrix} q_{x1} & q_{x2} & q_{x3} & q_{x4} & q_{x5} & q_{x6}\\ q_{y1} & q_{y2} & q_{y3} & q_{y4} & q_{y5} & q_{y6}\\ q_{z1} & q_{z2} & q_{z3} & q_{z4} & q_{z5} & q_{z6}\end{bmatrix} \times \begin{bmatrix}\sigma_1\\ \sigma_2\\ \sigma_3\\ \sigma_4\\ \sigma_5\\ \sigma_6\end{bmatrix}, \tag{173}$$

where the components of the piezomagnetic tensor depend on both the magnetic phase and the crystallographic symmetry of the material. Out of the 122 magnetic point groups, only 58 are compatible with a piezomagnetic response. These symmetry classes are associated with antiferromagnetic or ferrimagnetic phases, whereas purely paramagnetic and collinear ferromagnetic materials do not allow a linear coupling between stress and magnetization. The prototypical example is Cr_2O_3 (chromium (III) oxide), which was the first material in which piezomagnetism was experimentally demonstrated by Astrov in 1961 [128].

Importantly, as mentioned above, for a piezomagnetism sample, the change in magnetization induced by a strain is independent of the initial magnetization state and depends solely on the sign and magnitude of the applied strain or stress.

2.5 Magnetic precession

Taking into account the possible influence of magnetoelastic phenomena discussed earlier, we now introduce another magnetic mechanism that may occur during femtosecond pump-probe experiments: magnetization precession. Following the optical ultrafast demagnetization, the norm of the magnetization is reduced and its orientation is modified. Then, the magnetization progressively recovers its initial norm as the temperature returns to its equilibrium value. Meanwhile, its direction relaxes back toward the equilibrium orientation by precessing around it before fully collapsing onto it [129–132]. This return to equilibrium is described by the Landau–Lifshitz–Gilbert (LLG) equation, expressed as:

$$\frac{d\mathbf{M}}{dt} = -\gamma\,\mu_0\,\mathbf{M}\times\mathbf{H}_{\text{eff}} + \frac{\alpha_{\text{G}}}{M(t)}\,\mathbf{M}\times\frac{d\mathbf{M}}{dt}. \tag{174}$$

In this equation, the first term describes the precessional motion of the magnetization $\mathbf{M}$ around the effective field $\mathbf{H}_{\text{eff}}$. Here, γ is the gyromagnetic ratio, which determines the precession frequency. The second term, known as the Gilbert damping term, accounts for energy dissipation and drives the magnetization back to its equilibrium orientation. The damping strength is governed by the Gilbert factor α_G, and $M(t)$ denotes the time-dependent norm of the magnetization vector. As previously introduced in the context of MOKE geometry (see Equation (146)), we now consider the case of an external magnetic field applied purely along the z-axis, $\mathbf{H} = H_z\mathbf{e_z}$. In such a case, the equilibrium direction of the magnetization is aligned with the direction of the effective field $\mathbf{H}_{eff}$, which incorporates contributions from the external field as well as internal contributions. The equilibrium magnetization can therefore be expressed as:

$$\mathbf{M}_{\text{eq}} = M^{eq} \begin{pmatrix} \cos\alpha\cos\beta \\ \sin\alpha\cos\beta \\ \sin\beta \end{pmatrix}, \tag{175}$$

where α is the azimuthal angle (between $\mathbf{M}$ and the basis vector $\mathbf{e_x}$), and β is the elevation angle (between $\mathbf{M}$ and the (xy)-plane). Since the magnetization is parallel to the effective field at equilibrium, one can similarly express the effective field as:

$$\mathbf{H}_{eff} = H_0 \begin{pmatrix} \cos\alpha\cos\beta \\ \sin\alpha\cos\beta \\ \sin\beta \end{pmatrix}. \tag{176}$$

To compute the precessional motion of the magnetization, the self-consistent form of Equation (174) is replaced by its linearized version:

$$\frac{d\mathbf{M}}{dt} = -\frac{\gamma\cdot\mu_0}{1+\alpha_G^2}\left(\mathbf{M}\times\mathbf{H}_{eff}\right) - \frac{\gamma\cdot\mu_0\cdot\alpha_G}{(1+\alpha_G^2)\,M(t)}\left(\mathbf{M}\times(\mathbf{M}\times\mathbf{H}_{eff})\right). \tag{177}$$

The magnetization dynamics is simulated according to the LLG equation using a homemade Python script (see Appendix D.5). The results shown in Figure 42 are obtained by considering the temperature evolution predicted by the 3TM for nickel (see Figure 41). The temperature during the simulation time window is estimated using:

$$T(t) = T_{final} + (T_{initial} - T_{final})\, e^{-t/\tau_{th}}, \tag{178}$$

where $T_{final} = 293$ K is the room temperature, $T_{initial} = 580$ K is the peak spin temperature predicted from 3TM, and τ_{th} is the characteristic thermal relaxation time. The norm of the magnetization is evaluated at each simulation step by injecting Equation (178) into the Bloch relation given in Equation (166).

The parameters are chosen to match experimental observations: $\gamma = 1.93\cdot10^{11}$ rad$\cdot$s$^{-1}\cdot$T^{-1}, $\alpha_G = 0.05$, and $\tau_{th} = 0.5$ ns. The 3D trajectory in Figure 42(a) illustrates the rapid recovery of the magnetization amplitude during the early precessional motion as the system cools down, followed by a conical precession toward the equilibrium direction. In Figure 42(a), the blue arrow represents the magnetization state immediately after laser pulse heating, while the black arrow indicates the equilibrium direction and amplitude. Although the relative amplitude of the initial magnetization is determined from thermal modeling, its orientation relative to the equilibrium state is arbitrarily chosen. The equilibrium direction is defined by $\alpha = \beta = 45°$, whereas the perturbed state is set to $\alpha_0 = \beta_0 = 0°$. Figure 42(b) presents the out-of-plane component of the magnetization, which is the component probed in our MOKE setup. The exponential temperature decrease is clearly visible,

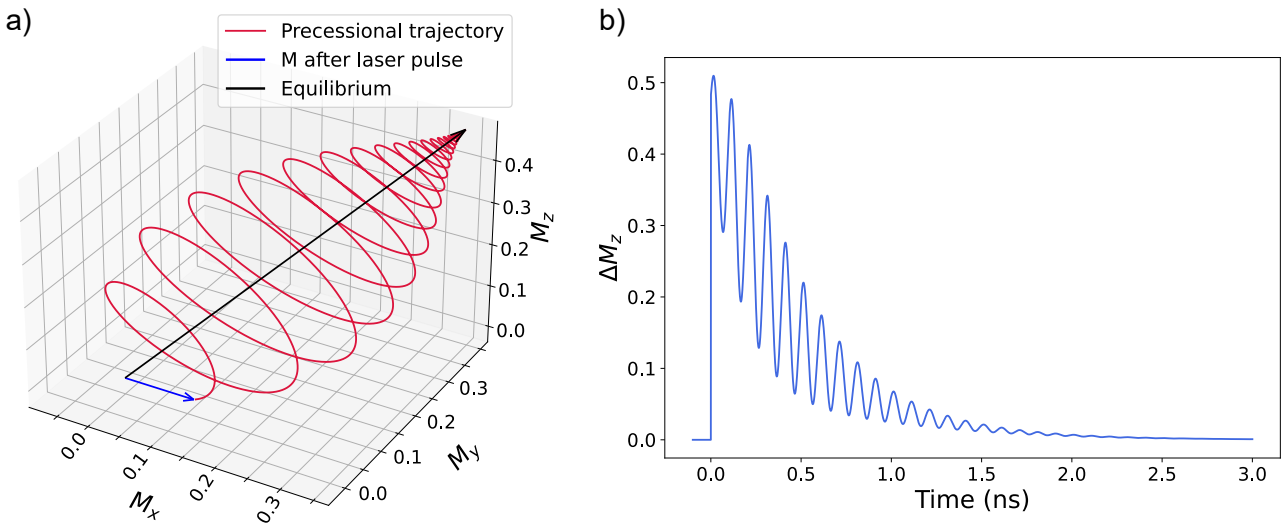

Figure 42: Simulation of precessional relaxation in nickel for $\gamma = 1.93 \cdot 10^{11}$ rad $\cdot$ s^{-1} T^{-1} and $\alpha_G = 0.05$. a) 3D modelization of magnetic precession. b) Extraction of the out-of-plane magnetization change ΔM_z.

revealing the recovery of magnetization. Moreover, the precession frequency is well-defined. The selected parameters lead to a precession frequency of 10 GHz, which is related to the gyromagnetic ratio γ and to the norm of the effective field H_{eff} by:

$$f_p = \frac{\gamma \cdot \mu_0 \cdot H_{eff}}{2\pi} \tag{179}$$

Referring back to Equation (151) highlights that the detected Kerr rotation is directly proportional to the out-of-place magnetization component $M_z(t)$, which is modulated by the precessional motion.

So far, we have discussed the microscopic origin of magnetism and the associated magnetic phases, the magneto-optical response of materials with a focus on the MOKE as a probing tool, ultrafast laser-driven demagnetization, magneto-acoustic interactions, and precessional dynamics. We now address the last theoretical element required for our study: interfacial magnetic anisotropy.

2.6 Interfacial anisotropy

In general, the magnetization of thin ferromagnetic films tends to lie in the (xy)-plane rather than out-of-plane. We have previously shown how an external magnetic field applied along the z-axis can induce an out-of-plane component of the magnetization, thereby enhancing the detected Kerr rotation in polar geometry. However, an alternative way to achieve an out-of-plane equilibrium magnetization without applying any external field is to exploit interfacial magnetic anisotropy [133–135]. This anisotropy, which arises at the interfaces between different materials, can stabilize a magnetization direction perpendicular to the film plane. For a single thin magnetic film, the total anisotropy energy E_{anis} results from the competition between volumetric and interfacial contributions and is given by:

$$E_{\text{anis}} = K_v \, d + K_s, \tag{180}$$

where K_v is the volumetric anisotropy constant, K_s is the surface anisotropy constant, and d is the film thickness.

In our case, we have studied a heterostructure composed of alternating layers of two distinct ferromagnetic materials, A and B, grown on a substrate and capped with a transparent layer to protect

the stack and enable optical investigations. The structure has the form: substrate/[A/B]^n/A/cap. We assume that each A layer has thickness d_A and each B layer has thickness d_B. The total thickness of the magnetic stack is $d = n(d_A + d_B) + d_A$. The total anisotropy energy per unit area of the stack is then given by:

$$\varepsilon_{anis}^{tot} = [(n+1)\, d_A\, K_v^A + n\, d_B\, K_v^B] \cdot \sin^2\theta + [2n\, K_s^{int} + 2K_s^{surf}] \cdot \sin^2\theta, \tag{181}$$

where θ is the angle between the magnetization vector and the normal to the film (the z-axis). The two parameters K_v^A and K_v^B are the volumetric anisotropies of materials A and B, respectively. The constant K_s^{surf} accounts for the top and bottom surface anisotropies (at the substrate/A and A/cap interfaces). The parameter K_s^{int} is the interfacial anisotropy at each A/B or B/A boundary. The equilibrium orientation of the magnetization is determined by the sign of the effective anisotropy constant K_{eff}, defined as the total anisotropy energy per unit volume.

$$K_{eff} = \frac{\varepsilon_{anis}^{tot}}{d_{tot}} \tag{182}$$

If $K_{eff} > 0$, the energy is minimized for $\theta = 0$, meaning that the magnetization spontaneously aligns out-of-plane, even in the absence of an external field. Conversely, if $K_{eff} < 0$, the magnetization remains confined to the (xy)-plane at equilibrium.

3 Spin-lattice interactions at picosecond timescale

The coupling between the lattice and spins has long been investigated, primarily for samples exhibiting magnetostriction. Synchrotron-based experiments have shown that applying a compressive stress in the range of 1-100 GPa to the bulk of pure cobalt and nickel leads to a marked reduction in the K-edge x-ray magnetic dichroism [136–139]. This technique for probing spin-lattice coupling is primarily sensitive to the 4p orbital moment rather than to the total spin moment. To broaden the investigation of spin-lattice coupling to a wider variety of materials, we propose using a femtosecond laser to generate strain waves and to resolve, on the picosecond timescale, their influence on magnetization through MOKE, which is sensitive to the total spin moment.

For this all-optical investigation of spin-lattice interactions, cobalt-nickel superlattices were specifically elaborated, as sketched in Figure 43. Basically the samples have the following structure: $Al_2O_3(11\bar{2}0)$/V(5 nm)/Au(20 nm)/Ni(3 ML)/[Co(X)/Ni(3 ML)]×5/MgO (100 nm). The sapphire substrate is a single crystal, and each deposited layer is epitaxially grown following the process described in [140, 141]. This architecture exhibits a spontaneous out-of-plane magnetization arising from interfacial anisotropy, making it relevant for spintronic applications [140, 142]. A polar magnetization combined with normal-incidence optical probing provides an ideal geometry for magneto-optic studies, as it maximizes Kerr rotation while suppressing Larmor precession. Three samples were prepared, differing only in cobalt layer thickness, one, two, or three mono-layers (ML), while nickel layers were kept at a constant 3 ML. These are referred to as Co1Ni3, Co2Ni3, and Co3Ni3, respectively. The choice of Co/Ni multilayers is motivated by their perpendicular magnetic anisotropy, which can be tuned via the cobalt layer thickness [142, 142, 143]. Due to the epitaxial growth process, the gold, nickel, cobalt, and MgO layers adopt a (111) crystallographic orientation along the out-of-plane z-axis, whereas the vanadium layer exhibits a (110) orientation. The vanadium layer serves as a transducer that absorbs the femtosecond pump and launches strain waves into the stack, as discussed in detail in the first part of this document. The gold and MgO layers act as spacers, introducing a time delay in the arrival of acoustic waves from the vanadium to the magnetic stack, as well as in the reflection of acoustic waves from the MgO/air interface. The optical spin-lattice coupling in these magnetic superlattices

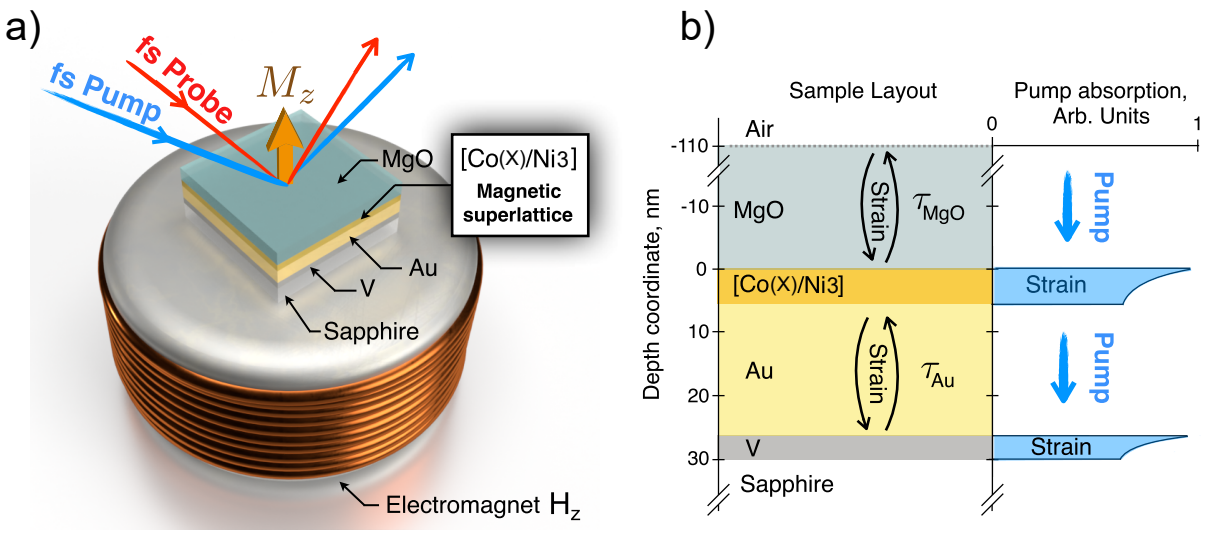

Figure 43: Pump-probe opto-magneto-acoustic experiments. a) The investigated samples are composed of ferromagnetic [Co(X)/Ni(3 ML)] superlattices designed to promote out-of-plane net magnetization M_z, stacked between a Au/V buffer layer and a transparent polycrystalline MgO protective layer. A static out-of-plane external magnetic field B_z is applied to monitor the hysteretic net magnetization of the sample. A femtosecond laser pump pulse optically excites the multilayer sample structure. The sample optical response is measured by a time-delayed femtosecond laser probe pulse through magneto-optical Kerr effect. b) Close view of the multilayer sample structure. We estimate that the acoustic waves are predominantly laser-excited in the buried vanadium layer and in the [Co/Ni] superlattice.

was investigated using a time-resolved magneto-optical pump-probe setup in a front-front geometry for which both pump and probe pulses are focused at normal incidence on the sample surface, as sketched in Figure 43(b), with identical temporal resolution as that previously employed for TDBS.

3.1 Magneto-optical experimental setup

The magneto-optical experimental setup presented in Figure 44 bears strong resemblance to the setup used for the investigations of longitudinal acoustic waves, presented in Figure 7 in Part I. Due to this similarity, we focus here only on the differences, which concern the probe path exclusively. Firstly, the GT prism is used to adjust the optical probe power and to ensure that the transmitted polarization is purely horizontal. We also note that the PBS has been replaced by a 50/50 non-polarizing beam splitter (NPBS), and the QWP has been removed. These changes imply an inherent 50 % loss at the beam splitter transmission and another 50 % loss at reflection of the backscattered beam from the sample. Despite these significant losses, this configuration was chosen to maintain a normal incidence of the probe beam on the sample surface. In this configuration, the use of a PBS/QWP collector is excluded, since it cannot detect polarization rotation. The collected probe beam is then passed through an HWP, which rotates its polarization. The beam is then separated into its S and P components by a Wollaston prism (WP). The HWP is adjusted such that the balanced photodetection yields a zero signal at equilibrium. In the specific case of the magnetic multilayers with a polar magnetization, the HWP is positioned to provide equal Kerr rotation (equal signal intensities) with opposite signs under a saturated magnetic field applied along $+z$ and $-z$. The balanced photodiode equilibrium is always achieved without the pump beam. A final modification to note in the setup is that the sample is fixed directly on an electromagnet, which is used to apply various magnetic fields to the sample.

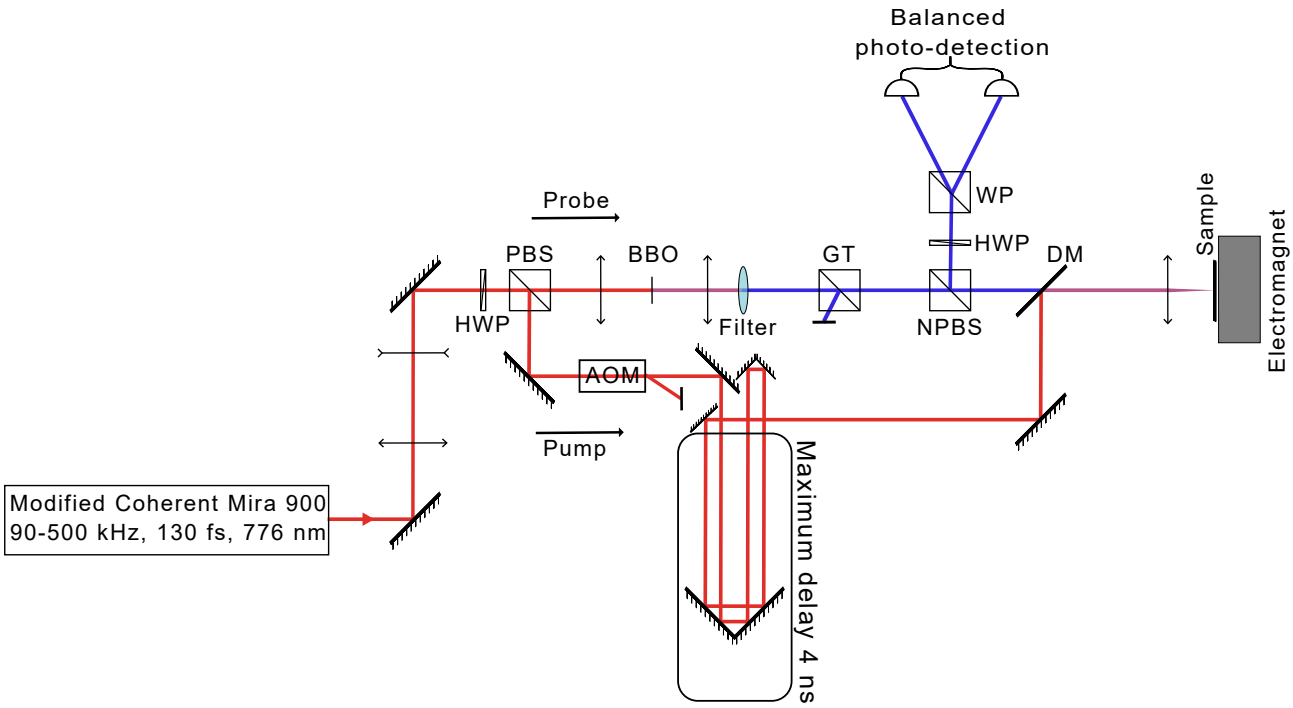

Figure 44: Experimental femtosecond pump-probe setup for time-resolved Kerr rotation measurements. HWP: Half Wave Plate. PBS: Polarizing Beam Splitter. BBO: barium β-borate. GT: Glan-Taylor. NPBS: Non-Polarizing Beam Splitter. AOM: Acousto-Optic Modulator. WP: Wollaston Prism.

3.2 Static investigations

To optically characterize the magnetic superlattices, we begin by determining their static magnetic hysteresis loops. By static, we mean that the samples were not perturbed by the femtosecond optical pump; only the continuous probe beam was used to monitor the magnetization state. A sequence of external magnetic fields was applied to the sample, starting from a minimum value $B_{min} < -B_{sat}$, up to a maximum value $B_{max} > +B_{sat}$, where B_{sat} denotes the saturation field. After reaching B_{max}, the field was decreased back to B_{min} to complete a full magnetic loop. The Kerr rotation is deduced from the signal intensity at each magnetic field step throughout the loop, yielding the magneto-optical hysteresis loop. The results are presented in Figure 45. The optical probe consists of a train of femtosecond pulses, generated by a laser delivering 130 fs pulses at a repetition rate of 95 kHz and a central wavelength of 780 nm. This repetition rate is used as the reference clock for synchronous detection, which is limited to a maximum frequency of 100 kHz.

These results, characterized by the presence of well-defined hysteresis loops, magnetic saturation, finite coercivity, and remanent magnetization in the absence of an external magnetic field, confirm the ferromagnetic nature of the samples. From the experimental data, we extract the saturation fields to be B_{sat}(Co1Ni3) = 42 mT, B_{sat}(Co2Ni3) = 25 mT, and B_{sat}(Co3Ni3) = 65 mT. Another key parameter of magnetic materials that can be extracted from the hysteresis loop is the coercive field, B_c. At this specific magnetic field, the net magnetization of the material vanishes, and the Kerr rotation goes to zero due to the direct proportionality between the magnetization M and the Kerr rotation angle Θ_K. For the Co1Ni3 and Co2Ni3 samples, the coercive field is close to the saturation field due to the abrupt reversal of magnetization. In contrast, the Co3Ni3 sample exhibits an elongated hysteresis loop, indicating a more gradual magnetization reversal. The measured coercive fields are B_c(Co1Ni3) = 41.25 mT, B_c(Co2Ni3) = 19.5 mT, and B_c(Co3Ni3) = 10.5 mT.

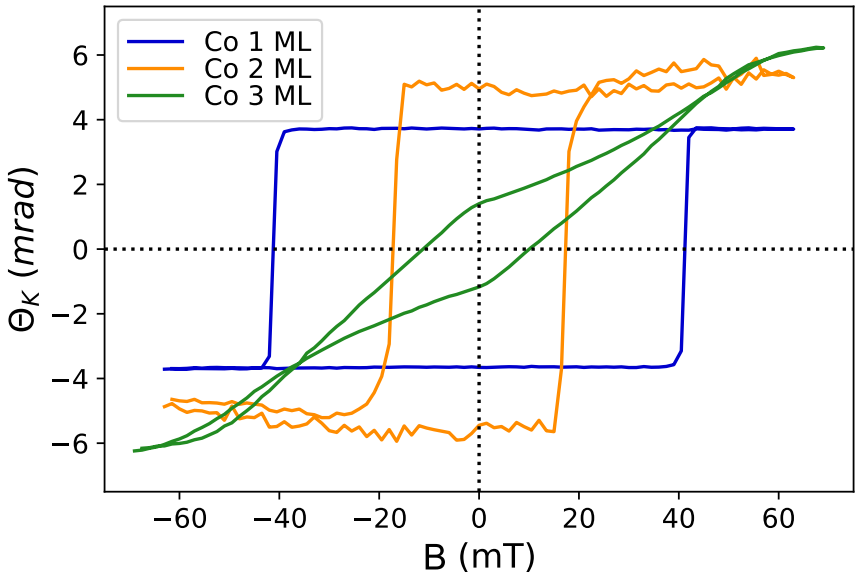

Figure 45: Magneto-optical determination of static hysteresis loops for Co/Ni superlattices with cobalt layer thicknesses of 1, 2, and 3 ML.

These preliminary investigations confirmed the ferromagnetic nature of the superlattices and enabled the determination of key magnetic parameters that will help guide future experiments. In addition, the present results are consistent with those obtained by T. Hauet and co-workers at the Institut Jean Lamour (Nancy), who fabricated these superlattices, thereby validating both the accuracy of our experimental setup and the reliability of our data analysis procedure.

A notable difference between our results and those obtained by C. Pfaff [144], on the Co2Ni3 superlattice is that, in their case, the hysteresis loop exhibits a distinct break near its center, rather than an abrupt magnetization reversal. To investigate why we did not observe such a break, we performed static hysteresis measurements on Co2Ni3 sample while varying the average optical probe power; see Figure46. The optical probe itself is the same as that used in our previous measurements of the three superlattices; only its mean power was varied.

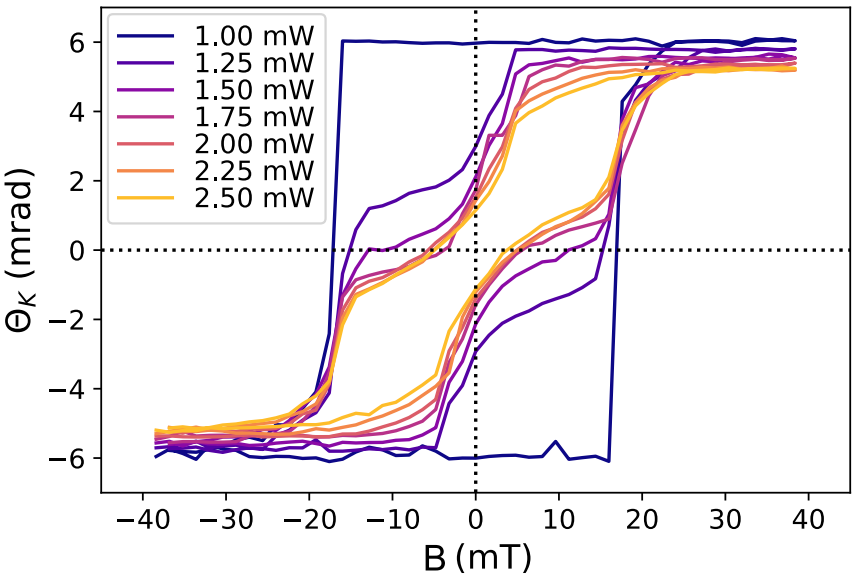

Figure 46: Static hysteresis loops of the Co2Ni3 superlattice measured at different probe beam powers.

This type of hysteresis loop distortion has already been observed in magnetic multilayers and is known as sequential magnetization reversal. According to the literature, this phenomenon can arise from structural deformations [145], or from a reduced interlayer exchange energy, specifically when it drops below one-third of the bulk exchange energy, according to micromagnetic simulations achieved by [146]. Another possible origin is frustrated magnetism, where coexisting magnetic domains reverse at different magnetic fields [147]. In this last study, these domains were observed by X-ray investigations.

In the case of our samples, due to the precision and tight control during the growth process, the presence of pre-existing frustrated magnetic states or large domain heterogeneity is very unlikely. Furthermore, if the two-step reversal were intrinsic to the distinct behavior of cobalt and nickel layers, it would manifest regardless of the optical probe power. The fact that the deformation of the hysteresis loop is reversible when the probe power is reduced back to its initial value strongly suggests that the effect is optically induced. A plausible explanation may involve thermal effects, either by shifting the magnetization equilibrium or by modifying the lattice parameters through thermal expansion.

These investigations, along with theoretical considerations, have highlighted the technical origin of the sequential magnetization reversal and provided possible explanations for its occurrence. However, no further studies have been conducted on this phenomenon within the scope of the present work; it will simply be taken into account in the analysis of future dynamical investigations.

3.3 Dynamical investigations

Now that the static magnetic behavior of the superlattices under investigation has been established, along with their stability under optical probe intensity, we proceed to the investigation of their magnetization dynamics in response to femtosecond optical perturbations on the picosecond timescale.

To carry out these dynamic measurements, the laser repetition rate is set back to 250 kHz. The optical probe has a wavelength of 780 nm, while the pump is set to 380 nm. The AOM provides a 50/50 modulation of the pump beam at 30 kHz. The first superlattice investigated is Co1Ni3. The detection principle is the same as previously described for the static regime; however, in this case, the optical pump perturbs the magnetization, inducing a small variation in the Kerr rotation.

Measurements taken under various magnetic fields are shown in Figure 47(a). We observe a fast partial demagnetization occurring at time zero, induced by the ultrafast optical excitation, as theoretically described earlier. This is followed by a slow return to the initial equilibrium state. Notably, all measured signals are nearly superimposed either on the signals obtained at B_{max} or B_{min}, suggesting that a net magnetization reversal will appear in the dynamic hysteresis loop. Figure 47(b) shows only the acquisitions at B_{max} and B_{min}, providing a clearer view of the signal quality and shape described above. The dynamic hysteresis loop is obtained by plotting the Kerr rotation as a function of the applied magnetic field for a fixed time delay. Figure 47(c) shows the loop evaluated at the peak of the signals (t = 1.7 ps), where the Kerr rotation reaches its maximum. The saturation field extracted from this loop is consistent with the one previously determined in the static regime, confirming that the pump does not significantly perturb the magnetization state of the sample. Figure 47(d) shows the magnetic and non-magnetic contributions to the measured signal. These two components are calculated using:

$$S_{\text{mag}}(t) = \frac{S(t,+B) - S(t,-B)}{2}, \tag{183}$$

$$S_{\text{non-mag}}(t) = \frac{S(t,+B) + S(t,-B)}{2}. \tag{184}$$

We note that the magnetic component closely matches the overall signal, indicating that the response is nearly purely magnetic. A small non-magnetic contribution is visible, particularly at time zero,

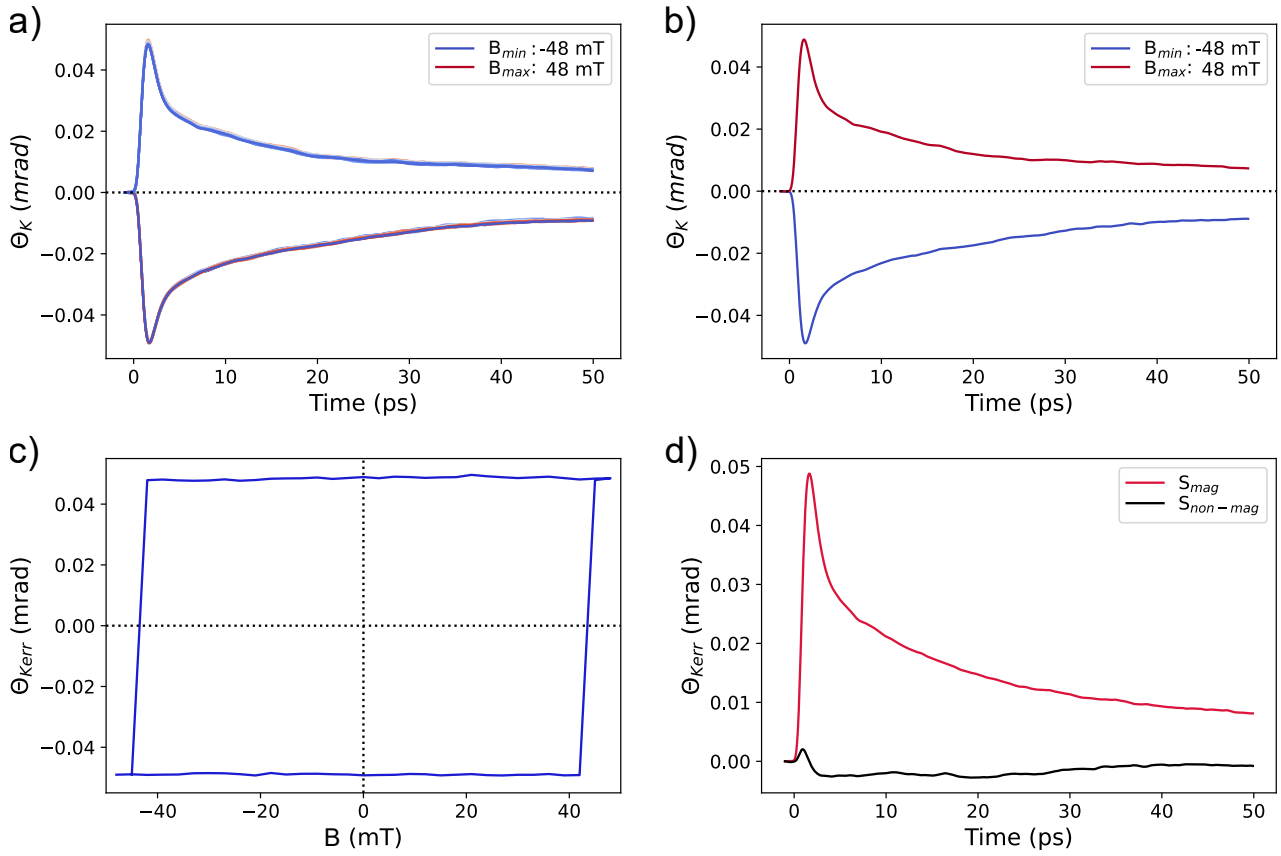

Figure 47: Time-resolved magneto-optic investigations of the Co1Ni3 superlattice. a) Kerr rotation signals acquired at various magnetic field strengths. b) Selected signals at B_{max} and B_{min}, extracted from subfigure a. c) Dynamic magnetic hysteresis loop at t = 1.7 ps, corresponding to the maximum Kerr rotation. d) Separation of the magnetic and non-magnetic contributions to the signal.

along with a slowly decaying background that resembles a thermal response induced by the optical pump. Another important aspect of these results lies in the fact that our measurements do not feature GHz magnetic precession. This is in agreement with the fact that the applied magnetic field H_z, the net magnetization M_z, as well as the ultrafast acoustic stress are all collinear, and there is no magnetic torque that could trigger magnetic precession. So far, only GHz precession triggered from magneto-elastic coupling has been observed [148–153]. Our measurements highlight a non-thermal ultrafast change of magnitude of the magnetization, without triggering rather slow precession.

The same set of measurements was carried out on the two other superlattices, Co2Ni3 and Co3Ni3. The corresponding results are shown in Figure 48 and Figure 49, respectively.

The secondary peaks are temporally fixed and appear independently of the applied magnetic field. In Figure 48(b), they are labeled "compressive" and "tensile", as they originate from the propagation of longitudinal acoustic waves in the superlattice. These acoustic waves are generated by the absorption of the femtosecond pump pulse by the vanadium at the vanadium/gold interface. The first secondary peak, observed at 7.8 ps, corresponds to the time-of-flight of an acoustic wave through the 20 nm gold layer. The second secondary peak results from the reflection of the acoustic wave at the MgO/air interface, which inverts the strain polarity, hence the "tensile" label. We emphasize here that no acoustic wave is expected to originate from optical absorption in the gold layer itself, due to the weak electron-phonon coupling in gold, which prevents acoustic generation on the timescale investigated. To support this exclusion of gold as a generation site, we refer to Table [1] of Part I.

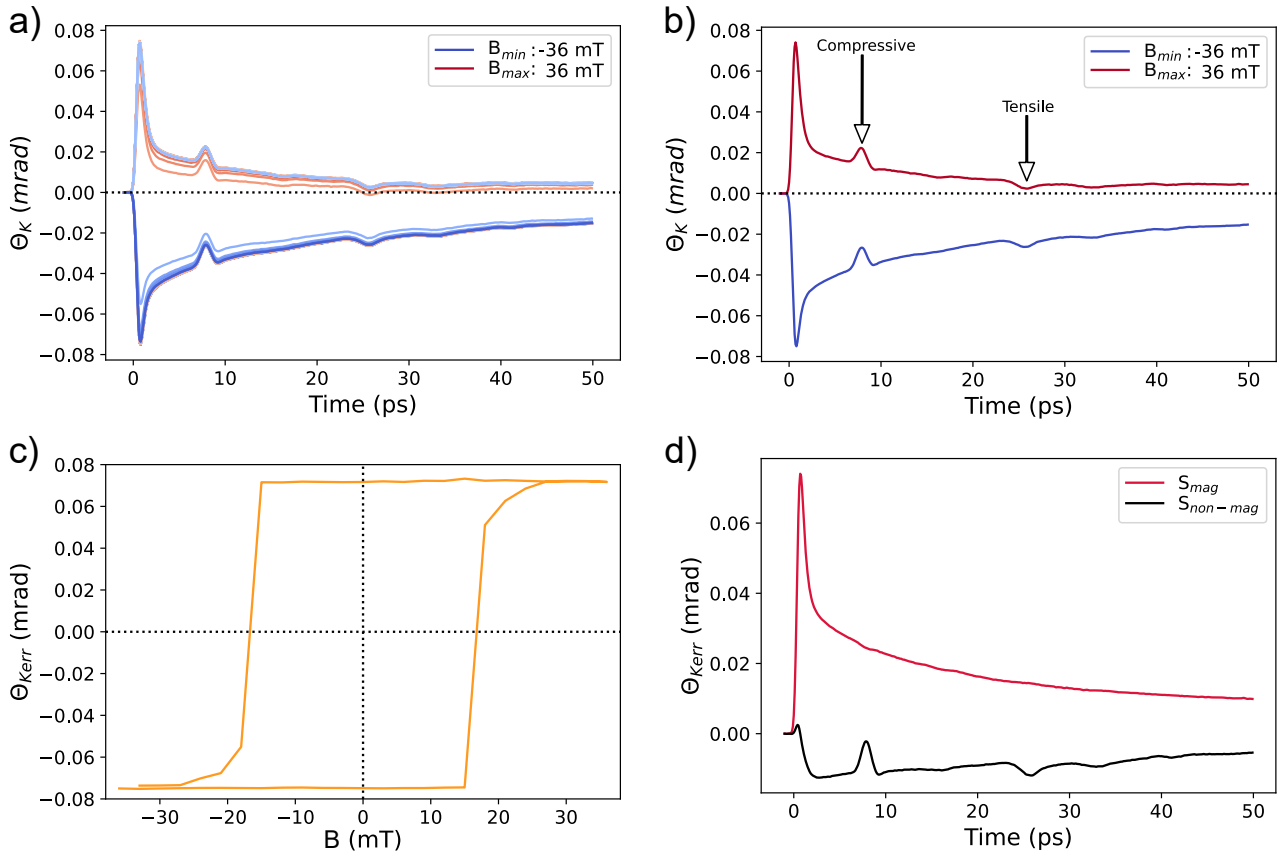

Figure 48: Time-resolved magneto-optic investigations of the Co2Ni3 superlattice. a) Kerr rotation signals acquired at various magnetic field strengths. b) Selected signals at B_{max} and B_{min}, extracted from subfigure a. c) Dynamic magnetic hysteresis loop at t = 1.7 ps, corresponding to the maximum Kerr rotation. d) Separation of the magnetic and non-magnetic contributions to the signal.

The separation of magnetic and non-magnetic signal components is shown in Figure 48(d). The magnetic contribution exhibits the same characteristic behavior as observed for the Co1Ni3 superlattice and matches well with theoretical expectation for a femtosecond excitation in a material with purely polar magnetization under this optical configuration. In contrast, the non-magnetic contribution in Co2Ni3 is significantly stronger than in Co1Ni3. This component entirely accounts for the observed secondary peaks, indicating a purely acoustic origin at first glance. However, the situation is more complex if we take into account the possibility of piezomagnetism in such a superlattice sample with surface symmetry breaking that is predicted to obey the rules for piezomagnetism. The observation that the secondary peaks evolve differently under opposite applied magnetic fields indicates that the magnetoelastic effect observed in our experiments is not related to conventional magnetostriction. If magnetostriction were responsible, the secondary peaks would follow the sign of the external magnetic field and reverse accordingly. Therefore, any magnetoelastic mechanism dependent on the magnetization vector can be ruled out. These observations point toward a piezomagnetic contribution as a plausible explanation. However, its unambiguous identification remains challenging, as the corresponding signal can easily be misinterpreted as an artifact or as a spurious acoustic contribution. So far, we haven't succeeded in proving the piezomagnetic response of the magneto-elastic interaction. To confirm this interpretation, it would likely be necessary to perform additional experiments based on X-ray magnetic dichroism, which could directly probe the magnetic symmetry changes associated with the piezomagnetic response.

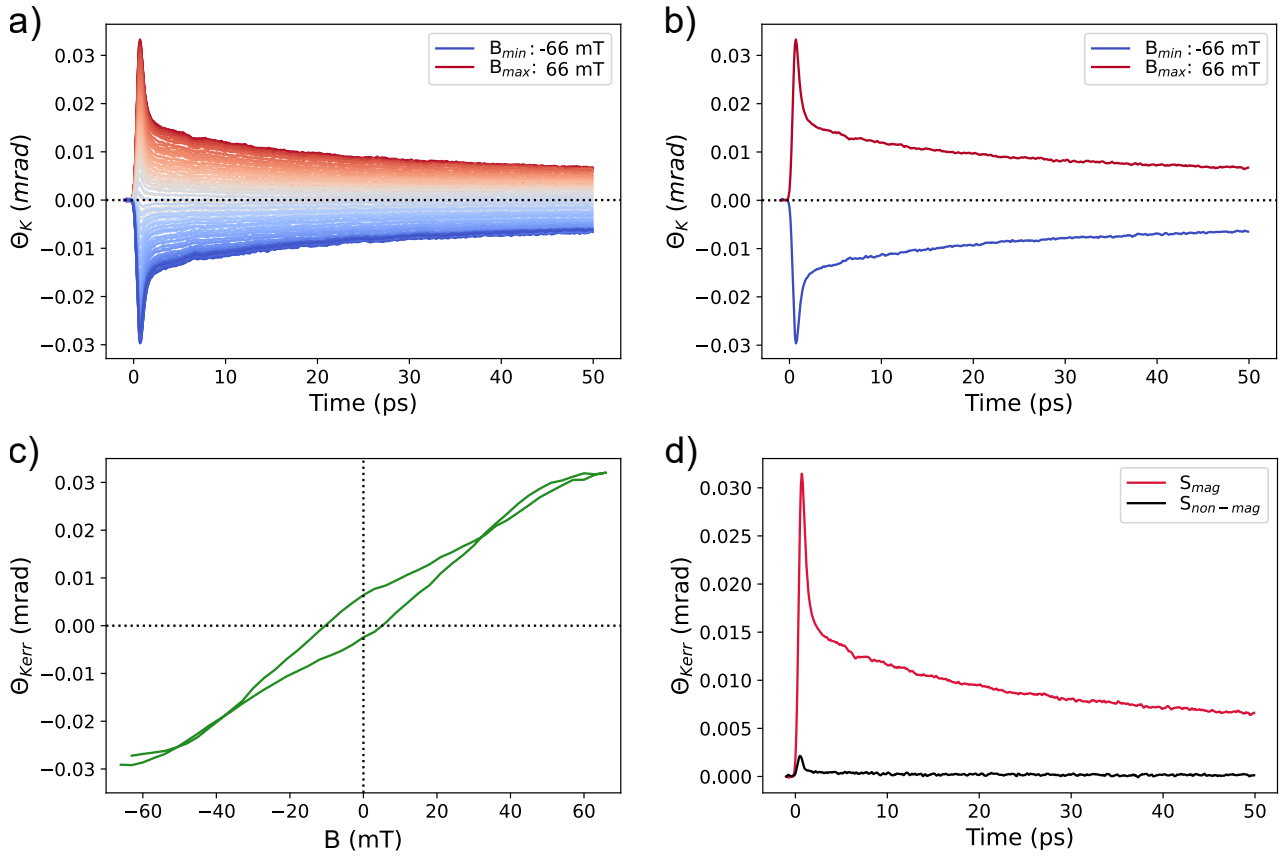

Figure 49: Time-resolved magneto-optic investigations of the Co3Ni3 superlattice. a) Kerr rotation signals acquired at various magnetic field strengths. b) Selected signals at B_{max} and B_{min}, extracted from subfigure a. c) Dynamic magnetic hysteresis loop at t = 1.7 ps, corresponding to the maximum Kerr rotation. d) Separation of the magnetic and non-magnetic contributions to the signal.

The dynamical investigation of the third superlattice, Co3Ni3, also reveals a strong similarity between the dynamical and the static hysteresis loop, both in the slow magnetization reversal and in the magnetic saturation field. These similarities are clearly visible in Figure 49(a) and 49(c). The isolated signals at maximum and minimum magnetic fields, shown in Figure 49(b), emphasize the absence of any secondary peak during the relaxation. This absence of non-magnetic contribution is further confirmed by the component separation displayed in Figure 49(d).

Given that all three superlattices share the same general structure and were specifically designed to study ultrafast acoustic perturbations of magnetization, with the only difference lying in the magnetic stack, which tunes the strength of interfacial anisotropy and spontaneous magnetization, the appearance of a non-magnetic component exclusively in Co2Ni3 raises important questions. We have already ruled out the gold layer as a potential generation site for longitudinal acoustic waves due to its weak electron-phonon coupling. Similarly, we exclude the sapphire substrate as a source, since its large optical bandgap (∼8.7 eV), nearly independent of crystallographic orientation [154, 155], lies far beyond the photon energies accessible in our setup, even when considering two-photon absorption. The layer of particular interest for acoustic wave generation is the vanadium, which is the only layer not grown along the (111) direction, but rather along (110). Vanadium is a transition metal with a body-centered-cubic (bcc) structure. For this class of materials, the dependency of intraband transitions with respect to crystallographic orientation has been well documented [156]. Although transition metals are often approximated as optically isotropic, we have performed comple-

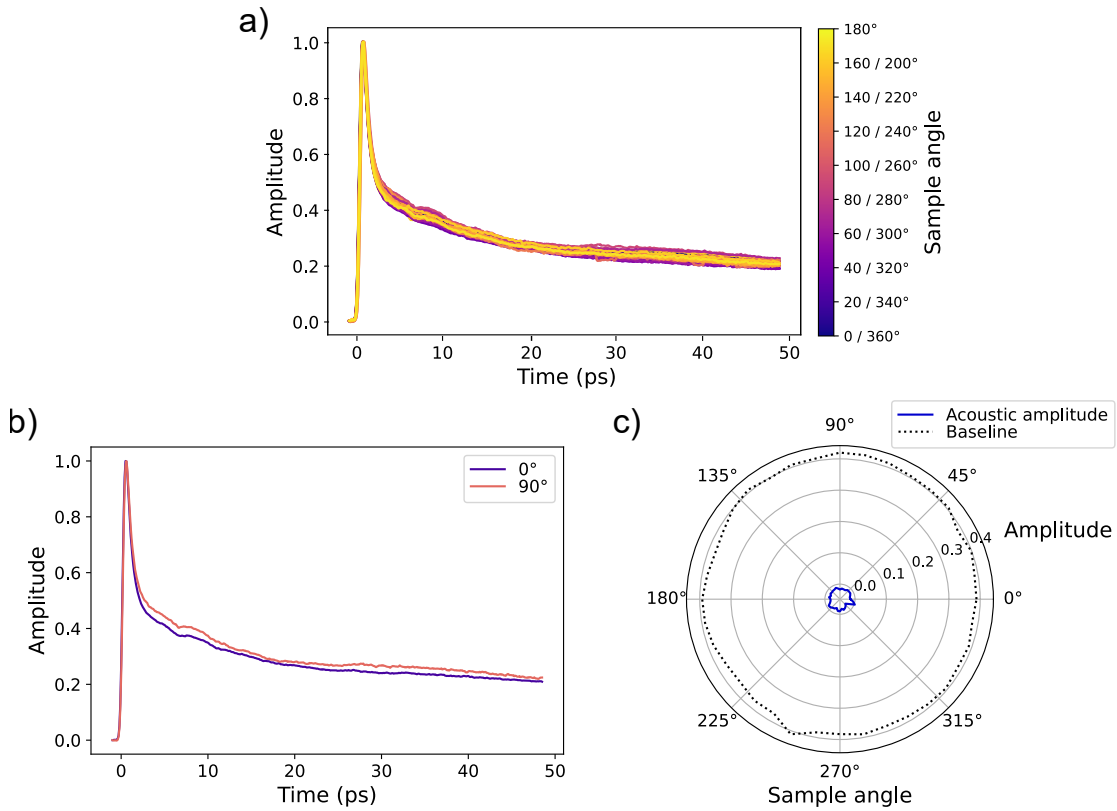

Figure 50: Rotation-dependent investigations on the Co1Ni3 sample at magnetic saturation. a) Time-resolved magnetic response to femtosecond laser excitation at various sample rotation angles. b) Signals extracted at 0° and 90°. c) Polar plot of the acoustic peak relative amplitude and the baseline as a function of the sample rotation angle.

mentary polarization-dependent dynamical measurements on the superlattices to probe the possibility of anisotropic magneto-acousto-optic detection from the birefringent vanadium layer.

To achieve these polarization-dependent measurements, the electromagnet holding the sample is mounted on a rotation stage. For each measurement, both the laser focusing on the sample and the equilibrium balancement are carefully checked. The photodiode voltage V is recorded each time to account for slow drifts in laser intensity and potential changes in the sample's equilibrium reflectivity caused by rotation, even though the laser spot is positioned as close as possible to the sample's rotation axis.

The first rotation-dependent investigations were carried out on the Co1Ni3 sample, with an external magnetic field exceeding the saturation field to maintain the magnetization along the out-of-plane direction. The results are presented in Figure 50. Figure 50(a) shows the time evolution of the magnetization state under optical perturbation. The acquisitions are normalized to their respective peak Kerr rotation values in order to suppress variations in absolute signal amplitude arising from changes in alignment, reflectivity, or laser power, thereby isolating genuine changes in the signals. The signals display the same behavior as previously described: a fast partial demagnetization followed by a slow return to equilibrium. We note a small perturbation around 8 ps after the pump excitation, which could correspond to an acoustic wave propagating in the magnetic multilayers. In Figure 50(b), only the acquisitions at 0° and 90° are plotted. The perturbation at 8 ps is visible, though not as pronounced as that observed for Co2Ni3 in Figure 48. To examine a potential angular dependence of this feature, we extract the amplitude of the secondary peak by computing the difference between its value at 8 ps and the theoretical baseline of the relaxation at the same time had the peak been

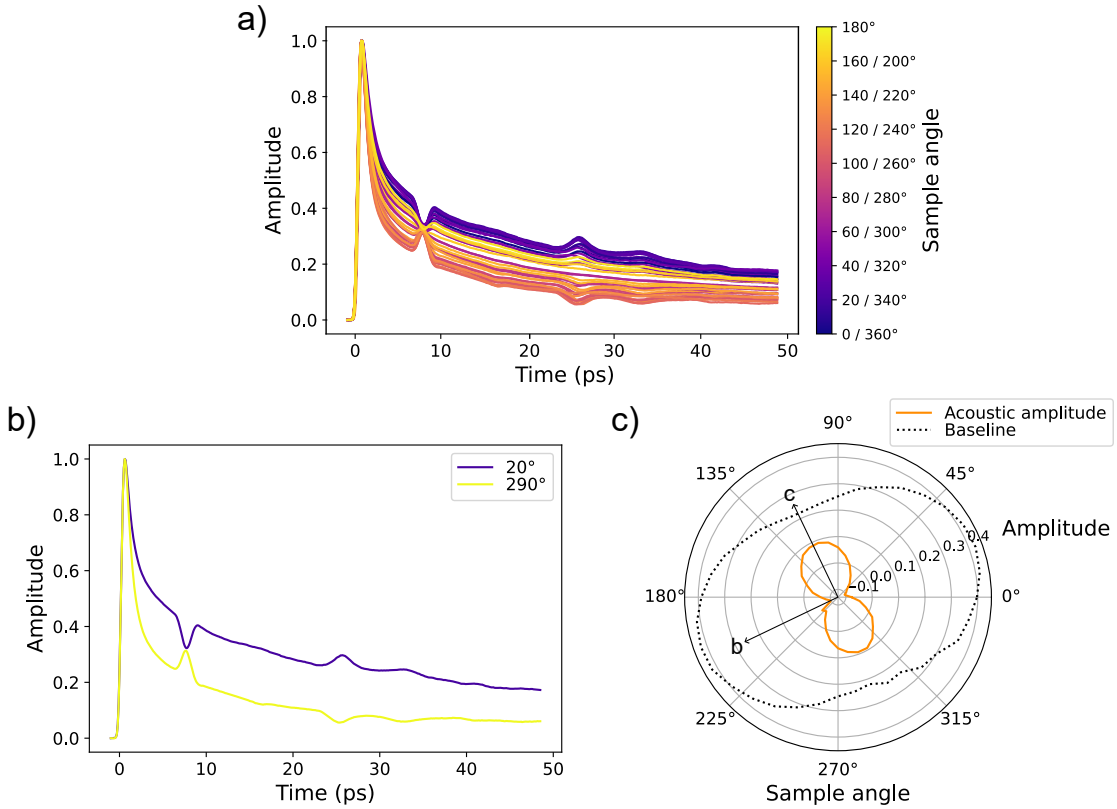

Figure 51: Rotation-dependent investigations on the Co2Ni3 sample at magnetic saturation. a) Time-resolved magnetic response to femtosecond laser excitation at various sample rotation angles. b) Signals extracted at 20° and 290°. c) Polar plot of the acoustic peak relative amplitude and the baseline as a function of the sample rotation angle with crystallographic directions of the sapphire substrate.

absent. The baseline is estimated by linearly extrapolating the relaxation from -0.5 ps to +0.5 ps to the secondary peak. The relative amplitudes of the secondary peaks, referred to as the "acoustic amplitude", are presented in the polar plot in Figure 50(c), along with the corresponding baseline values. We find that the secondary peak amplitude is close to zero and that the baseline remains essentially invariant.

Further investigations were carried out on the Co2Ni3 sample, which had already exhibited strong secondary peaks. The measurement procedure was identical to that used for the Co1Ni3 sample. The results are displayed in Figure 51. In Figure 51(a), the time-resolved magnetic signals following the femtosecond optical excitation are presented. As in Figure 48, pronounced secondary peaks are clearly visible. In addition, these peaks appear to depend on the sample rotation angle, both in sign and in amplitude. To illustrate this angular dependence, Figure 51(b) shows the signals obtained at 20° and 290°, corresponding to the minimum and maximum amplitudes of the acoustic peak, respectively. This variation exhibits both a sign reversal and an amplitude change over a 90° rotation, with a continuous evolution between these extrema. The polar plot in Figure 51(c) highlights the clear angular dependence of amplitude and sign of the acoustic peak. It is also apparent that the acoustic amplitude varies inversely with the baseline through the sample rotation. On the polar plot, two axes, b and c, were added. They correspond to the crystallographic directions of the sapphire substrate. Notably, these directions coincide with the angles where the acoustic peak amplitude reaches its extrema.

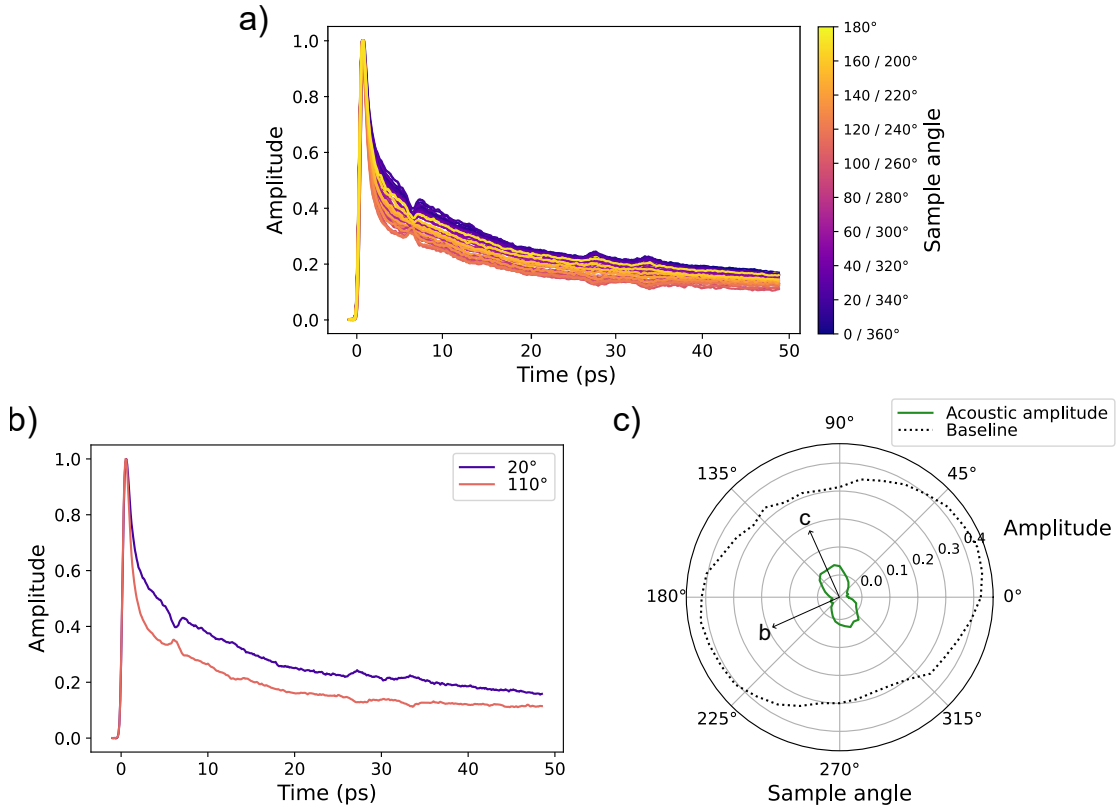

Figure 52: Rotation-dependent investigations on the Co3Ni3 sample at magnetic saturation. a) Time-resolved magnetic response to femtosecond laser excitation at various sample rotation angles. b) Signals extracted at 20° and 290°. c) Polar plot of the acoustic peak relative amplitude and the baseline as a function of the sample rotation angle with crystallographic directions of the sapphire substrate.

The measurements on the Co3Ni3 sample are presented in Figure 52. In Figure 52(a), the signals exhibit a similar behavior to those of Co2Ni3 in Figure 51(a), but with a weaker secondary peak amplitude. The occurrence of these secondary peaks is consistent with measurements reported by other groups, and the observed angular dependence explains their absence in the previous measurements presented in Figure 49. Figure 52(b) shows the signals extracted at 20° and 110°, corresponding to the minimal and maximal amplitudes of the acoustic peak, respectively. The angular dependence of both the secondary peak and the relaxation baseline is clearly visible in the polar plot of Figure 52(c). In this plot, the crystallographic directions of the sapphire substrate, determined from X-ray diffraction, have also been added.

The strong dependence of the acoustic peak on sample orientation observed in Co2Ni3 and Co3Ni3 can be attributed to the anisotropy of vanadium, as evidenced by the correlation between the substrate crystallographic orientations and the extrema of the acoustic peaks. Given the similarity of the non-magnetic parts of the three samples, the difference in secondary peak amplitude, and its near absence in Co1Ni3, suggest that this amplitude is strongly influenced by the magnetic behavior of the samples.

To investigate the influence of the magnetic behavior on the magnetoelastic peak, we exploit the known dependence of the effective magnetic anisotropy K_{eff} of Co/Ni multilayers on cobalt layer thickness. The effective magnetic anisotropy of our samples is determined using the data and adapted formula of [157], where the magnetic anisotropy of Co/Ni stacks was measured by SQUID magnetometry at 300 K.

$$K_{eff} \cdot D = \sum (K_{int} + K_V \cdot t_{layer} + K_{shape} \cdot t_{layer}) \tag{185}$$

In Equation (185), D is the total thickness of the magnetic stack, while K_{int}, K_V, and K_{shape} are the interfacial, volumetric, and shape contributions to the magnetic anisotropy, respectively. The t_{layer} coefficients correspond to the thicknesses of each individual layer. In our samples, the total thickness of the magnetic stack can be expressed as a function of the thickness of cobalt and nickel layers.

$$D = 6 \cdot t_{Ni} + 5 \cdot t_{Co} = 6 \cdot X_{Ni} \cdot e_{Ni} + 5 \cdot X_{Co} \cdot e_{Co} \tag{186}$$

In Equation (186), X_{Ni} and X_{Co} are the number of Ni and Co MLs, respectively. The monolayer thicknesses are $e_{Ni} = 0.203$ nm and $e_{Co} = 0.208$ nm. The computed values of D for our three samples are $D_1 = 4.694$ nm, $D_2 = 5.734$ nm, and $D_3 = 6.774$ nm.

The interfacial contributions to the effective magnetic anisotropy arise from the Co/Ni interfaces as well as from the Au/Ni and Ni/MgO edge interfaces, leading to:

$$K_{int} = 10 \cdot X_{Co} \cdot K_s^{Co/Ni} + K_s^{Au/Ni} + K_s^{Ni/MgO}. \tag{187}$$

This expression needs to be adjusted depending on the number of cobalt MLs. For $X_{Co} \leq 1$, the X_{Co} factor must be taken into account, reflecting the possibility of an incomplete cobalt layer (fractional ML values correspond to partial coverage). For $X_{Co} > 1$, the Co/Ni interface contribution becomes independent of the cobalt thickness, and X_{Co} should be set to 1. Based on this consideration, K_{int} is constant for our three samples. We assume $K_s^{Co/Ni} = 0.443$ mJ $\cdot$ m^{-2} [158]. However, reliable data for $K_s^{Au/Ni}$ and $K_s^{Ni/MgO}$ are lacking; therefore, we estimate their contribution as $K_s^{Au/Ni} + K_s^{Ni/MgO} = 0.63$ mJ $\cdot$ m^{-2} to match the experimentally determined $K_{eff} = 0.35$ MJ $\cdot$ m^{-3} so that the calculated K_{eff} matches the experimental value of 0.35 MJ $\cdot$ m^{-3} for the Co2Ni3 sample [144]. Since these two edge interfaces are identical across all investigated samples, their interfacial contributions remain unchanged. With this assumption, we obtain $K_{int} = 5.06$ mJ $\cdot$ m^{-2}.

The shape contribution to the anisotropy is defined as:

$$K_{shape} \cdot t_{layer} = -5 \cdot t_{Co} \cdot \frac{1}{2}\mu_0 M_{Co}^2 - 6 \cdot t_{Ni} \cdot \frac{1}{2}\mu_0 M_{Ni}^2, \tag{188}$$

where $M_{Co} = 1400$ kA/m and $M_{Ni} = 485$ kA/m are the saturation magnetizations of cobalt and nickel, respectively. As for K_{int}, two cases must be distinguished for the volumetric contribution. If $X_{Co} \leq 1$, the Co contribution is included in the interfacial anisotropy. Ni layers contribute via their magnetocrystalline anisotropy constant K_V^{Ni}. Since Ni atoms at interfaces contribute only half compared to bulk-line atoms, the total Ni contribution is $6 \cdot K_V^{Ni}(t_{Ni} - e_{Ni})$. For $X_{Co} > 1$, the magnetocrystalline contribution of Co must also be included, yielding $6 \cdot K_V^{Ni}(t_{Ni} - e_{Ni}) + 5 \cdot K_V^{Co}(t_{Co} - e_{Co})$. The case $X_{Co} = 1$ reduces to this last expression with $t_{Co} - e_{Co} = 0$. Combination of these considerations gives:

$$\begin{aligned} K_{eff} D \;=\; & 10 K_s^{Co/Ni} + K_s^{Au/Ni} + K_s^{Ni/MgO} \\ & + 6\left(K_V^{Ni}(t_{Ni} - e_{Ni}) - \frac{\mu_0}{2} t_{Ni} M_{Ni}^2\right) + 5\left((t_{Co} - e_{Co}) K_V^{Co} - \frac{\mu_0}{2} t_{Co} M_{Co}^2\right) \end{aligned} \tag{189}$$

To compute K_{eff} for our samples, we compute each contribution separately, and we report the results in Table [7]. The interfacial contributions are the same for all samples and yield $K_{int} = 5.06$ mJ $\cdot$ m^{-2}. The magnetocrystalline volume anisotropy constants used are $K_V^{Co} = +6.0 \cdot 10^4$ J $\cdot$ m^{-3} and $K_V^{Ni} = -4.5 \cdot 10^3$ J $\cdot$ m^{-3}.

These values reproduce the expected decrease of K_{eff} with increasing Co thickness. They also confirm the strong anisotropy of Co1Ni3, consistent with previous studies showing that only two Co/Ni bilayers are sufficient to exhibit perpendicular magnetization [142]. The critical Co thickness for reorientation is found to be around 3.5 ML.

Sample	D (nm)	$K_V \cdot t_{layer}$ (mJ · m^{-2})	$K_{shape} \cdot t_{layer}$ (mJ · m^{-2})	K_{eff} (MJ · m^{-3})
Co1Ni3	4.694	-0.011	-1.802	0.69
Co2Ni3	5.734	0.051	-3.065	0.35
Co3Ni3	6.774	0.114	-4.327	0.12
Co3.5Ni3	7.294	0.145	-4.958	0.02
Co4Ni3	7.814	0.176	-5.589	-0.05

Table 7: Effective magnetic anisotropy and its interfacial, volumetric, and shape contributions for the investigated Co/Ni superlattices.

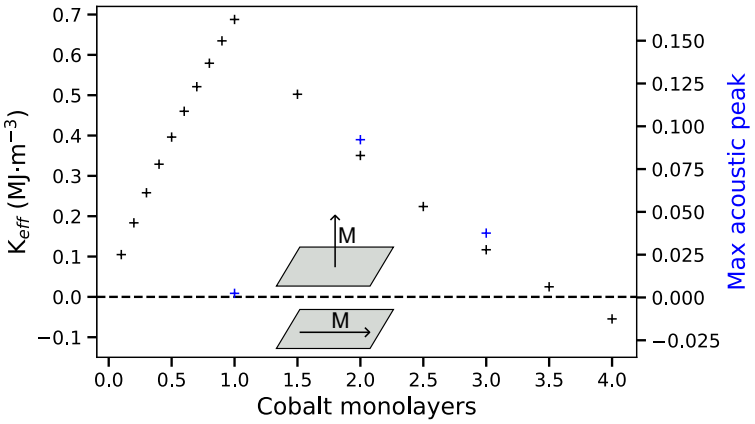

Figure 53: Computed effective magnetic anisotropy K_{eff} (black markers) and maximum magnetoelastic peak amplitude (blue markers) as a function of the number of cobalt monolayers X_{Co}.

Now that the K_{eff} has been established and the maximum acoustic peak amplitudes extracted from the rotation-dependent investigations, we compare these two quantities as a function of the number of cobalt monolayers in the Co/Ni multilayers; see Figure 53. A decrease of K_{eff} is expected to allow a larger rotation of the magnetic moment due to the weaker restoring torque of the transverse magnetic equilibrium. This intuitive picture seems to be supported by Co1Ni3 but is contradicted by Co2Ni3 and Co3Ni3. In fact, we observe that for Co2Ni3 and Co3Ni3 the acoustic peak amplitude decreases with decreasing K_{eff}, in agreement with earlier results obtained with optical pumping through the sapphire substrate and extended to Co3.5Ni3, but not reported for Co1Ni3 [144]. The puzzling case remains Co1Ni3, where no clear acoustic peak is detected. Static and dynamic investigations do not indicate any structural defect in the magnetic stack, and the femtosecond laser excitation produces the same magnetization response (apart from the absence of acoustic generation) in all samples. Furthermore, calculations of K_{eff} for $X_{Co} \leq 1$ rule out partial completion of the Co layers as a possible explanation for the weak acoustic peaks. This strongly suggests that the weakness of the acoustic peaks in Co1Ni3 originates from its generation site. The angular independence of the signal points to the possibility that the vanadium transducer layer behaves as if replaced by a centrosymmetric transducer. Because acoustic generation is impossible in sapphire and too weak in gold within our configuration, the absence of a transducer is unlikely. Therefore, further investigations are required to clarify the Co1Ni3 case. Experiments with stronger pumping could highlight a possible generation threshold, while DFT calculations may help circumscribe the expected response.

Turning back to the Co2Ni3 and Co3Ni3 results, if a reduction of the anisotropy due to the laser pulse or to the laser-induced strain pulse were the dominant mechanism, it should trigger the magnetic moment precession at the GHz frequency [148, 151, 159]. In the investigated superlattices, such a precession is only observed when the magnetization equilibrium position, set by the effective field

H_{eff}, and the laser incidence are not collinear, as demonstrated in the theoretical part dedicated to the magnetic precession [160]. Moreover, when present, laser-induced magnetic precession exhibits a frequency of one-tenth of GHz and lasts far longer than the 50 ps time window used here to investigate magnetoelastic coupling. We therefore conclude that the observed magnetoelastic peaks in Co2Ni3 and Co3Ni3 originate from a direct modification of the magnetic moment induced by compression, consistent with previous diamond anvil cell experiments showing a quasistatic reduction of the magnetic moment under pressure [139, 161–163], and consistent with MD simulations performed in our recent paper on this topic [144].

3.4 Outlook: Spin-lattice interactions at picosecond timescale

In this section, we have demonstrated the ability of our optical setup to resolve the magnetic behavior of complex epitaxial heterostructures, both at equilibrium under a static magnetic field and under femtosecond optical excitation. The sapphire/V/Au/Ni[Co/Ni]5/MgO superlattices were chosen for their well-known tunability of magnetic anisotropy through the cobalt layer thickness. Taking advantage of this controllable anisotropy, we studied the spin-lattice coupling by propagating strain waves through the magnetic stack. Our investigations reveal the possibility to control (increase or decrease) the magnetic moment of a ferromagnetic superlattice on a picosecond timescale using transient unipolar strain.

Owing to the fact that ultrafast strain acoustic waves can be laser-excited non-destructively with amplitudes reaching 1% and corresponding pressures of a couple of GPas in a similar sample geometry [164, 165], these nonlinear strain waves, combined with the demonstrated acoustic control on the magnetization state of the cobalt nickel superlattices, could most probably drive volatile or nonvolatile magnetization reversal. These results surely open many significant new experimental opportunities for magnetization manipulation that are not based on direct light interaction with the magnetic sample.

In the following, we investigate the possibility to launch giant surface acoustic waves and monitoring the magnetic perturbation induced to the sample.

4 Giant surface acoustic waves for the manipulation of magnetization

After having demonstrated the complex acousto-magneto-optical interactions in magnetic superlattices, we now continue investigating spin-lattice coupling with stronger deformations. Here the purpose is to optically generate focused surface acoustic waves that are known to locally induce giant strains in the percent range [47]. As previously mentioned in the section dedicated to spin-lattice coupling in superlattices, the degree of control over the magnetic moment is limited by the magnitude of the strain. This is why the use of giant surface acoustic waves is particularly attractive.

To investigate the influence of such acoustic waves on magnetic behavior, modifications of our experimental setup were implemented, and theoretical considerations are presented below.

4.1 Theory of giant surface acoustic wave generation and propagation

Before introducing the experimental setup, we develop some theoretical considerations about the optical induction of giant surface displacements. In practice, the generation of strong SAWs can be achieved by constructive interference of multiple sources [47]. Various techniques have been employed, such as phase velocity scanning of laser interference fringes, moving laser sources, or even interdigital

annular transducers [166–168]. In our case, we chose to use a ring-shaped pump and observe the surface displacement at the center, where the SAWs generated by the laser ring interfere constructively.

Experimentally, we model the excitation ring as a radial Gaussian distribution, where the section width σ of the ring corresponds to the FWHM of the Gaussian. This leads to the deposited energy distribution $\mathcal{Q}$ given by:

$$\mathcal{Q}(r,z,t) = \mathcal{Q}_0 \exp\left[-\frac{(r-R_0)^2}{2\sigma^2}\right] \Pi(r; r_{in}, r_{out}) e^{-z/l_p} g(t), \tag{190}$$

where r_{in} and r_{out} are the internal and external radii of the ring, respectively. σ is the FWHM of the Gaussian energy distribution, R_0 is the mean value of r_{in} and r_{out}, Π is the radial top-hat window, and $g(t)$ is the temporal profile of the laser pulse. The temperature rise ΔT is linked to the deposited optical energy according to:

$$\Delta T(r,z,t) = \frac{\mathcal{Q}(r,z,t)}{\rho\, C_p}, \tag{191}$$

where ρ is the mass density, and C_p is the specific heat. This temperature induces a thermoelastic stress $\sigma^{(th)}$ given by:

$$\sigma^{(th)}(r,z,t) \simeq 3K\alpha \Delta T(r,z,t), \tag{192}$$

with K the bulk modulus and α the thermal expansion coefficient. Both the temperature rise and the resulting thermal stress are assumed to be isotropic.

An important consideration for the next part of the theoretical description is the nature of the material where the SAWs are generated. In our experiment, we use niobium-doped $SrTiO_3$ (STO:Nb) as a transducer to generate the SAWs. This choice is particularly relevant because pure STO, exhibiting a band gap around 3.2 eV, is transparent in the visible-IR range. However, its absorption can be tuned by controlled niobium doping, which drives STO from a strong dielectric insulator to an n-type conductor [169, 170]. With appropriate doping, STO exhibits optical absorption at 1064 nm, such that the optical penetration depth l_p becomes small compared to the acoustic wavelength, $l_p \ll \lambda_{ac}$. Under this condition, the source of the elastic waves is confined close to the surface, allowing efficient generation of surface modes while minimizing the excitation of bulk modes (longitudinal and transverse) [38]. It is then convenient to remove the z-dependence by integration over depth and to introduce the depth-integrated thermoelastic stress (also referred to as a stress resultant or effective surface traction acting as a boundary condition for SAW generation):

$$\Sigma(r,t) = \int_0^\infty \sigma^{(th)}(r,z,t)dz \simeq 3K\alpha \frac{\mathcal{Q}_0\, l_p}{\rho\, C_p} \exp\left[-\frac{(r-R_0)^2}{2\sigma^2}\right] \Pi(r; r_{in}, r_{out}) g(t). \tag{193}$$

The zero-order Hankel transform of this effective surface stress is then written as:

$$\tilde{\Sigma}(k,\omega) = 2\pi \int_0^\infty r\, \Sigma(r,\omega)\, J_0(kr)\, dr = \tilde{g}(\omega)\, \tilde{\Sigma}_0(k) \tag{194}$$

where J_0 is the zero-order Bessel function [171]. In Equation (194), $\tilde{g}(\omega)$ is the Fourier transform of the temporal profile of the pulse $g(t)$, and $\tilde{\Sigma}_0(k)$ is the radial excitation profile. In our case, the FWHM of the Gaussian distribution is in the order of a few microns, while the ring radius is on the order of 50 µm. For such a thin Gaussian ring, $\sigma \ll R_0$, the truncation due to the top-hat window can be neglected in the Hankel transform, yielding:

$$\tilde{\Sigma}_0(k) \approx 2\pi \Sigma_{pk} R_0 \exp\left[-\frac{(k\sigma)^2}{2}\right] J_0(kR_0), \tag{195}$$

where Σ_{pk} is the peak amplitude. Two main factors govern the spectral content: first, the finite radial width σ of the ring excitation defines a SAW spectrum, acting as a low-pass filter with a cutoff

$k \sim 1/\sigma$. Second, the Bessel term reflects the cylindrical symmetry of the excitation and governs the spatial interference and focusing of these SAW components during their propagation toward the ring center. The surface displacement can then be expressed using the Rayleigh-wave Green's function G_R, as:

$$u_z(r,t) = \int_0^\infty k\, dk\, \tilde{\Sigma}_0(k)\, G_R(k,\omega)\, J_0(kr)\Big|_{\omega=v_{SAW}k} *_t\, g(t), \tag{196}$$

where v_{SAW} is the SAW velocity and $*_t$ denotes convolution over time. The temporal structure of the surface displacement observed at the ring center results from the coherent superposition of broadband SAWs generated along the ring and propagating over a distance R_0. This propagation geometry introduces a characteristic wavenumber scale $k_\star \sim 1/R_0$, associated with the oscillatory behavior of $J_0(kR_0)$, and thus a characteristic frequency scale

$$f_\star \sim \frac{v_{SAW}}{2\pi R_0}. \tag{197}$$

This frequency does not characterize the photo-thermoelastic source itself, which generates broadband SAW pulses for $\sigma \ll R_0$, but rather reflects a propagation-induced temporal scale associated with the geometrical focusing at the ring center. The spectral bandwidth is primarily governed by the ring width σ and the laser pulse duration τ.

To visualize this generation process, numerical simulations have been performed using a homemade Python script (see Appendix D.6). The simulations presented in Figure 54 were done for a 50 µm ring pump, with a FWHM ring section of 5 µm, a pulse duration of 600 ps, a laser beam mean power of 100 mW, and a 100 nm penetration depth. The optical energy distribution presented in Figure 54(a) is a qualitative view of the modeled pump distribution. In practice, the calculations of surface displacements are done using Equation (195). Figure 54(b) shows a side view so that we see the surface displacement in the (xy)-plane cutting the y-axis at its zero value. We note that at

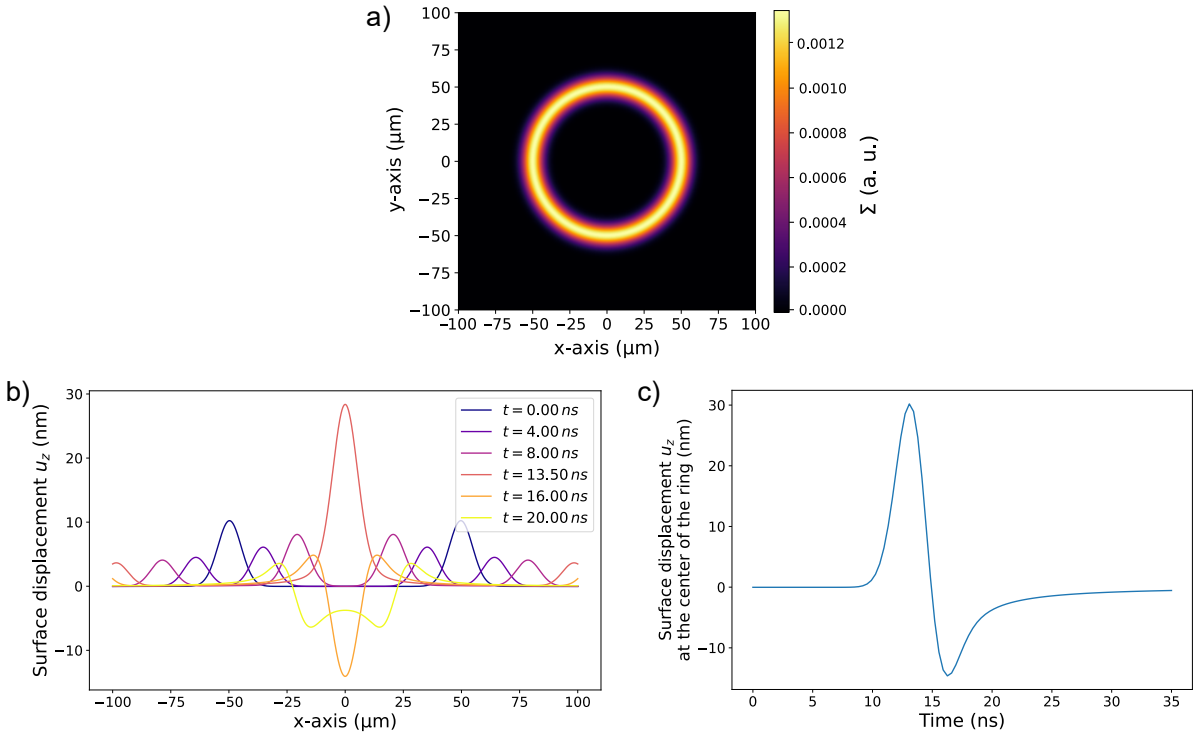

Figure 54: Simulation of giant surface acoustic wave generation from laser ring pulse. a) Surface stress distribution induced by a 50 µm radius laser ring. b) Surface displacement at various delays after the ring pumping. c) Surface displacement at the center of the ring depending on time.

$t = 0$, two equal surface displacements centered at the ring pump position are visible. They are part of the initial laser-induced ring surface displacement. Then, these initial peaks will separate into a focusing component and a diverging one. We immediately observe that the converging one is stronger because it has constructively interfered with neighboring SAWs that have reached the same location while propagating through the center. The maximal surface displacement is obtained at the center of the ring when all the SAWs have constructively interfered. Then, a weaker depressive wave occurs, visible by its negative sign, and propagates away from the center. Simulating a continuum of time delay values allows us to plot the time-resolved surface displacement at the center of the ring pump; see Figure 54(c). The surface displacement exhibits the classical compression/depression profile. In addition, the choice of parameters close to those used experimentally reveals a peak-to-peak amplitude of around 50 nm, which is very close to experimental measurements. This allows us to be confident in the implemented model to predict surface displacements induced by optical sub-picosecond ring pumps.

4.2 Nanosecond time-domain MOKE setup for probing SAW effects in ferromagnetic thin films

The experimental setup presented in Figure 55 differs from the previous one (Figure 44) in several ways. First, no second harmonic generation is used to produce pump and probe beams of different wavelengths. In addition, the custom femtosecond laser is replaced by the Mira-RegA system, previously presented in Figure 7 and in Appendix C. The reason for using pump and probe beams of the same wavelength is twofold: the probe beam lies in the region of maximal optical sensitivity of the balanced photodiodes, ensuring optimal detection, and the pump beam carries the highest possible energy to efficiently trigger strong magnetic precession in the investigated ferromagnetic thin films.

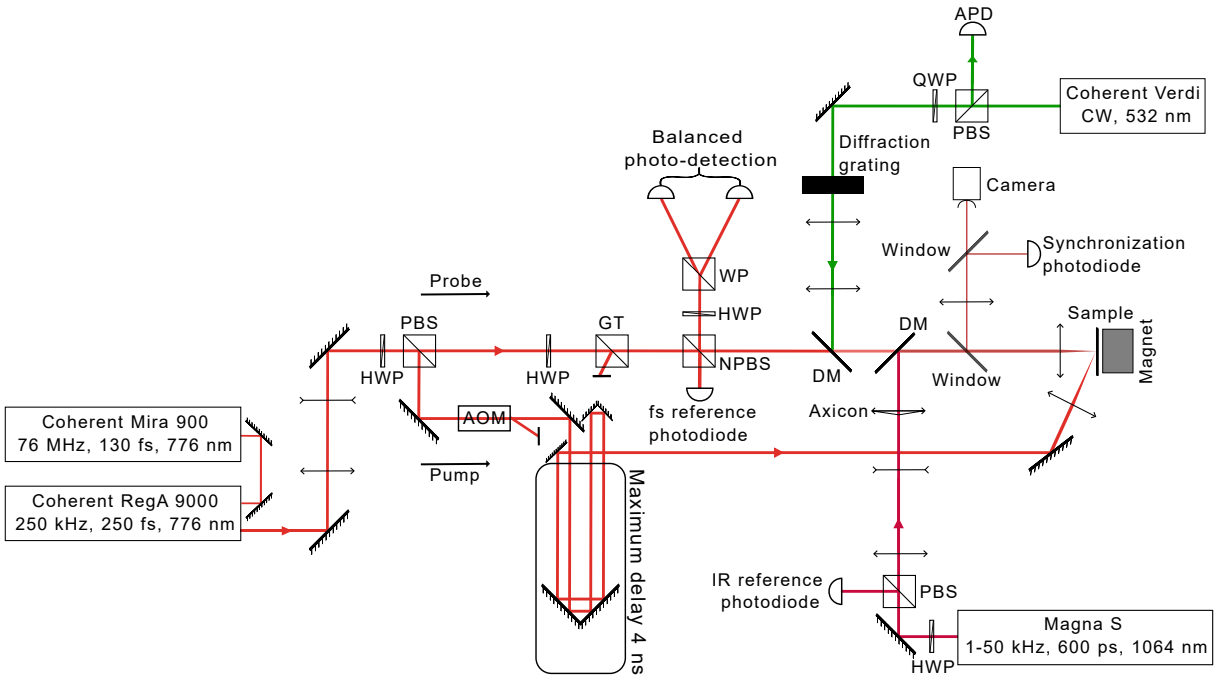

Figure 55: Time-resolved experimental setup for femtosecond-induced perturbations, surface acoustic wave generation, and probing of magnetization via MOKE, along with surface displacement measurements via interferometry. HWP: Half Wave Plate. QWP: Quarter Wave Plate. PBS: Polarizing Beam Splitter. NPBS: Non-Polarizing Beam Splitter. GT: Glan-Taylor. AOM: Acousto-Optic Modulator. DM: Dichroic Mirror. WP: Wollaston Prism. APD: Avalanche Photodiode.

In this new configuration, a second optical pump was added to generate the SAWs. This pump is provided by the Magna S laser source, which delivers 600 ps pulses at 1064 nm, with typically about 10 µJ energy per pulse, with a variable repetition rate from 1 to 50 kHz. The collimation of the IR pump is adjusted with a telescope in order to optimize its focusing on the sample and to compensate, as much as possible, for the slight chromatic aberrations of the optics design for the visible range. Additionally, this IR beam passes through a 1° axicon lens. The axicon, a conical lens, modifies the beam wavefront, transforming its shape from a Gaussian spot into a ring; see Figure 56(a). Ring-shaped pumping is advantageous as it allows the delivery of maximum laser energy while preventing optical damage. The resulting surface displacement on the ring converges toward the center, thereby generating a strong local deformation. Furthermore, by avoiding direct illumination of the central detection area, ring pumping minimizes parasitic optical perturbations.

At the output of the sub-nanosecond laser, a HWP and a PBS are used to control the pump power. The unused fraction of the beam is collected by a photodiode, which continuously monitors the stability of the laser emission during the experiments. The surface displacements induced by the IR pump ring are probed using a common-path phase-mask interferometer, which is extremely stable and does not require any electronics for feedback phase stabilization [47, 172]. The optical setup of the interferometer is schematically shown in three dimensions in Figure 57. This view is particularly useful because the superposition of the interfering beams cannot be represented in the top-view scheme of Figure 55. The interferometric probe relies on a continuous-wave laser source that emits a polarized beam at 532 nm. The beam first passes through a PBS/QWP assembly, which serves as the collector for the backscattered probe light from the sample. The operating principle of this collector has already been described in Part I 3.1.5. A diffraction grating is then used to split the incoming beam into multiple diffraction orders. Only the ± 1 orders are transmitted, while the others are spatially blocked. The choice of ± 1 orders ensures two beams of equal intensity and identical diffraction angles. The diffraction grating is placed in the focal plane of the lens L1 so that the diffracted beams propagate parallel to each other between L1 and L2. Lens L2 is positioned such that the beams are optimally focused on the sample. The interferometer beams are combined with the femtosecond probe beam by means of a dichroic mirror (not shown in Figure 57). The apochromatic microscope objective (MO) is fixed in position.

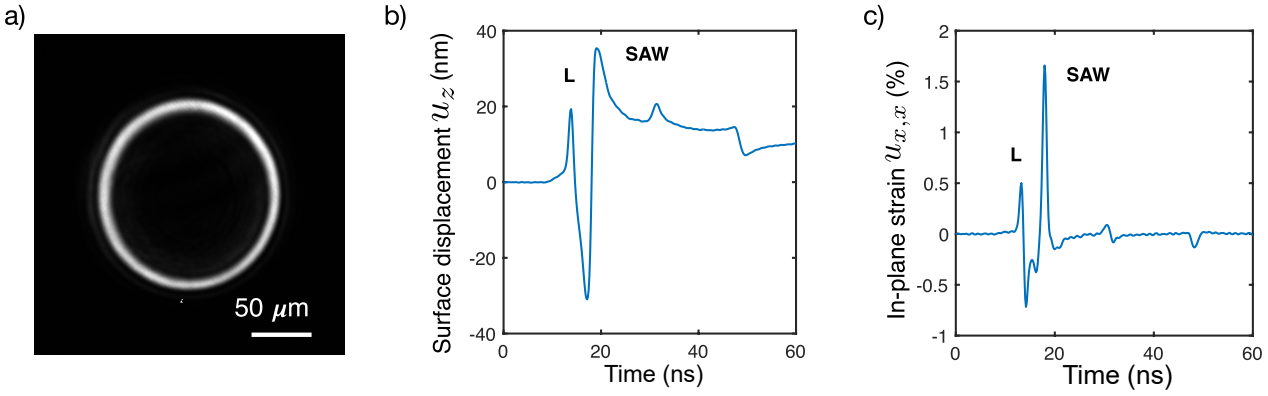

Figure 56: a) Ring-shaped laser beam for the excitation of focusing SAWs and longitudinal skimming wave L. b) At the convergence of the acoustic waves, we record the interferometric time-trace of the surface displacement from a niobium-doped $SrTiO_3$ (STO:Nb) substrate. c) After derivation, we obtain a reliable strain evaluation of the converging predominant SAW, as well as a weaker converging L.

During the alignment procedure, one of the interferometer beams is superimposed with the 780 nm femtosecond probe. These two beams, the fs probe and the overlapped 532 nm interferometer beam, define the center of the pump ring, where the maximum surface displacement occurs. The second interferometer beam is positioned outside the pump ring and therefore does not probe the central surface displacement. The two interferometer beams are backscattered with an optical path difference that depends on the local surface displacement. Upon recombination in the diffraction grating, their interference encodes this path difference. The recombined beam is directed to an avalanche photodiode (APD), which records the time-resolved interference signal and thereby the temporal evolution of the surface displacement induced by SAWs in the investigated material.

In practice, the APD used in our setup does not detect the continuous component of the signal. Therefore, a calibration procedure is performed using a photomultiplier tube (PMT). The principle is the following: while no ring pump is applied to the sample, the diffraction grating is vertically translated in order to find the maximum and minimum phase-matching conditions, and the associated voltages provided by the PMT are recorded on an oscilloscope. The relation between these two voltages, U_{max} and U_{min}, and the optical path difference δ is given by:

$$U = \frac{U_{max} + U_{min}}{2} + \frac{U_{max} - U_{min}}{2} \sin\left(\frac{2\pi\delta}{\lambda} + \phi_0\right). \tag{198}$$

The variation of the detected voltage with respect to the optical path difference is obtained by differentiation of Equation (198):

$$dU = \frac{2\pi}{\lambda} \cdot \frac{U_{max} - U_{min}}{2} \cos\left(\frac{2\pi\delta}{\lambda} + \phi_0\right) d\delta. \tag{199}$$

The phase matching is adjusted to maximize the interference contrast, such that $\cos\left(\frac{2\pi\delta}{\lambda} + \phi_0\right) \simeq 1$. Furthermore, the optical path difference is directly related to the normal surface displacement by $du_\perp(t) = d\delta/2$. The calibration factor is thus given by:

$$\frac{dU}{du_\perp} = \frac{2\pi}{\lambda}(U_{max} - U_{min}). \tag{200}$$

This relation allows us to convert the voltage measured by the APD into the absolute surface displacement. Since the interferometer is operated close to the point of maximum contrast, the cosine response can be considered quasi-linear with the measured voltage. The PMT is used only for calibration purposes, owing to its ability to detect the continuous component of the signal. For the actual time-resolved measurements, it is replaced by the APD, which offers a faster rise time and a larger bandwidth, making it more suitable for tracking the rapid displacements induced by SAWs.

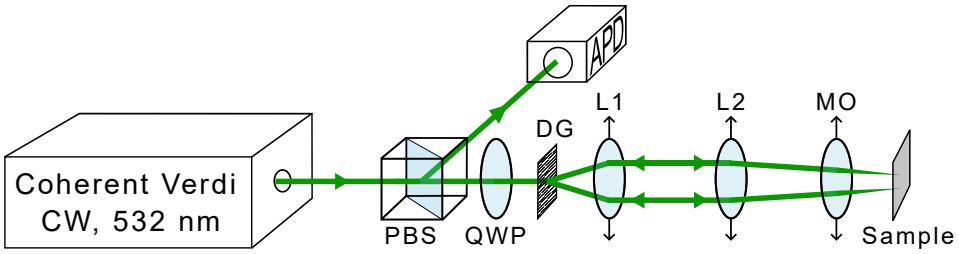

Figure 57: 3D schematic of the interferometric setup to probe surface displacement. PBS: Polarizing Beam Splitter. QWP: Quarter Wave Plate. DG: Diffraction Grating. L1 and L2: convergent lenses. MO: microscope objective. APD: Avalanche Photodiode.

A typical recorded interferometer time trace, plotted in absolute value after voltage calibration, is shown in Figure 56(b). The significant 60 nm displacement jump, from -30 nm to +30 nm, corresponds to the SAW focusing at about 18 ns time delay after laser excitation, which corresponds to the time-of-flight from the ring to the center of convergence of the SAW. Time-derivation of this time-trace signal and multiplication of the SAW speed in the niobium-doped $SrTiO_3$ (STO:Nb) substrate of about 3600 m/s gives a good estimate of the in-plane strain ε_{xx} related to the SAW. Basically we assume $\varepsilon_{xx} = \partial u_x/\partial \delta x \simeq 1/v_{SAW} \cdot \partial u_x/\partial \delta t$. As shown in Figure 56(b), the nearly unipolar compressive SAW strain reaches amplitudes of approximately 1.5%, which is remarkably large. Moreover, owing to the high mechanical strength of the substrate used in this experiment, no mechanical or optical damage is observed either at the convergence center or along the ring location. This ring configuration thus proves highly advantageous, as it enables the generation of exceptionally strong strain levels in a much simpler manner compared to the multi-line setup, which is considerably more complex to implement [47].

Another important technical consideration concerns the synchronization of the two laser emissions. This synchronization is achieved using a delay generator triggered by the femtosecond laser, which in turn sends a trigger signal to the sub-nanosecond laser. The femtosecond laser operates at a repetition rate of 250 kHz, which defines the repetition rate of the optical probe. To ensure the stability of the sub-nanosecond laser emission and to maximize its output power, it is triggered to emit at a repetition rate of 10 kHz. The acousto-optic modulation of the femtosecond pump, which initiates the magnetic precession, is accordingly adjusted to match this 10 kHz rate. This guarantees that each initiated precession corresponds to a single ring pump event. Finally, the synchronization jitter between the two oscillators is measured using a 1.5 GHz oscilloscope, revealing a jitter of approximately 130 ps; see Figure 58.

After confirming the good synchronization quality between the two lasers with respect to the ring pump pulse duration, we determined the temporal zero delay corresponding to the overlap of the two pump pulses. In practice, the femtosecond pump, the probe, and one beam from the interferometer are all focused at the center of the ring. The time-zero of the femtosecond pump-probe setup is known from magnetic precession measurements. The current objective is to determine the setting of the delay generator that synchronizes the two lasers such that the acoustic wave reaches the center of the ring simultaneously with the femtosecond beams.

To this end, the optical power of the femtosecond laser was increased to allow the detection of sample heating by the interferometer. In Figure 59(a), the femtosecond pulse is detected by its reference photodiode (red), by the synchronization photodiode after it reaches the sample (blue), and

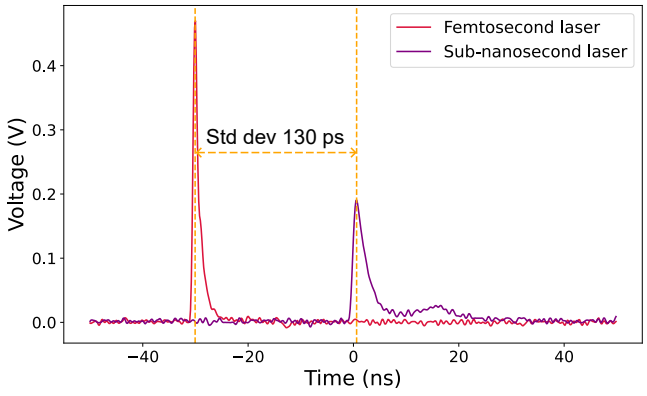

Figure 58: Oscilloscope trace showing the determination of synchronization jitter through standard deviation measurement.

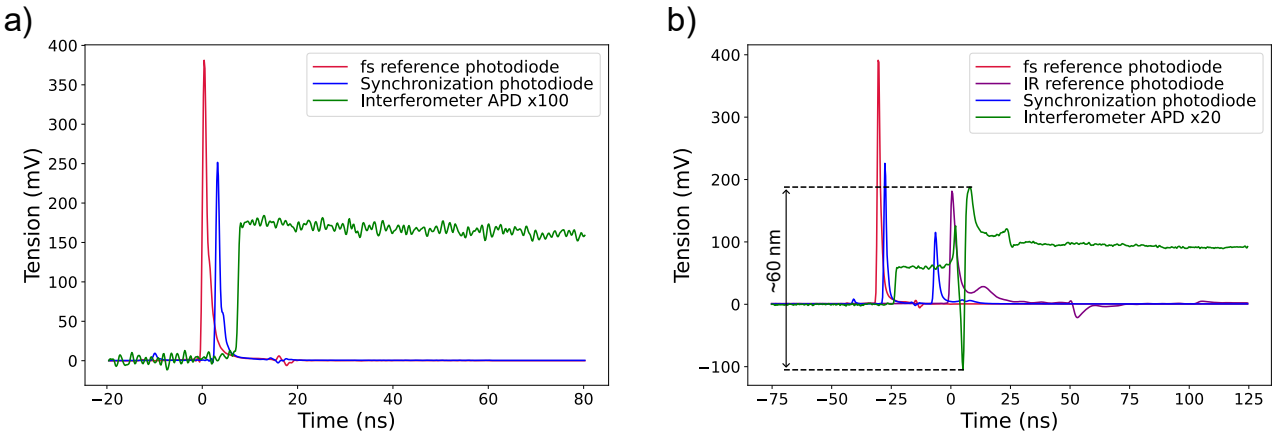

Figure 59: Calibration of the surface displacement and determination of the delay generator time that synchronizes the two pumps. a) Optimization of spatial overlap between the femtosecond beams and the interferometer. b) Detection of surface displacement from the ring pump and temporal matching of the optical pumps.

by the interferometer as a thermal effect on the sample (green). This signal is used to optimize the spatial overlap between the femtosecond beams and the interferometer detection spot. Figure 59(b) shows the same configuration, with the addition of the ring pump. The surface displacement induced by the ring excitation is clearly visible. Its amplitude is maximized by adjusting the ring position to ensure that detection occurs exactly at the center. Temporal overlap between the two pumps is then achieved by aligning the femtosecond heating signal with the surface displacement signal.

4.3 Nanosecond time-domain MOKE probing of SAW effects in ferromagnetic cobalt thin film

Based on the theoretical framework and the calibration measurements on a STO:Nb substrate, we performed time-resolved MOKE experiments on a layered sample with the following structure: STO:Nb/Co(15 nm)/Al(5 nm). The STO:Nb substrate was selected due to its efficient SAW generation under 1064 nm optical excitation. A thin aluminum capping layer was deposited on top of the cobalt to protect it from oxidation. Measurements were conducted over a delay range of ± 5 ns around the temporal overlap of the two optical pumps. The delay was varied automatically in 100 ps steps. For each delay value, the magnetic precession was resolved using a mechanical delay stage, as in all previously described time-resolved MOKE experiments.

Figure 60(a) shows the normalized derivative of the precession signal recorded for a delay of -5 ns (before SAW arrival). A clear oscillation is observed, and its Fourier transform (Figure 60(b)) reveals a Larmor precession frequency of 9.4 GHz. The FFT amplitude at 9.4 GHz was extracted from each precession signal acquired over the full delay range and plotted as a function of time delay in Figure 61. Unfortunately, this figure shows that no measurable modulation of the magnetic behavior of the cobalt layer by the SAW is detected. At this point, there is no doubt regarding successful SAW generation in the sample, nor about the temporal synchronization of the relevant physical phenomena.

Although a SAW-induced influence on magnetization dynamics is expected based on both theory and previous studies, the absence of a clear modulation in the signal does not necessarily mean that no effect occurs.

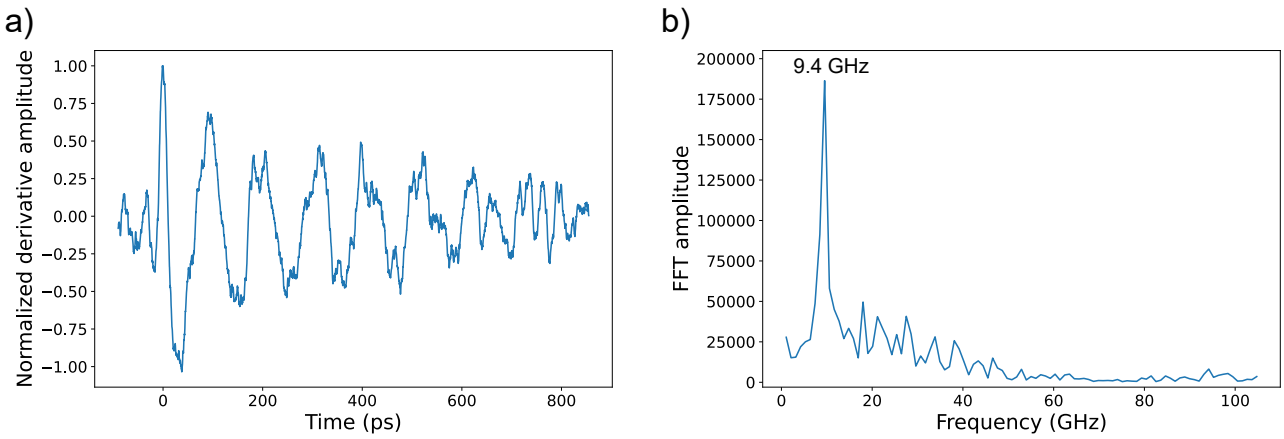

Figure 60: Time-domain MOKE probing of SAW effects in a ferromagnetic thin cobalt layer. a) Normalized derivative of the precession signal recorder of a delay of -5 ns.b) FFT of the derivative presented in Figure 60(a) subplot.

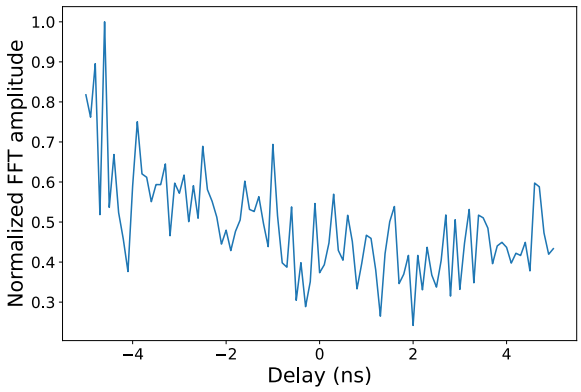

Figure 61: FFT amplitude of the recorder precession signals at various delays.

4.4 Summary: Giant surface acoustic waves for the manipulation of magnetization

In this section, the generation of giant SAWs using a ring-shaped optical pump has been described theoretically and demonstrated experimentally. This excitation scheme was then combined with magnetic precession measurements in order to investigate the possibility of manipulating magnetization via SAWs. However, even though both the surface displacement and the magnetic precession were clearly identified, no coupling between them could be clearly established.

To confirm or rule out the absence of any influence of SAWs on the sample, further studies are required. Several possibilities can be examined, such as reducing the femtosecond probe pulse duration to narrow the frequency gap with the pumps and improve the signal-to-noise ratio in the synchronous detection, increasing the number of averaged precession acquisitions, or even lowering the SAW amplitude to prevent potential delamination at the STO:Nb/Co interface.

5 Ultrafast optical probing of the superconducting transition

In our previous studies, we introduced a method to optically generate strong local lattice deformations using annular optical pumping. At high optical power, such strain levels should induce remanent structural modifications—at the SAW focus point in some correlated materials known to be sensitive

to strain. This is particularly interesting, since studies have shown that hydrostatic pressure can modify the superconducting transition temperature T_c in high-temperature superconductors. In the case of $YBa_2Cu_3O_{7-\delta}$ (YBCO), the pressure-induced change of T_c depends on the oxygen doping level (the value of δ), and can result in an increase, a decrease, or a negligible variation of T_c [173, 174]. In YBCO, optimal doping occurs for $\delta \sim 0.1$, corresponding to the highest critical temperature, $T_c \simeq 92$ K. For both lower and higher doping levels, T_c decreases. In the extreme case, where $\delta \sim 1$ ($YBa_2Cu_3O_6$), YBCO becomes an antiferromagnetic insulator [175].

The purpose of the present study is to investigate whether the superconducting transition can be optically probed through the Meissner effect and/or Brillouin scattering. The long-term aim is to pave the way for investigations of the influence of transient strain, induced by enhanced SAWs, on the critical temperature. To this end, the optical setup was modified to include a helium-cooled cryostat with optical access. Before presenting the experimental setup, we first recall some theoretical considerations about YBCO, superconductivity, and the Meissner effect.

5.1 Theoretical considerations about YBCO, superconductivity, and the Meissner effect

When a material becomes superconducting below its critical temperature T_c, it not only exhibits zero electrical resistance but also expels magnetic flux from its interior. This phenomenon is known as the Meissner effect, and it distinguishes a perfect conductor from a true superconductor [176]. Theoretically, the Meissner effect is described by the London equations, which relate the superconducting current density $\mathbf{J}_s$ to the vector potential $\mathbf{A}$ according to:

$$\mathbf{J}_s = -\frac{n_s\, q_e^2}{m}\mathbf{A}, \tag{201}$$

where n_s is the density of superconducting carriers (Cooper pairs), q_e is the electron charge, and m is the effective mass. The penetration depth λ_L, which characterizes the exponential decay of magnetic fields inside the superconductor, is obtained by combining Maxwell's equations with Equation (201), leading to:

$$\nabla^2\mathbf{B} = \frac{1}{\lambda^2}\mathbf{B}, \tag{202}$$

where the London penetration depth is given by $\lambda_L = \sqrt{\frac{m}{\mu_0 n_s q_e^2}}$. As a result, an external magnetic field applied to a superconductor is expelled from its interior and only penetrates over a distance on the order of λ_L. This expulsion of magnetic flux can affect Kerr rotation measurements, especially when a ferromagnetic layer is deposited on top of a superconducting material. In the presence of an external magnetic field, an out-of-plane component of the magnetization is induced in the ferromagnetic layer, enhancing Kerr rotation through increased sensitivity to M_z. However, when the underlying superconductor temperature is below its critical temperature, the Meissner effect screens the magnetic field. This suppression/decrease of the magnetic field can lead to a reorientation of the magnetization in the ferromagnetic layer toward the in-plane direction, thereby reducing the M_z amplitude and leading to a net decrease in the Kerr rotation.

We now discuss the specific case of magnetic field penetration in YBCO, which is a high-T_c anisotropic superconductor. In the superconducting phase, the effective mass of the charge carriers is typically taken as $m = 2m_e$, reflecting the fact that superconductivity arises from Cooper pairs. Similarly, the effective charge is $q = 2q_e$. Assuming that the applied magnetic field remains below the lower critical field B_{c1}, the density of superconducting carriers n_s stays constant, and so does the London penetration depth λ_L. In this regime, the magnetic field decays exponentially inside the

superconductor over a characteristic distance given by λ_L. However, it is essential to take into account that YBCO is strongly anisotropic. The YBCO structure and the reference directions are presented in Figure 62. This anisotropy manifests in the magnetic penetration depth being direction-dependent. It is conventional to describe this behavior using three crystallographic directions: the a and b axes lying in the Cu-O planes and the c-axis perpendicular to these planes. We refer to published estimations of the directional London penetration depths [177–180], but we emphasize that both the critical temperature and the penetration depths are highly sensitive to the oxygen content δ in YBCO. For a doping level such that $T_c \simeq 84$ K, which matches our sample composition, we report the following low-temperature values: $\lambda_a \sim 100$ nm, $\lambda_b \sim 80$ nm, and $\lambda_c \sim 635$ nm. We note that these values are temperature-dependent and tend to increase significantly as the temperature approaches the critical temperature T_c. Additionally, the much larger value of λ_c compared to λ_a and λ_b highlights the markedly reduced conductivity and Cooper-pair stiffness along the c-axis, which is the one along which the magnetic field is applied in our experiments.

An empirical model for the temperature dependence of the London penetration depth is given by the Gorter-Casimir two-fluid model [181–184]:

$$\lambda(T) \simeq \lambda(T=0)\left[1-\left(\frac{T}{T_c}\right)^n\right]^{-1/2}. \tag{203}$$

For YBCO, a typical value for the exponent is $n \simeq 2$, though it depends on sample quality, oxygen content, and measurement method. The parameter n is generally empirically determined from experimental data.

Another important aspect of YBCO is its nature as a type-II superconductor, which arises from its relatively large London penetration depth λ_L and its small coherence length ξ. These two parameters define the Ginzburg-Landau parameter, $\kappa = \lambda_L/\xi$, which determines whether a material is a type-I or type-II superconductor. In the case of YBCO, $\kappa > 1/\sqrt{2}$, which confirms its classification as a type-II superconductor. In a type-II superconductor, two critical magnetic fields exist: the lower critical field B_{c1} and the upper critical field B_{c2}. This leads to three distinct regimes. For magnetic fields $B < B_{c1}$, the material remains in the pure Meissner state, fully expelling magnetic flux. For intermediate fields, $B_{c1} < B < B_{c2}$, the superconductor enters the mixed state, where magnetic flux penetrates the material in the form of quantized vortexes. Finally, for $B > B_{c2}$, superconductivity is destroyed, and the material returns to the normal conducting state. Both B_{c1} and B_{c2} are anisotropic; their values strongly depend on the direction of the applied magnetic field with respect to the crystallographic axes.

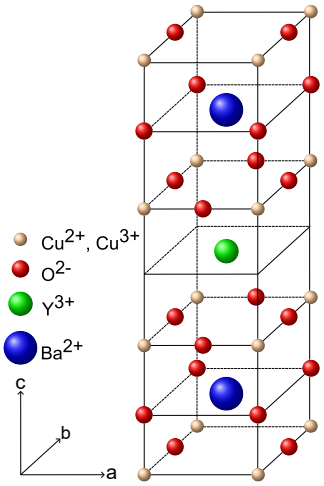

Figure 62: Crystallographic structure of YBCO.

They are also highly temperature dependent. As the temperature approaches the superconducting critical temperature, both critical fields decrease and eventually vanish at $T = T_c$. We refer to the book by H. Weber [185], which compiles practical experimental values for various superconducting materials. The lower critical fields for YBCO are estimated to be $B_{c1}^{ab} \simeq 12$ mT for magnetic fields parallel to the Cu-O plane, $B \parallel (a, b)$, and $B_{c1}^{c} \simeq 69$ mT for a field normal to the Cu-O plane, $C \parallel c$. The upper critical fields are estimated to be $B_{c2}^{ab} \simeq 230$ T and $B_{c2}^{c} \geq 35$ T. The temperature dependence of the upper critical field can often be described by the same phenomenological expression as follows:

$$B_{c2} = B_{c2}(0)\left[1 - \left(\frac{T}{T_c}\right)^2\right]. \tag{204}$$

The previous considerations assume a bulk or thick-film geometry, where the magnetic field decays exponentially over a distance characterized by the London penetration depth λ_L. However, when the thickness d of the superconducting film becomes smaller than λ_L, this standard London description must be revised. In this thin-film limit, the effective magnetic screening is governed by the Pearl penetration depth, denoted by λ_P [186–188]. The Pearl penetration depth is defined in terms of the London penetration depth and the film thickness:

$$\lambda_P = \frac{2\lambda_L^2}{d}. \tag{205}$$

The Pearl regime applies when $\lambda_L/d \gtrsim 5$. Since the YBCO films we have studied are thinner than λ_L and probed along the c-axis, only weak magnetic screening is expected. Nevertheless, experiments were performed to assess the detection sensitivity and to explore the optical probing of the superconducting transition.

5.2 Time-resolved optical probing of the YBCO superconducting transition: experimental setup

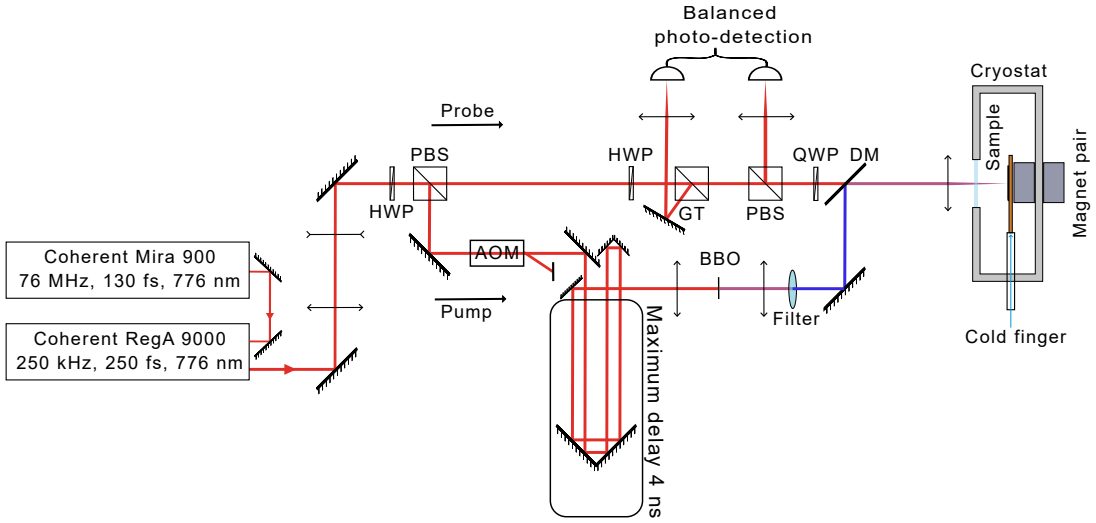

Figure 63: Time-resolved experimental setup for reflectivity and magnetization temperature-dependent measurements on the picosecond timescale. HWP: Half Wave Plate. PBS: Polarizing Beam Splitter. NPBS: Non-Polarizing Beam Splitter. GT: Glan-Taylor. AOM: Acousto-Optic Modulator. DM: Dichroic Mirror. WP: Wollaston Prism.

The experimental setup is similar to that used for time-resolved MOKE (Figure 44) for magnetization studies and to the TDBS setup (Figure 7) for reflectivity studies. The main difference is the addition of a microscopy cryostat. The detection scheme depends on the measurement type as presented in Figure 63. Both reflectivity and polarization-rotation detection principles were already introduced in previous sections. The new element is the cryostat, which is a vacuum chamber maintained at $\sim 10^{-9}$ bar by a turbo-molecular pump. A quartz window provides optical access. The sample is fixed on a copper plate with vacuum grease to ensure good thermal contact. This copper plate is cooled via a cold finger connected to a liquid helium reservoir, ensuring the T_c is crossed. A permanent magnet inside the cryostat provides a $\sim$ 100 mT field. A second external magnet allows the field direction to be varied during the experiment, enabling quasi-zero-field cooling conditions.

5.3 Time-resolved optical probing of the YBCO superconducting transition: TDBS results

The objectives of these investigations are twofold: first, to verify that the temperature indicated by the cryostat servo loop corresponds to the actual temperature of the sample or if a shift exists; and second, to investigate whether the superconducting phase transition of YBCO can be tracked through TDBS.

The first set of measurements was performed on a 75 nm YBCO film deposited on an STO:Nb substrate, using Brillouin-type signal recording. The superconducting transition temperature of the investigated YBCO film was determined by J. Briatico and coworkers (Laboratoire Albert Fert), who fabricated the samples. The resistivity/temperature curve that they have established is given in Figure 64. On this figure, we observe an abrupt fall of the YBCO resistivity while the sample is cooled below 87 K. The TDBS measurements were carried out through laser-excitation of a YBCO film, that serves as a transducer to launch the LAWs in a STO:Nb substrate on which the film is deposited. In our experiments, the signals are recorded while the sample is cooled from 150 K down to 50 K. The sample was then reheated to 150 K in order to perform a control measurement. For each measurement, the surface quality of the sample is checked visually on a CCD camera (not shown in Figure 63 but placed like in Figure 55), as well as the laser focus and the quality of the photodiode balancing. The results and their analysis are presented in Figure 65. In Figure 65(a), the recorded TDBS signals are shown for temperatures ranging from 50 K to 150 K. The characteristic features of TDBS signals are clearly visible; an electronic peak, a decaying thermal background, and well-defined Brillouin oscillations are observed. We note that the electronic peak appears to depend on temperature. To investigate this effect, the amplitudes of the electronic peaks were extracted and plotted as a function of temperature

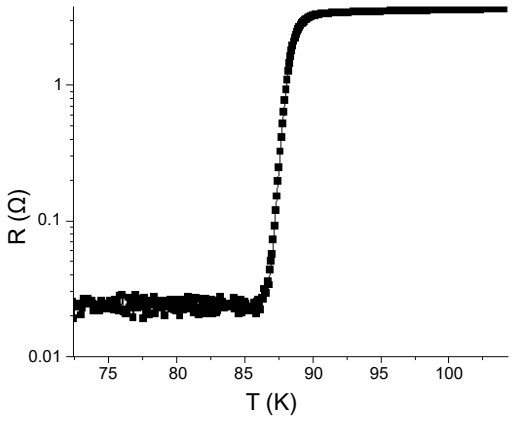

Figure 64: Calibration of YBCO critical temperature.

in Figure 65(b), which reveals a quasi-linear dependence of the electronic peak on temperature. The increase of the electronic peak amplitude with the temperature decrease is consistent with a slower electron-phonon relaxation in the cooled regime. Indeed, as the temperature decreases, the lattice vibrations diminish, electron-phonon scattering events become less frequent, and the electrons remain in their excited state for longer times. This trend has been experimentally observed in metals [189] and theoretically predicted [110]. A similar temperature dependence of the electronic response after ultrafast excitation has also been reported in superconductors, including cuprate superconductors [190–192]. These studies confirm that the behavior we observe is consistent with established ultrafast relaxation dynamics. However, it is rather surprising that there is no discontinuity at all on the electronic peak amplitude around the superconducting transition. The distinction between laser-induced heating of normal electrons and that of Cooper pairs is most likely too weak to be detected.

In addition to the variation of the amplitude of the electronic peak with temperature, the Brillouin frequency dependence on temperature was also studied. To accurately resolve the dominant frequency, FFTs were performed on the derivative of the signal (to remove the baseline), a zero-padding of the recorded data length was applied, and the Brillouin FFT peaks were fitted using a Lorentzian function. The Lorentzian fit function is given by:

$$\mathcal{L}(f) = \frac{A}{1 + \left(\frac{f - f_0}{\gamma}\right)^2} + C, \tag{206}$$

where A is the amplitude, f is the frequency, f_0 is the central frequency (the Brillouin frequency), γ is the linewidth parameter, and C is an offset. With this analysis procedure, we extracted the position, the width, and the phase of the Brillouin peaks across the temperature range investigated. A clear change in the central Brillouin frequency f_0 is observed around 110 K; see Figure 65(c), which matches quite well the expected phase transition of STO around 105 K. Below this temperature, STO adopts a tetragonal structure, whereas above it the crystal structure becomes cubic [193]. The slight 5 K difference could come from the fact that our substrate differs from those studied in [193], since niobium doping might modifies its initial phase. Anyhow, the detection of the STO transition around 105 K through TDBS measurements provides a reliable control of the sample effective temperature and a cross-check of the temperature sensor accuracy.

A direct comparison between our data and recently published TDBS measurements in STO [193] confirms the same trend and indicates that cumulative laser heating is minimal, thanks to the use of our low-repetition-rate amplified laser system. In contrast, as reported in [193], laser-induced heating can cause detrimental effects, shifting the transition temperature by several tens of degrees. The key advantage in our case is that overheating effects can be neglected, allowing us to safely assume that the superconductor fully relaxes back to its ground state after each pump pulse. The only remaining uncertainty concerns the actual sample temperature measured by the sensor, which could differ by up to 5 K, a small but noteworthy deviation.

On the same plot of Figure 65(c), we can notice a small discontinuity around 70 K. This variation lies well below the superconducting transition temperature of our YBCO, and therefore it is difficult, *a priori*, to unambiguously attribute it to the superconducting transition. The phase of the central Brillouin frequency f_0 was also extracted from the FFTs. Its temperature dependence is presented in Figure 65(d). The Brillouin phase also exhibits a strong change at 110 K, which corresponds to the STO structural transition, and a smaller variation at 70 K. The Brillouin amplitude A displayed in Figure 65(e) supports the observations from the Brillouin frequency and phase. No clear variation is identified around the superconducting transition of YBCO that could indicate a change in its optical constants.

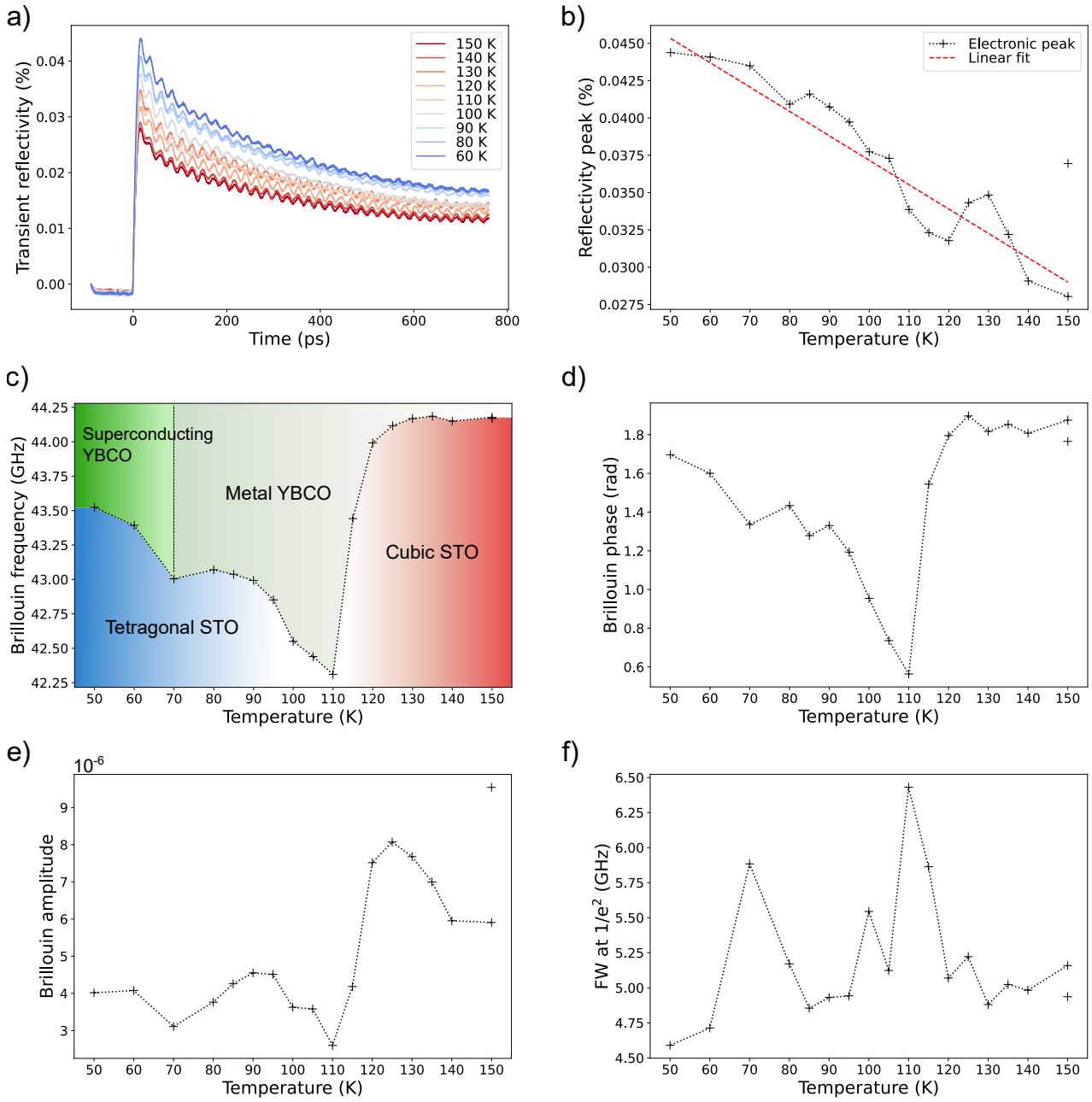

Figure 65: TDBS measurements on YBCO (75 nm)/STO:Nb: results and analysis. a) Recorded transient reflectivity changes at various temperatures. b) Amplitude of the electronic peak as a function of temperature, with a linear fit of the trend. c) Temperature dependence of the Brillouin frequency. d) Temperature dependence of the Brillouin phase. e) Temperature dependence of the Brillouin amplitude. f) Temperature dependence of the full width at $1/e^2$ obtained from Lorentzian fits of the Brillouin spectral peak in the FFT.

Finally, Figure 65(f) presents the spectral width of the Brillouin peaks obtained from the FFTs. These widths correspond to the full width at $1/e^2$ of Lorentzian fits of the Brillouin spectral peaks. The full width at $1/e^2$ is extracted from the numerical determination of the γ parameter of Equation (206), using the relation $FW_{1/e^2} = 2\gamma\sqrt{e^2-1}$. The spectral width analysis provides complementary information to that of the Brillouin frequency, phase, and amplitude. In particular, it reveals a pronounced broadening of the Brillouin peak centered at about 70 K, in addition to the feature observed around

110 K. The last point to address is the control measurement performed after reheating the sample. For clarity, this acquisition is not plotted in Figure 65(a); however, it was analyzed using the same procedure as for the other signals. The extracted quantities (electronic peak amplitude, Brillouin frequency, Brillouin phase, Brillouin amplitude, and the full width at $1/e^2$ of the Lorentzian fit) are shown in the corresponding panels of Figure 65. These control points at 150 K are displayed separately from the other acquisition (connected by dotted lines). We note that the electronic peak amplitude is significantly larger than in the first measurement at 150 K, although it does not reach the maximum intensity observed when the sample was cooled below 100 K. Similarly, the Brillouin amplitude is noticeably higher than for any of the other data points. Despite these variations in intensity, the Brillouin frequency remains extremely close to that of the initial 150 K measurement. In addition, the phase and the spectral width are also close to the initial values. These observations of strong differences in raw intensity but stability of frequency, phase, and linewidth indicate that the phenomena induced by cooling are reversible.

These first TDBS investigations on a 75 nm YBCO film deposited on an STO:Nb substrate have allowed us to clearly identify the STO:Nb structural transition, which is expected to occur close to the transition of pure STO. However, this transition is known to be antiferrodistortive (rotation of TiO_6 octahedra) and mainly driven by the lattice instability of these octahedra [194, 195]. Moreover, niobium doping, particularly at the level of 0.7 %, is sufficient to induce a magnetic phase in STO [170], even if it does not induce significant changes in the overall crystal structure. This supports that a shift in temperature is possible and the niobium doping increases the STO structural transition temperature. It is also possible that the niobium doping of STO does not change its transition temperature and only the YBCO transition temperature is shifted. This explanation lies in the fact that the laser pulse goes through the YBCO layer before reaching the STO:Nb substrate, depositing energy in the YBCO before it goes to the substrate. Local heating induced in the thin film may be stronger and less efficiently dissipated than in the STO:Nb bulk, leading to a small temperature rise of a few Kelvin and thereby shifting the apparent transition. In this case, the measured temperature, supported by the STO antiferrodistortive transition, would still be correct; however, it would be necessary to cool the sample further in order to compensate for the local heating of the YBCO and to observe its superconducting transition. This would explain why the superconducting temperature transition seems to be shifted towards 70 K in our measurements.

Based on these considerations, namely the low niobium content of our STO and the abruptness of the identified transition, it is not possible at this point to unambiguously attribute the variation observed around 70 K to the superconducting transition of YBCO, but it is very likely to be the case. Even in the worst-case scenario, where the superconducting transition cannot be detected through TDBS, this outcome is intriguing in itself and very interesting. It suggests that laser heating of a metal and a superconductor leads to indistinguishable lattice strain responses. In other words, heating Cooper pairs or normal electrons does not appear to alter the electron–phonon coupling responsible for strain generation.

5.4 Time-resolved optical probing of the YBCO superconducting transition: MOKE results

After studying the influence of temperature on the reflectivity of YBCO via TDBS measurements in the STO:Nb substrate through the YBCO, we now investigate the possibility of optically detecting the superconducting transition of YBCO through the Larmor precession of a ferromagnetic material placed on top of YBCO, as illustrated in Figure 66. In these new time-resolved MOKE experiments, a 200 nm YBCO film deposited on a sapphire substrate is fixed to the cooled copper plate using

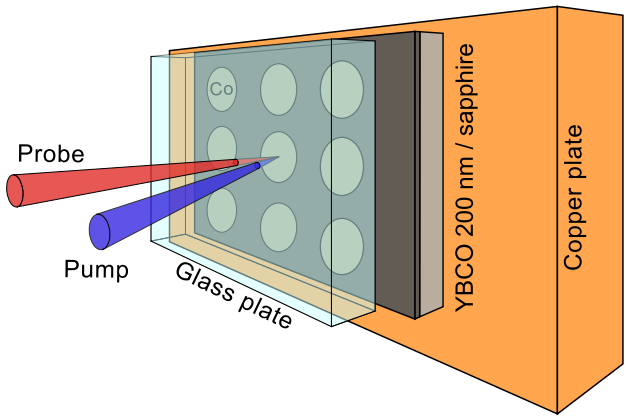

Figure 66: Schematic view of the sample configuration used to investigate the optical detection of the superconducting transition through the Larmor precession in cobalt disks deposited on YBCO.

vacuum grease. A glass plate coated with cobalt disks of 20 nm thickness on its surface is then placed in contact with the YBCO/sapphire sample, such that the cobalt disks top surface directly faces the YBCO top surface. The glass plate with the disks is held in place by a holed copper plate screwed onto the copper sample holder. Experimentally, the 780 nm probe and the 390 nm pump are focused through the glass substrate on a cobalt disk at the cobalt/glass interface. The backscattered probe is then split into polarizations, and the signal is acquired in a MOKE configuration.

When the sample is placed in the vacuum chamber and the precession in cobalt is observed, the magnetic field is reduced by sliding the external magnet positioned at the rear side of the cryostat, thereby moving the internal magnet. The sample is then cooled down to 40 K in a quasi-zero-field configuration. Zero-field cooling is particularly important to avoid magnetic flux pinning, which would otherwise reduce the effective magnetic screening in the superconducting phase [196, 197].

The acquired Kerr rotation signals at various temperatures are plotted in Figure 67(a). Clear Larmor precession oscillations are observed after the initial electronic excitation peak. The frequencies of these oscillations are determined using the same procedure as for TDBS analysis: FFT performed on the signal derivative (to remove the baseline), with zero-padding and Lorentzian fitting. The FFTs at different temperatures and an example of Lorentzian fitting are presented in Figure 67(b). The main isolated frequency lies around 12 GHz, which corresponds to the Larmor precession frequency. A second peak around 23 GHz is also observed. This peak corresponds to the Brillouin frequency of LAWs in the glass plate probed at 780 nm, where the cobalt disk acts as a transducer. The Brillouin peak is relatively small because of polarization balancing in the detection but remains visible due to the practical limits of the balancing, which cannot reach a perfect zero.

The temperature dependence of the Larmor precession frequency is shown in Figure 67(c). The frequency is relatively stable in the 70 K–150 K range but exhibits a strong linear decrease from 12.7 GHz down to 12.1 GHz below 70 K. This rather significant change is also observed in the Larmor phase (Figure 67(d)), in the FFT peak amplitude (Figure 67(e)), and in the spectral width (Figure 67(f)). Here the bandwidths are taken as the FWHM of Lorentzian fits, which reproduce the peak broadening correctly around the half-maximum despite some discrepancies in the tails.

Since the Larmor frequency is linked to the magnetic field by Equation (179), a reduction of the magnetic field should result in a decrease of the precession frequency. Given that the applied magnetic field originates from a fixed permanent magnet, the reduction of the local field at the cobalt disk position can reasonably be attributed to the Meissner expulsion of the magnetic field by YBCO in its superconducting phase.

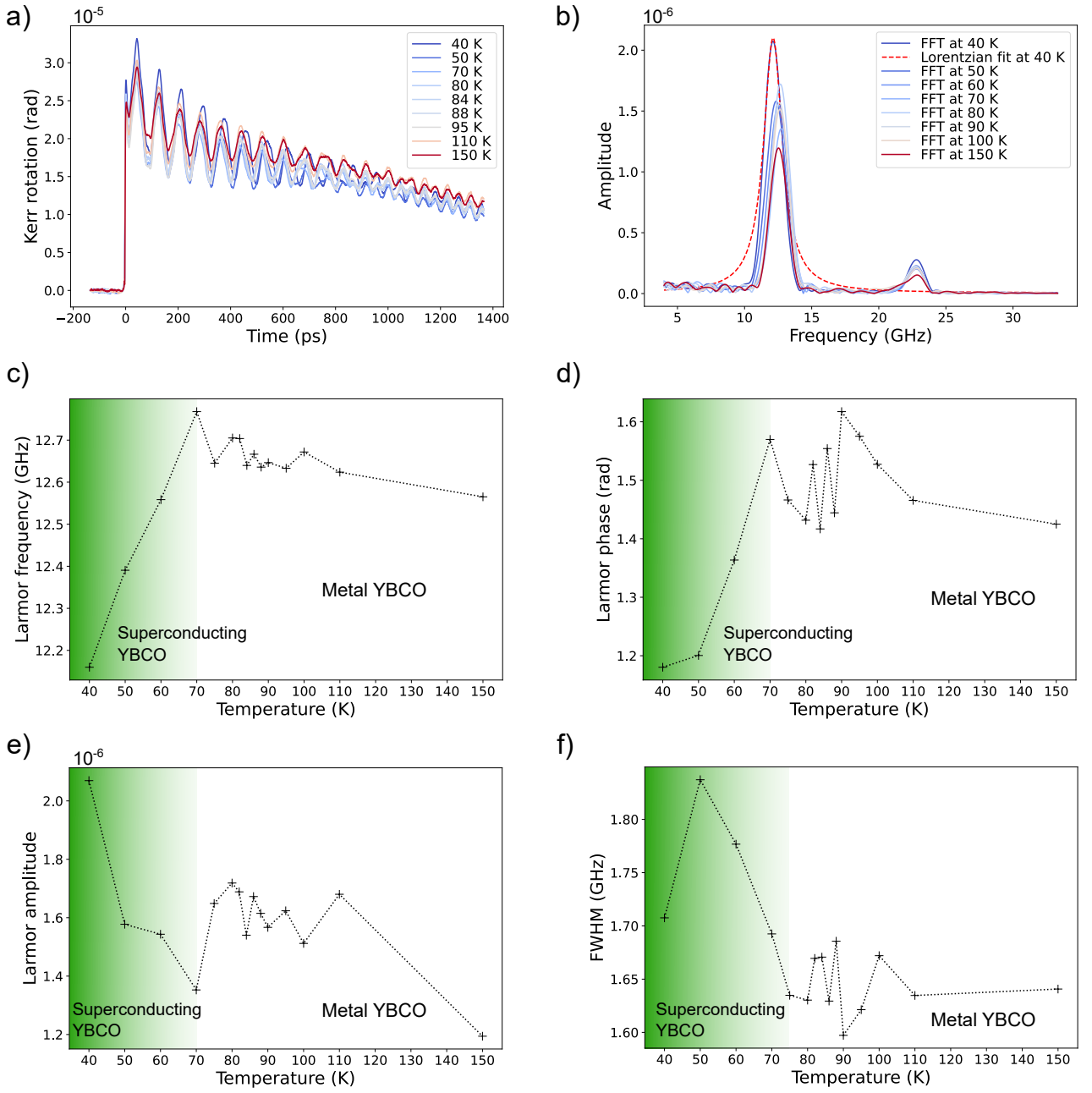

Figure 67: Time-resolved MOKE measurements on YBCO (200 nm)/sapphire: results and analysis. a) Recorded transient Kerr rotation at various temperatures. b) FFTs at various temperatures with a Lorentzian fit example at 40 K. c) Temperature dependence of the Larmor frequency. d) Temperature dependence of the Larmor phase. e) Temperature dependence of the Larmor amplitude. f) Temperature dependence of the FWHM obtained from Lorentzian fits of the Larmor spectral peaks in the FFTs.

If the reduction of the Larmor frequency can be attributed to the Meissner effect, the question arises: why is the transition not abrupt as demonstrated in Figure 64? A plausible explanation is that the measurements were performed after a quasi-zero field cooling. In this regime, residual vortices can be trapped due to magnetic flux pinning, reducing the efficiency of magnetic field expulsion and broadening the apparent superconducting transition. It is also important to consider the role of the external magnetic field on the transition temperature. It is well established that the application of

a magnetic field can suppress superconductivity in cuprates like YBCO. This notion of critical field and its temperature dependence has already been discussed in the theoretical considerations about YBCO. Increasing the applied magnetic field can shift the apparent transition temperature to lower values or broaden the resistive transition [198–200]

Based on these considerations, the gradual decrease of the Larmor frequency observed below 70 K can be interpreted as the combined effect of magnetic field expulsion by the Meissner effect and field-induced broadening of the superconducting transition. This interpretation suggests that the 70 K TDBS anomaly discussed in the previous section can indeed be attributed to the onset of superconductivity. However, an important question remains: why does the superconducting transition not have a more pronounced influence on the generation of LAWs? In other words, why does the breaking of Cooper pairs by laser heating not produce any significant change in the lattice excitation?

5.5 Outlook: Optical probing and future directions for superconductivity in cuprates

Based on the theoretical considerations introduced at the beginning of this section, together with our TDBS investigations and MOKE measurements, we can conclude that both techniques enable detection of the superconducting transition in YBCO, with an advantage for MOKE. Furthermore, the reliability of the cryostat servo-loop temperature control is supported by the STO structural transition, which, despite light niobium doping, provides a robust temperature marker.

Regarding the determination of the superconducting transition temperature of YBCO, further investigations under true zero-field cooling conditions, such as in [200], are required to confirm whether the observed shift originates from the quasi-zero field cooling configuration used here. Achieving this would require modifications to the cryostat, for instance by incorporating an internal electromagnet to allow controlled field cancellation inside the vacuum chamber.

More broadly, these results pave the way for pressure-dependent time-resolved studies. A key challenge for the cuprate superconductor remains to understand how the superconducting transition can be modified or even transiently controlled by external perturbations. The Bardeen–Cooper–Schrieffer (BCS) theory established the central role of phonons in mediating electron pairing [201], motivating decades of investigations into the interplay between lattice dynamics and superconductivity. In cuprates, both hydrostatic and uniaxial pressure have revealed strong anisotropic effects on T_c: a-axis compression often enhances superconductivity, while c-axis compression tends to suppress it [199]. More recently, ultrafast optical studies have opened a new frontier. Femtosecond mid-infrared pulses resonantly driving phonon modes in YBCO were shown to transiently enhance superconducting-like conductivity above equilibrium T_c, with lifetimes on the order of picoseconds [202, 203]. Time-resolved X-ray diffraction confirmed that such excitation induces anisotropic lattice distortions, such as intra- and inter-bilayer modulations [204]. Even more intriguingly, non-resonant near-infrared excitation has also been reported to induce similar transient superconducting signatures [205], raising fundamental questions about whether the lattice or electronic mechanisms dominate these phenomena.

In this context, our combined use of magneto-optical and photoacoustic techniques to probe YBCO offers a valuable and complementary approach. It is worth noting that we have also extended our ultrafast characterization capabilities to include time-resolved second-harmonic generation (SHG) polarization measurements, in a manner similar to that reported in [206], where SHG polarization was employed to track the “strange metal” behavior in YBCO thin films.

All these methods are intrinsically sensitive to both electronic and structural modifications, making them particularly well-suited to study how strain waves, external magnetic fields, or ultrafast excitations affect superconductivity in complex oxides. Future experiments will exploit giant SAWs,

from the platform described earlier, to selectively drive anisotropic lattice deformations in YBCO, while monitoring their influence on the Meissner response or on magnetic dynamics in adjacent ferromagnetic layers. Such studies would contribute to the broader effort of disentangling the intertwined roles of lattice, charge, and spin degrees of freedom in cuprates and could help clarify the mechanisms underlying both equilibrium and light-induced superconductivity.

6 Conclusion

In this second chapter, theoretical considerations about magnetism were introduced, from general concepts regarding the origin of magnetism and the resulting magnetic phases to the modeling and simulation of the three-temperature model aimed at predicting the influence of ultrafast laser pulses on magnetization and the magnetic precession they can induce. In addition, aspects related to magnetoacoustic effects and interfacial anisotropy were discussed. Furthermore, the optical detection of magnetic phenomena via magneto-optic coupling was also introduced. Building on this theoretical foundation and numerical predictions, several all-optical experimental configurations were implemented to investigate spin-lattice coupling as well as the superconducting transition.

The first experimental investigations were carried out on epitaxial superlattices composed of heterostructures of ultra-thin ferromagnetic layers exhibiting pure out-of-plane magnetization. Thanks to this configuration, no magnetic precession was observed in the Kerr rotation signal, which revealed only changes in magnetization magnitude. Moreover, the samples were designed such that LAWs could be optically generated directly inside the structure and delayed relative to the ultrafast demagnetization. Thanks to this clever design, we demonstrated the possibility of manipulating magnetization via LAWs, paving the way for studies on acoustic control of magnetization through strong transient strain waves.

Magnetization control through strong transient strain was then attempted in a cobalt thin film deposited on an STO:Nb substrate and coated with a 5 nm aluminum layer for protection. The strain was induced by giant surface displacements (60 nm), generated by SAWs optically excited in a ring-shaped geometry and constructively interfering at the ring center. This generation process was theoretically described and modeled. Theoretical predictions were confirmed experimentally via interferometric measurement of the surface displacement. The magnetic state of the cobalt layer was probed via magnetic precession, initiated by a femtosecond laser pump. A permanent magnet was used to establish a magnetic equilibrium with an out-of-plane component, allowing precession detection via normal-incidence MOKE.

Even though both the giant SAWs and the magnetic precession were clearly identified and probed, no acoustically induced variations in the magnetic state were observed. Further investigations aiming to improve the resolution of the detection system are planned, and additional experiments are scheduled.

The final experimental investigations of this chapter were conducted on YBCO in order to determine whether its superconducting transition could be optically probed via TDBS and MOKE. The YBCO thin films investigated were deposited on an STO substrate, which also served for temperature calibration via the TDBS detection of its antiferrodistortive phase transition. Since the LAWs propagating in the substrate were generated from the YBCO layer, a variation in the Brillouin frequency observed below the superconducting transition was suspected to originate from a shift in the critical temperature of YBCO, likely due to quasi-zero-field cooling and the film thickness (200 nm), which allows magnetic flux pinning. To attribute the observed variation in the TDBS signal to the superconducting transition in YBCO, MOKE-based investigations were carried out. For this purpose, a glass plate with cobalt disks was placed onto the sapphire/YBCO sample such that the cobalt disks were in

direct contact with the YBCO. Magnetic precession was optically initiated and probed within a cobalt disk in order to observe Meissner-effect magnetic screening, signaling the onset of superconductivity. A clear change was observed around 70 K, indicating magnetic screening. This confirms that the variation observed in the TDBS signals was indeed linked to changes in YBCO. However, two questions remain: Why is the transition not abrupt? And why does it occur 16 K below the expected 86 K critical temperature? Both questions may find answers in the quasi-zero-field cooling conditions and in an incomplete superconducting transition. To test this hypothesis, experiments under real zero-field cooling conditions with a thicker film could be conducted; however, this would require modifications to the cryostat currently in use.

In conclusion, this chapter has introduced a wide range of magnetic phenomena and demonstrated their resolution at picosecond to nanosecond timescales. Several promising avenues for future experimental investigations have also been outlined.

General conclusion

The purpose of this thesis was to contribute to the development of an all-optical tool for analyzing the acoustic and magnetic properties of materials, with particular emphasis on their ultrafast response at picosecond timescale. To achieve this, theoretical frameworks for the optical generation and detection of acoustic waves were introduced and implemented through numerical modeling. Additional theoretical developments and simulations were also carried out to describe ultrafast optical demagnetization and magnetic precession. Based on these theoretical and numerical predictions, optical experiments using a femtosecond laser source were designed and performed.

The first chapter of this thesis focused on picosecond acoustics. A database of Brillouin frequencies for a wide range of materials was established and successfully compared with values reported in the literature. These results helped guide the development of a custom laser system by our collaborators from the Bordeaux Optics Institute as part of an ANR project. This laser features a tunable repetition rate in the gigahertz range and enabled the successful generation of resonant TDBS signals in materials, enhancing both the generation and detection of longitudinal acoustic waves. Following these results in the linear transparency regime, the reliability of our measurements was confirmed, allowing the study to be extended to the nonlinear generation of longitudinal acoustic waves through multiphoton absorption. To this end, a collaboration was established with chemists from the Rennes Institute of Chemical Sciences to optically investigate organometallic compounds specifically designed for two-photon absorption in the near-infrared biological transparency window. These materials are being developed for biomedical applications such as contrast agents and photothermal therapy, and accurate quantification of their thermal response under optical excitation is essential. By implementing a beam-shaping strategy that enabled the optical pump to propagate continuously along the sample, high fluences were reached without causing damage. The resulting thermal activation was probed through the strength of the generated acoustic waves in a transparent substrate. Additionally, complementary measurements using a single photon with energy equivalent to the two-photon excitation allowed us to estimate the nonlinear absorption cross-section without requiring further sample characterization. The same setup was then used to generate longitudinal acoustic waves through two-photon absorption in transparent solids with a bandgap below the two-photon energy, leading to promising results in strontium titanate ($SrTiO_3$). Similar tests were conducted on materials with a bandgap above the two-photon energy. In lithium niobate ($LiNbO_3$), longitudinal acoustic waves were generated, likely through optical rectification. In contrast, in lanthanum aluminate ($LaAlO_3$), although acoustic waves were not observed, optical signals were detected that are believed to originate from defect states populated by third-order nonlinear optical processes. While these results for the latter two materials are promising, they remain inconclusive at this stage.

The second chapter is dedicated to magneto-acousto-optic phenomena. The first study presented in this chapter focuses on spin–lattice coupling in epitaxial ferromagnetic heterostructures. To optically investigate this coupling, complex heterostructures were designed with the following structure: sapphire/V/Au/[Co X/Ni 3]×5/MgO. In this stack, vanadium acts as a transducer, generating acoustic waves through thermoelastic effects, while the gold layer serves to delay the acoustic wave, making it possible to distinguish its contribution from that of the ultrafast demagnetization in the cobalt/nickel multilayer. Thanks to this design and to our magneto-optical probe setup, samples with different Co/Ni stacking sequences—resulting in different magnetic anisotropies—were characterized both statically and dynamically. Additionally, angle-dependent investigations revealed anisotropic acoustic generation within the vanadium layer. Based on all these results, the spin–lattice coupling was demonstrated as well as its dependence on the effective magnetic anisotropy, which was tuned by varying the cobalt thickness in the ferromagnetic stack. Following this, we investigated the influence

of giant surface acoustic waves on the magnetic state of a thin ferromagnetic cobalt thin film. To this end, an optical ring-shaped pump was added to the setup, along with an optical interferometer to measure the surface displacement at the center of the ring, where the surface acoustic waves interfere constructively and generate important surface displacements. However, despite the successful generation and detection of these giant SAWs and the clear observation of magnetic precession in cobalt, no influence of the induced high pressure on the magnetization was established.

Finally, we explored the possibility of optically probing the superconducting transition of YBCO via picosecond acoustics and magnetic precession. To perform these investigations, a helium-cooled cryostat with optical access was integrated into our experimental setup. In a first study, a YBCO thin film was deposited on an STO substrate and used as a transducer. The objectives of this initial experiments were twofold: first, to calibrate the cryostat temperature via the well-known antiferrodistortive transition of STO; and second, to identify any changes in the optical or acoustic properties of YBCO near its superconducting transition temperature. The antiferrodistortive transition of STO was clearly detected, validating the cryostat temperature regulation. In addition, a small variation around 70 K was observed. However, since this occurs well below the critical temperature of YBCO, it could not be definitively attributed to the superconducting transition. A second experiment was thus carried out to probe the superconducting transition via magnetic precession. For this, a glass plate with cobalt discs was placed in front of the YBCO sample, with the cobalt facing the superconductor. A magnet was positioned at the rear of the cryostat, and magnetic precession was launched and probed in the cobalt discs using our optical pump–probe setup. The aim was to detect changes in the MOKE signal caused by a reduction of the magnetic field at the cobalt position, resulting from Meissner screening in the superconducting YBCO. These measurements were successful, and the variation observed around 70 K using picosecond acoustics was clearly confirmed by magneto-optical probing. One question remains: why is the apparent transition temperature so low? A possible explanation is the quasi-zero-field cooling condition, which may lead to magnetic flux pinning in the sample. Investigating this would require revisiting the cryostat design. Nevertheless, these results pave the way for time-resolved studies of superconducting materials under ultrafast transient perturbations.

In addition to these two chapters, an appendix has been included, presenting investigations of crystallographic structures using second harmonic generation. This appendix briefly introduces the theoretical background of SHG for structural analysis, along with results obtained in thin films and monolayer dichalcogenides. The SHG response of a twisted stack composed of two monolayers is also presented.

It is now possible to state that the objective of designing a fully optical tool to investigate the acoustic and magnetic properties of materials at the picosecond timescale has been achieved. This work has led to several results in the linear transparency regime, nonlinear photoacoustics, spin-lattice coupling, and superconductivity, with a small extension to optical crystallography.

Résumé en français

Cette thèse s'inscrit dans le cadre de l'étude des matériaux et vise à apporter une contribution originale à la compréhension des dynamiques acoustiques et magnétiques à l'échelle picoseconde, ainsi qu'à la possibilité de contrôler ces dynamiques à cette même échelle de temps. En mettant en place différents montages pompe-sonde tout optique femtoseconde et en exploitant les réponses électroniques ultrarapides, de nombreux résultats et pistes de développements futurs ont été établis.

Ce document est composé de trois parties, dont la première est dédiée à l'acoustique picoseconde et, plus précisément, à l'étude des propriétés acoustiques et thermiques des matériaux solides. Cette partie débute par une présentation de la théorie de la génération d'ondes longitudinales à partir de l'absorption d'une impulsion laser femtoseconde. Cette génération ultrarapide d'ondes acoustiques longitudinales peut se résumer comme suit : Dans un premier temps, une impulsion laser femtoseconde est absorbée, en général par un transducteur métallique déposé sur le substrat à étudier. L'impulsion, étant beaucoup plus courte que le temps de réponse de la maille cristalline, excite principalement le nuage électronique, ce qui conduit à une élévation quasi instantanée de la température des électrons. La chaleur est ensuite progressivement transférée à la maille cristalline du transducteur via le couplage électron-phonon. Ce processus est décrit par le modèle à deux températures (température électronique et température de la maille), introduit dans la section Theory: Time-domain Brillouin scattering. Une fois l'énergie de l'impulsion femtoseconde transmise aux électrons puis à la maille de transducteur métallique, ce dernier subit une expansion thermique, induisant une contrainte transitoire locale. Cette contrainte génère l'onde acoustique longitudinale qui se propage par la suite dans le substrat étudié. La propagation de cette onde est détectée par un second faisceau laser, la sonde, qui est à la fois réfléchie à l'interface transducteur/substrat et partiellement rétrodiffusée par l'onde acoustique, comme prédit par Léon Brillouin. En faisant varier continûment le délai entre l'arrivée de la pompe et celle de la sonde, il est possible de résoudre la propagation de l'onde acoustique grâce à l'interférence entre la composante de la sonde réfléchie à l'interface transducteur/substrat et celle partiellement réfléchie par l'onde acoustique. L'oscillation enregistrée dans le signal de réflectivité se produit à la fréquence Brillouin et est reliée à la vitesse de l'onde acoustique par la relation $f_B = (2nv_s/\lambda)\cos\theta$ où n est l'indice optique du substrat à la longueur d'onde λ de la sonde, et θ l'angle d'incidence. La vitesse acoustique v_s, directement reliée à la structure cristalline du substrat, permet d'identifier des directions cristallographiques, des structures, des modifications ou des inhomogénéités acoustiques du substrat.

De plus, ce développement théorique s'accompagne d'une modélisation numérique du modèle à deux températures permettant d'estimer le chauffage induit par une impulsion laser ultracourte, d'une modélisation du profil des impulsions acoustiques, ainsi que d'une modélisation de la détection photoacoustique d'ondes acoustiques générées depuis un film mince. Cette dernière modélisation permet de rendre compte de la réalité de la détection optique d'ondes acoustiques en incluant interférences optiques et réflexions acoustiques.

Après avoir introduit la théorie sous-jacente à la génération et à la détection tout optique d'ondes acoustiques, et avoir fait des prédictions numériques, cette dernière a été mise en pratique sur une dizaine de substrats transparents dont l'une des faces a été recouverte d'un mince film de chrome. Le montage expérimental est présenté sur la Figure 68.

Les différents éléments de ce montage, leurs fonctionnements et leurs utilités sont décrits en détail dans la section TDBS: Experimental setup. On rappellera ici que la première lame demi-onde et le premier cube polarisant servent à ajuster la puissance du laser utilisée pour la pompe et celle utilisée pour la sonde. La sonde est ensuite doublée en fréquence par un cristal BBO, après quoi le résidu du faisceau à 776 nm est arrêté par un filtre. La sonde à 388 nm est ensuite séparée en deux parties

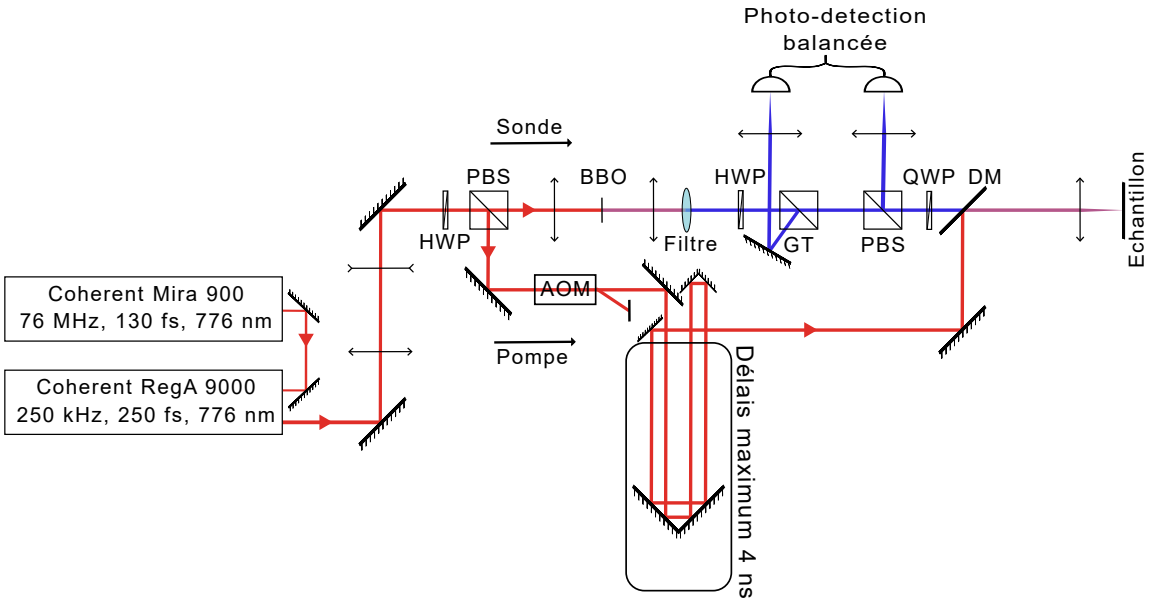

Figure 68: Montage expérimental pompe-sonde femtoseconde pour les mesures Brillouin résolues en temps. HWP : lame demi-onde. PBS : cube polarisant. BBO : β-borate de baryum. GT : Glan-Taylor. QWP : lame quart d'onde. AOM : modulateur acousto-optique. DM : miroir dichroïque.

: l'une sert à sonder l'échantillon, l'autre sert de référence pour la détection balancée, améliorant ainsi le rapport signal sur bruit. La sonde rétrodiffusée par l'échantillon est collectée par un système QWP/PBS. La pompe, quant à elle, est modulée par un acousto-optique. Cette modulation sert de référence à la détection synchrone, grâce à laquelle le signal est enregistré. La pompe passe ensuite par une ligne à délai qui modifie la durée de son trajet et permet de résoudre la propagation des ondes acoustiques. Enfin, pompe et sonde sont superposées par un miroir dichroïque avant d'atteindre l'échantillon.

Les échantillons étudiés avec ce montage expérimental sont reportés dans le Tableau [8], avec les fréquences Brillouin mesurées pour une sonde à 776 nm et à 388 nm. Les vitesses des ondes acoustiques longitudinales, calculées à partir de nos données expérimentales, y sont également présentées et comparées aux valeurs théoriques issues des tenseurs élastiques disponibles dans la littérature.

	$f_B(\lambda)$ (GHz)		Vitesse de l'onde longitudinale ($m \cdot s^{-1}$)	
Substrat	$\lambda = 388$ nm	$\lambda = 776$ nm	Expérience	Littérature
SiO_2	43,9	21,7	5790	5953
MgO (001)	80,3	39,6	8841	9016
MgO (111)	90,0	44,1	9896	9788
STO	105,6	46,2	7608	7842
$SmScO_3$ (110)	/	35,1	/	6846
$GdScO_3$ (110)	73,0	34,5	6481	6728
Al_2O_3 c-face	100,4	/	10889	11200
YAl_2O_3 (001)	80,7	39,4	/	/
GGG	65,1	/	6444	6441
SGGG	64,4	31,1	/	/

Table 8: Fréquences Brillouin déterminées expérimentalement, vitesses des ondes longitudinales déduites de l'expérience et vitesses théoriques calculées à partir des tenseurs élastiques.

Ces premiers résultats en régime linéaire confirment la fiabilité de nos mesures. Les expériences ont ensuite été étendues à la génération directe (sans transducteur) via l'absorption multiphotonique. Pour ce faire, un miroir tournant a été ajouté au montage expérimental entre le miroir dicroïque et l'échantillon (Figure 25). Ce dispositif permet d'imprimer aux faisceaux pompe et sonde une trajectoire elliptique sur la surface de l'échantillon, autorisant ainsi des densités d'énergie de pompe plus élevées sans provoquer de chauffage cumulatif dommageable.

Grâce à cette méthode, nous avons étudié un organométallique prometteur pour des applications en imagerie médicale et en thérapie thermique. Cet organométallique a été conçu pour présenter une absorption à deux photons autour de 800 nm, de façon à pouvoir être activé dans le domaine de transparence de la peau humaine. Il a été déposé par spin-coating sur une lame de verre. L'idée était d'utiliser l'organométallique comme transducteur activable par absorption à deux photons à 1,6 eV, et la lame de verre comme substrat dans lequel seraient détectées les ondes longitudinales générées par la réponse thermique de l'organométallique. Les mesures effectuées avec une pompe à 1,6 eV et une sonde à 3,2 eV ont révélé une réponse quadratique de la génération acoustique en fonction de la densité d'énergie de la pompe. De plus, des mesures réalisées avec pompe et sonde à 3,2 eV ont mis en évidence une dépendance linéaire, comme attendu. La combinaison de ces deux jeux de résultats a permis de simplifier les modèles théoriques et de déterminer l'absorption effective à deux photons ainsi que le relargage effectif de chaleur à l'échelle de la picoseconde. Ces mesures évitent de devoir caractériser d'autres paramètres que la densité de matériau, l'épaisseur du dépôt (mesurée par AFM) et l'indice optique (déterminé par ellipsométrie). Les résultats détaillés figurent dans la section TDBS: 2PA organometallic et dans notre article [207].

Cette méthode expérimentale a également permis de générer directement des ondes acoustiques longitudinales dans $SrTiO_3$ par absorption à deux photons. Cela a été possible car le gap optique de $SrTiO_3$ est inférieur à l'énergie des deux photons (3,2 eV), ce qui permet l'excitation interband d'électrons et l'émission de phonons cohérents lors de la relaxation intrabande dans la bande de conduction. D'autres mesures ont été réalisées sur des matériaux dont le gap optique est supérieur à l'énergie des deux photons, en premier lieu sur un prisme de $LiNbO_3$ puis sur une plaque de $LaAlO_3$. Bien que l'excitation à deux photons ne permette pas de franchir le gap optique dans $LiNbO_3$, une oscillation Brillouin a pu être observée, avec une amplitude suivant une réponse quadratique à la densité d'énergie de la pompe à 1,6 eV. Une hypothèse pour expliquer l'origine de ces ondes longitudinales et leur dépendance quadratique à la puissance de la pompe repose sur le fait que $LiNbO_3$ est utilisé pour générer une émission optique térahertz via la rectification optique. Ce phénomène non linéaire d'ordre deux peut également générer des ondes acoustiques. Toutefois, nos mesures ne permettent pas de conclure définitivement sur l'origine des ondes détectées. Pour ce faire, des investigations complémentaires sont nécessaires, notamment en polarisation (la rectification optique étant fortement sensible à la polarisation) et suivant l'axe de symétrie polaire c.

Enfin, des mesures similaires réalisées sur $LaAlO_3$, isolant à large gap, ont révélé une croissance linéaire du signal électronique en fonction de l'intensité de la pompe, sans oscillations Brillouin détectées. En raison du grand gap optique de $LaAlO_3$ ($\sim 5,6$ eV), trois photons seraient nécessaires pour le franchir, et une dépendance cubique du signal serait attendue. Ce n'est pas le cas et, de plus, l'absence d'oscillations Brillouin supporte le fait que le gap n'a pas été franchi. Les effets optiques non linéaires d'ordre deux (tels que la réctification optique) sont aussi exclus, car $LaAlO_3$ est centrosymétrique. Restent les effets linéaires et ceux d'ordre trois. Le scénario le plus probable, compte tenu des densités d'énergie allant de 100 $mJ \cdot cm^{-2}$ à 1400 $mJ \cdot cm^{-2}$ et de l'absence de signal électronique identifiable en dessous de 100 $mJ \cdot cm^{-2}$, est l'effet Kerr, impliquant la susceptibilité $\chi^{(3)}$, qui varie linéairement avec la puissance de la pompe. Le mécanisme le plus probable est ici le peuplement électronique de niveaux de défauts induits par des lacunes d'oxygène, des impuretés ou des

dislocations.

La deuxième partie de cette thèse porte sur l'étude des dynamiques magnétiques à l'échelle picoseconde. Les objectifs sont d'explorer le contrôle tout optique ultrarapide de l'état magnétique des matériaux en y générant des ondes acoustiques transitoires. Dans cette partie, la détection de la transition supraconductrice de YBCO à partir de sa réflectivité et de l'écrantage magnétique qu'elle induit via l'effet Meissner a aussi été étudiée. Comme pour la première partie, celle-ci commence par une introduction théorique consacrée à l'origine de l'aimantation, aux phases magnétiques courantes, aux effets magnéto-optiques Faraday et Kerr, ainsi qu'aux effets mécano-magnétiques.

Dans cette ouverture théorique, un modèle à trois températures a été introduit et simulé. Ce modèle ajoute une troisième température au modèle à deux températures : la température de spin. C'est à partir de cette température, et de l'équation de Bloch, que l'on estime la désaimantation induite par une impulsion femtoseconde. De plus, nous avons aussi profité de cette introduction théorique pour modéliser la précession magnétique qui peut être induite par notre laser femtoseconde et que nous détectons grâce à l'effet Kerr magnéto-optique.

Les études expérimentales ont été réalisées grâce à des montages optiques basés sur le même principe de résolution temporelle que celui présenté en Figure 68. Cependant, la détection du signal est différente. Ici, aucun faisceau sonde de référence n'est employé, et la paire PBS/QWP collectant habituellement le faisceau réfléchi par l'échantillon est remplacée par un cube séparateur non polarisant 50/50. Avec cette méthode, 50 % de l'intensité incidente et 50 % de l'intensité rétrodiffusée sont perdues. Malgré ces pertes, l'utilisation d'optiques polarisantes est impossible, car la sonde doit être analysée en polarisation afin de mesurer la rotation Kerr induite par l'aimantation de l'échantillon traversé.

La première étude expérimentale de cette partie concerne le couplage spin-réseau dans des hétérostructures ferromagnétiques. Ces structures sont composées comme suit :
$Al_2O_3(11\bar{2}0)$/V(5 nm)/Au(20 nm)/Ni(3 ML)/[Co(X)/Ni(3 ML)]×5/MgO(100 nm). Dans ces structures, les différentes couches sont épitaxiées les unes sur les autres et présentent toutes une structure cubique à faces centrées avec une orientation (111) hors plan, à l'exception du substrat de saphir, hexagonal, et de la couche de vanadium, cubique centrée avec une orientation (110) hors plan. Les épaisseurs des couches ferromagnétiques de cobalt et de nickel sont exprimées en nombre de monocouches (ML) atomiques. Les couches de nickel ont toujours 3 ML, tandis que l'épaisseur des couches de cobalt varie entre 1 et 3 ML. En ajustant l'épaisseur du cobalt, l'anisotropie effective K_{eff}, contrôlant l'orientation hors plan de l'aimantation, est modulée. Cette configuration, présentant une aimantation hors plan avec une force de rappel variable, est idéale car aucune précession magnétique n'est visible dans les mesures (laser incident suivant l'axe d'aimantation), et seule la désaimantation partielle induite par l'impulsion femtoseconde est visible. Afin d'étudier l'influence de la déformation de la maille sur l'aimantation, des ondes acoustiques sont générées optiquement dans l'échantillon par l'impulsion pompe femtoseconde atteignant la couche de vanadium. Les ondes acoustiques longitudinales ainsi générées atteignent l'hétérostructure magnétique avec un délai de 8 ps dû à la traversée de la couche d'or. Ce délai permet de distinguer l'influence de l'onde acoustique de celle de la pompe femtoseconde.

Avant d'examiner l'influence des ondes acoustiques, les échantillons ont été caractérisés statiquement, c'est-à-dire sans pompe femtoseconde, en mesurant la rotation Kerr de la sonde en fonction du champ magnétique appliqué. Ces premières caractérisations ont permis d'établir les cycles d'hystérésis et de circonscrire les études dynamiques à une plage de champs magnétiques précise. Des mesures statiques complémentaires en fonction de la puissance de la sonde ont révélé une puissance limite de la sonde à ne pas dépasser afin de conserver un retournement magnétique abrupt.

Les mesures dynamiques ont fourni des résultats intéressants, en accord avec la théorie. Les signaux

révèlent une variation abrupte de la rotation Kerr de la sonde au temps zéro, suivie d'un lent retour vers l'équilibre magnétique initial. Dans les multicouches avec 2 ML et 3 ML de cobalt, des pics secondaires sont identifiés. Ils correspondent à l'arrivée de l'onde longitudinale issue du vanadium (à $t \simeq 8$ ps) et à sa réflexion depuis l'interface MgO/air (à $t \simeq 28$ ps). Ces pics sont indépendants du champ magnétique appliqué, mais une étude en rotation a montré que leur intensité et leur signe dépendent de l'angle entre la polarisation de la pompe et les axes cristallographiques de la couche de vanadium.

L'analyse de ces résultats montre que l'intensité des pics acoustiques diminue avec K_{eff} dans les échantillons contenant 2 ML et 3 ML de cobalt, démontrant ainsi la modification de l'état d'aimantation par l'onde acoustique. En revanche, l'échantillon contenant 1 ML de cobalt ne suit pas cette tendance et ne présente aucun pic acoustique.

À la suite de ces résultats sur le couplage spin-réseau dans les superstructures ferromagnétiques, nous avons étudié la possibilité de changer l'état d'aimantation du film mince de cobalt en y induisant de fortes déformations de surface. Ces déformations, pouvant atteindre 1,5 % d'élongation, ont été induites optiquement grâce à un laser délivrant des impulsions de 10 µJ à 1064 nm, avec une durée d'impulsion de 600 ps. Les impulsions de ce laser ont été mises en forme pour pomper l'échantillon sous la forme d'un anneau laser. Le déplacement de surface induit en anneau converge ainsi vers son centre, où l'ensemble des ondes de surface interfèrent constructivement et induisent un fort déplacement vertical. Cette méthode de génération, ainsi que le déplacement de surface associé, ont également été simulés numériquement. Pour ces mesures, l'état d'aimantation du cobalt a été mesuré grâce à la précession magnétique, induite au centre de l'anneau par une pompe laser femtoseconde. Cependant, bien que les déplacements de surface et la précession aient bien été générés et mesurés, aucun couplage entre les deux n'a pu être établi.

Une dernière étude, portant sur la détection optique de la transition supraconductrice dans un film mince d'YBCO, a été menée. Dans cette étude, un cryostat muni d'une fenêtre optique a été intégré à notre montage pompe-sonde magnéto-optique. Un échantillon d'YBCO déposé sur un substrat de STO a été placé à l'intérieur et refroidi à l'hélium liquide. Dans un premier temps, des mesures TDBS ont été réalisées. L'idée était ici d'utiliser l'YBCO comme transducteur pour générer des ondes longitudinales dans le substrat de STO et ainsi identifier la transition antiferrodistorsive du substrat attendue autour de 110 K. Cette transition a bien été identifiée, et a permis d'établir que le contrôleur de température de notre cryostat indiquait la bonne valeur — chose qui n'avait pas pu être vérifiée auparavant. De plus, ces mesures ont mis en évidence une autre variation dans les signaux TDBS à 70 K. Cette température étant 16 K en dessous de la température critique de transition de l'YBCO, il n'a pas été possible a priori de l'attribuer directement à cette transition.

Par la suite, une plaque de verre, sur laquelle avaient été réalisés des plots de cobalt, a été placée sur l'échantillon d'YBCO de sorte que les plots soient en contact direct avec la surface de l'YBCO. Un aimant a été placé à l'arrière de l'échantillon, à l'intérieur du cryostat, et déplacé depuis l'extérieur grâce à un second aimant afin d'induire une composante hors plan de l'aimantation dans le cobalt. Cela a permis d'y induire et d'y détecter une précession magnétique. L'idée ici est qu'une transition supraconductrice du film d'YBCO induirait un écrantage magnétique via l'effet Meissner, réduisant ainsi le champ magnétique au niveau du cobalt et modifiant la dynamique de précession. Ces mesures ont permis d'identifier clairement une transition à 70 K et de l'attribuer à la transition supraconductrice de l'YBCO.

Cependant, la température à laquelle cette transition est observée, ainsi que sa variation progressive et non abrupte, doivent être discutées. L'hypothèse la plus probable est que notre cryostat ne permet pas, en l'état, d'assurer des conditions de "zéro-field cooling" et d'éviter le "flux pinning" magnétique. Ces résultats très intéressants ouvrent la voie à l'étude des supraconducteurs sous con-

traintes mécaniques ou pressions transitoires intenses, ce qui est très prometteur, sachant qu'il a été démontré que des variations de pression peuvent engendrer des changements significatifs de la température de transition supraconductrice — à la hausse comme à la baisse.

Nous pouvons conclure ce résumé en disant que de nombreux résultats ont été obtenus, à la fois grâce à des études acoustiques en régime linéaire et non linéaire, mais aussi sur des structures magnétiques complexes et dans des supraconducteurs. De nombreuses techniques expérimentales ont été développées et présentées, ainsi que diverses considérations théoriques et modélisations numériques. Nous dirons également que les structures cristallographiques de monocouches atomiques ainsi que d'empilements twistés ont été étudiées grâce à la SHG. Ces résultats sont fournis en annexe, accompagnés des descriptions des sources laser utilisées et des codes Python ayant permis de modéliser la théorie.

References

References

[1] L. Brillouin. *Diffusion de la lumière et des rayons X par un corps transparent homogène, influence de l'agitation thèrmique*. Masson et Cie, Paris, 1922.

[2] M. Merklin, I.V. Kabakova, A. Zarifi, B. J. Eggleton. 100 years of Brillouin scattering: Historical and future perspectives. *Applied physics reviews*, 9(041306), 2022.

[3] C. W. Ballmann, J. V. Thompson, A. J. Traverso, Z. Meng, M. O. Scully, V. V. Yakovlev. Stimulated Brillouin scattering microscopic imaging. *Nature scientific reports*, 5(18139), 2016.

[4] M. M. Robinson, Y.-X. Yan, E. B. Gamble Jr., L. R. Williams, J. S. Meth, K. A. Nelson. Picosecond impulsive stimulated brillouin scattering: Optical excitation of coherent transverse acoustic waves and application to time-domain investigations of structural phase transitions. *Chemical physics letters*, 112(6):491–496, 1984.

[5] M. Farrar, L.-T. Cheng, Y.-X. Yan, K. A. Nelson. Impulsive stimulated Brillouin scattering in KD2PO4near the structural phase transition. *IEEE journal of quantum electronics*, 22(8):1453 – 1456, 1986.

[6] L.-T. Cheng, K. A. Nelson. Ferroelectric phase transition in RbH2PO4: Picosecond time-resolved impulsive stimulated Brillouin scattering experiments. *Physical review B*, 37(7), 1988.

[7] L.-T. Cheng, K. A. Nelson. Impulsive stimulated Brillouin scattering studies of the ferroelectric phase transition in tris-sarcosine calcium chloride. *Physical review B*, 39(13), 1989.

[8] Y. Zhang, D. Y. Tzou, J. K. Chen. Micro- and nanoscale heat transfer in femtosecond laser processing of metals. *Arxiv*, 2015.

[9] J. K. Chen ,D. Y. Tzou, J. E. Beraun. A semi-classical two-temperature model for ultrafast laser heating. *International journal of heat and mass transfer*, 49(1-2):307–316, 2006.

[10] E. Majchrzak, J. Dziatkiewicz. Analysis of ultrashort laser pulse interactions with metal films using a two-temperature model. *Journal of applied mathematics and computational mechanics*, 14(2):31–39, 2015.

[11] J. Dziatkiewicz, W. Kus, E. Majchrzak, T. Burczynski, L. Turchan. Bioinspired identification of parameters in microscale heat transfer. *Journal for multiscale computational engineering*, 12(1):79–89, 2014.

[12] S. T. Murphy, Y. Giret, S. L. Daraszewicz, A. C. Lim, A. L. Shluger, K. Tanimura, D. M. Duffy. Contribution of electronic excitation to the structural evolution of ultrafast laser-irradiated tungsten nanofilms. *Physical Review B*, 93(104105), 2016.

[13] D. Y. Tzou. *Macro- to Microscale Heat Transfer: The Lagging Behavior, Chapter I*. John Wiley & Sons, Ltd., 2014.

[14] M. I. Kaganov, I. M. Lifshitz, L. V.Tanatarov. Relaxation between Electrons and the Crystalline Lattice. *Soviet Physics JETP*, 4(2):173–178, 1957.

[15] T. Q. Qiu, C. L. Tien. Size Effects on Nonequilibrium Laser Heating of Metal Films. *ASME Journal of Heat and Mass Transfer*, 115(4):842–847, 1993.

[16] L. M. Falicov, H. Stachowiak. Theory of the de Haas-van Alphen Effect in a System of Coupled Orbits. Application to Magnesium. *Physical Review B*, 147(2):505–515, 1966.

[17] A. I. Kiselev, L. A. Akashev, V. I. Kononenko. Effective Electron Mass in Melts of Aluminum, Cerium, and Al–3 at.% Ce Binary System. *Technical Physics*, 49(3):302–305, 2004.

[18] B. Bosacchi, J. B. Ketterson, I . R. Windmiller. Measurement and Inversion of de Haas-van Alphen Data in Gold. *Physical Review B*, 4(1197), 1971.

[19] J. E. Graebner, J. A. Marcus. de Haas-van Alphen Effect in Antiferromagnetic Chromium. *Physical Review Journals Archive*, 175(2):659–673, 1968.

[20] A. S. Belozerov, A. A. Katanin, V. I. Anisimov. Itinerant magnetism of chromium under pressure: a DFT+DMFT study. *Journal of Physics: Condensed Matter*, 33(385601), 2021.

[21] D. L. Martin. Specific Heats below 3°K of Pure Copper, Silver, and Gold, and of Extremely Dilute Gold-Transition-Metal Alloys. *Physical Review Journals Archive*, 170(650), 1968.

[22] S. O. Kasap. *Principles of electronic materials and devices, fourth edition*. McGraw-Hill Education, 2018.

[23] N.W. Ashcroft, N. D. Mermin. *Solid State Physics*. Saunders Collage Publishing, 1976.

[24] C. Kittel. *Introduction to Solid State Physics, Eighth edition*. John Wiley and Sons, Inc, 2004.

[25] K. Maezawa, M. Takahashi, Y. Saito. de Haas-van Alphen Effect in Cobalt. *Journal of the Physical Society of Japan*, 45:869–874, 1978.

[26] D. C. Tsui. de Haas-van Alphen Effect and Electronic Band Structure of Nickel. *Physical Review Journals Archive*, 164(2):669–683, 1967.

[27] A G Mathewson, H Aronsson, L G Bernland. The conduction electron optical mass in pure silver. *Journal of Physics F: Metal Physics*, 2:39–41, 1972.

[28] C. Kittel. *Physique de l'état solide, 8em édition*. Dunod, 2019.

[29] V. E. Alexopoulou, A. P. Markopoulo. A Critical Assessment Regarding Two-Temperature Models: An Investigation of the Different Forms of Two-Temperature Models, the Various Ultrashort Pulsed Laser Models and Computational Methods. *Archives of Computational Methods in Engineering*, 31:93–123, 2024.

[30] P.-T. Tai, P. Yu, J. Tang. Laser-Fluence Dependence of Acoustic Phonon Excitation in Metallic Thin Films and Determination of the Grüneisen Parameter. *The Journal of Physical Chemistry C*, 113(33), 2009.

[31] D. G. Cahill, W. K. Ford, K. E. Goodson, G. D. Mahan, A. Majumdar, H. J. Maris, R. Merlin, S. R. Phillpot. Nanoscale thermal transport. *Journal of Applied Physics*, 93(2):793–818, 2003.

[32] P. E. Hopkins. Thermal Transport across Solid Interfaces with Nanoscale Imperfections: Effects of Roughness, Disorder, Dislocations, and Bonding on Thermal Boundary Conductance. *International Scholarly Research Notices*, 2013(1), 2013.

[33] S. I. Anisimov, B. L. Kapeliovich, T. L. Perel'man . Electron emission from metal surfaces exposed to ultrashort laser pulses. *Soviet Physics JETP*, 39(2):375–377, 1974.

[34] W. M. Haynes, D. R. Lide, T. J. Bruno. *CRC Handbook of Chemistry and Physics 97th Edition*. CRC Press, Taylor & Francis Group, 2016.

[35] J. Lemaitre, J.-L. Chaboche, A. Benallal. *Mécanique des matériaux solides 3e édition*. Dunod, 2020.

[36] L. Landau and E. Lifshitz. *Course of theoretical physics volume 7: Theory of elasticity*. Mir editions, 1967.

[37] M. A. Slawinski. On elastic-wave propagation in anisotropic media: reflection/refraction laws, raytracing, and traveltime inversion. *Thesis*, 1996.

[38] C. Thomsen, H. T. Grahn, H. J. Maris, J. Tauc. Surface generation and detection of phonons by picosecond light pulses. *Physical review*, 34(6), 1986.

[39] H.-N. Lin, R. J. Stoner, H. J. Maris, J. Tauc. Phonon attenuation and velocity measurements in transparent materials by picosecond acoustic interferometry. *Journal of Applied Physics*, 69(7):3816–3822, 1991.

[40] D. Mounier, K. Mansour, T. Pezeril, G. Vaudel, P. Ruello, P. Picart, J.-M. Breteau, V. Gusev. 4x4 matrix algebra in the theory of optical detection of picosecond acoustic pulses in anisotropic media. *Chinese journal of physics*, 49(1):191–200, 2011.

[41] P. Babilotte, P. Ruello, D. Mounier, T. Pezeril, G. Vaudel, J.-M. Breteau, V. Gusev, K. Blary. Femtosecond laser generation and detection of high-frequency acoustic phonons in GaAs semiconductors. *Physical review B*, 81(245207), 2010.

[42] V. Gusev. Detection of nonlinear picosecond acoustic pulses by time-resolved Brillouin scattering. *Journal of applied physics*, 116(6), 2014.

[43] J. F. Nye. *Physical Properties of Crystals : their representation by tensors and matrices*. Clarendon Press, Oxford University press, 1985.

[44] T. Pezeril. Laser generation and detection of ultrafast shear acoustic waves in solids and liquids. *Optics & Laser Technology*, 83:177–188, 2016.

[45] A. Polian, Dung Vo-Thanh, P. Richet. Elastic properties of a-SiO2 up to 2300 K from Brillouin scattering measurements. *Europhysics Letters*, 57(3):375–381, 2002.

[46] B. B. Karki, L. Stixrude, S. J. Clark, M. C. Warren, G. J. Ackland, J. Crain. Structure and elasticity of MgO at high pressure. *American Mineralogist*, 82:51–60, 1997.

[47] J. Deschamps, Y. Kai, J. Lem, I. Chaban, A. Lomonosov, A. Anane, S. E. Kooi, K. A. Nelson, T. Pezeril. Additive laser excitation of giant nonlinear surface acoustic wave pulses. *Physical Review Applied*, 20(044044), 2023.

[48] B. Samia, S. Salima. First principles study of the structural, elastic and thermodynamic properties of the cubic perovskite-type SrTiO3. *Modelling, Measurement and Control B*, 87(4):230–235, 2018.

[49] K. A. Pestka, E. S. Scott, Y. Le Page. Measurement of the elastic tensor of SmScO3 and NdScO3 using resonant ultrasound spectroscopy with ab initio calculations. *AIP Advances*, 1(3), 2011.

[50] S. N. Amanyan, P. A. Arsen'ev, Kh. S. Bagdasarov, A. M. Kevorkov, D. I. Korolev, A. V. Potemkin, V. V. Femin . Synthesis and examination of GdScO3 single crystals activated by Nd 3+. *Journal of Applied Spectroscopy*, 38:343–348, 1983.

[51] K. A. Pestka, J. D. Maynard, A. Soukiassian, X. X. Xi, D. G. Schlom, Y. Le Page, M. Bernhagen, P. Reiche, R. Uecker. Experimental measurement of the elastic constants of GdScO3 via resonant ultrasound spectroscopy utilizing ab initio calculations. *Applied Physics Letters*, 92(11), 2008.

[52] J. Ahn. Thermal and optical properties of gadolinium gallium garnet. *Materials Research Bulletin*, 17(11):1393–1399, 1982.

[53] Y. hang. Doctoral dissertation, High-pressure shock compression behaviors of Gd3Ga5O12, TiB2 and B4C. *Kumamoto University*, 2006.

[54] J. R. Hortensius, D. Afanasiev, A. Sasani, E. Bousquet, A. D. Caviglia. Ultrafast strain engineering and coherent structural dynamics from resonantly driven optical phonons in $LaAlO_3$. *npj, Quantum Materials*, 5(95), 2020.

[55] M. Först, C. Manzoni, S. Kaiser, Y. Tomioka, Y. Tokura, R. Merlin, A. Cavalleri. Nonlinear phononics as an ultrafast route to lattice control. *Nature Physics*, 7:854–856, 2011.

[56] J. M. Merkes, L. Zhu, S. B. Bahukhandi, M. Rueping, F. Kiessling, S. Banala. Photoacoustic Imaging Probes Based on Tetrapyrroles and Related Compounds. *International Journal of Molecular Sciences*, 21(9), 2020.

[57] W. Hu, P. N. Prasad, W. Huang. Manipulating the Dynamics of Dark Excited States in Organic Materials for Phototheranostics. *Accounts of Chemical Research*, 54(3), 2020.

[58] C. Xu, R. Ye, H. Shen, J. W. Y. Lam, Z. Zhao, B. Z. Tang. Molecular Motion and Nonradiative Decay: Towards Efficient Photothermal and Photoacoustic Systems. *Angewandte Chemie International Edition*, 61(30), 2022.

[59] A. E. Triadon, G. Grelaud, N. Richy, O. Mongin, G. J. Moxey, I. M. Dixon, X. Yang, G. Wang, A. Barlow, J. Rault-Berthelot, M. P. Cifuentes, M. G. Humphrey, F. Paul. Linear and Third-Order Nonlinear Optical Properties of Fe(η5-C5 Me 5)(κ2-dppe)- and trans-Ru(κ2-dppe)2-Alkynyl Complexes Containing 2-Fluorenyl End Groups. *Organometallics*, 37:2245–2262, 2018.

[60] G. Vaudel, T. Pezeril, A. Lomonosov, M. Lejman, P. Ruello, V. Gusev. Laser generation of hypersound by a terahertz photo-Dember electric field in a piezoelectric GaAs semiconductor. *Physical Review B*, 90(1), 2014.

[61] T. Parpiiev, M. Servol, M. Lorenc, I. Chaban, R. Lefort, E. Collet, H. Cailleau, P. Ruello, N. Daro, G. Chastanet, T. Pezeril. Ultrafast non-thermal laser excitation of gigahertz longitudinal and shear acoustic waves in spin-crossover molecular crystals [Fe(PM–AzA)2(NCS)2]. *Applied Physics Letters*, 111(15), 2017.

[62] S. P. Zeuschner, J.-E. Pudell, A. von Reppert, M. Deb, E. Popova, N. Keller, M. Rössle, M. Herzog, M. Bargheer. Measurement of transient strain induced by two-photon excitation. *Physical Review Research*, 2(022013), 2020.

[63] I. Chaban, R. Deska, G. Privault, E. Trzop, M. Lorenc, S. E. Kooi, K. A. Nelson, M. Samoc, K. Matczyszyn, T. Pezeril. Nonlinear Optical Absorption in Nanoscale Films Revealed through Ultrafast Acoustics. *Nano Letters*, 22(11):4362–4367, 2022.

[64] N. Liaros, J. T. Fourkas. The Characterization of Absorptive Nonlinearities. *Laser & Photonics Reviews*, 11(5), 2017.

[65] F. Opoku, K. K. Govender, C. G. C. E. van Sittert, P. P. Govender. Hybrid DFT study of MWCNT/Zr-doped SrTiO3 heterostructure: Hydrogen production, electronic properties and charge Carrier mediator role of Zr4+ ion. *International Journal of Hydrogen Energy*, 43(49):22253–22264, 2018.

[66] P. Ruello and V. Gusev. Physical mechanisms of coherent acoustic phonons generation by ultrafast laser action. *Ultrasonics*, 56:21–35, 2015.

[67] D. E. Zelmon, D. L. Small, D. Jundt. Infrared corrected Sellmeier coefficients for congruently grown lithium niobate and 5 mol.% magnesium oxide–doped lithium niobate. *Journal of the Optical Society of America B*, 14(12):3319–3322, 1997.

[68] H. Ogi, Y. Kawasaki, M. Hirao. Acoustic spectroscopy of lithium niobate: Elastic and piezoelectric coefficients. *Journal of Applied Physics*, 92(5):2451–2456, 2002.

[69] A. R. Zanatta. The optical bandgap of lithium niobate (LiNbO3) and its dependence with temperature. *Results in Physics*, 39(105736), 2022.

[70] M. Lejman, G. Vaudel, I. C. Infante, I. Chaban, T. Pezeril, M. Edely, G. F. Nataf, M. Guennou, J. Kreisel, V. E. Gusev, B. Dkhil, P. Ruello. Ultrafast acousto-optic mode conversion in optically birefringent ferroelectrics. *Nature communications*, 7(12345), 2016.

[71] G. Murtaza, I. Ahmad. Shift of indirect to direct bandgap and optical response of LaAlO3 under pressure. *Journal of Applied Physics*, 111(123116), 2012.

[72] M. Rizwan, S. Gul, T. Iqbal, U. Mushtaq, M. H. Farooq, M. Farman, R. Bibi, M. Ijaz. A review on perovskite lanthanum aluminate ($LaAlO_3$), its properties and applications. *Materials Research Express*, 6(112001), 2019.

[73] M. Kobayashi, Y. Minami, C. L. Johnson, P. D. Salmans, N. R. Ellsworth, J. Takeda, J. A. Johnson, I. Katayama. High-Acquisition-Rate Single-Shot Pump-Probe Measurements Using Time-Stretching Method. *Scientific Reports*, 6(37614), 2016.

[74] M. Kobayashi, Y. Arashida, G. Yamashita, E. Matsubara, M. Ashida, J. A. Johnson, I. Katayama. Fast-frame single-shot pump-probe spectroscopy with chirped-fiber Bragg gratings. *Optics Letters*, 44(1):163–166, 2019.

[75] R. Tamaki, M. Suzuki, S. Kusaba, J. Takeda, I. Katayama. Ultrafast pump-probe spectroscopy via chirped-pulse up-conversion with dispersion compensation. *Optics Express*, 31(24):40142–40150, 2023.

[76] T. Yu, J. Yang, Z. Li, X. Wu, Y. Fang, Y. Yang, Y. Song. Single-shot pump-probe technique by the combination of an echelon and a grating with a time window of 109 ps. *Journal of Optics*, 26(6), 2024.

[77] A. V. Kimel, M. Li. Writing magnetic memory with ultrashort light pulses. *Nature Reviews Materials*, 4:189–200, 2019.

[78] J. Stöhr, H. C. Siegmann. *Magnetism. From fundamentals to nanoscale dynamics*. Springer, Solid-state sciences 152, 2006.

[79] M. Getzlaff. *Fundamentals of Magnetism*. Springer, 2008.

[80] M. Reis. *Fundamentals of Magnetism*. Elsevier, 2013.

[81] L. Néel. Propriétés magnétiques de l'état métallique et énergie d'interaction entre atomes magnétiques. *Annales de physique*, 11(7):232 – 279, 1936.

[82] M. Mézard, G. Parisi, N. Sourlas, G. Toulouse, M. Virasoro. Nature of the Spin-Glass Phase. *Physical review letters*, 52(13):1156, 1984.

[83] A. J. Bray, M. A. Moore. Chaotic Nature of the Spin-Glass Phase. *Physical review letters*, 58(1):57, 1987.

[84] P. Schiffer, A. P. Ramirez, D. A. Huse, P. L. Gammel, U. Yaron, D.J. Bishop, A. J. Valentino. Frustration Induced Spin Freezing in a Site-Ordered Magnet: Gadolinium Gallium Garnet. *Physical Review Letters*, 74(12):2379–2382, 1995.

[85] Y. Tokura, N. Kanazawa. Magnetic Skyrmion Materials. *Chemical reviews*, 121(5):2857–2897, 2021.

[86] N. A. Clark. Ferromagnetic ferrofluids. *Nature*, 504:229–230, 2013.

[87] C. P. Bean, J. D. Livingston. Superparamagnetism. *Journal of applied physics*, 30(4), 1959.

[88] A. K. Zvezdin, V. A. Kotov. *Modern Magnetooptics and Magnetooptical Materials*. Taylor & Francis Group, 1997.

[89] S. Visnovsky. *Optics in Magnetic Multilayers and Nanostructures*. Taylor & Francis Group, 1997.

[90] H. S. Bennett, E. A. Stern. Faraday effect in solid. *Physical review*, 137(2A), 1965.

[91] H. R. Hulme. The Faraday effect in ferromagnetics. *Royal society*, 135(826), 1932.

[92] Z. Q. Qiu, S. D. Bader. Surface magneto-optic Kerr effect. *Review of Scientific Instruments*, 71(3):1243–1255, 2000.

[93] M. J. Freiser. A survey of magnetooptic effects. *IEEE*, 4(2):152 – 161, 1968.

[94] P. M. Oppeneer. Magneto-Optical Kerr Spectra. *Handbook of Magnetic Materials*, 13:229–422, 2001.

[95] P. M. Oppeneer. Magneto-optical spectroscopy in the valence-band energy regime: relationship to the magnetocrystalline anisotropy. *Journal of Magnetism and Magnetic Materials*, 188:275–285, 1998.

[96] N. P. Armitage. Constraints on Jones transmission matrices from time-reversal invariance and discrete spatial symmetries. *Physical Review B*, 90(035135), 2014.

[97] J. McCord. Progress in magnetic domain observation by advanced magneto-optical microscopy. *Journal of Physics D: Applied Physics*, 48(333001), 2015.

[98] M. Mansuripur. *The Physical Principles of Magneto-optical Recording*. Cambridge University Press, 1998.

[99] A. Kirilyuk, A. V. Kimel, T. Rasing. Ultrafast optical manipulation of magnetic order. *Reviews of modern physics*, 82, 2010.

[100] B. Koopmans, G. Malinowski, F. Dalla Longa, D Steiauf, M Fähnle, T Roth, M Cinchetti, M Aeschlimann. Explaining the paradoxical diversity of ultrafast laser-induced demagnetization. *Nature Materials*, 9:259–265, 2009.

[101] E. Carpene. Ultrafast laser irradiation of metals: Beyond the two-temperature model. *Physical Review B*, 74(024301), 2006.

[102] R. J. Elliott. Theory of the Effect of Spin-Orbit Coupling on Magnetic Resonance in Some Semiconductors. *Physical review*, 96(2), 1954.

[103] V. Kamberský. On ferromagnetic resonance damping in metals. *Czechoslovak Journal of Physics B*, 26:1366–1383, 1976.

[104] T. E. Mølholt, R. Mantovan, H. P. Gunnlaugsson, D. Naidoo, S. Ólafsson, K. Bharuth-Ram, M. Fanciulli, K. Johnston, Y. Kobayashi, G. Langouche, H. Masenda, R. Sielemann, G. Weyer, H. P. Gíslason. Observation of spin-lattice relaxations of dilute Fe^{3+} in MgO by Mössbauer spectroscopy. *Hyperfine Interactions*, 197:89–94, 2010.

[105] M. Günther, S. Kamusella, R. Sarkar, T. Goltz, H. Luetkens, G. Pascua, S.-H. Do, K.-Y. Choi, H. D. Zhou, C. G. F. Blum, S. Wurmehl, B. Büchner, H.-H. Klauss. Magnetic order and spin dynamics in $La_2O_2Fe_2OSe_2$ probed by ^{57}Fe Mössbauer, ^{139}La NMR, and muon-spin relaxation spectroscopy. *Physical Review B*, 90(184408), 2014.

[106] K. A. Béres, L. Kótai, E. Kuzmann, L. Machala, P. Novák, M. Pápai, S. Kubuki, Z. Homonnay. Unusual relaxation phenomena in the ^{57}Fe Mössbauer spectra of FeX_3 (X=Cl, NO_3, ClO_4, MnO_4, $1/2(S_2O_8)$) complex salts containing urea, methylated urea, chlorido or aquo ligands: studies on the influence of the ligand sphere and deuteration. *Journal of Radioanalytical and Nuclear Chemistry*, 334:873–889, 2024.

[107] E. Beaurepaire, J.-C. Merle, A. Daunois, J.-Y. Bigot. Ultrafast Spin Dynamics in Ferromagnetic Nickel. *Physical Review Letters*, 76(22):4250–4253, 1996.

[108] D. Zahn, F. Jakobs, H. Seiler, T. A. Butcher, D. Engel, J. Vorberger, U. Atxitia, Y. W. Windsor, R. Ernstorfer. Intrinsic energy flow in laser-excited 3d ferromagnets. *Physical Review Research*, 4, 2022.

[109] J.-Y. Bigot, M. Vomir, L. H. F. Andrade, E. Beaurepaire. Ultrafast magnetization dynamics in ferromagnetic cobalt: The role of the anisotropy. *Chemical Physics*, 318:137–146, 2005.

[110] U. Ritzmann, P. M. Oppeneer, P. Maldonado. Theory of out-of-equilibrium electron and phonon dynamics in metals after femtosecond laser excitation. *Physical Review B*, 102(214305), 2020.

[111] B. Y. Mueller, A. Baral, S. Vollmar, M. Cinchetti, M. Aeschlimann, H. C. Schneider, B. Rethfeld. Feedback Effect during Ultrafast Demagnetization Dynamics in Ferromagnets. *Physical Review Letters*, 111(167202), 2013.

[112] R. Li, H. E. Elsayed-Ali, J. Chen, D. Dhankhar, A. Krishnamoorthi, P. M. Rentzepis. Ultrafast time-resolved structural changes of thin-film ferromagnetic metal heated with femtosecond optical pulses. *The Journal of Chemical Physics*, 151(12), 2019.

[113] P.-W. Ma, S. L. Dudarev. Spin-lattice-electron dynamics simulations of magnetic materials. *Physical Review B*, 85(184301), 2012.

[114] E. Du Trémolet de Lacheisserie. *Magnétisme (Tome II)*. EDP sciences, 1999.

[115] B. D. Cullity, C. D. Graham. *Introduction to Magnetic Materials, Second Edition*. IEEE Press, Wiley, 2011.

[116] V. Apicella, C. S. Clemente, D. Davino, D. Leone, C. Visone. Review of Modeling and Control of Magnetostrictive Actuators. *MDPI Actuators*, 8(45), 2019.

[117] G. Riesgo, L. Elbaile, J. Carrizo, R. D. Crespo, M. Á. García, Y. Torres, J. Á. García. Villari Effect at Low Strain in Magnetoactive Materials. *MDPI Materials*, 13(2472), 2020.

[118] B. Spetzler, E. V. Golubeva, R.-M. Friedrich, S. Zabel, C. Kirchhof, D. Meyners, J. McCord, F. Faupel. Magnetoelastic Coupling and Delta-E Effect in Magnetoelectric Torsion Mode Resonators. *MDPI Sensors*, 21(2022), 2021.

[119] A. S. Borovik-Romanov. Piezomagnetism in the antiferromagnetic fluorides of cobalt and manganese. *Soviet Physics JETP*, 11(4):786–793, 1960.

[120] G. T. Rado, V. J. Folen. Magnetoelectric Effects in Antiferromagnetics. *Journal of Applied Physics*, 33(3):1126–1132, 1962.

[121] S. Sahoo, C. Binek. Piezomagnetism in epitaxial Cr2O3 thin films and spintronic applications. *Philosophical Magazine Letters*, 87(3-4):259–268, 2007.

[122] E. A. Eliseev, A. N. Morozovska, M. D. Glinchuk, B. Y. Zaulychny, V. V. Skorokhod, R. Blinc. Surface-induced piezomagnetic, piezoelectric, and linear magnetoelectric effects in nanosystems. *Physical Review B*, 82(085408), 2010.

[123] M. M. Vospon. Fundamentals of Multiferroic Materials and Their Possible Applications. *Critical Reviews in Solid State and Materials Sciences*, 40(4):223–250, 2015.

[124] M. Jaime, A. Saul, M. Salamon, V. S. Zapf, N. Harrison, T. Durakiewicz, J. C. Lashley, D. A. Andersson, C. R. Stanek, J. L. Smith, K. Gofryk. Piezomagnetism and magnetoelastic memory in uranium dioxide. *Nature Communications*, 8(9), 2017.

[125] D. Boldrin, A. P. Mihai, B. Zou, J. Zemen, R. Thompson, E. Ware, B. V. Neamtu, L. Ghivelder, B. Esser, D. W. McComb, P. Petrov, L. F. Cohen. Giant Piezomagnetism in Mn_3NiN. *ACS Applied Materials & Interfaces*, 10(22), 2018.

[126] A. S. Disa, M. Fechner, T. F. Nova, B. Liu, M. Först, D. Prabhakaran, P. G. Radaelli, A. Cavalleri. Polarizing an antiferromagnet by optical engineering of the crystal field. *Nature Physics*, 16:937–941, 2020.

[127] T. G. Phillips, R. L. Townsend, R. L. White. Piezomagnetism of α-Fe2O3, and the Magnetoelastic Tensor of Fe3+ in Al2O3. *Physical Review*, 162(2), 1967.

[128] D. N. Astrov. Magnetoelectric effect in chromium oxide. *Soviet Physics JETP*, 13(4):729–733, 1961.

[129] A. Prohl. *Computational Micromagnetism*. Springer Fachmedien Wiesbaden GmbH, 2001.

[130] M. Lakshmanan. The fascinating world of the Landau–Lifshitz–Gilbert equation: an overview. *Philosophical Transactions of the Royal Society A*, 369:1280–1300, 2011.

[131] U. Atxitia, O. Chubykalo-Fesenko. Ultrafast magnetization dynamics rates within the Landau-Lifshitz-Bloch model. *Physical Review B*, 84(144414), 2011.

[132] R. Behbahani Diba, M. L. Plumer, I. Saika-Voivod. Ultrafast magnetization dynamics rates within the Landau-Lifshitz-Bloch model. *Advances in Physics: X*, 9(01):1–30, 2024.

[133] P. F. Carcia. Perpendicular magnetic anisotropy in Pd/Co and Pt/Co thin-film layered structures. *Journal of Applied Physics*, 63(10):5066–5073, 1988.

[134] M. T. Johnson, R. Jungblut, P.J. Kelly, F. J. A. den Breeder. Perpendicular magnetic anisotropy of multilayers: recent insights. *Journal of Magnetism and Magnetic Materials*, 148:118–124, 1995.

[135] B. Heinrich, Z. Celinski, J. F. Cochran, A. S. Arrott, K. Myrtle. Magnetic anisotropies in single and multilayered structures. *Journal of Applied Physics*, 70(10):5769–5774, 1991.

[136] T. Jarlborg. Spin fluctuations, electron–phonon coupling and superconductivity in near-magnetic elementary metals–Fe, Co, Ni and Pd. *Physica C: Superconductivity*, 385(4):513–524, 2003.

[137] P. Modak, A. K. Verma, R. S. Rao, B. K. Godwal, R. Jeanloz. Ab initio total-energy and phonon calculations of Co at high pressures. *Physical Review B*, 74(012103), 2006.

[138] G. Steinle-Neumann. Magneto-elastic effects in compressed cobalt from first-principles. *Physical Review B*, 77(104109), 2008.

[139] R. Torchio, C. Marini, Y. O. Kvashnin, I. Kantor, O. Mathon, G. Garbarino, C. Meneghini, S. Anzellini, F. Occelli, P. Bruno, A. Dewaele, S. Pascarelli. Structure and magnetism of cobalt at high pressure and low temperature. *Physical Review B*, 94(024429), 2016.

[140] S. Girod, M. Gottwald, S. Andrieu, S. Mangin, J. McCord et Al. Strong perpendicular magnetic anisotropy in Ni/Co(111) single crystal superlattices. *Applied physics letters*, 94(26), 2009.

[141] M. Gottwald, S. Andrieu, F. Gimbert, E. Shipton, L. Calmels, C. Magen, E. Snoeck, M. Liberati, T. Hauet, E. Arenholz, S. Mangin, E. E. Fullerton. Co/Ni(111) superlattices studied by microscopy, x-ray absorption, and ab initio calculations. *Physical Review B*, 86, 2012.

[142] S. Andrieu, T. Hauet, M. Gottwald, A. Rajanikanth, L. Calmels et Al. Co/Ni multilayers for spintronics: high spin-polarization and tunable magnetic anisotropy. *Physical review materials*, 2(6):064410 (1–12), 2018.

[143] G. H. O. Daalderop, P. J. Kelly, F. J. A. den Broeder. Prediction and confirmation of perpendicular magnetic anisotropy in Co/Ni multilayers. *Physical Review Letters*, 68(682), 1992.

[144] C. Pfaff, T. Pezeril, R. Arras, L. Calmels, V. Cherruault, S. Andrieu, K. Dumesnil, J. Gorchon, T. Hauet. Strain-induced magnetic moment variations at the picosecond timescale. *Physical Review B*, 111(064405), 2025.

[145] A. Paul, E. Kentzinger, U. Rücker, D. E. Bürgler, P. Grünberg. Nonuniform and sequential magnetization reversal via domain structure formation for multilayered system with grain size induced enhanced exchange bias. *The European Physical Journal B*, 45:249–260, 2005.

[146] V. D. Tsiantos, T. Schrefl, D. Suess, W. Scholz, J. Fidler, J. M. Gonzales. Micromagnetic simulations of magnetization reversal in Co/Ni multilayers. *Physica B*, 306:38–43, 2001.

[147] J. E. Davies, O. Hellwig, E. E. Fullerton, M. Winklhofer, R. D. Shull, K. Liu. Frustration driven stripe domain formation in Co/Pt multilayer film. *Applied Physics Letters*, 95(022505), 2009.

[148] A. V. Scherbakov, A. S. Salasyuk, A. V. Akimov, X. Liu, M. Bombeck, C. Brüggemann, D. R. Yakovlev, V. F. Sapega, J. K. Furdyna, M. Bayer. Coherent Magnetization Precession in Ferromagnetic (Ga,Mn)As Induced by Picosecond Acoustic Pulses. *Physical Review Letters*, 105(117204), 2010.

[149] L. Thevenard, E. Peronne, C. Gourdon, C. Testelin, M. Cubukcu, E. Charron, S. Vincent, A. Lemaître, B. Perrin. Effect of picosecond strain pulses on thin layers of the ferromagnetic semiconductor (Ga,Mn)(As,P). *Physical Review B*, 82(104422), 2010.

[150] M. Bombeck, A. S. Salasyuk, B. A. Glavin, A. V. Scherbakov, C. Bruggemann, D. R. Yakovlev, V. F. Sapega, X. Liu, J. K. Furdyna, A. V. Akimov, M. Bayer. Excitation of spin waves in ferromagnetic (Ga,Mn)As layers by picosecond strain pulses. *Physical Review B*, 85(195324), 2012.

[151] J.-W. Kim, M. Vomir, J.-Y. Bigot. Ultrafast Magnetoacoustics in Nickel Films. *Physical Review Letters*, 109(166601), 2012.

[152] O. Kovalenko, T. Pezeril, V. V. Temnov. New Concept for Magnetization Switching by Ultrafast Acoustic Pulses. *Physical Review Letters*, 110(266602), 2013.

[153] D. Afanasiev, I. Razdolski, K. M. Skibinsky, D. Bolotin, S. V. Yagupov, M. B. Strugatsky, A. Kirilyuk, Th. Rasing, A. V. Kimel. Laser Excitation of Lattice-Driven Anharmonic Magnetization Dynamics in Dielectric $FeBO_3$. *Physical Review Letters*, 112(147402), 2014.

[154] A. K. Harman, S. Ninomiya, S. Adachi. Optical constants of sapphire (α-Al2O3) single crystals. *Journal of Applied Physics*, 76(12), 1994.

[155] H. Yao, C. H. Yan. Anisotropic optical responses of sapphire (α-Al2O3) single crystals. *Journal of Applied Physics*, 85(9), 1999.

[156] P. Romaniello, P. L. de Boeij. Optical properties of bcc transition metals in the range 0-40 eV. *Physical Review B*, 73(075115), 2006.

[157] M. Gottwald, S. Girod, S. Andrieu, S. Mangin. Tuneable perpendicular magnetic anisotropy in single crystal [Co/Ni](111) superlattices. *IOP Conference Series: Materials Science and Engineering*, 12(012018), 2010.

[158] M. Gottwald. New model systems with perpendicular magnetic anisotropy for spin transfer torque experiments. *Thesis*, 2011.

[159] M. Deb, E. Popova, M. Hehn, N. Keller, S. Mangin, G. Malinowski. Picosecond acoustic-excitation-driven ultrafast magnetization dynamics in dielectric Bi-substituted yttrium iron garnet. *Physical Review B*, 98(174407), 2018.

[160] J. Jarecki, M. Mattern, F.-C. Weber, J.-E. Pudell, X.-G. Wang, J.-C. Rojas Sánchez, M. Hehn, A. von Reppert, M. Bargheer. Controlling effective field contributions to laser-induced magnetization precession by heterostructure design. *Communications Physics*, 7(112), 2024.

[161] V. Iota, J.-H. Park Klepeis, C.-S. Yoo, J. Lang, D. Haskel, G. Srajer. Electronic structure and magnetism in compressed 3d transition metals. *Applied Physics Letters*, 90(4), 2007.

[162] R. Torchio, Y. O. Kvashnin, S. Pascarelli, O. Mathon, C. Marini, L. Genovese, P. Bruno, G. Garbarino, A. Dewaele, F. Occelli, P. Loubeyre. X-Ray Magnetic Circular Dichroism Measurements in Ni up to 200 GPa: Resistant Ferromagnetism. *Physical Review Letters*, 107(237202), 2011.

[163] R. Torchio, A. Monza, F. Baudelet, S. Pascarelli, O. Mathon, E. Pugh, D. Antonangeli, J. Paul Itie. Pressure-induced collapse of ferromagnetism in cobalt up to 120 GPa as seen via x-ray magnetic circular dichroism. *Physical Review B, Rapid Communications*, 84(060403(R)), 2011.

[164] V. V. Temnov, C. Klieber, K. A. Nelson, T. Thomay, V. Knittel, A. Leitenstorfer, D. Makarov, M. Albrecht, R. Bratschitsch. Femtosecond nonlinear ultrasonics in gold probed with ultrashort surface plasmons. *Nature Communications*, 4(1468), 2013.

[165] T. Pezeril, C. Klieber, V. Shalagatskyi, G. Vaudel, V. Temnov, O. G. Schmidt, D. Makarov. Femtosecond imaging of nonlinear acoustics in gold. *Optics Express*, 22(4):4590–4598, 2014.

[166] H. Nishinoa, Y. Tsukahara, Y. Nagata, T. Koda, K. Yamanaka. Excitation of high frequency surface acoustic waves by base velocity scanning of a laser interference fringe. *Applied Physics Letters*, 62(17):2036–2038, 1993.

[167] Z. Li, D. Su, X. Sun. The generation of large-amplitude surface acoustic waves induced by a moving laser source. *AIP Advences*, 13(065212), 2023.

[168] V. Laude, D. Gérard, N. Khelfaoui, C. F. Jerez-Hanckes, S. Benchabane, A. Khelif. Annular interdigital transducer focuses piezoelectric surface waves to a single point. *ArXiv*, 2007.

[169] Y. Zhang, B. Feng, H. Hayashi, T. Tohei, I. Tanaka, Y. Ikuhara, H. Ohta. Thermoelectric phase diagram of the SrTiO3-SrNbO3 solid solution system. *Journal of Applied Physics*, 121(185102), 2017.

[170] N. Nepomniashchaia, V. Vetokhina, D. Chvostova, Z. Bryknar, M. Tyunina, A. Dejneka. Effect of doping SrTiO3 with Nb studied with wide-range spectroscopic ellipsometry. *Journal of Applied Physics*, 134(034102), 2023.

[171] L. Debnath, D. Bhatta. *Integral Transforms and Their Applications, 2nd Edition*. Chapman and Hall/CRC, 2007.

[172] C. Glorieux, J. D. Beers, E. H. Bentefour, K. Van de Rostyne, Keith A. Nelson. Phase mask based interferometer: Operation principle, performance, and application to thermoelastic phenomena. *Review of Scientific Instruments*, 75(9), 2004.

[173] B. Lorenz, C. W. Chu. Frontiers in Superconducting Materials chapter: High Pressure Effects on Superconductivity. *Springer Nature*, pages 459–497, 2005.

[174] J. R. Schrieffer, J. S. Brooks. *Handbook of High-Temperature Superconductivity*. Springer Nature, 2007.

[175] Y. Ando, S. Komiya, K. Segawa, S. Ono, Y. Kurita. Electronic Phase Diagram of High-Tc Cuprate Superconductors from a Mapping of the In-Plane Resistivity Curvature. *Physical Review Letters*, 93(277001), 2004.

[176] F. S. Henyey. Distinction between a Perfect Conductor and a Superconductor. *Physical Review Letters*, 49(416), 1982.

[177] D. N. Basov, R. Liang, D. A. Bonn, W. N. Hardy, B. Dabrowski, M. Quijada, D. B. Tanner, J. P. Rice, D. M. Ginsberg, T. Timusk. In-Plane Anisotropy of the Penetration Depth in YBa2Cu3O72x and YBa2Cu4O8 Superconductors. *Physical Review Letters*, 74(4), 1995.

[178] H. Jiang, T. Yuan, H. How, A. Widom, C. Vittoria, A. Drehman. Measurements of anisotropic characteristic lengths in YBCO films at microwave frequencies. *Journal of Applied Physics*, 73(10), 1993.

[179] C. C. Homes, T. Timusk, D. A. Bonn, R. Liang, W. N. Hardy. Optical properties along the c-axis of YBa 2Cu306+x, for x = 0.50 0.95. Evolution of the pseudogap. *Physica C*, 254:265–280, 1995.

[180] T. Pereg-Barnea, P. J. Turner, R. Harris, G. K. Mullins, J. S. Bobowski, M. Raudsepp, Ruixing Liang. Absolute values of the London penetration depth in YBa2Cu3O6¿y measured by zero field ESR spectroscopy on Gd doped single crystals. *Physical Review B*, 69(184513), 2004.

[181] S. Pal, K. Ganguly, A. Basu, U. D. Sharma. Gorter-Casimir two fluid model revisited and possible applications to superconductivity. *International Journal Of Innovative Research In Physics*, 1(1):17–26, 2019.

[182] C. J. Gorter. Note on the supraconductivity of alloys. *International Journal Of Innovative Research In Physics*, 2(1-12):449–452, 1935.

[183] R. T. Gordon. London penetration depth measurements in Ba(Fe1-xTx)2As2 (T=Co,Ni,Ru,Rh,Pd,Pt,Co+Cu) superconductors. *Thesis*, 2011.

[184] A. A. El Hassan, A. Labrag, A. Taoufik, M. Bghour, H. El Ouaddi, A. Tirbiyine, B. Lmouden, A. Hafid, H. El Hamidi. Magnetic Penetration Depth and Coherence Length in a Single-Crystal YBa2Cu3O7-δ. *Physica Status Solidi b, Basic solid state physics*, 258(11), 2021.

[185] H. W. Weber. *High-Tc superconductors*. Springer Science+Business Media, LLC, 1988.

[186] J. Pearl. Current distribution in superconducting films carrying quantized fluxoids. *Applied Physics Letters*, 5(4), 1964.

[187] F. Tafuri, J. R. Kirtley, P. G. Medaglia, P. Orgiani, G. Balestrino. Magnetic imaging of Pearl vortices. *arXiv.cond-mat*, 2004.

[188] V. G. Kogan, N. Nakagawa, J. R. Kirtley. Pearl vortices in anisotropic superconducting films. *Physical Review B*, 104, 2021.

[189] M. Hase, K. Ishioka, J. Demsar, K. Ushida, M. Kitajima. Ultrafast dynamics of coherent optical phonons and nonequilibrium electrons in transition metals. *Physical Review B*, 71(184301), 2005.

[190] J. Demsar, B. Podobnik, V. V. Kabanov, T. Wolf, D. Mihailovic. Superconducting Gap Δ_c, the Pseudogap Δ_p, and Pair Fluctuations above Tc in Overdoped $Y_{1-x}Ca_xBa_2Cu_3O_{7-\delta}$ from Femtosecond Time-Domain Spectroscopy. *Physical Review Letters*, 82(4918), 1999.

[191] V. V. Kabanov, J. Demsar, D. Mihailovic. Kinetics of a Superconductor Excited with a Femtosecond Optical Pulse. *Physical Review Letters*, 95(147002), 2005.

[192] L. Perfetti, P. A. Loukakos, M. Lisowski, U. Bovensiepen, H. Eisaki, M. Wolf. Ultrafast Electron Relaxation in Superconducting $Bi_2Sr_2CaCu_2O_{8+\delta}$ by Time-Resolved Photoelectron Spectroscopy. *Physical Review Letters*, 99(197001), 2007.

[193] S. Adnan, A. Khanolkar, S. Zhou, D. H. Hurley, M. Khafizov. Optical pulse-induced ultrafast antiferrodistortive transition in SrTiO3. *Applied Physics Reviews*, 11(031402), 2024.

[194] T. Sakudo, H. Unoki. Dielectric Properties of SrTiO3 at Low Temperatures. *Physical Review Letters*, 26(1147), 1971.

[195] G. Shirane, Y. Yamada. Lattice-Dynamical Study of the 110°K Phase Transition in SrTiO3. *Physical Review Journals Archive*, 177(858), 1969.

[196] P. K. Mishra, G. Ravikumar, P. Chaddah, S. Kumar, B. A. Dasannacharya. Lattice-Dynamical Study of the 110°K Phase Transition in SrTiO3. *Japanese Journal Of Applied Physics*, 29(9):1612–1614, 1990.

[197] T. Oka, K. Yokoyama, H. Fujishiro, M. Kaneyama, K. Noto. Temperature changes in a melt-processed YBCO superconductor activated by field cooling magnetizing process. *Physica C*, 426-431(1):794–799, 2005.

[198] P. Rani, A. Pal, V. P. S. Awana. High field magneto-transport study of YBa2Cu3O7:Agx (x = 0.00–0.20). *Physica C*, 497:19–23, 2014.

[199] O. Cyr-Choinière, D. LeBoeuf, S. Badoux, S. Dufour-Beauséjour, D. A. Bonn, W. N. Hardy, R. Liang, D. Graf, N. Doiron-Leyraud, et al. Sensitivity of T^c to pressure and magnetic field in the cuprate superconductor $YBa^2Cu^3O^y$: Evidence of charge-order suppression by pressure. *Physical Review B*, 98(064513), 2014.

[200] G. De Vecchi, G. Jotzu, M. Buzzi, S. Fava, T. Gebert, M. Fechner, A. V. Kimel, A. Cavalleri. Generation of ultrafast magnetic steps for coherent control. *Nature Photonics*, 19:601–606, 2025.

[201] J. Bardeen, L. N. Cooper, J. R. Schrieffer. Microscopic Theory of Superconductivity. *Physical Review Journals Archive*, 106(162):162–164, 1957.

[202] D. Fausti, R. I. Tobey, N. Dean, S. Kaiser, A. Dienst, M. C. Hoffmann, S. Pyon, T. Takayama, H. Takagi, A. Cavalieri. Light-Induced Superconductivity in a Stripe-Ordered Cuprate. *Science*, 331(6014):189–191, 2011.

[203] S. Kaiser, C. R. Hunt, D. Nicoletti, W. Hu, I. Gierz, H. Y. Liu, M. Le Tacon, T. Loew, D. Haug, B. Keimer, A. Cavalleri. Optically induced coherent transport far above T^c in underdoped $YBa^2Cu^3O^{6+\delta}$. *Physical Review B*, 89(184516), 2014.

[204] W. Hu, S. Kaiser, D. Nicoletti, C. R. Hunt, I. Gierz, M. C. Hoffmann, M. Le Tacon, T. Loew, B. Keimer, A. Cavalleri. Optically enhanced coherent transport in $YBa^2Cu^3O^{6.5}$ by ultrafast redistribution of interlayer coupling. *Nature Materials*, 13:705–711, 2014.

[205] M. Mitrano, A. Cantaluppi, D. Nicoletti, S. Kaiser, A. Perucchi, S. Lupi, P. Di Pietro, D. Pontiroli, M. Riccò, S. R. Clark, D. Jaksch, A. Cavalleri. Possible light-induced superconductivity in K^3C^{60} at high temperature. *Nature*, 530:461–464, 2016.

[206] L. Zhao, C. A. Belvin, R. Liang, D. A. Bonn, W. N. Hardy, N. P. Armitage, D. Hsieh. A global inversion-symmetry-broken phase inside the pseudogap region of $YBa_2Cu_3O_y$. *Nature Physics*, 13:250–254, 2016.

[207] V. Cherruault, F. Camerel, J. Morin, A. Triadon, N. Godin, R. Lefort, O. Mongin, J.-F. Bergamini, A. Vacher, M. G. Humphrey, M. Lorenc, F. Paul, T. Pezeril. Quantification of ultrafast nonlinear photothermal and photoacoustic effects in molecular thin films via time-domain Brillouin scattering. *The Journal of Chemical Physics*, 163(024201), 2025.

[208] J. A. Mejía Gómez, C. Canaria, R. Ochoa Burgos, C. A. Ortiz, G. I. Supelano, C. A. Parra Vargas. Structural study of yttrium substituted BiFeO3. *Journal of Physics: Conference Series*, 687(012091), 2016.

[209] M. Trassin, G. De Luca, S. Manz, M. Fiebig. Probing Ferroelectric Domain Engineering in BiFeO3 Thin Films by Second Harmonic Generation. *Advanced Materials*, 27(33):4871–4876, 2015.

[210] J.-S. Wang, K.-J. Jin, H.-S. Guo, J.-X. Gu, Q. Wan, X. He, X.-L. Li, X.-L. Xu, G.-Z. Yang. Evolution of structural distortion in BiFeO3 thin films probed by second-harmonic generation. *Scientific Reports*, 3(38268), 2016.

[211] Y. A. Du, S. Sakong, P. Kratzer. As vacancies, Ga antisites, and Au impurities in zinc blende and wurtzite GaAs nanowire segments from first principles. *Physical Review B*, 87(075308), 2013.

[212] A. M. Malvezzi, G. Vecchi, M. Patrini, G. Guizzetti, L. C. Andreani, F. Romanato, L. Businaro, E. Di Fabrizio, A. Passaseo, M. De Vittorio. Resonant second-harmonic generation in a GaAs photonic crystal waveguide. *Physical Review B*, 68(161306), 2003.

[213] H. Hardhienata, A. Alejo-Molina, A. Prylepa, C. Reitböck, D. Stifter, K. Hingerl. Bond Model and Group Theory of Second Harmonic Generation in GaAs(001). *ArXiv*, 2014.

[214] D. Brunne, M. Lafrentz, V. V. Pavlov, R. V. Pisarev, A. V. Rodina, D. R. Yakovlev, M. Bayer. Electric field effect on optical harmonic generation at the exciton resonances in GaAs. *Physical Review B*, 92(085202), 2015.

[215] Y.-M. Wei, Y. Yu, J. Wang, L. Liu, H.-Q. Ni, Z.-C. Niu, J.-T. Li, X.-H. Wanga, S.-Y. Yu. Structural discontinuity induced surface second harmonic generation in single, thin zinc-blende GaAs nanowires. *Nanoscale*, 9(16066), 2017.

[216] K. A. Morey, B. T. Fichera, B. Lv, Z. Shen, N. Gedik. Automated polarization rotation for multi-axis rotational-anisotropy second harmonic generation experiments. *Review of Scientific Instruments*, 96(043002), 2025.

[217] T. Cao, G. Wang, W. Han, H. Ye, C. Zhu, J. Shi, Q. Niu, P. Tan, E. Wang, B. Liu, J. Feng. Valley-selective circular dichroism of monolayer molybdenum disulphide. *Nature Communications*, 3(887), 2012.

[218] L. M. Malard, T. V. Alencar, A. P. M. Barboza, K. F. Mak, A. M. de Paula. Observation of intense second harmonic generation from MoS_2 atomic crystals. *Physical Review B*, 87(201401), 2013.

[219] N. Kumar, S. Najmaei, Q. Cui, F. Ceballos, P. M. Ajayan, J. Lou, H. Zhao. Second harmonic microscopy of monolayer MoS_2. *Physical Review B*, 87(161403), 2013.

[220] Y. Li, Y. Rao, K. F. Mak, Y. You, S. Wang, C. R. Dean, T. F. Heinz. Probing Symmetry Properties of Few-Layer MoS_2 and h-BN by Optical Second-Harmonic Generation. *Nano Letters*, 13(7):3329–3333, 2013.

[221] X. Yin, Z. Ye, D. A. Chenet, Y. Ye, K. O'Brien, J. C. Hone, X. Zhang. Edge Nonlinear Optics on a MoS_2 Atomic Monolayer. *Science*, 344(6183):488–490, 2014.

[222] C. Janisch, Y. Wang, D. Ma, N. Mehta, A. L. Elías, N. Perea-López, M. Terrones, V. Crespi, Z. Liu. Extraordinary Second Harmonic Generation in Tungsten Disulfide Monolayers. *Scientific Reports*, 4(5530), 2014.

[223] W.-T. Hsu, Z.-A. Zhao, L.-J. Li, C.-H. Chen, M.-H. Chiu, P.-S. Chang, Y.-C. Chou, W.-H. Chang. Second Harmonic Generation from Artificially Stacked Transition Metal Dichalcogenide Twisted Bilayers. *ACS Nano*, 8(3):2951–2958, 2014.

[224] K. Yao, N. R. Finney, J. Zhang, S. L. Moore, L. Xian, N. Tancogne-Dejean, F. Liu, J. Ardelean, X. Xu, D. Halbertal, K. Watanabe, T. Taniguchi, H. Ochoa, A. Asenjo-Garcia, X. Zhu, D. N. Basov, A. Rubio, C. R. Dean, J. Hone, P. James Schuck. Enhanced tunable second harmonic generation from twistable interfaces and vertical superlattices in boron nitride homostructures. *Science Advences*, 7(10), 2021.

[225] I. Paradisanos, A. M. S. Raven, T. Amand, C. Robert, P. Renucci, K. Watanabe, T. Taniguchi, I. C. Gerber, X. Marie, B. Urbaszek. Second harmonic generation control in twisted bilayers of transition metal dichalcogenides. *Physical Review B*, 105(115420), 2022.

[226] S. Puri, S. Patel, J. L. Cabellos, L. E. Rosas-Hernandez, K. Reynolds, H. O. H. Churchill, S. Barraza-Lopez, B. S. Mendoza, H. Nakamura. Substrate Interference and Strain in the Second-Harmonic Generation from $MoSe_2$ Monolayers. *Nano Letters*, 24(41):13061–13067, 2024.

Appendix

Appendix A: Second harmonic generation in crystals

Additional investigations were conducted on dichalcogenide atomic monolayers and thin crystalline films. Their structure was probed using second harmonic generation with an 800 nm femtosecond laser. These investigations fall outside the scope of time-resolved experiments, but they support the development of the main work and demonstrate an extension of our experimental capabilities in material studies. For this reason, they are briefly presented in this appendix, along with a short theoretical overview.

A.1 Theory: Second harmonic generation

Second harmonic generation (SHG) originates from the second-order nonlinear optical susceptibility $\chi^{(2)}$, which produces a polarization oscillating at 2ω inside the medium:

$$P_i(t) = \epsilon_0 \left(\chi_{ij}^{(1)} E_j(t) + \chi_{ijk}^{(2)} E_j(t) E_k(t) + \dots \right). \tag{207}$$

For a monochromatic field $E(t) = E_0 \cos(\omega t)$, the second-order polarization becomes:

$$P^{(2)}(t) = \frac{1}{2} \epsilon_0 \chi^{(2)} E_0^2 \left[\cos(2\omega t) + 1 \right], \tag{208}$$

which acts as a source term for light emission at 2ω. The intensity of the SHG signal under plane-wave and phase-matched conditions is:

$$I_{2\omega} = \frac{2\omega^2 d_{\text{eff}}^2}{n_{2\omega} n_\omega^2, \epsilon_0 c^3}, I_\omega^2, L^2, \text{sinc}^2! \left(\frac{\Delta k L}{2} \right), \tag{209}$$

indicating a quadratic dependence on both the fundamental intensity and interaction length. In monolayers, although L is minimal, SHG remains a powerful probe of symmetry and crystal orientation.

In birefringent materials, phase matching depends on both refractive indices and polarization. Two typical configurations are:

- **Type I:** $o + o \to e$ with $n_{2\omega}^{(e)} = n_\omega^{(o)}$,
- **Type II:** $o + e \to e$ with $n_{2\omega}^{(e)} = n_\omega^{(e)}$.

However, in atomically thin layers, phase matching becomes irrelevant. Instead, SHG directly reflects the symmetry via the $\chi^{(2)}$ tensor.

Monolayers of MoS_2 and WSe_2, both with D_{3h} symmetry, lack inversion symmetry and thus exhibit strong SHG, with intensity following $I_{2\omega}(\theta) \propto \cos^2(3\theta)$. In contrast, bilayers with 2H stacking are centrosymmetric (D_{3d}), suppressing SHG. In MoS_2/WSe_2 heterostructures, SHG persists and depends on the twist angle due to interference between the nonlinear responses of each layer.

In our reflection geometry, where the monolayer lies on a SHG-inactive substrate, the field undergoes multiple internal reflections, which must be considered. The field amplitude at the mth pass is:

$$E_\omega^{(m)} = t_\omega E_0, \alpha^{,m}, \quad \alpha = r_\omega^{\text{eff}} e^{i\phi_\omega}, \tag{210}$$

leading to a nonlinear polarization:

$$P_{2\omega}^{(m)} = \varepsilon_0 \chi_s^{(2)} (t_\omega E_0)^2 \alpha^{2m}. \tag{211}$$

The emitted SHG field for the mth pass, accounting for reflections of the 2ω field, is:

$$E_{2\omega}^{(m)} = C_{2\omega} t_{2\omega} P_{2\omega}^{(m)} \frac{1}{1-\beta}, \quad \beta = r_{2\omega}^{\text{eff}} e^{i\phi_{2\omega}}. \tag{212}$$

Coherently summing all contributions yields:

$$E_{2\omega}^{\text{tot}} = C_{2\omega} t_{2\omega} \epsilon_0 \chi_s^{(2)} (t_\omega E_0)^2 \cdot \frac{1}{(1-\beta)(1-\alpha^2)}, \tag{213}$$

and the total intensity is:

$$I_{2\omega}^{\text{tot}} \propto |E_{2\omega}^{\text{tot}}|^2 \propto |\chi_s^{(2)}|^2 I_\omega^2 \cdot \frac{1}{|1-\beta|^2 |1-\alpha^2|^2}. \tag{214}$$

This shows that SHG from a monolayer in reflection geometry is a multipass process. When reflection effects are negligible ($\alpha, \beta \to 0$), the result reduces to the usual single-pass expression.

A.2 Investigations of mono-atomic layer material structures through SHG: Experiments

The SHG experimental setup is schematically represented in Figure 69, and is based on the Mira/RegA laser-re-amplifier source described in Appendix B. In the SHG experimental setup, a first HWP/PBS pair splits and controls the optical power between the SHG arm and parallel experiments. An AOM modulates the pump beam, providing a reference for synchronous detection. After beam collimation, a second HWP/PBS pair fine-tunes the pump power. Polarization is then adjusted via a motorized HWP. Bandpass filters centered at 780 nm ensure spectral purity before the pump is focused onto the sample. The reflected SHG is separated by a dichroic mirror and passes through a motorized analyzer. This, along with the motorized HWP, allows fully automated polarization-resolved SHG measurements. A PMT, protected by 390 nm filters, detects only the 2ω component. The signal is recorded via lock-in detection synchronized to the AOM frequency. Since a HWP rotation by α induces a 2α polarization rotation, the analyzer is co-rotated by 2α to maintain proper alignment.

Four different materials were investigated: two thin films ($BiFeO_3$ and GaAs) and two atomic monolayers (MoS_2 and WSe_2). The dependence of the SHG intensity on the incident pump polarization was measured for each material and is reported in Figure 70.

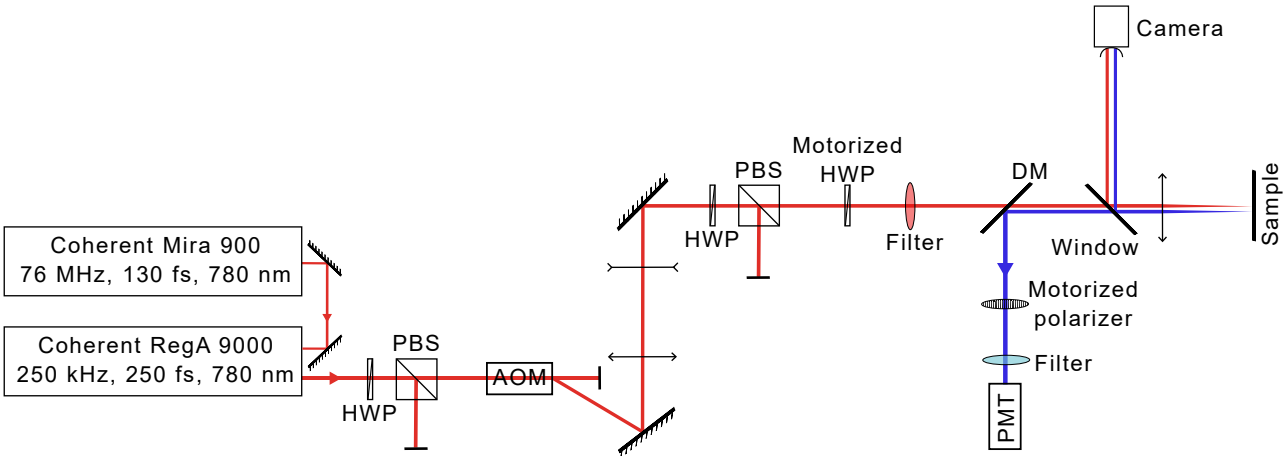

Figure 69: Schematic view of the experimental setup used for SHG investigation of crystallographic structures.

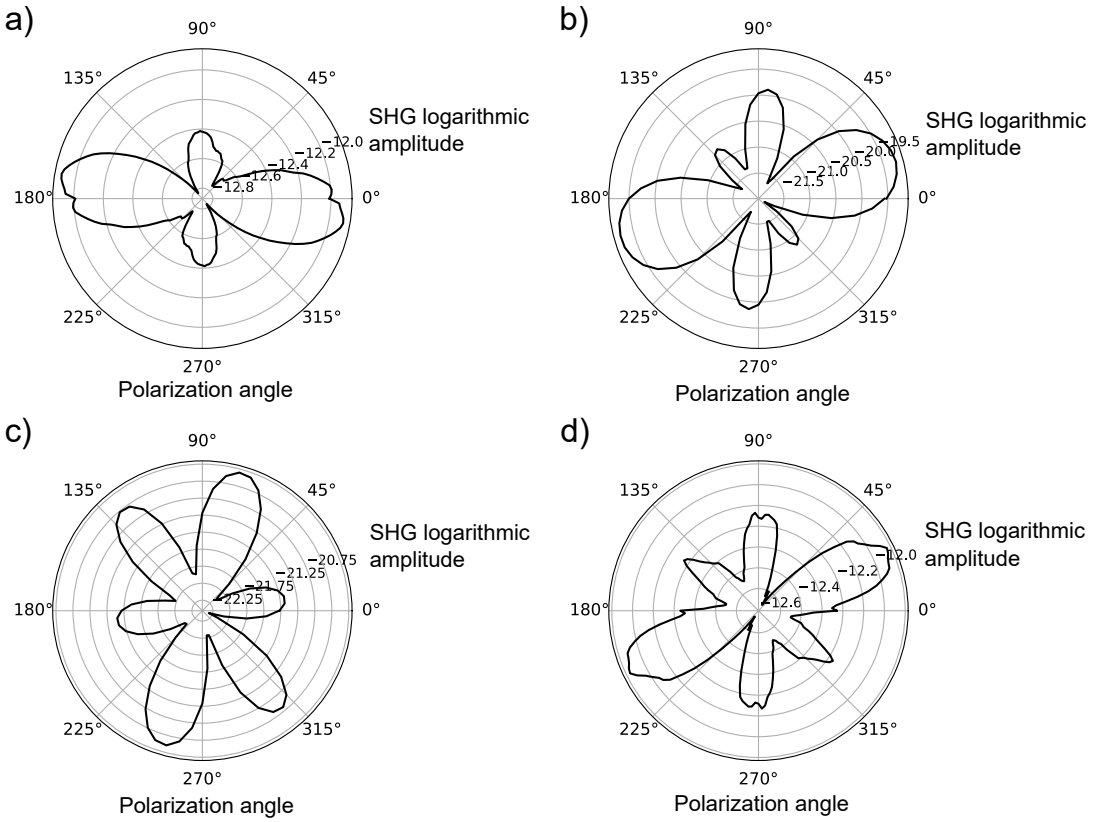

Figure 70: SHG identification of crystallographic structure on four materials. a) $BiFeO_3$ thin film. b) GaAs thin film. c) MoS_2 atomic monolayer. d) WSe_2 atomic monolayer.

The SHG response obtained from the $BiFeO_3$ (BFO) thin film is shown in Figure 70(a). In this case, a characteristic four-lobed pattern is observed, with two large and two smaller lobes. This specific four-petal structure directly originates from the non-centrosymmetric crystallographic symmetry of BFO. At room temperature, BFO crystallizes in a rhombohedral structure. This material exhibits a spontaneous ferroelectric polarization oriented along the pseudocubic (111) axis, which defines a unique polar direction. Because of this polar axis, the second-order nonlinear susceptibility tensor $\chi^{(2)}$ of BFO is anisotropic and contains only a few independent non-zero components, mainly d_{15}, d_{22}, d_{31}, and d_{33}.

$$\chi^{(2)}_{BFO} = \begin{pmatrix} 0 & 0 & 0 & 0 & d_{15} & -d_{22} \\ 0 & 0 & 0 & d_{22} & d_{15} & 0 \\ d_{31} & d_{31} & d_{33} & 0 & 0 & 0 \end{pmatrix}$$

When the linearly polarized fundamental field is rotated in the plane of incidence, its electric field components project differently onto the crystallographic axes of the film. Each orientation excites distinct elements of the $\chi^{(2)}$ tensor, leading to a modulation of the generated SHG intensity. The resulting dependence can be expressed as a combination of $\cos(2\theta)$ and $\cos(4\theta)$ terms, where θ is the polarization angle of the incident field. The $\cos(4\theta)$ term, arising from the trigonal symmetry, produces a four-lobed pattern in the polar representation of the SHG intensity. The unequal size of the lobes indicates that the nonlinear tensor components are not of equal amplitude ($|d_{33}| > |d_{31}|, |d_{22}|, |d_{15}|$). The strongest SHG signal is obtained when the pump polarization is aligned close to the projection of the spontaneous polarization $\mathbf{P_s}$ in the sample plane, while the weaker lobes correspond to polarization directions orthogonal to this projection. Thus, the anisotropy of the SHG pattern provides a direct

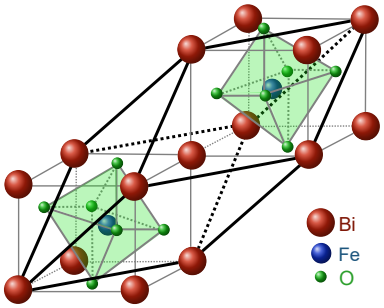

Figure 71: Crystallographic structure of $BiFeO_3$ constructed from the structural data reported in [208].

optical fingerprint of the crystal symmetry and of the orientation of the ferroelectric polarization in the film.

Similar fourfold SHG patterns in BFO thin films have been consistently reported in the literature and used to probe ferroelectric domain orientation and switching behavior [209, 210]. The present observation is therefore fully consistent with the trigonal 3m symmetry of the BFO crystal structure in the R3c space group. The crystallographic structure of BFO established in [208] is reported in Figure 71.

The second investigated thin film is a GaAs layer. For this material, the polarization-dependent SHG measurement reveals a six-lobed pattern, as shown in Figure 70(b). The lobes are not all of equal amplitude, with two large, two intermediate, and two smaller maxima. This complex anisotropic pattern arises from the crystallographic symmetry of GaAs and the projection of its nonlinear susceptibility tensor $\chi^{(2)}$ onto the measurement plane.

Gallium arsenide has a cubic zinc-blende structure, which belongs to the $F\bar{4}3m$ (T_d) point group. The corresponding nonlinear susceptibility tensor $\chi^{(2)}$ contains only one independent non-zero coefficient, conventionally denoted d_{14}. The zinc-blend crystallographic structure of GaAs given in [211] is reported in Figure 72.

$$\chi^{(2)}_{GaAs} = \begin{pmatrix} 0 & 0 & 0 & 0 & d_{14} & 0 \\ 0 & 0 & 0 & d_{14} & 0 & 0 \\ 0 & 0 & 0 & 0 & 0 & d_{14} \end{pmatrix}.$$

In an ideal bulk crystal, this single non-zero component would produce an isotropic nonlinear response under rotation about the (001) axis. However, in thin films and especially under reflection geometry, the situation is more intricate. The electric field at the interface has both in-plane and out-of-plane components, and the SHG signal results from their interference after projection onto the detection

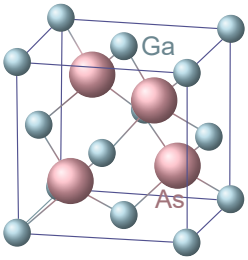

Figure 72: Crystallographic structure of zinc-blend GaAs constructed from the structural data reported in [211].

polarization. When the incident polarization is rotated, these field components mix according to the symmetry operations of the F$\bar{4}$3m group, generating intensity terms proportional to $\cos(2\theta)$, $\cos(4\theta)$, and $\cos(6\theta)$, where θ is the polarization angle of the incident pump beam.

The $\cos(6\theta)$ term leads to the characteristic six-lobed pattern typically observed in GaAs. The presence of lobes of unequal magnitude (two large, two intermediate, and two smaller) indicates that the experimental geometry introduces asymmetries in the projection of the nonlinear polarization. These asymmetries may result from the film orientation deviating from an ideal (001) cut, or slight birefringence or surface reconstruction breaking the cubic equivalence of the (100), (010), and (110) directions, or even interference between bulk and surface SHG contributions.

The overall sixfold structure thus reflects the underlying cubic symmetry of the zinc-blende lattice, while the amplitude variations encode fine details of the local crystal orientation and interface anisotropy. This type of sixfold anisotropic SHG pattern in GaAs has been widely reported and exploited to probe surface symmetry breaking, epitaxial strain, and interfacial electric fields [212–216].

After the two thin films (BFO and GaAs), two monoatomic layer materials were investigated. The SHG measurement pattern for MoS_2 is presented in Figure 70(c). Here, six lobes are observed; two of them are quasi-equal, while the third pair appears smaller. This anisotropic pattern directly reflects the crystallographic symmetry of monolayer MoS_2, which belongs to the D_{3h} point group. The atomic structure of MoS_2 presented in Figure 73 is adapted from [217].

The second-order nonlinear susceptibility tensor for MoS_2 in contracted notation is given by:

$$\chi^{(2)}_{MoS_2} = \begin{pmatrix} d & -d & 0 & 0 & 0 & 0 \\ 0 & 0 & 0 & 0 & 0 & -d \\ 0 & 0 & 0 & 0 & 0 & 0 \end{pmatrix},$$

where d is the effective nonlinear coefficient representing the in-plane component of the second-order response. In monolayer MoS_2, the lack of inversion symmetry allows a strong second-harmonic generation, in contrast to the bulk 2H-MoS_2 structure, which is centrosymmetric [218, 219]. The hexagonal lattice consists of one molybdenum atom coordinated to six sulfur atoms in a trigonal prismatic configuration, giving rise to threefold rotational symmetry and mirror planes every 60°, consistent with the observed six-lobed SHG polar pattern [220]. Each pair of lobes corresponds to constructive interference along equivalent crystallographic directions (armchair directions), whereas the smaller lobes are associated with lower effective nonlinear susceptibility components due to strain or dielectric asymmetry.

The intensity of the SHG signal in MoS_2 is highly sensitive to the orientation of the pump polarization with respect to the crystal axes. The non-vanishing tensor components of the second-order susceptibility impose a $\cos(3\theta)$ dependence on the emitted second-harmonic field amplitude, leading

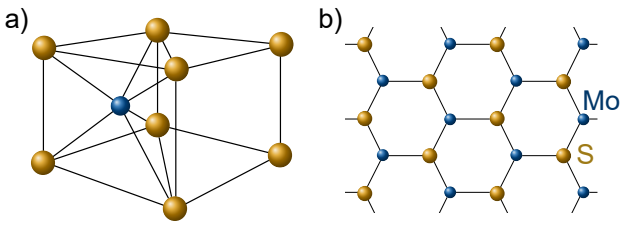

Figure 73: Crystallographic structure of MoS_2 constructed from the structural data reported in [217]. a) Coordination of molybdenum (blue sphere) with sulphur (golden spheres) in a trigonal prismatic geometry. b) Top view of a monolayer MoS_2 lattice.

to an intensity proportional to $\cos^2(3\theta)$ and hence to a six-lobed pattern over 360°. The slight amplitude asymmetry between lobes observed experimentally may arise from substrate-induced strain, grain boundaries, or local variations in the dielectric environment that perturb the perfect D_{3h} symmetry, or from imperfect control of the pump polarization purity.

The observed SHG pattern thus provides a direct optical fingerprint of the underlying crystal orientation, making SHG polarimetry a powerful, nondestructive method to determine the crystallographic axes and assess strain or stacking effects in TMDs. These measurements also serve as a crucial baseline for the subsequent study of bilayers and heterostructures, where the overall symmetry can be deliberately restored or broken depending on the relative stacking order [221].

The last investigated sample is a monoatomic layer of tungsten diselenide (WSe_2). The SHG generation pattern is shown in Figure 70(d). As in the case of MoS_2, the WSe_2 monolayer belongs to the D_{3h} point group and thus exhibits a sixfold SHG polar pattern consistent with the trigonal prismatic coordination of tungsten with selenium atoms. The second-order nonlinear susceptibility tensor $\chi^{(2)}_{WSe_2}$ has the same symmetry form as for MoS_2.

The six-lobed SHG pattern observed in Figure 70(d) reveals the threefold rotational symmetry and the absence of inversion center in the monolayer WSe_2. This is in agreement with earlier studies showing that monolayer WSe_2 exhibits strong SHG due to its non-centrosymmetric structure, while bilayer WSe_2 in the 2H stacking becomes inversion symmetric and thus SHG-inactive [222, 223]. The SHG intensity varies as $\cos^2(3\theta)$ with the pump polarization angle θ, reflecting the underlying D_{3h} symmetry of the lattice.

The magnitude of the SHG response in WSe_2 is typically weaker than in MoS_2, which can be attributed to its smaller bandgap (~ 1.65 eV) and the resonance condition relative to the excitation photon energy. When the excitation wavelength is tuned close to the excitonic transitions (A or B excitons), resonant enhancement of the SHG can be observed [223]. Moreover, slight deviations from perfect sixfold symmetry in the polar plot, as occasionally observed, can originate from local strain fields, substrate interactions, or the presence of multiple crystalline domains.

Overall, the SHG response of monolayer WSe_2 provides a sensitive probe of its crystal symmetry, layer number, and excitonic resonance effects. Together with MoS_2, it demonstrates how second-harmonic generation can be used as a non-destructive optical tool to characterize TMDs and their heterostructures.

Having successfully investigated the crystallographic order of bulk and monolayer materials through SHG using our experimental setup, we extended our study to a twisted bilayer WSe_2 stack. This sample consists of two monoatomic WSe_2 layers with a 30° twist angle between them. A photo of the sample surface is shown in Figure 74.

The investigation of this twisted bilayer was performed using the same experimental setup. However, three distinct sets of measurements were recorded, each corresponding to a fixed position of the output polarizer: 0°, 45°, and 90°. This measurement configuration allows us to probe specific components of the $P_{2\omega}$ tensor. In our case, the goal of this approach is to examine SHG intensity variations between the twisted bilayer and the monolayer under long acquisition times while reducing the number of analyzed polarization angles.

The results for the three fixed positions of the analyzer polarizer are shown in Figure 75. For each analyzer orientation, two sets of measurements were recorded: one on the monoatomic WSe_2 sublayer and the other on the twisted bilayer stack. In each subfigure of Figure 75, the solid lines represent the SHG signal from a single monolayer, while the dotted lines correspond to the twisted bilayer.

From these results, it is clear that the SHG signal intensity is significantly weaker in the twisted

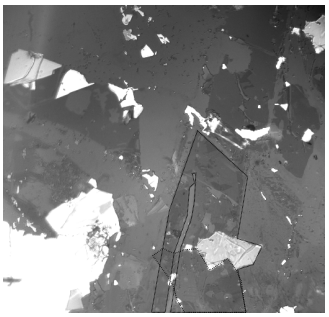

Figure 74: Photograph of the 30° twisted bilayer stack of WSe_2 atomic monolayers.

bilayer compared to the single layer. This reduction does not originate from an increase in crystal symmetry due to the twist—which does not restore inversion symmetry—but rather from destructive interferences between the second-harmonic fields generated independently in each monolayer [223–226]. The total second-harmonic electric field can be expressed by:

$$E_{\text{tot}}^{(2\omega)} = E_1^{(2\omega)} + E_2^{(2\omega)} e^{i\Delta\phi(\theta)}, \tag{215}$$

where $E_1^{(2\omega)}$ and $E_2^{(2\omega)}$ are the second-harmonic fields generated in the bottom and top monolayers, respectively. $\Delta\phi(\theta)$ is the relative phase between them, which depends on the twist angle θ, the relative orientation of their $\chi^{(2)}$ tensors, and the optical path difference. When the two contributions are out of phase, their interference becomes partially destructive, leading to a reduced net SHG intensity:

$$I^{(2\omega)} \propto \left|E_{\text{tot}}^{(2\omega)}\right|^2 = \left|E_1^{(2\omega)}\right|^2 + \left|E_2^{(2\omega)}\right|^2 + 2\Re\left[E_1^{(2\omega)}\left(E_2^{(2\omega)}\right)^* e^{i\Delta\phi(\theta)}\right]. \tag{216}$$

The twist angle modifies both the amplitude and the orientation of the nonlinear response in the top monolayer. As a result, the second-harmonic fields generated in each layer can interfere either constructively or destructively, leading to a significant modulation and, in some cases, to a strong reduction of the total SHG signal. This reduction can mimic the effect of increased centrosymmetry, even though inversion symmetry is not restored in a twisted bilayer structure.

In a reflection geometry, the excitation beam passes through both layers, reflects on the substrate, and then passes back through the layers before being detected. The SHG detected field is the results of the coherent sum of the second harmonic fields generated in each monolayer. The relative phase between these contributions is governed by the phase-matching factor $\Delta\phi(\theta)$, which incorporates three distinct contributions:

$$\Delta\phi(\theta) = \phi_{geom} + \phi_{opt} + \phi_{\chi^{(2)}}(\theta), \tag{217}$$

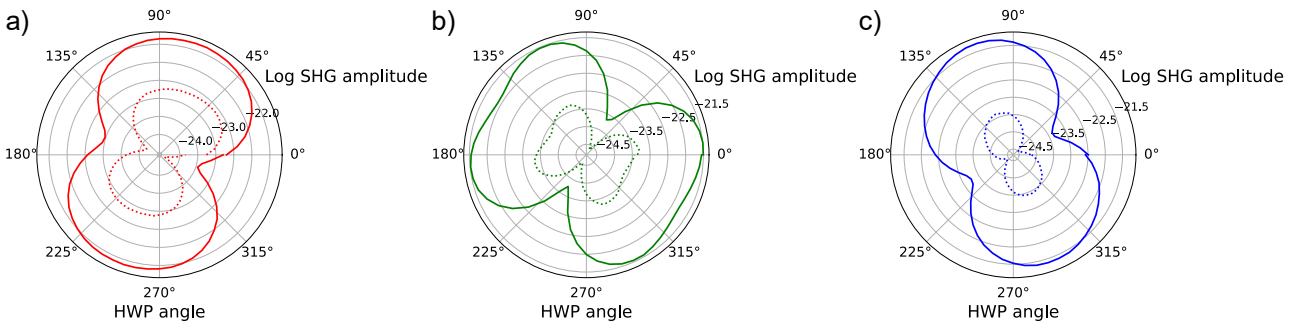

Figure 75: Second harmonic generation in a WSe_2 atomic monolayer (solid lines) and in a 30° twisted bilayer stack (dotted lines) for three fixed polarizer orientations: (a) horizontal, (b) vertical, and (c) 45°.

ϕ_{geom} arises from the geometric delay between the two layers, ϕ_{opt} accounts for the optical path difference of the second-harmonic beam between the two generation events, and $\phi_{\chi^{(2)}}(\theta)$ includes the relative orientation of the nonlinear susceptibility tensors, which is directly controlled by the twist angle. In the case of atomically thin layers, the interlayer distance is typically d $\simeq$ 0.6 nm. The corresponding optical phase delay induced by a round trip is given by:

$$\phi_{opt} = \frac{4\pi n_{2\omega} d}{\lambda_{2\omega}}. \tag{218}$$

Considering a refractive index of $n_{2\omega} \simeq 3$ and a wavelength of the second harmonic of $\lambda_{2\omega} = 400$ nm leads to $\phi_{opt} \simeq 3.3°$. This term can therefore be considered as a secondary contribution to the phase-matching factor. Similarly, ϕ_{geom} yields a comparable contribution due to the extreme thickness of two atoms stack. Both are essentially constant with respect to the twist angle and do not significantly affect the angular dependence of the SHG interference. In contrast, $\phi_{\chi^{(2)}}(\theta) \simeq 3\theta$ due to the D_{3h} point group of WSe_2, and it constitutes the dominant contribution to the phase matching factor $\Delta\phi(\theta)$. This phase term governs the angular modulation of the SHG interference pattern. For instance, at a twist angle of $\theta = 30°$, the relative phase becomes $\Delta\phi \simeq 90°$, which leads to a near-destructive interference between the second harmonic fields generated in each layer. The weak detected SHG is obtained thanks to the minor contribution of ϕ_{geom} and ϕ_{opt}.

Appendix B: Custom femtosecond laser

Preliminary TDBS and MOKE measurements were performed using a Coherent Mira 900 femtosecond Ti:sapphire oscillator, delivering 130 fs pulses at a repetition rate of 76 MHz. Although this laser successfully demonstrated the validity of the time-resolved optical setup, its high repetition rate induced strong cumulative heating of the samples. This cumulative heating resulted in a significant thermal baseline, increased noise, and long-term degradation of the investigated materials. To mitigate these thermal issues, we first implemented an external pulse picker. However, due to its low efficiency, no reliable measurements could be achieved. We therefore introduced an intracavity pulse picker, transforming the oscillator into a cavity-dumped laser, which allows more efficient repetition rate reduction while preserving pulse energy.

The custom cavity-dumped laser is schematized in Figure 76. The rear section of the cavity (M_7 – M_9) is identical to the standard Mira 900 design. In this region, a pair of prisms is used to control the group-velocity dispersion, thereby adjusting the spectral bandwidth and ensuring stable mode-locking with short pulse durations. The gain medium is a Ti:Al_2O_3 crystal pumped by a continuous-wave 532 nm laser. The main cavity consists of all components between mirrors M_1 and M_9, while M_{10} and M_{11} form an auxiliary alignment cavity. The mirrors with a letter as an index are outside the main cavity but are part of the custom laser. The D-shaped mirror M_a extracts the pulses selected by the acousto-optic Bragg cell, after which mirrors M_b and M_c direct the output beam. Convex mirrors M_2, M_3, M_6, and M_7 focus the intracavity beam into both the Ti:sapphire crystal and the Bragg cell. A birefringent Lyot filter provides tunability over the 710 – 1000 nm range. A slit placed before M_1 blocks the continuous-wave component of the intracavity beam and improves Kerr-lens mode-locking. Photodiode D_1, which collects a small reflection from the Lyot filter, provides the electronic synchronization signal for cavity dumping. Its repetition rate corresponds to the cavity round-trip frequency adjusted by the spacing between mirrors M_4 and M_5, and set to 76 MHz, ensuring compatibility with the Mira 900 electronics. The cavity dumper extracts individual pulses from the cavity, producing an output beam with a reduced tunable repetition rate below 4.7 MHz, and pulse durations of 140 fs. A second slower photodiode D_2 monitors the average intracavity power and laser stability. The cavity dumper was implemented in a double-pass configuration, as presented in Figure 77, in order to enhance the dumped intensity compared with single-pass dumping. The incident beam $E(t) = E_0 \cos(\omega t + \Phi)$ yields after the first pass in the Bragg cell a scattered pulse E_s and a

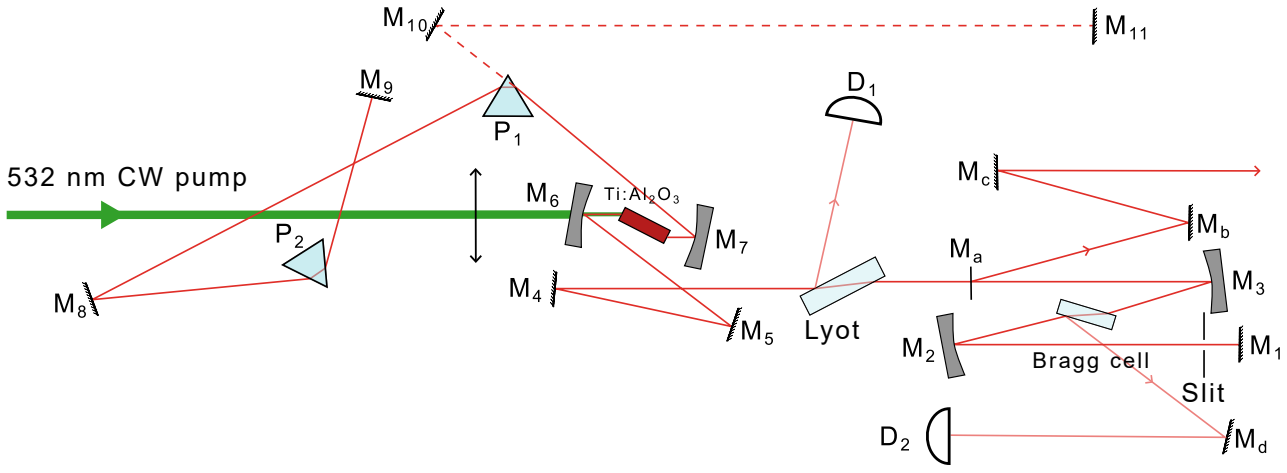

Figure 76: Schematic representation of the custom femtosecond cavity-dumped laser. M: Mirror, D: photodiode, Lyot: birefringent Lyot filter.

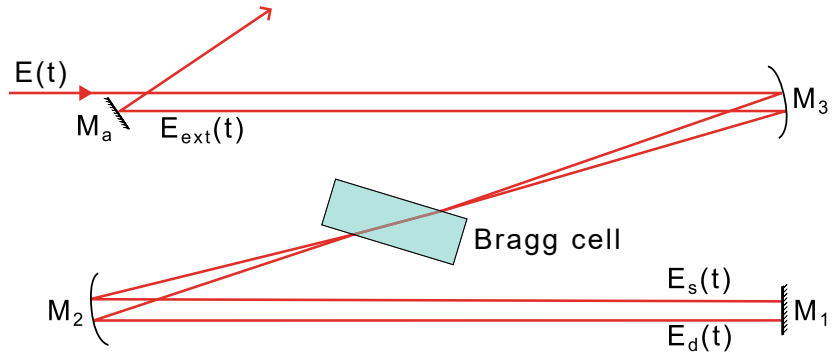

Figure 77: Double-pass cavity dumping in the custom femtosecond laser using an acousto-optic Bragg cell.

transmitted (depleted) intracavity pulse E_d, defined by:

$$E_s = \sqrt{\eta}\, E_0 \cos\big((\omega + \Omega)t + \Phi + \varphi_s\big) \tag{219}$$

$$E_d = \sqrt{1-\eta}\, E_0 \cos\big(\omega t + \Phi + \varphi_d\big) \tag{220}$$

In these expressions, η is the diffraction efficiency, Ω is the acoustic frequency driving the Bragg cell, and $\phi_{s,d}$ denote additional phase shifts on the scattered and transmitted beams. After the second pass through the Bragg cell, the extracted pulse E_{ext} is described by:

$$E_{\text{ext}}(t) = \sqrt{\eta\,(1-\eta)}\, E_0 \big[\cos\big((\omega + \Omega)t + \phi_1\big) + \cos\big((\omega - \Omega)t + \phi_2\big)\big] \tag{221}$$

where $\phi_1 = \Phi + \varphi_s$ and $\phi_2 = \Phi + \varphi_d$. Averaging over the fast optical oscillations yields the extracted I_{ext} given by:

$$I_{ext} = 2\eta\,(1-\eta)\,|E_0|^2 \cos^2(\Omega t + \Delta\phi) \tag{222}$$

where $\Delta\phi = (\phi_1 - \phi_2)/2$ is the effective relative phase between the two contributions (E_s and E_d). For our investigations, the laser repetition rate was set between 90 kHz and 500 kHz. The upper limit corresponds to the point above which the dumping is too fast for the intracavity lasing to reach its maximum power before another pulse is ejected. Within this operation repetition-rate window, the pulse energy is approximately 30 nJ. For comparison, the pulse energy of the 76 MHz Mira oscillator, emitting an average power of 1 W, is about 13 nJ.

In summary, our custom laser provides a tunable repetition rate (optimally below 500 kHz), an output pulse duration of ∼140 fs, and a pulse energy of ∼30 nJ, which is more than twice the pulse energy of the original Mira system.

Appendix C: Mira 900/RegA laser

The custom laser presented in Appendix A provided several interesting results, particularly in investigations of spin-lattice coupling. However, its output power was too low to explore nonlinear regimes. Therefore, in order to reduce the initial emission rate of the Mira 900 and to achieve higher pulse energies, a regenerative amplifier (Coherent RegA) was added after the Mira 900 output. The optical layout of the Mira/RegA system is shown in Figure 78.

In the Coherent Mira 900 cavity, the rear section (M_5 to M_7) is similar to our custom laser, and its function is not described here another time. The original Mira includes a starter consisting of two glass rods sets at the Brewster angle. The starter perturbs the continuous component of the lasing by shaking to initiate mode-locking. This element could not be implemented in our custom laser because the mirror arrangement prevents sufficient space to maintain the Brewster geometry. In the standard Mira, the output beam is extracted from the partial mirror M_1. The slit and the Lyot birefringent filter functions have already been introduced in Appendix A.

The Mira output is injected into the RegA by aligning it with the diffracted beam from the Bragg cell cavity dumper. The input power is adjusted using an HWP/PBS pair. The injected beam is then

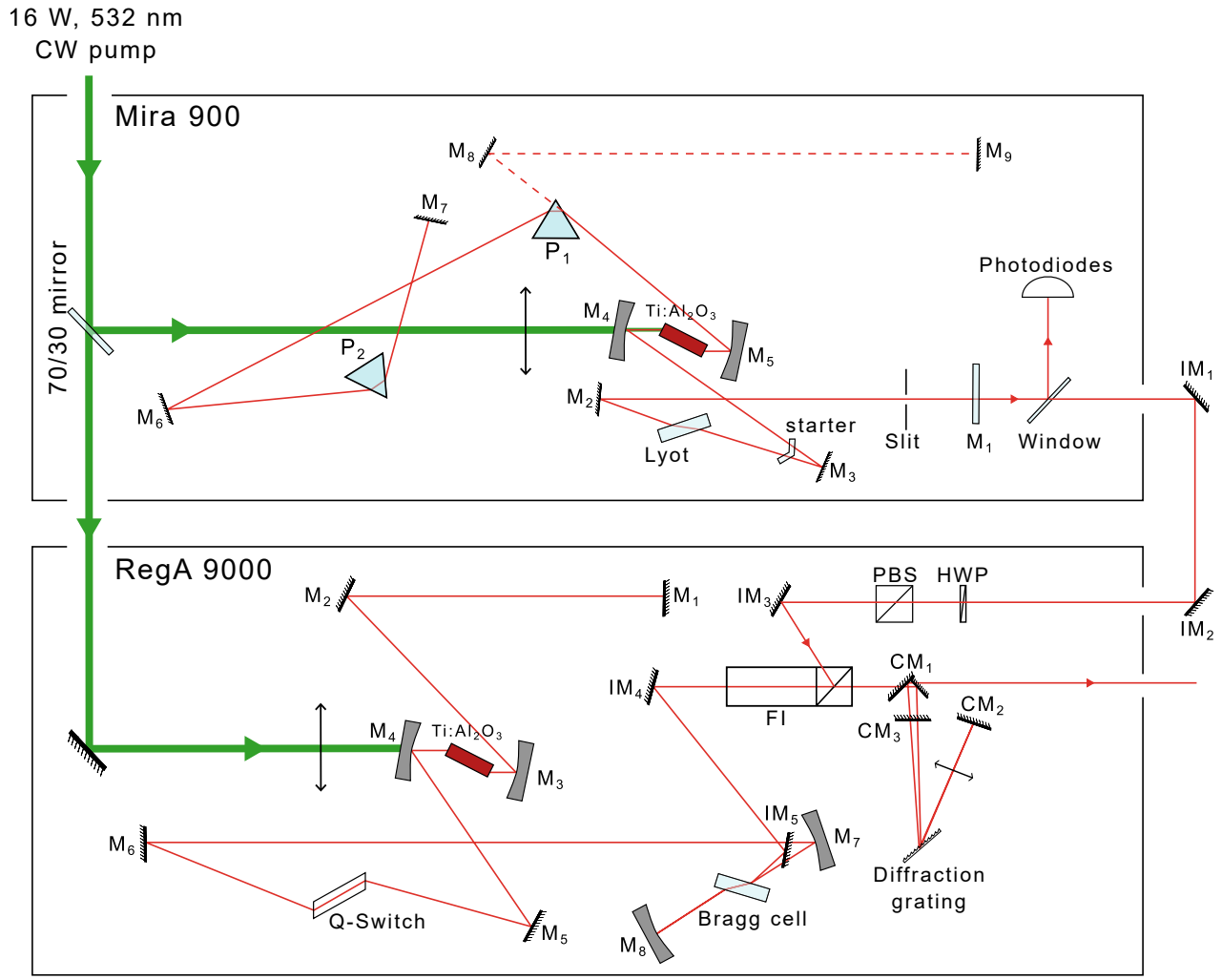

Figure 78: Schematic of the Coherent Mira 900/RegA femtosecond laser. M: Mirror, P: prism, Lyot: birefringent Lyot filter, HWP: Half-Wave Plate, PBS: Polarizing Beam Splitter, IM: Injection Mirror, CM: Compressor Mirror, FI: Faraday Isolator.

coupled into the Rega laser cavity (M_1 to M_8), where it is re-amplified in the Ti:sapphire crystal.

Amplification in the Ti:sapphire is relatively slow and does not directly yield ultrashort high-peak-power pulses. This limitation is overcome by incorporating a Q-switch into the continuous RegA cavity. When the Q-switch blocks lasing, the amplification medium is still pumped, but no stimulated emission occurs. During this blocking phase, gain accumulates in the crystal. When the Q-switch opens, lasing resumes at high gain, and the stored energy in the amplification medium is released within a few nanoseconds. Proper synchronization between the injected Mira pulse and the Q-switching event produces a highly amplified pulse.

The amplified pulse is then extracted by the Bragg cell (in a double-pass configuration) and follows the same optical path as the injected Mira beam. The amplified output and the injection beam are separated using a Faraday isolator (based on the Faraday effect described in the theoretical section Theory: Faraday effect).

After separation, the amplified pulse is temporally recompressed in a Martinez-type compressor with multiple passes. At the final pass, the beam exits spatially displaced from the input and is guided through the RegA output.

For our experiments, the RegA was operated at a repetition rate of 250 kHz, delivering 350 mW average power (1.4 µJ per pulse). The shortest accessible pulse duration is approximately 250 fs.

Appendix D: Numerical simulations using Python

D.3 Numerical simulation of the two-temperature model

```
import numpy as np
from scipy.integrate import solve_ivp
import scipy.constants as const
import matplotlib.pyplot as plt

materials = {
    "Mg": {
        "rho": 1.74e3, "Cp": 1020, "n_e": 8.6e28, "E_F_eV": 7.1, "k_e": 160.0, "k_l": 160.0,
        "T_D": 400.0, "v_F": 1.3e6, "Lambda_0": 20e-9, "tau_e": 9.11e-15, "R": 0.95, "xi": 8.33e-9
    },
    "Al": {
        "rho": 2.7e3, "Cp": 900, "n_e": 18.1e28, "E_F_eV": 11.7, "k_e": 237.0, "k_l": 1.5,
        "T_D": 390.0, "v_F": 2.03e6, "Lambda_0": 15e-9, "tau_e": 8.59e-15, "R": 0.88, "xi": 7.24e-9
    },
    "V100_111": {
        "rho": 6.11e3, "Cp": 489, "n_e": 14.4e28, "E_F_eV": 9.0, "k_e": 30.0, "k_l": 15.0,
        "T_D": 380.0, "v_F": 1.5e6, "Lambda_0": 10e-9, "tau_e": 2.23e-15, "R": 0.54, "xi": 19.2e-9
    },
    "V110": {
        "rho": 6.11e3, "Cp": 489, "n_e": 14.4e28, "E_F_eV": 9.0, "k_e": 30.0, "k_l": 15.0,
        "T_D": 380.0, "v_F": 1.5e6, "Lambda_0": 10e-9, "tau_e": 2.72e-15, "R": 0.54, "xi": 19.2e-9
    },
    "Cr": {
        "rho": 7.19e3, "Cp": 448, "n_e": 8.33e28, "E_F_eV": 9.3, "k_e": 93.0, "k_l": 3.0,
        "T_D": 630.0, "v_F": 1.4e6, "Lambda_0": 15e-9, "tau_e": 3.97e-15, "R": 0.57, "xi": 18.0e-9
    },
    "Fe": {
        "rho": 7.87e3, "Cp": 450, "n_e": 17.0e28, "E_F_eV": 11.1, "k_e": 80.0, "k_l": 5.0,
        "T_D": 470.0, "v_F": 1.98e6, "Lambda_0": 7e-9, "tau_e": 17.1e-15, "R": 0.56, "xi": 18.6e-9
    },
    "Co": {
        "rho": 8.9e3, "Cp": 421, "n_e": 18.2e28, "E_F_eV": 10.4, "k_e": 100.0, "k_l": 4.0,
        "T_D": 445.0, "v_F": 1.3e6, "Lambda_0": 10e-9, "tau_e": 4.37e-15, "R": 0.71, "xi": 13.1e-9
    },
    "Ni": {
        "rho": 8.9e3, "Cp": 440, "n_e": 18.3e28, "E_F_eV": 11.7, "k_e": 91.0, "k_l": 4.0,
        "T_D": 450.0, "v_F": 1.3e6, "Lambda_0": 10e-9, "tau_e": 3.05e-15, "R": 0.74, "xi": 12.9e-9
    },
    "Cu": {
        "rho": 8.96e3, "Cp": 385, "n_e": 8.49e28, "E_F_eV": 7.0, "k_e": 400.0, "k_l": 2.0,
        "T_D": 343.0, "v_F": 1.57e6, "Lambda_0": 39e-9, "tau_e": 32.0e-15, "R": 0.96, "xi": 12.8e-9
    },
    "Ga": {
        "rho": 5.91e3, "Cp": 370, "n_e": 1.53e28, "E_F_eV": 10.2, "k_e": 40.0, "k_l": 28.0,
        "T_D": 320.0, "v_F": 1.2e6, "Lambda_0": 25e-9, "tau_e": 0.98e-15, "R": 0.65, "xi": 18.0e-9
    },
    "Ge": {
        "rho": 5.32e3, "Cp": 320, "n_e": 2.5e19, "E_F_eV": 0.66, "k_e": 1e-3, "k_l": 60.0,
        "T_D": 374.0, "v_F": 1e5, "Lambda_0": 10e-9, "tau_e": 284e-15, "R": 0.43, "xi": 1.80e-3
    },
    "Ag": {
        "rho": 10.49e3, "Cp": 235, "n_e": 5.9e28, "E_F_eV": 5.48, "k_e": 429.0, "k_l": 2.3,
        "T_D": 215.0, "v_F": 1.39e6, "Lambda_0": 52e-9, "tau_e": 31.8e-15, "R": 0.995, "xi": 11.5e-9
    },
    "Gd": {
        "rho": 7.90e3, "Cp": 240, "n_e": 9.06e28, "E_F_eV": 7.2, "k_e": 11.0, "k_l": 8.0,
        "T_D": 170.0, "v_F": 1.5e6, "Lambda_0": 12e-9, "tau_e": 0.36e-15, "R": 0.55, "xi": 17.0e-9
    },
    "Au": {
        "rho": 19.32e3, "Cp": 129, "n_e": 5.9e28, "E_F_eV": 5.53, "k_e": 318.0, "k_l": 2.6,
        "T_D": 170.0, "v_F": 1.4e6, "Lambda_0": 40e-9, "tau_e": 30.1e-15, "R": 0.98, "xi": 13.1e-9
    }
}

material = "Cr"
params = materials[material]

k_B = const.Boltzmann
rho = params["rho"] # kg/m3
C_p = params["Cp"] # J/(kg K)
C_l = rho * C_p # J/(m3 K)
n_e = params["n_e"] # m^-3
E_F = params["E_F_eV"] * const.e # J
k_e = params["k_e"] # W/(m K)
k_l = params["k_l"] # W/(m K)
T_D = params["T_D"] # K
v_F = params["v_F"] # m/s
tau_e = params["tau_e"] # s
Lambda_0 = params["Lambda_0"]
R = params["R"]
xi = params["xi"]
gamma_e = (np.pi**2 / 2.0) * (n_e * k_B**2) / E_F # J/m3/K2
T_ref = 293.15 #Reference temperature (K)
```

```
h = 1e7 # W/m2/K
T_inf = 293.15 # K

# Laser parameters
Phi = 10.0 # Fluence (J/m2)
t_p = 100e-15 # Pulse duration (s)
t0 = 2.0 * t_p

def Lambda(Tl):
    return Lambda_0 * (T_ref / np.maximum(Tl, 1.0))

def G_of_Tl(Tl):
    return (9.0/16.0) * (n_e * k_B**2 * T_D**2 * v_F) / (Lambda(Tl) * Tl * E_F)

prefactor = np.sqrt(4*np.log(2)/np.pi) * (1-R) * Phi / (xi * t_p)
def S_of_z_t(z, t):
    return prefactor * np.exp(-z/xi) * np.exp(-4*np.log(2)*((t - t0)/t_p)**2)

# Domain and boundary conditions
L = 5.0 * xi
Nz = 121
z = np.linspace(0.0, L, Nz)
dz = z[1] - z[0]

# Initial conditions
T0 = 293.15 # K
Te0 = np.ones(Nz) * T0
Tl0 = np.ones(Nz) * T0
Qe0 = np.zeros(Nz)

def pack(Te, Tl, Qe): return np.concatenate([Te, Tl, Qe])
def unpack(y):
    N = Nz
    return y[0:N], y[N:2*N], y[2*N:3*N]

def grad_central(a):
    g = np.zeros_like(a)
    g[1:-1] = (a[2:] - a[:-2]) / (2*dz)
    g[0] = (-3*a[0] + 4*a[1] - a[2]) / (2*dz)
    g[-1] = (3*a[-1] - 4*a[-2] + a[-3]) / (2*dz)
    return g

def laplacian(a):
    l = np.zeros_like(a)
    l[1:-1] = (a[2:] - 2*a[1:-1] + a[:-2]) / (dz**2)
    l[0] = (2*a[0] - 5*a[1] + 4*a[2] - a[3]) / (dz**2)
    l[-1] = (2*a[-1] - 5*a[-2] + 4*a[-3] - a[-4]) / (dz**2)
    return l

def deriv(t, y):
    Te, Tl, Qe = unpack(y)
    Te = np.maximum(Te, 1.0)
    Tl = np.maximum(Tl, 1.0)
    Ce = gamma_e * Te
    G = G_of_Tl(Tl)

    dQe_dz = grad_central(Qe)
    dTe_dz = grad_central(Te)
    d2Tl_dz2 = laplacian(Tl)
    Svec = S_of_z_t(z, t)

    dQe_dt = (-k_e * dTe_dz - Qe) / tau_e
    dTe_dt = (-dQe_dz - G*(Te - Tl) + Svec) / Ce
    dTl_dt = (k_l * d2Tl_dz2 + G*(Te - Tl)) / C_l

    # BC: no electronic flux
    Qe[0] = Qe[-1] = 0.0
    dQe_dt[0] = dQe_dt[-1] = 0.0

    # Newton cooling at bottom
    q_int = -k_l * (Tl[0] - Tl[1]) / dz
    q_bnd = h * (Tl[0] - T_inf)
    dTl_dt[-1] = (G[-1]*(Te[-1]-Tl[-1]) + (q_int - q_bnd)/dz) / C_l

    return pack(dTe_dt, dTl_dt, dQe_dt)

# Temporal integration
t_final = 1e-12
t_eval = np.linspace(0.0, t_final, 800)
y0 = pack(Te0, Tl0, Qe0)

sol = solve_ivp(deriv, (0.0, t_final), y0, method='BDF',
                t_eval=t_eval, rtol=1e-6, atol=1e-8, max_step=1e-14)

Te = sol.y[0:Nz, :]
Tl = sol.y[Nz:2*Nz, :]

# Diagnostics
G0 = G_of_Tl(300)
Ce0 = gamma_e * 300
```

```
# Find max temperatures times
idx_Te_max = np.argmax(Te[0, :])
idx_Tl_max = np.argmax(Tl[0, :])

t_Te_max = sol.t[idx_Te_max] * 1e12 # ps
t_Tl_max = sol.t[idx_Tl_max] * 1e12 # ps

Te_max = Te[0, idx_Te_max]
Tl_max = Tl[0, idx_Tl_max]

# Plot
plt.figure(figsize=(9,6))
plt.plot(sol.t*1e12, Te[0,:], color='darkorange', label="T$_e$ (z=0)")
plt.plot(sol.t*1e12, Tl[0,:], color='darkslategray', label="T$_l$ (z=0)")
plt.scatter(t_Te_max, Te_max, color='darkorange', s=50, zorder=5)
plt.scatter(t_Tl_max, Tl_max, color='darkslategray', s=50, zorder=5)
plt.annotate(
    f"T$_{{e,\\,max}}$ = {Te_max:.0f} K\n(t = {t_Te_max:.2f} ps)",
    xy=(t_Te_max, Te_max),
    xytext=(t_Te_max + 0.2, Te_max - 0.1*(Te_max - Tl_max)),
    arrowprops=dict(arrowstyle="->", color='darkorange', lw=1.5),
    fontsize=16, color='darkorange'
)
plt.annotate(
    f"T$_{{l,\\,max}}$ = {Tl_max:.0f} K\n(t = {t_Tl_max:.2f} ps)",
    xy=(t_Tl_max, Tl_max),
    xytext=(t_Tl_max + 0.2, Tl_max + 0.2*(Te_max - Tl_max)),
    arrowprops=dict(arrowstyle="->", color='darkslategray', lw=1.5),
    fontsize=16, color='darkslategray'
)
plt.xlabel("Time (ps)", fontsize=20)
plt.ylabel("Temperature (K)", fontsize=20)
plt.xticks(fontsize=15); plt.yticks(fontsize=15)
plt.legend(loc='upper right', fontsize=16, labelspacing=0.04)
plt.savefig("TTM_simulation_Cr.svg", format="svg")
plt.show()

print(f"T_e max at the surface = {Te_max:.1f} K (t = {t_Te_max:.3f} ps)")
print(f"T_l max at the surface = {Tl_max:.1f} K (t = {t_Tl_max:.3f} ps)")
```

D.4 Numerical simulation of the strain profile in Thomsen's formalism

```
import numpy as np
import matplotlib.pyplot as plt
import matplotlib.cm as cm
from matplotlib.ticker import ScalarFormatter

# ---------------------------
# Materials & parameters
# ---------------------------
# Film (Cr)
nu_f = 0.21 # Poisson's ratio (film)
rho_f = 7190.0 # film density (kg/m^3)
v_f = 6.0e3 # longitudinal sound velocity in the film (m/s)

# Substrate (SiO2)
rho_s = 2200.0 # substrate density (kg/m^3)
v_s = 5.9e3 # longitudinal sound velocity in the substrate (m/s)

# Acoustic impedances
Z_f = rho_f * v_f
Z_s = rho_s * v_s

# Interface transmission coefficient (normal incidence, L->L)
t_ac = (2.0 * Z_s) / (Z_s + Z_f) # transmission into the substrate

# Thermoelastic source in the film
alpha = 4.9e-6 # thermal expansion coefficient in Cr (1/K)
DeltaT = 150.0 # temperature rise in the film in Cr (K)
epsilon_th = alpha * DeltaT

# Effective width and attenuation in the substrate
tau_eff = 0.4e-12 # effective electron-phonon thermalization time (s)
xi = 18e-9 # penetration depth in Cr at 800 nm (m)
gamma = 1.5e6 # acoustic attenuation in SiO2 at ~40 GHz (1/m)

epsilon0 = ((1.0 + nu_f) / (1.0 - nu_f)) * epsilon_th * t_ac * (v_f / v_s)

# ---------------------------
# Spatial and temporal domains
# ---------------------------
z = np.linspace(0, 1000e-9, 50000) # depth (m)
n_values = np.array([ 5, 10, 20, 30, 40, 50])
times = n_values * xi / v_s
```

```
# --------------------------
# Plot of the strain profile
# --------------------------
colors = cm.viridis(np.linspace(0, 1, len(times)))
plt.figure(figsize=(10, 5))

for i, (n, t) in enumerate(zip(n_values, times)):
    # Temporal Heaviside (here t>=0 so =1; kept for clarity)
    H_t = 1.0 if t >= 0 else 0.0

    # Causal bipolar profile (film -> substrate), propagation along +z
    term = np.where(
        z > v_s * t,
        -0.5 * np.exp(-(z - v_s * t) / xi),
        +0.5 * np.exp((z - v_s * t) / xi)
    )

    epsilon = epsilon0 * H_t * np.exp(-gamma * z) * term

    z_nm = z * 1e9
    plt.plot(z_nm, epsilon, color=colors[i], label=rf"$t = {n}\,\xi_{{\rm eff}}/v_s$")

    # Annotate at z = v_s * t only if within the plotted range
    z_ann = v_s * t
    if z_ann <= z[-1]:
        plt.text(
            z_ann * 1e9,
            max(epsilon) + 1e-5,
            rf"$\frac{{{n}\,\xi}}{{v_s}}$",
            fontsize=20, ha='center', va='bottom', color=colors[i]
        )

# Envelope of extrema over time: +-(epsilon0/2) * exp(-gamma*z)
env = 0.5 * epsilon0 * np.exp(-gamma * z)
z_nm = z * 1e9
plt.plot(z_nm, +env, linestyle="dotted", linewidth=2, color='k')
plt.plot(z_nm, -env, linestyle="dotted", linewidth=2, color='k')

plt.xlabel("Depth $z$ (nm)", fontsize=20)
plt.ylabel("Strain $\\varepsilon$", fontsize=20)
ax = plt.gca()
formatter = ScalarFormatter(useMathText=True); formatter.set_powerlimits((-3, 3))
ax.yaxis.set_major_formatter(formatter); ax.yaxis.get_offset_text().set_fontsize(16)
plt.xticks(fontsize=15); plt.yticks(fontsize=15)
plt.axhline(0, color='k', linewidth=0.8)
plt.xlim(0, z[-1] * 1e9)
plt.ylim(-3e-4, 4e-4)
plt.savefig("strain_profile_film_to_substrate.svg", format="svg")
plt.show()
```

D.5 Numerical simulation of the photoelastic detection of longitudinal acoustic waves

```
import numpy as np
import matplotlib.pyplot as plt
from scipy.fft import fft, fftfreq
from scipy.constants import c
from scipy.interpolate import interp1d
import time
import pandas as pd

# Start timer
start_time = time.time()

#####################################
# Complex refractive indices of metal films are extracted from refractiveindex.info
# and stored in a CSV database to enable automatic wavelength interpolation.
# If the database is unavailable, manually define n, kappa, and xi.
#####################################

# Optical property database
optical_db = pd.read_csv("metal_optical_database.csv")

def get_nk_from_csv(filepath, material, lambda_m):
    lambda_um = lambda_m * 1e6 # Convert wavelength to microns

    df = pd.read_csv(filepath, sep=";")
    df.columns = df.columns.str.strip()

    if material not in df.columns:
        print("Requested material:", material)
        print("Available columns:", df.columns.tolist())
        raise ValueError(f"Material '{material}' is not found in the file.")

    col_data = df[material].dropna().iloc[1:]
```

```
    wavelengths = []
    n_vals = []
    kappa_vals = []

    for line in col_data:
        try:
            parts = line.strip().split(",")
            if len(parts) != 3:
                continue
            wl, n, kappa = map(float, parts)
            wavelengths.append(wl)
            n_vals.append(n)
            kappa_vals.append(kappa)
        except Exception as e:
            print(f"Error parsing line '{line}': {e}")
            continue

    interp_n = interp1d(wavelengths, n_vals, kind="cubic", fill_value="extrapolate", bounds_error=False)
    interp_k = interp1d(wavelengths, kappa_vals, kind="cubic", fill_value="extrapolate", bounds_error=False)

    n = float(interp_n(lambda_um))
    kappa = float(interp_k(lambda_um))
    return n + 1j * kappa

####################################
# Dispersion relations for transparent substrates
####################################

def dispersion_substrate(substrate, wavelength_nm):
    wavelength_um = wavelength_nm * 1e-3 # Convert nm to microns
    wl2 = wavelength_um**2

    if substrate == "SiO2":
        # Fused silica (Malitson)
        B1, B2, B3 = 0.6961663, 0.4079426, 0.8974794
        C1, C2, C3 = 0.0684043**2, 0.1162414**2, 9.896161**2
        n2 = 1 + B1*wl2/(wl2 - C1) + B2*wl2/(wl2 - C2) + B3*wl2/(wl2 - C3)
        return complex(np.sqrt(n2), 0.0)

    elif substrate == "Sapphire":
        # Sapphire (ordinary axis) approximation
        B1, B2, B3 = 1.4313493, 0.65054713, 5.3414021
        C1, C2, C3 = 0.0726631**2, 0.1193242**2, 18.028251**2
        n2 = 1 + B1*wl2/(wl2 - C1) + B2*wl2/(wl2 - C2) + B3*wl2/(wl2 - C3)
        return complex(np.sqrt(n2), 0.0)

    else:
        raise ValueError(f"Substrate '{substrate}' not implemented in dispersion model.")

OPTICAL_DB_PATH = "metal_optical_database.csv"

films = {
    "Au": {"rho": 19300, "vf": 3.24e3, "alpha": 14.2e-6, "gamma_f": 1e10,
        "get_nk": lambda lambda_probe: get_nk_from_csv(OPTICAL_DB_PATH, "Au", lambda_probe)
    },
    "Al": {"rho": 2700, "vf": 3.1e3, "alpha": 23e-6, "gamma_f": 1e10,
        "get_nk": lambda lambda_probe: get_nk_from_csv(OPTICAL_DB_PATH, "Al", lambda_probe)
    },
    "Ni": {"rho": 8900, "vf": 4.9e3, "alpha": 13.4e-6, "gamma_f": 1e10,
        "get_nk": lambda lambda_probe: get_nk_from_csv(OPTICAL_DB_PATH, "Ni", lambda_probe)
    },
    "Co": {"rho": 8900, "vf": 5.0e3, "alpha": 13.0e-6, "gamma_f": 1e10,
        "get_nk": lambda lambda_probe: get_nk_from_csv(OPTICAL_DB_PATH, "Co", lambda_probe)
    },
    "Cr": {"rho": 7150, "vf": 5.94e3, "alpha": 4.9e-6, "gamma_f": 1e10,
        "get_nk": lambda lambda_probe: get_nk_from_csv(OPTICAL_DB_PATH, "Cr", lambda_probe)
    }
}

# Substrate materials
substrates = {
    "SiO2": {"rho": 2200, "vs": 5.9e3, "gamma": 2e5, "p33": 0.22,
            "get_nk": lambda lambda_probe: dispersion_substrate("SiO2", lambda_probe * 1e9)},
    "Sapphire": {"rho": 3980, "vs": 11.0e3, "gamma": 2e5, "p33": 0.18,
            "get_nk": lambda lambda_probe: dispersion_substrate("Sapphire", lambda_probe * 1e9)}
}

# Initialize physical parameters
def init_params(film_name, substrate_name, lambda_probe_nm, lambda_pump_nm):
    lambda_probe = lambda_probe_nm * 1e-9 # probe wavelength in meters
    lambda_pump = lambda_pump_nm * 1e-9 # pump wavelength in meters

    film = films[film_name]
    sub = substrates[substrate_name]

    # Optical properties at probe wavelength
    n_complex_probe = film["get_nk"](lambda_probe)
    n_f = n_complex_probe.real
    kappa_f = n_complex_probe.imag
```

```
    # Compute xi using imaginary part at pump wavelength
    kappa_pump = get_nk_from_csv(OPTICAL_DB_PATH, film_name, lambda_pump).imag
    xi = lambda_pump / (4 * np.pi * kappa_pump)

    # Substrate index at probe wavelength
    n_s = sub["get_nk"](lambda_probe).real

    # Wavevectors
    k0 = 2 * np.pi / lambda_probe
    k = n_s * k0
    k_f = k0 * (n_f + 1j * kappa_f)

    return {"lambda_probe": lambda_probe, "lambda_pump": lambda_pump, "n_f": n_f,
        "kappa_f": kappa_f, "n_s": n_s, "k0": k0, "k": k, "k_f": k_f, "rho_f": film["rho"],
        "vf": film["vf"], "alpha": film["alpha"], "p33": sub["p33"], "xi": xi, "rho_s": sub["rho"],
        "vs": sub["vs"], "gamma": sub["gamma"], "gamma_f": film["gamma_f"]}

# Initialize for specific wavelength
lambda_pump_nm = 587
lambda_probe_nm = 587
params = init_params("Cr", "SiO2", lambda_probe_nm, lambda_pump_nm)

# === CONSTANT PARAMETERS ===
# Pump laser pulse
tau_p = 1000e-15
# Optical constants
n_s = params["n_s"]
n_f = params["n_f"]
kappa_f = params["kappa_f"]
vs = params["vs"]
vf = params["vf"]
xi = params["xi"]
gamma = params["gamma"]
gamma_f = params["gamma_f"]
lambda_probe = params["lambda_probe"]
k0 = params["k0"]
k = params["k"]
k_f = params["k_f"]
rho_f = params["rho_f"]
rho_s = params["rho_s"]

Z_f = rho_f * vf
Z_s = rho_s * vs
r_ac = (Z_s - Z_f) / (Z_s + Z_f)
t_ac = 2 * Z_f / (Z_f + Z_s)

# Thermal loading
DeltaT = 150
nu = 0.44
epsilon_0 = (1 + nu)/(1 - nu) * params["alpha"] * DeltaT * t_ac * vf / vs

# Photoelasticity
p33 = params["p33"]
photoelastic_coeff = k0 * n_s**3 * p33

# Time grid for time-domain trace
t_min_plot = -50e-12
t_max_plot = 1.5e-9
N_plot = 50000
t_array_plot = np.linspace(t_min_plot, t_max_plot, N_plot)
dt_plot = t_array_plot[1] - t_array_plot[0]

# Time grid for FFT (reduced grid reduces complexity)
t_min_fft = 20e-12
t_max_fft = 500e-12
N_fft = 2500
t_array_fft = np.linspace(t_min_fft, t_max_fft, N_fft)
dt_fft = t_array_fft[1] - t_array_fft[0]

# Spatial grid
z = np.linspace(0, vs * t_max_plot + 3 * xi, 15000)
attenuation_z = np.exp(-gamma * z)

# Electronic peak + thermal background
sigma_elec = 100e-15
A_elec = 2.0e-3
A_th = 1.0e-3
tau_th = 0.7e-9
t_th_delay = 500e-15

# === MAIN COMPUTATION FUNCTION ===
def calcul_deltaR(d, plot_trace=False):
    t_array = t_array_plot if plot_trace else t_array_fft
    dt = dt_plot if plot_trace else dt_fft

    d_prime = d * vs / vf

    # Optical reflection coefficient of the multilayer
    r1 = (n_s - n_f - 1j * kappa_f) / (n_s + n_f + 1j * kappa_f)
```

```
    r2 = (n_f + 1j * kappa_f - 1) / (n_f + 1j * kappa_f + 1)
    t1 = 2 * n_s / (n_s + n_f + 1j * kappa_f)
    tau1 = (2 * n_f + 2j * kappa_f) / (n_s + n_f + 1j * kappa_f)
    r_sf = r1 + (t1 * tau1 * r2 * np.exp(2j * k_f * d)) / (1 + r1 * r2 * np.exp(2j * k_f * d))
    R = np.abs(r_sf)**2
    phi = np.angle(r_sf)

    psi = (
        np.pi + 2 * k * d_prime - phi
        - np.arctan((r_ac * np.sin(4 * k * d_prime)) / (1 + r_ac * np.cos(4 * k * d_prime)))
    )

    # Fabry-Perot amplitude modulation
    FP_factor = (np.sqrt(R) * (1 - R)) / np.abs(1 + r_ac * np.exp(4j * k * d_prime))


    deltaR_total = np.zeros_like(t_array)

    for i, t_eff in enumerate(t_array):
        if t_eff < 0:
            continue

        # Temporal coherence factor
        t_coh = np.exp(- (4 * np.log(2) * n_s**2 * t_eff**2) / (c**2 * tau_p**2))

        bipolar_strain = np.where(
            z >= vs * t_eff,
            -0.5 * np.exp(-(z - vs * t_eff) / xi),
            +0.5 * np.exp(+(z - vs * t_eff) / xi)
        )
        epsilon = epsilon_0 * bipolar_strain * attenuation_z

        integrand = epsilon * np.cos(2 * k * z - psi)
        integral = np.trapz(integrand, z)
        deltaR_total[i] += -1 * k0 * n_s**3 * p33 * FP_factor * t_coh * integral * (1 - np.cos(2 * k * d_prime))

        # Visualization of the strain pulse propagating in the substrate
        '''
        if i % 200 == 0:
            plt.plot(z * 1e9, epsilon, label=f"t = {t_eff*1e12:.1f} ps")
            plt.xlabel("z (nm)")
            plt.ylabel(r"$\varepsilon(z, t)$")
            plt.legend()
            plt.show()
        '''

    # Add electronic and thermal contributions
    deltaR_total += A_elec * np.exp(- t_array**2 / (2 * sigma_elec**2))
    deltaR_total += np.where(t_array >= t_th_delay, A_th * np.exp(-t_array / tau_th), 0)

    # Plot time-domain trace
    if plot_trace:
        plt.figure(figsize=(9,6))
        plt.plot(t_array * 1e12, deltaR_total, label=f"d = {d*1e9:.1f} nm", color='royalblue')
        plt.xlabel("Time (ps)", fontsize=20)
        plt.ylabel(r"$\Delta R$", fontsize=20)
        plt.xticks(fontsize=15); plt.yticks(fontsize=15)
        plt.ticklabel_format(axis='y', style='sci', scilimits=(0,0))
        plt.legend(loc='upper right', fontsize=16)
        filename = f"Delta_R_at_d_{d*1e9:.0f}nm.svg"
        plt.savefig(filename, format="svg")
        plt.show()

    # FFT
    freqs = fftfreq(len(t_array), d=dt)
    deltaR_derivative = np.gradient(deltaR_total, dt)
    fft_data = fft(deltaR_derivative)
    mag = (2 / len(t_array)) * np.abs(fft_data)
    freqs_GHz = freqs[freqs >= 0] * 1e-9
    mag = mag[freqs >= 0]

    # Brillouin frequency window
    f_brillouin = 2 * n_s * vs / lambda_probe
    f_brillouin_GHz = f_brillouin * 1e-9
    f_min = f_brillouin_GHz - 5
    f_max = f_brillouin_GHz + 5
    window = (freqs_GHz > f_min) & (freqs_GHz < f_max)
    max_amp = np.max(mag[window])

    return max_amp

# FFT sweep over thickness
d_array = np.linspace(1e-9, 450e-9, 450)
amplitudes = [calcul_deltaR(d) for d in d_array]
amplitudes /= np.max(amplitudes)

# Identify max and min FFT amplitudes
idx_max = np.argmax(amplitudes)
idx_min = np.argmin(amplitudes)
```

```
d_max = d_array[idx_max]
d_min = d_array[idx_min]

print(f"Max FFT at d = {d_max*1e9:.1f} nm")
print(f"Min FFT at d = {d_min*1e9:.1f} nm")

# Plot time-domain traces for min and max FFT cases
_ = calcul_deltaR(d=d_max, plot_trace=True)
_ = calcul_deltaR(d=d_min, plot_trace=True)
#_ = calcul_deltaR(d=70e-9, plot_trace=True)

# Plot result
plt.figure(figsize=(9, 6))
plt.plot(d_array * 1e9, amplitudes, color='crimson')
plt.xlabel("Film thickness $d$ (nm)", fontsize=20)
plt.ylabel("Normalized acoustic amplitude", fontsize=20)
plt.xticks(fontsize=15); plt.yticks(fontsize=15)
plt.savefig("Acoustic_amplitude_vs_film_thickness.svg", format="svg")
plt.show()

# Execution time
end_time = time.time()
elapsed = end_time - start_time
print(f"\nTotal execution time: {elapsed:.2f} seconds\n")
```

D.6 Numerical simulation of the three-temperature model

```
import numpy as np
from scipy.integrate import solve_ivp
import matplotlib.pyplot as plt

# ============================================================
# 0D THREE-TEMPERATURE MODEL (AT THE SURFACE)
# ============================================================

materials = {
    "Ni": {"G_el": 9.4e17, "G_es": 1.31e18, "G_sl": 0.3e17, "gamma_e": 92, "C_l": 3.9e6, "C_s": 2.78e6,
           "R": 0.74, "xi": 12.9e-9, "J": 1.0, "S": 1.0, "L": 0.0, "T_C": 627},
    "Co": {"G_el": 1e18, "G_es": 4e17, "G_sl": 5e16, "gamma_e": 5.1e3, "C_l": 3.8e6, "C_s": 1e5,
           "R": 0.71, "xi": 13.0e-9, "J": 1.5, "S": 1.5, "L": 0.0, "T_C": 1388},
    "Fe": {"G_el": 1e18, "G_es": 5e17, "G_sl": 1e17, "gamma_e": 4.5e3, "C_l": 3.5e6, "C_s": 1e5,
           "R": 0.56, "xi": 18.6e-9, "J": 2.0, "S": 2.0, "L": 0.0, "T_C": 1043}
}

# ----------------------
# Material selection
# ----------------------
material = "Ni"
p = materials[material]
J = p["J"]
S = p["S"]
L = p["L"]

# ----------------------
# Laser parameters: adjust penetration depth xi to match the wavelength
# ----------------------
Phi = 10.0 # J/m^2
t_p = 100e-15 # s (pulse duration)
t0 = 2 * t_p # s (pulse peak time)
prefactor = np.sqrt(4 * np.log(2) / np.pi) * (1 - p["R"]) * Phi / (p["xi"] * t_p)

def S_laser(t):
    return prefactor * np.exp(-4 * np.log(2) * ((t - t0) / t_p)**2)

# ----------------------
# Initial conditions
# ----------------------
T0 = 293.15 # Initial temperature (K)
y0 = [T0, T0, T0] # [Te, Tl, Ts]

# ----------------------
# 3TM differential equations
# ----------------------
def deriv(t, y):
    Te, Tl, Ts = y
    Ce = p["gamma_e"] * Te
    dTe_dt = (p["G_el"] * (Tl - Te) + p["G_es"] * (Ts - Te) + S_laser(t)) / Ce
    dTs_dt = (p["G_es"] * (Te - Ts) + p["G_sl"] * (Tl - Ts)) / p["C_s"]
    dTl_dt = (p["G_el"] * (Te - Tl) + p["G_sl"] * (Ts - Tl)) / p["C_l"]
    return [dTe_dt, dTl_dt, dTs_dt]

# ----------------------
# Time integration (only positive time)
# ----------------------
t_final = 6e-12
t = np.linspace(0, t_final, 20000)
```

```
sol = solve_ivp(deriv, (0, t_final), y0, method="Radau", t_eval=t, rtol=1e-7, atol=1e-9)
Te, Tl, Ts = sol.y

# Peak temperatures and corresponding times
idx_Te_max = np.argmax(Te)
idx_Tl_max = np.argmax(Tl)
idx_Ts_max = np.argmax(Ts)

Te_max, t_Te_max = Te[idx_Te_max], sol.t[idx_Te_max] * 1e12
Tl_max, t_Tl_max = Tl[idx_Tl_max], sol.t[idx_Tl_max] * 1e12
Ts_max, t_Ts_max = Ts[idx_Ts_max], sol.t[idx_Ts_max] * 1e12

print(f"Material: {material}")
print(f"T_e max = {Te_max:.1f} K at t = {t_Te_max:.3f} ps")
print(f"T_l max = {Tl_max:.1f} K at t = {t_Tl_max:.3f} ps")
print(f"T_s max = {Ts_max:.1f} K at t = {t_Ts_max:.3f} ps")

# ----------------------
# Add negative time range for visualization
# ----------------------
t_start = -0.5e-12 # e.g., -0.5 ps before pulse
nb_pt_neg = 100
t_neg = np.linspace(t_start, 0, nb_pt_neg, endpoint=False)
Te_neg = Tl_neg = Ts_neg = np.full_like(t_neg, T0) # Constant before pulse

# Merge negative and computed parts
t_full = np.concatenate((t_neg, t))
Te = np.concatenate((Te_neg, Te))
Tl = np.concatenate((Tl_neg, Tl))
Ts = np.concatenate((Ts_neg, Ts))
t = t_full

# ----------------------
# Plot temperatures vs time
# ----------------------
plt.figure(figsize=(9, 6))
plt.plot(t * 1e12, Te, color='darkorange', label="T$_e$")
plt.plot(t * 1e12, Ts, color='seagreen', label="T$_s$")
plt.plot(t * 1e12, Tl, color='darkslategray', label="T$_l$")
plt.xlabel("Time (ps)", fontsize=20)
plt.ylabel("Temperature (K)", fontsize=20)
plt.xticks(fontsize=15); plt.yticks(fontsize=15)
plt.legend(loc='upper right', fontsize=16)

# Text box including peak values and laser parameters
textstr = '\n'.join((
    r'$\Phi = %.1f\,\mathrm{J/m^2}$' % Phi,
    r'$\tau_p = %.1f\,\mathrm{fs}$' % (t_p * 1e15),
    r'$T_{e,\max} = %.1f\,\mathrm{K}$' % Te_max,
    r'$T_{s,\max} = %.1f\,\mathrm{K}$' % Ts_max,
    r'$T_{l,\max} = %.1f\,\mathrm{K}$' % Tl_max,
))

# Add box in the center of the plot
plt.text(0.5, 0.5, textstr, transform=plt.gca().transAxes,
        fontsize=16, verticalalignment='center', horizontalalignment='center',
        bbox=dict(boxstyle="round,pad=0.4", facecolor='white', alpha=0.8))

#plt.savefig("fast_3TM_our_laser.svg", format="svg")
plt.show()

# ----------------------
# Magnetization using Bloch's law
# ----------------------
T_C = 628 # Curie temperature for Ni
B_bloch = 1.0 # Adjustable coefficient if needed

solutions_norm = np.zeros_like(Ts)
for i, T in enumerate(Ts):
    if T < T_C:
        solutions_norm[i] = 1 - B_bloch * (T / T_C)**1.5
    else:
        solutions_norm[i] = 0.0 # Force zero if Ts exceeds TC

M_norm = solutions_norm / solutions_norm[0] # Normalize to initial value

# Find maximum demagnetization
idx_M_norm_min = np.argmin(M_norm)
t_M_norm_min = t[idx_M_norm_min] * 1e12

# ----------------------
# Plot normalized magnetization vs time
# ----------------------
plt.figure(figsize=(9,6))
plt.plot(t * 1e12, M_norm, color='dodgerblue')
plt.scatter(t_M_norm_min, min(M_norm), color='dodgerblue', s=50, zorder=5)
plt.xlabel("Time (ps)", fontsize=20)
plt.ylabel("Normalized demagnetization", fontsize=20)
plt.xticks(fontsize=15); plt.yticks(fontsize=15)
plt.xlim(t_start * 1e12, t_final * 1e12); plt.ylim(min(M_norm)-0.03, 1.03)
```

```
plt.annotate(
    f"Maximum demagnetization = {(1-min(M_norm))*100:.0f} % \n(t = {t_M_norm_min:.2f} ps)",
    xy=(t_M_norm_min, np.mean([min(M_norm),max(M_norm)])),
    xytext=(t_M_norm_min, np.mean([min(M_norm),max(M_norm)])),
    fontsize=16, color='k'
)
#plt.savefig("fast_3TM_our_laser_demagnetization.svg", format="svg")
plt.show()

# ----------------------
# Print maximum demagnetization percentage
# ----------------------
deltaM = 1 - np.min(M_norm)
print(f"Maximum demagnetization: {deltaM * 100:.1f}%")
```

D.7 Numerical simulation of the Landau-Lifshitz-Gilbert equation

```
import numpy as np
import matplotlib.pyplot as plt
from mpl_toolkits.mplot3d import proj3d
from scipy.constants import mu_0

# ---------- Thermal magnetization function ----------
def Thermal_decrease(T_init, T_final, times, tau_th):
    return T_final + (T_init - T_final) * np.exp(-times / tau_th)

def M_norm(T, T_C, B):
    ratio = T / T_C
    return np.where(ratio >= 1, 0.0, (1 - B * ratio**1.5))

# ---------- Physical parameters ----------
gamma = 1.93e11 # Gyromagnetic ratio (rad/s/T)
alpha = 0.05 # Gilbert damping
T0 = 293 # Initial temperature (K)
T_init = 580 # Maximum temperature after laser heating (K)
T_final = 293 # Final temperature (K)
tau_th = 5e-10 # Thermal relaxation time (s)
T_C = 627 # Curie temperature (K)
B = 1 # Empirical constant
times = np.linspace(-0.1e-9, 3e-9, 100000)
dt = times[1] - times[0]

# Linear cooling
T_list = Thermal_decrease(T_init, T_final, times, tau_th)
M_list = M_norm(T_list, T_C, B)

M_s_eq = M_norm(T0, T_C, B) # Magnetization magnitude at equilibrium temperature

# ---------- Initial angles ----------
alpha0_deg = 0; beta0_deg = 0
alpha_H_deg = 45; beta_H_deg = 45
a0, b0 = np.radians(alpha0_deg), np.radians(beta0_deg)
aH, bH = np.radians(alpha_H_deg), np.radians(beta_H_deg)

# ---------- Effective magnetic field ----------
H_eff = np.array([
    np.cos(aH) * np.cos(bH),
    np.sin(aH) * np.cos(bH),
    np.sin(bH)
])
H_eff = H_eff / np.linalg.norm(H_eff) * 2.6e5 # Chosen magnitude (A/m)
#2.6e5 corresponds to 2*pi*10 GHz / (ommega * mu_0)

# ---------- Initial magnetization states ----------
M_pre = M_s_eq * H_eff / np.linalg.norm(H_eff) # Aligned before laser pulse
M = M_s_eq * np.array([np.cos(a0)*np.cos(b0),
                       np.sin(a0)*np.cos(b0),
                       np.sin(b0)]) # Deviation after laser pulse

trajectory = []

# ---------- Time loop ----------
for i, t in enumerate(times):
    if t <= 0:
        M_current = M_pre.copy()
    else:
        M_s = M_list[i] # Local magnetization magnitude
        M_cross_H = np.cross(M, H_eff)
        double_cross = np.cross(M, M_cross_H)

        dM_dt = (-gamma * mu_0 / (1 + alpha**2)) * M_cross_H \
        - (gamma * mu_0 * alpha / ((1 + alpha**2) * M_s)) * double_cross

        M += dt * dM_dt
        if np.linalg.norm(M) > 0:
            M = M_s * M / np.linalg.norm(M)
```

```
        M_current = M.copy()

    trajectory.append(M_current)

trajectory = np.array(trajectory)

# ---------- 3D visualization ----------
idx_t0 = np.argmin(np.abs(times - 0))
m_t0 = trajectory[idx_t0]
h_unit = H_eff / np.linalg.norm(H_eff)

fig = plt.figure(figsize=(10, 8))
ax = fig.add_subplot(111, projection='3d')
ax.plot(trajectory[3250:,0], trajectory[3250:,1], trajectory[3250:,2],
        color='crimson', linewidth=1.5, label='Precessional trajectory')
ax.quiver(0,0,0,m_t0[0],m_t0[1],m_t0[2],color='blue',linewidth=2,
          label='M after laser pulse')
ax.quiver(0,0,0,M_pre[0], M_pre[1], M_pre[2],color='black',linewidth=2,
          label='Equilibrium',normalize=False)

ax.set_xlabel(r'$M_x$', fontsize=20)
ax.set_ylabel(r'$M_y$', fontsize=20)
ax.set_zlabel(r'$M_z$', fontsize=20)
ax.xaxis.set_tick_params(labelsize=15)
ax.yaxis.set_tick_params(labelsize=15)
ax.zaxis.set_tick_params(labelsize=15)
ax.legend(loc='upper right', fontsize=16)
#plt.savefig('LLG_simulation_3D.svg', format ="svg")
plt.show()

# ---------- Kerr signal ----------
Mz_eq = M_pre[2] # Equilibrium magnetization before the laser pulse
delta_mz = trajectory[:,2] - Mz_eq # Delta Mz relative to equilibrium
delta_mz_norm = delta_mz / M_s_eq # Normalization

plt.figure(figsize=(9,6))
plt.plot(times*1e9, -1*delta_mz, color='royalblue')
plt.xlabel("Time (ns)", fontsize=20)
plt.ylabel("$\Delta M_z$", fontsize=20)
plt.xticks(fontsize=15); plt.yticks(fontsize=15)
#plt.savefig('LLG_simulation_Mz.svg', format ="svg")
plt.show()
```

D.8 Numerical simulation of giant SAW generation from optical ring pump

```
import numpy as np
import matplotlib.pyplot as plt
from scipy.special import j0 # Bessel function J0
from mpl_toolkits.mplot3d import Axes3D

# ================================================
# PHYSICAL AND GEOMETRIC PARAMETERS
# ================================================

# --- Energy deposition geometry ---
R0 = 50e-6 # Ring radius [m]
sigma = 5e-6 # Width (FWHM or std dev) [m]
lp = 100e-9 # Optical penetration depth [m]

# --- Thermo-mechanical properties ---
rho = 5100 # Density [kg/m^3]
Cp = 400 # Specific heat [J/kg/K]
K = 1.6e11 # Bulk modulus [Pa]
alpha = 9e-6 # Thermal expansion coefficient [1/K]

# --- Laser pulse ---
Q0 = 6369 # Energy density deposited [J/m^3]
tau = 600e-12 # Pulse duration [s]

# --- Surface acoustic wave (SAW) ---
v_R = 3600 # Rayleigh wave speed [m/s]

# ================================================
# THERMOELASTIC STRESS PROFILE Sigma(r)
# ================================================

r = np.linspace(0, 2 * R0, 8000)
Sigma_pk = 3 * K * alpha * Q0 * lp / (rho * Cp)
Sigma_r = Sigma_pk * np.exp(- (r - R0)**2 / (2 * sigma**2))

# ================================================
# ANALYTICAL HANKEL TRANSFORM
# ================================================

k = np.linspace(1e3, 5e7, 8000) # Wavenumbers [rad/m]
```

```
Sigma_k = 2 * np.pi * Sigma_pk * R0 * np.exp(-(k * sigma)**2 / 2) * j0(k * R0)

# ================================================
# SIMPLIFIED DISPLACEMENT SPECTRUM u_k ~ Sigma_k / k
# ================================================

u_k = Sigma_k / (k + 1e-6) # Avoid division by zero
f = v_R * k / (2 * np.pi) # Frequency [Hz]

# Key frequencies
f_star = 0.382 * v_R / R0 # Theoretical prediction
f_max = f[np.argmax(np.abs(u_k))] # Peak frequency

# ================================================
# PLOT DISPLACEMENT SPECTRUM u_k
# ================================================

plt.figure(figsize=(8, 5))
plt.plot(f * 1e-6, np.abs(u_k), label="Displacement spectrum $u_z$ (amplitude)")
plt.axvline(f_max * 1e-6, color='green', linestyle='--', label=f"Max frequency = {f_max*1e-6:.1f} MHz")
plt.axvline(f_star * 1e-6, color='red', linestyle='--', label=f"Theoretical prediction = {f_star*1e-6:.1f} MHz")
plt.xlabel("Frequency (MHz)")
plt.ylabel("Amplitude (arb. units)")
plt.title("Surface acoustic wave spectrum induced by ring-shaped laser heating")
plt.legend()
plt.grid(True)
plt.tight_layout()
plt.show()

# ================================================
# PLOT HANKEL TRANSFORM |Sigma_k|
# ================================================

plt.figure(figsize=(8, 5))
plt.plot(f[:100] * 1e-6, np.abs(Sigma_k)[:100], label=r"Hankel transform $|\tilde{\Sigma}_k|$")
plt.axvline(f_max * 1e-6, color='green', linestyle='--', label=f"Max frequency = {f_max*1e-6:.1f} MHz")
plt.axvline(f_star * 1e-6, color='red', linestyle='--', label=f"$J_0$ zero = {f_star*1e-6:.1f} MHz")
plt.xlabel("Frequency (MHz)")
plt.ylabel("Amplitude $|\Sigma_k|$")
plt.title("Unfiltered Hankel transform")
plt.grid()
plt.legend()
plt.tight_layout()
plt.show()

# ================================================
# 2D PLOT OF THE THERMAL RING PROFILE Sigma(x,y)
# ================================================

L = 2 * R0 # Window size [m]
N = 500 # Grid resolution
x = np.linspace(-L, L, N)
y = np.linspace(-L, L, N)
X, Y = np.meshgrid(x, y)
r_xy = np.sqrt(X**2 + Y**2)
Sigma_xy = Sigma_pk * np.exp(- (r_xy - R0)**2 / (2 * sigma**2))

plt.figure(figsize=(6, 5))
plt.imshow(Sigma_xy, extent=(-L*1e6, L*1e6, -L*1e6, L*1e6), origin='lower', cmap='inferno')
plt.colorbar(label="Thermal stress amplitude $\Sigma$ (arb. units)")
plt.xlabel("x-axis ($\mu$m)", fontsize=20)
plt.ylabel("y-axis ($\mu$m)", fontsize=20)
plt.xticks(fontsize=14)
plt.yticks(fontsize=14)
plt.gca().set_aspect('equal')
# plt.savefig('constraint_spatial_distribution_moke_saw.svg', format="svg")
plt.show()

# ================================================
# 3D PLOT OF Sigma(x, y) in MPa
# ================================================

fig = plt.figure(figsize=(8, 6))
ax = fig.add_subplot(111, projection='3d')

X_plot = X * 1e6 # in microns
Y_plot = Y * 1e6 # in microns
Z_plot = Sigma_xy / 1e6 # in MPa

surf = ax.plot_surface(X_plot, Y_plot, Z_plot, cmap='viridis', edgecolor='none')
ax.set_title("Projected thermoelastic stress $\Sigma$(x, y) at t = 0")
ax.set_xlabel("x ($\mu$m)")
ax.set_ylabel("y ($\mu$m)")
ax.set_zlabel("$\Sigma$ (MPa)")
ax.set_zlim(0, np.max(Z_plot) * 1.1)
fig.colorbar(surf, shrink=0.6, aspect=10, label='Stress amplitude $\Sigma$ (MPa)')
plt.tight_layout()
plt.show()

# ================================================
```

```
# 3D PLOT OF APPROXIMATED HANKEL TRANSFORM Sigma_0(k)
# ====================================================

Sigma_0 = 2 * np.pi * Sigma_pk * R0 * np.exp(-(k * sigma)**2 / 2) * j0(k * R0)

# ====================================================
# COMPUTE u_z(r, t) FOR MULTIPLE TIME STEPS
# ====================================================

from matplotlib.cm import get_cmap

# --- Time samples (seconds) ---
t_list = np.linspace(0.0, 35e-9, 100)
omega = v_R * k
G_R = 1 / (rho * v_R**2) # [m/Pa]

# --- Colormap for time series ---
cmap = get_cmap('plasma')
colors = cmap(np.linspace(0, 1, len(t_list)))
u_at_center = np.zeros(len(t_list))

# --- Main figure ---
plt.figure(figsize=(10, 6))

for idx, t0 in enumerate(t_list):
    phase = np.exp(1j * omega * t0)
    u_r = np.zeros_like(r)

    for i, ri in enumerate(r):
        J = j0(k * ri)
        integrand = k * Sigma_0 * G_R * J * phase
        u_r[i] = np.trapz(integrand, k).real

    u_at_center[idx] = u_r[0]

    # Symmetry around r = 0
    r_full = np.concatenate([-r[::-1], r])
    u_r_full = np.concatenate([u_r[::-1], u_r])

    plt.plot(r_full * 1e6, u_r_full * 1e9, color=colors[idx],
             label=fr"$t = {t0*1e9:.2f}$ ns")

# --- Labels and formatting ---
plt.xlabel("x-axis ($\mu$m)", fontsize=20)
plt.ylabel("Surface displacement $u_z$ (nm)", fontsize=20)
plt.xticks(fontsize=15)
plt.yticks(fontsize=15)
plt.legend(loc='upper right', fontsize=16)
# plt.savefig('u_z_moke_saw.svg', format="svg")
plt.show()

# --- Plot time evolution at the ring center ---
plt.figure(figsize=(9, 6))
plt.plot(t_list * 1e9, u_at_center * 1e9)
plt.xlabel("Time (ns)", fontsize=20)
plt.ylabel("Surface displacement $u_z$\nat the center of the ring (nm)", fontsize=18)
plt.xticks(fontsize=15)
plt.yticks(fontsize=15)
plt.savefig('u_z_center_temporal_moke_saw.svg', format="svg")
plt.show()
```

COLLEGE SCIENCES DE LA MATIERE
DOCTORAL DES MOLECULES
BRETAGNE ET MATERIAUX

Université de Rennes

Titre : Étude acoustique, magnétique, et structurale de matériaux corrélés via l'optique ultrarapide

Mot clés : Optique ultrarapide, acoustique, magnétisme, supraconductivité

Résumé : Cette thèse s'inscrit dans le cadre de l'étude des dynamiques ultrarapides à l'échelle picoseconde dans les matériaux. Une première partie est consacrée à l'acoustique picoseconde. Elle présente la génération et la détection tout optique d'ondes longitudinales dans des matériaux transparents, via la transduction thermoélastique et la détection photoacoustique. La génération non linéaire par absorption multiphotonique est également abordée, ainsi que les résultats obtenus, permettant l'étude de solides cristallins et la quantification du relargage thermique dans des composés organométalliques complexes étudiés pour des applications biomédicales. Une seconde partie porte sur l'étude tout optique des propriétés magnétiques des matériaux. Elle traite du couplage spin–réseau dans des hétérostructures ferromagnétiques épitaxiées à forte anisotropie magnétique, ainsi que de l'influence d'ondes de surface intenses, générées optiquement, sur l'état d'aimantation d'un film mince ferromagnétique. Cette partie se termine par la détection optique de la transition supraconductrice dans un film mince d'YBCO, mise en évidence grâce à l'acoustique picoseconde et à la précession magnétique gigahertz. Cette thèse démontre les capacités de l'optique ultrarapide à induire et sonder une grande variété de phénomènes dans une large gamme de matériaux.

Title: Ultrafast Optical Studies of Acoustic, Magnetic, and Structural Phase Dynamics in Correlated Materials

Keywords: Ultrafast optics, acoustics, magnetism, superconductivity

Abstract: This thesis is part of the broader effort to study ultrafast dynamics at the picosecond scale in materials. The first part focuses on picosecond acoustics. It presents the all-optical generation and detection of longitudinal acoustic waves in transparent materials via thermoelastic transduction and photoacoustic detection. Nonlinear generation through multiphoton absorption is also investigated, along with results enabling the study of crystalline solids and the quantification of picosecond-scale thermal release in complex organometallic compounds designed for biomedical applications. The second part deals with the all-optical investigation of magnetic properties in materials. It explores spin–lattice coupling in epitaxial ferromagnetic heterostructures with strong magnetic anisotropy, as well as the influence of intense surface acoustic waves—optically generated—on the magnetization state of a ferromagnetic thin film. This section concludes with the optical detection of the superconducting transition in a thin YBCO film, observed through picosecond acoustics and gigahertz magnetic precession. This work demonstrates the capabilities of ultrafast optics to induce and probe a wide range of phenomena in various material systems.